

# UC Riverside

## UC Riverside Electronic Theses and Dissertations

### Title

The Impact of Roadside Barriers and Buildings on Near Road Concentrations of Vehicle Emissions

### Permalink

<https://escholarship.org/uc/item/0qf034wj>

### Author

Schulte, Nico

### Publication Date

2015

Peer reviewed|Thesis/dissertation

UNIVERSITY OF CALIFORNIA  
RIVERSIDE

The Impact of Roadside Barriers and Buildings on Near Road Concentrations of Vehicle  
Emissions

A Dissertation submitted in partial satisfaction  
of the requirements for the degree of

Doctor of Philosophy

in

Mechanical Engineering

by

Nico Schulte

December 2015

Dissertation Committee:

Dr. Akula Venkatram, Chairperson

Dr. Marko Princevac

Dr. Heejung Jung

Copyright by  
Nico Schulte  
2015

The Dissertation of Nico Schulte is approved:

---

---

---

Committee Chairperson

University of California, Riverside

## Acknowledgments

Many individuals have supported me during the work on this dissertation. I am grateful for the mentoring of my advisor, Dr. Akula Venkatram. He is an excellent teacher and role model. He has provided great opportunities, taught me much, and has been a huge influence on my life and career. I thank my committee members, Dr. Marko Princevac and Dr. Heejung Jung, who challenged me to improve and supported my work. I am grateful for my colleagues and friends, Dr. Si Tan, Mr. Faraz Enayati Ahangar, Mr. Morteza Amini, Dr. Qiguo Jing, and Dr. Sam Pournazeri. We have spent countless hours working together during field measurements and data analysis. This work could not have been completed without them. I thank my fiancée, Mayra, who has always supported and encouraged me. I thank my parents, brothers, and sister for their support and encouragement.

The research in chapter 2 was supported by funding provided by the South Coast Air Quality Management District. I thank the U.S. EPA for providing the wind tunnel and Idaho Falls data.

The research in chapter 3 was supported by funding provided by the California Air Resources Board under contract number 12-308 and the University of California Transportation Center under contract number 65A0460. I thank the Lower Saxony Ministry for Environment, Energy, and Climate for providing the data collected in Göttinger Strasse.

I thank the University of California Center on Economic Competitiveness in Transportation (UCCONNECT), for providing financial support during the final year of my dissertation work.

I thank the University of California Riverside Dissertation Year Program for providing financial support to me during the completion of my dissertation.

I am grateful for the support of the city workers and building managers who have enabled this research: Bo Harper, Melanie Cariaga, Fabian Cheng at the Los Angeles Bureau of Street Lighting, Mark Persico and Mike Schnepf at Temple City, Jesse De Anda and Renato Talavera at Beverly Hills, Kirsten Rosales, Jim Stone, and Ed Luke at Riverside. I thank Michelle Peralta, Fernando Rodriguez, and Alexander Jaramillo for helping with field measurements and traffic counting.

The text in chapter 2 of this dissertation is in part a reprint of the material as it appears in Schulte, N., Snyder, M., Isakov, V., Heist, D., Venkatram, A., 2014. Effects of solid barriers on dispersion of roadway emissions. *Atmospheric Environment* 97, 286-295.

The text in chapter 3 of this dissertation is in part a reprint of the material as it appears in Schulte, N., Tan, S., Venkatram, A., 2015. The Ratio of Effective Building Height to Street Width Governs Dispersion of Local Vehicle Emissions. *Atmospheric Environment* 112, 54-63.

To Mayra, with love

## ABSTRACT OF THE DISSERTATION

The Impact of Roadside Barriers and Buildings on Near Road Concentrations of Vehicle Emissions

by

Nico Schulte

Doctor of Philosophy, Graduate Program in Mechanical Engineering  
University of California, Riverside, December 2015  
Dr. Akula Venkatram, Chairperson

Exposure to elevated concentrations of vehicle emitted pollutants is associated with negative health effects. Elevated concentrations are typically found within several hundred meters of high traffic roads, where atmospheric dispersion has not sufficiently diluted pollutants. Tall buildings next to roads reduce dispersion, thereby creating pollutant hot spots and increasing exposure to vehicle emissions for city residents. Roadside barriers enhance dispersion of roadway emissions and thus can be used to mitigate elevated concentrations next to large roads. The work in this thesis develops semi-empirical dispersion models that are useful for estimating near road concentrations of vehicle emissions when there are buildings or barriers next to the road.

Dispersion models that account for the effect of near road barriers on concentrations are developed and evaluated with data from a wind tunnel and a field tracer study. The model evaluation shows that the primary effect of roadside barriers is enhancement of the vertical mixing by an amount proportional to the barrier height. Additionally, turbulence is enhanced in the barrier's wake, resulting in more rapid growth of the pollutant plume. The

models perform well during neutral and stable atmospheric conditions. During unstable conditions the models overestimate concentrations. A model that accounts for reduction of the mean wind speed in the barrier wake is unbiased for all stabilities.

Models of the impact of tall buildings next to the road on near road concentrations of vehicle emissions are developed. The models are evaluated with data from field measurements conducted in Los Angeles and Riverside counties, CA, and with data from an urban area in Hannover, Germany. The study specifically investigates dispersion in cities with significant building height variability. Model evaluation shows that vertical turbulent transport dominates dispersion in cities. The primary variables governing near road concentrations of vehicle emissions in cities are the ratio of area weighted building height to street width and the vertical averaged standard deviation of vertical velocity fluctuations. The model informs design of transit oriented developments, dense residential areas located in close proximity to transportation infrastructure, which are used to reduce pollution and greenhouse gas emissions due to transportation.

# Contents

<b>List of Figures</b>	<b>xii</b>
<b>List of Tables</b>	<b>xxiv</b>
<b>1 Motivation, Objectives, and Approach</b>	<b>1</b>
1.1 Problem Statement . . . . .	1
1.2 Background . . . . .	4
1.2.1 Assessment of the variables governing dispersion of traffic emissions in transit oriented developments with nonuniform building height . . . . .	4
1.2.2 Evaluating the effectiveness of solid barriers next to roads to reduce near-road pollutant concentrations . . . . .	8
1.3 Objectives . . . . .	11
1.4 Structure of the Dissertation . . . . .	12
<b>2 Effect of Solid Barriers on Dispersion from Roads</b>	<b>13</b>
2.1 Introduction . . . . .	13
2.2 Background . . . . .	14
2.2.1 Wind Tunnel Study . . . . .	21
2.2.2 Tracer Study . . . . .	25
2.3 Model Evaluation . . . . .	29
2.3.1 Source Shift Model . . . . .	35
2.3.2 Mixed wake Model . . . . .	43
2.3.3 Puttock-Hunt Model . . . . .	48
2.3.4 Modification of Mean Wind Profile Downwind of the Barrier . . . . .	58

2.4	Effectiveness of Roadside Barriers to Reduce Near-Road Concentrations of Vehicle Emissions . . . . .	61
2.5	Conclusions . . . . .	65
<b>3</b>	<b>Assessment of the variables governing dispersion of traffic emissions in transit oriented developments with nonuniform building height</b>	<b>69</b>
3.1	Introduction . . . . .	69
3.2	Background . . . . .	71
3.2.1	Operational Street Pollution Model (OSPM) . . . . .	78
3.2.2	Urban Canopy Models . . . . .	80
3.3	Analysis of Long Term Measurements of Near Road Concentrations of Vehicle Emissions to Determine the Primary Variables Governing Dispersion in Urban Streets . . . . .	88
3.3.1	Data Set . . . . .	89
3.3.2	Method . . . . .	90
3.3.3	Results . . . . .	92
3.3.4	Effect of Initial Vertical Mixing . . . . .	97
3.3.5	Influence of Receptor Height . . . . .	99
3.3.6	Discussion . . . . .	104
3.4	Design of Field Measurements in Los Angeles . . . . .	105
3.4.1	Instrumentation . . . . .	109
3.4.2	Los Angeles - 8th St, April 23 - May 13 2014 . . . . .	110
3.4.3	Los Angeles - 7th St and Broadway, September 20, 2013 . . . . .	116
3.4.4	Temple City - Las Tunas Dr and Temple City Blvd . . . . .	118
3.4.5	Beverly Hills - Wilshire Blvd . . . . .	120
3.5	Interpretation of Ultrafine Particle Concentration Data From the Los Angeles Field Study Using Several Dispersion Models . . . . .	127
3.5.1	Vertical Dispersion Model . . . . .	132
3.5.2	Evaluation of VDM With the Local Contribution . . . . .	137
3.5.3	Discussion . . . . .	143
3.6	Evaluation of Vertical Dispersion Model with Measurements in Riverside	144
3.6.1	Description of Field Measurements in Riverside, CA . . . . .	145
3.6.2	Evaluation of the Vertical Dispersion Model . . . . .	153

3.6.3	Evaluation of a Model to Estimate the Standard Deviation of Vertical Velocity Fluctuations in the Urban Area . . . . .	160
3.6.4	Discussion . . . . .	163
3.7	Conclusions . . . . .	166
<b>4</b>	<b>Conclusion</b>	<b>169</b>
<b>A</b>	<b>Calibration of Condensation Particle Counters</b>	<b>175</b>
<b>B</b>	<b>Design of a System to Enable Long Term Measurements of Near Road UFP Concentrations Using TSI3022A Condensation Particle Counters</b>	<b>181</b>
B.1	System Design . . . . .	182
B.2	Power Supply . . . . .	185
B.3	Cooling System . . . . .	187
B.4	Data Logger . . . . .	193

# List of Figures

2.1	Flow induced by a solid barrier. The mean wind direction upwind of the barrier is along the x axis. Arrows represent wind direction vectors. The black rectangle represents the barrier location. Data from EPA wind tunnel study (Heist et al., 2009). . . . .	15
2.2	Increase in turbulent kinetic energy (TKE) in the presence of a solid barrier at different distances from the 6 m tall (full scale) barrier. The increased TKE is the difference between the TKE measured in the presence of a barrier and the TKE with no barrier present. Data from EPA wind tunnel study (Heist et al., 2009). . . . .	15
2.3	Particle number and mass concentrations at different distance downwind of the freeway (a) I-710 no noise barrier (b) I-5 no noise barrier; (c) I-710 with noise barrier; (d) I-5 with noise barrier. Note: The total particle number and mass concentrations at $X = 0$ are derived from SMPS (10-225 nm) data at stationary sampling station; the concentrations at $X > 0$ are derived from FMPS (6-523 nm) data. From Ning et al. (2010). . . . .	19
2.4	Filter panel installed on a noise barrier for the SPAS study. (Magistrat Klagenfurt, 2011) . . . . .	20
2.5	Elevation view showing cross sections through the various roadway configurations studied (cases A through L corresponding to figure lettering). Flow is from left to right. Dashed line in (b) through (f) represents at-grade elevation. From (Heist et al., 2009) . . . . .	22

2.6	(a) Ground-level concentration as a function of downwind distance. (b) Inverse ground-level concentration as a function of downwind distance. Solid line is a straight-line fit to flat terrain data. Other lines show the effect of shifting source location for flat case a distance of 6H (dashed) and 11H (dotted) upwind. (A = flat terrain; E = depressed roadway, sloped walls; F = depressed roadway, sloped wall, and noise barriers; G = noise barrier at $x/H = 3$ ). From (Heist et al., 2009) . . . . .	24
2.7	(a) Ground-level concentration versus downwind distance for two boundary layer wind profiles with different roughness lengths and for two different roadway configurations (Cases A and H). (b) Inverse ground-level concentration for the same cases, scaled to yield $w_e/u_*$ as slope of best-fit line (axes units are full-scale meters). (A = flat terrain; H = noise barrier at $x/H = 3$ ). From (Heist et al., 2009) . . . . .	24
2.8	Mock straw bale sound barrier, 6 m high and 90 m long. From (Finn et al., 2010) . . . . .	26
2.9	Average crosswind maximum concentration measurements from the Idaho Falls tracer study on day 1 (neutral), day 2 (unstable), day 3 (stable), and day 5 (stable). Error bars represent one standard deviation of the observations at each downwind distance. . . . .	27
2.10	Contour maps of the ratio between barrier and non-barrier tracer concentrations at corresponding grid locations for the selected (a) unstable, (b) neutral, (c) weakly stable, and (d) stable cases. Tracer release line (bright red) and barrier (bold black) are shown for reference. From (Finn et al., 2010) . . . . .	28

2.11	Comparison of Gaussian plume dispersion model with wind tunnel infinite source concentration during the control experiments (no barrier present) for receptors below a height of 6 m. Center black lines correspond to 1 to 1 lines and observations within outer two lines are within a factor of two of model estimates. Bottom figures show modeled and observed ground level concentrations as a function of distance from the road. The smooth approach flow wind tunnel case ( $z_0 = 0.27\text{ m}$ , $u_* = 0.25\text{ m/s}$ ) is on the left and the rough approach flow wind tunnel case ( $z_0 = 0.78\text{ m}$ , $u_* = 0.3\text{ m/s}$ , displacement height = 8.1 m) is on the right. . . . .	34
2.12	Comparison of Gaussian plume dispersion model with crosswind maximum concentrations observed during Idaho Falls control experiments (no barrier present). Center black lines correspond to 1 to 1 lines and observations within outer two lines are within a factor of two of model estimates. The 4 days of the Idaho Falls study represent measurements during atmospheric stability conditions that are: neutral - day 1, unstable - day 2, stable - day 3, and very stable - day 5. . . . .	36
2.13	Downwind variation of Gaussian plume dispersion model and crosswind maximum concentration of Idaho Falls observations during the control experiments (no barrier present) . Error bars show standard deviation of observations. The 4 days of the Idaho Falls study represent measurements during atmospheric stability conditions that are: neutral - day 1, unstable - day 2, stable - day 3, and very stable - day 5. . . . .	37
2.14	Schematic of the source-shift model. The physical source is indicated in black. If the source is shifted upwind the plume spread at some distance from the source is increased. . . . .	38

<p>2.15 Comparison of the source-shift model with crosswind maximum concentrations observed during Idaho Falls. Center black lines correspond to 1 to 1 lines and observations within outer two lines are within a factor of two of model estimates. The 4 days of the Idaho Falls study represent measurements during atmospheric stability conditions that are: neutral - day 1, unstable - day 2, stable - day 3, and very stable - day 5. The model was run with <math>\beta = 0.4</math>.</p>	41
<p>2.16 Downwind variation of source-shift model and crosswind maximum concentration of Idaho Falls observations. Error bars show standard deviation of observations. The 4 days of the Idaho Falls study represent measurements during atmospheric stability conditions that are: neutral - day 1, unstable - day 2, stable - day 3, and very stable - day 5. The model was run with <math>\beta = 0.4</math>.</p>	42
<p>2.17 Comparison of source-shift model with wind tunnel infinite source concentration for receptors below a height of 1H. Center black lines correspond to 1 to 1 lines and observations within outer two lines are within a factor of two of model estimates. The smooth approach flow wind tunnel case (<math>z_0 = 0.27\text{ m}</math>, <math>u_* = 0.25\text{ m/s}</math>) is on the left and the rough approach flow wind tunnel case (<math>z_0 = 0.78\text{ m}</math>, <math>u_* = 0.3\text{ m/s}</math>, displacement height = 8.1 m) is on the right. The model was run with <math>\beta = 0.4</math>.</p>	44
<p>2.18 Schematic of the mixed-wake model. The pollutant mass is well-mixed below the barrier height in the mixed-wake model and then follows a Gaussian profile above the barrier height.</p>	45
<p>2.19 Comparison of the mixed wake model with crosswind maximum concentrations observed during Idaho Falls. Center black lines correspond to 1 to 1 lines and observations within outer two lines are within a factor of two of model estimates. The 4 days of the Idaho Falls study represent measurements during atmospheric stability conditions that are: neutral - day 1, unstable - day 2, stable - day 3, and very stable - day 5.</p>	46

2.20	Downwind variation of mixed wake model and crosswind maximum concentration of Idaho Falls observations. Error bars show standard deviation of observations. The 4 days of the Idaho Falls study represent measurements during atmospheric stability conditions that are: neutral - day 1, unstable - day 2, stable - day 3, and very stable - day 5. . . . .	47
2.21	Comparison of mixed wake model with wind tunnel infinite source concentration for receptors below a height of 1H. Center black lines correspond to 1 to 1 lines and observations within outer two lines are within a factor of two of model estimates. The smooth approach flow wind tunnel case ( $z_0 = 0.27\text{ m}$ , $u_* = 0.25\text{ m/s}$ ) is on the left and the rough approach flow wind tunnel case ( $z_0 = 0.78\text{ m}$ , $u_* = 0.3\text{ m/s}$ , displacement height = 8.1 m) is on the right. . . . .	48
2.22	Schematic defining the boundary of the potential flow region. The variables are: $H$ , the barrier height, $w_d$ , the distance from the wall where the separation streamline touches the ground, and $w_u$ , the upwind distance where the displacement zone begins. . . . .	52
2.23	Comparison of the Puttock Hunt model with crosswind maximum concentrations observed during Idaho Falls. Center black lines correspond to 1 to 1 lines and observations within outer two lines are within a factor of two of model estimates. The 4 days of the Idaho Falls study represent measurements during atmospheric stability conditions that are: neutral - day 1, unstable - day 2, stable - day 3, and very stable - day 5. . . . .	54
2.24	Downwind variation of Puttock Hunt model and crosswind maximum concentration of Idaho Falls observations. Error bars show standard deviation of observations. The 4 days of the Idaho Falls study represent measurements during atmospheric stability conditions that are: neutral - day 1, unstable - day 2, stable - day 3, and very stable - day 5. . . . .	55

2.25	Comparison of Puttock Hunt model with wind tunnel infinite source concentration for receptors below a height of 1H. Center black lines correspond to 1 to 1 lines and observations within outer two lines are within a factor of two of model estimates. The smooth approach flow wind tunnel case ( $z_0 = 0.27m, u_* = 0.25m/s$ ) is on the left and the rough approach flow wind tunnel case ( $z_0 = 0.78m, u_* = 0.3m/s, \text{displacement height} = 8.1 \text{ m}$ ) is on the right. . . . .	57
2.26	Comparison of the modified mixed wake model with crosswind maximum concentrations observed during Idaho Falls. Center black lines correspond to 1 to 1 lines and observations within outer two lines are within a factor of two of model estimates. Error bars on downwind variation figures show standard deviation of observations. The 3 days of the Idaho Falls study included in the figure represent measurements during atmospheric stability conditions that are: neutral - day 1, unstable - day 2, stable - day 3. . . . .	60
2.27	Sensitivity of concentration at a receptor 10 m from the barrier to barrier height and meteorological conditions for $z_0$ of (top left) 0.005 m, (top right) 0.02 m, (bottom) 0.05 m. . . . .	63
2.28	Sensitivity of concentration at a receptor 10 m from the barrier to road width. The surface roughness length is 0.2 m. . . . .	64
2.29	Concentration ratio at various distances from the barrier for different barrier heights and Monin-Obukhov lengths. Monin-Obukhov length has values of (top left) $\infty$ , (top right) -20 m, (bottom) 20 m. . . . .	65
3.1	Street Canyon Schematic. From Berkowicz et al. (1997) . . . . .	72
3.2	Building array flow regimes. (Oke, 1988) . . . . .	73
3.3	Transfer velocity normalized by approach wind speed as a function of canyon aspect ratio measured by Barlow & Belcher (2002). IR, WI, and SF represent the individual roughness, wake interference, and skimming flow regimes (Oke, 1988). . . . .	76

3.4	Schematic of an urban boundary layer. From Fisher et al. (2006) . . . . .	82
3.5	Concentration magnification predicted using OSPM. . . . .	86
3.6	Map of Göttinger Strasse showing locations of concentration and micro meteorology stations and building heights. . . . .	90
3.7	Comparison of equation (3.4) with observations during 2003. Top left shows scatter plot. Top right shows variation of observations (blue) and model (green) with wind speed. Bottom left shows variation with $1/\sigma_w$ . Bottom right shows variation with wind direction. Wind directions parallel to the street are 163 and 343 degrees, . . . . .	94
3.8	Comparison of equation (3.14) with observations during 2003. Top left shows scatter plot. Top right shows variation of observations (blue) and model (green) with wind speed. Bottom left shows variation with $1/\sigma_w$ . Bottom right shows variation with wind direction. . . . .	95
3.9	Scatterplot comparing model assuming plume spread is dominated by the initial vertical dispersion with observations. . . . .	96
3.10	Comparison of equation (3.15) with observations during 2003. Top left shows scatter plot. Top right shows variation of observations (blue) and model (green) with wind speed. Bottom left shows variation with $1/\sigma_w$ . Bottom right shows variation with wind direction. . . . .	98
3.11	Wind roses for the 10 m (left) and rooftop (right) anemometers in the Göttinger Strasse data. . . . .	100
3.12	Difference between a receptor at height $z$ and a receptor at 20 m AGL calculated with equation (3.16) for parallel flow. The model is run with a street length of 100 m, width of 20 m, and with $\sigma_w = 0.5 \text{ m s}^{-1}$ . Note that $z = 0 \text{ m}$ corresponds to equation (3.4). . . . .	101
3.13	Sensitivity of dispersion model of equation (3.4) ( $z = 0 \text{ m}$ ) and equation (3.16) to initial vertical spread and receptor height. . . . .	102

3.14	Comparison of equation (3.16) with observations during 2003. Top left shows scatter plot. Top right shows variation of observations (blue) and model (green) with wind speed. Bottom left shows variation with $1/\sigma_w$ . Bottom right shows variation with wind direction. . . . .	103
3.15	Campbell scientific CSAT3 sonic anemometer. . . . .	110
3.16	Condensation particle counter. . . . .	111
3.17	AQMesh concentration monitor (at top of photo). . . . .	112
3.18	Overview of 8th St field study. . . . .	113
3.19	Sonic anemometer and AQMesh monitor mounted to light pole next to 8th St. . . . .	114
3.20	Co-location of CPCs before start of measurements on 8th St. . . . .	114
3.21	Instrument locations on 8th St. See Table 3.4 for symbol definitions. . .	122
3.22	Instrument locations at 7th St and Broadway field site. See Table 3.5 for symbol definitions. . . . .	123
3.23	Location of rooftop sonic anemometer near the edge of a section of roof about 10 m above the rest of the roof. A small structure sites about 7 m to the east of the sonic. . . . .	124
3.24	Temple City experiment site. For marker definitions see table 3.6. . . .	125
3.25	View of Wilshire Blvd field site. For marker definitions see table 3.7. . .	126
3.26	Wind roses for the LA 8th St building (left) and open (right) locations. . .	127
3.27	Evaluation of OSPM recirculating contribution model with data collected on 8th St, LA. The comparison with building section data is on the left and that with open section data is on right. The concentration has been normalized by the 30 minute average emission rate assuming an emission factor of $10^{14} \text{ veh}^{-1} \text{ km}^{-1}$ . . . . .	128

3.28	Evaluation of OSPM recirculating contribution model with data collected on 8th St, LA. The comparison with building section data is on the left and that with open section data is on right. The concentration has been normalized by the daily average emission rate assuming an emission factor of $10^{14} \text{ veh}^{-1} \text{ km}^{-1}$ . . . . .	129
3.29	Evaluation of OSPM recirculating contribution model with data collected in the LA field study at 8th St, Temple City Blvd, Broadway, and Seventh St. The concentration has been normalized by the daily average emission rate assuming an emission factor of $10^{14} \text{ veh}^{-1} \text{ km}^{-1}$ . . . . .	131
3.30	VDM model prediction compared with data in the LA 8th St building section (left) and open section (right). The concentration has been normalized by the daily average emission rate assuming an emission factor of $10^{14} \text{ veh}^{-1} \text{ km}^{-1}$ . . . . .	136
3.31	Evaluation of VDM model with data collected in the Los Angeles field studies. The concentration has been normalized by the daily average emission rate assuming an emission factor of $10^{14} \text{ veh}^{-1} \text{ km}^{-1}$ . . . . .	138
3.32	Baseline and total concentration. . . . .	139
3.33	Sensitivity of calculated baseline to window size. . . . .	140
3.34	Sensitivity of calculated baseline to cutoff percentile. . . . .	141
3.35	Comparison of vertical dispersion model with 30 minute averaged local contribution. Concentration is normalized by daily average emission rate, assuming an emission factor of $10^{14} \text{ veh}^{-1} \text{ km}^{-1}$ . . . . .	142
3.36	Comparison of vertical dispersion model with 30 minute averaged local contribution. Concentration is normalized by daily average emission rate, assuming an emission factor of $10^{14} \text{ veh}^{-1} \text{ km}^{-1}$ . The building height of the 8th St open section has been set equal to that of the 8th St building section. . . . .	143

3.37	Location of instruments in May 2015 Riverside, CA field study. ● - Condensation Particle Counter (CPC). - AQMesh. ▲ - Sonic Anemometer. ■ - Camera. Map Data: Google . . . . .	150
3.38	Residuals of AQMesh calibration models 1 (left) and 3 (right) vs hour of day. . . . .	152
3.39	Assumed daily variation of vehicle traffic. Observed traffic flow rate for August 31 and September 3 and 4 are also shown. . . . .	153
3.40	Comparison of Vertical Dispersion Model with vertical difference of 1-hour average carbon monoxide concentrations in Riverside, CA. Observations are normalized by the emission rate assuming an emission factor of $3.3 \text{ g km}^{-1}$ for light duty vehicles and $33 \text{ g km}^{-1}$ for heavy duty vehicles. . . . .	155
3.41	Variation of vertical difference of 2-hour average carbon monoxide concentrations with the rooftop $\sigma_w$ (top left), the surface scalar wind speed (top right), and the wind direction relative to the normal to the road (bottom). Observations are normalized by the emission rate assuming an emission factor of $3.3 \text{ g km}^{-1}$ for light duty vehicles and $33 \text{ g km}^{-1}$ for heavy duty vehicles. . . . .	157
3.42	Comparison of Vertical Dispersion Model with measurements of ultrafine particle concentrations in Riverside, CA. . . . .	158
3.43	Variation of observed local contribution and VDM estimates with rooftop $\sigma_w$ . (left) Building section. (right) Open section. . . . .	159
3.44	Variation of observed local contribution and VDM estimates with surface scalar wind speed. (left) Building section. (right) Open section. . . . .	160
3.45	Comparison of modeled and observed rooftop $u_*$ . (left) The model estimate is determined using the complete IBL model. (right) The model estimate assumes neutral atmospheric conditions (infinite Monin-Obukhov length). . . . .	162

3.46	Comparison of $u_*$ (left) and $\sigma_w$ (right) predicted by the simple IBL model (equation (3.32)) with observations. . . . .	163
3.47	Comparison of $\sigma_w$ at rooftop with the near surface $\sigma_w$ at the building and open sections. The black line represents the model of (3.26) . . . . .	164
A.1	Calibration derived from co-location of instruments next to 8th St on May 7th . . . . .	176
A.2	Calibration derived from co-location of instruments next to 8th St on May 9th . . . . .	177
A.3	Calibration derived from co-location of instruments next to Broadway on September 20th. The calibration factor between DiSCmini 2 and CPC 483 was 1.34 (not shown). . . . .	178
A.4	Calibration derived from co-location of instruments next to Temple City Blvd on January 16, 2014. . . . .	179
A.5	Calibration derived from co-location of instruments next to Wilshire Blvd on May 30, 2014. . . . .	180
B.1	CPC measurement system mounted to a tripod. . . . .	183
B.2	CPC measurement system. . . . .	184
B.3	Daily usable energy from a solar panel located at 34 degrees N, 117 degrees W facing south and tilted at 34 degrees and with an efficiency of 15%. Cloud cover is 50%. . . . .	186
B.4	Schematic of solar power system. . . . .	187
B.5	Drawing of the CPC sensor. From TSI (2002) . . . . .	188
B.6	Top view of the CPC saturator (model 3022A). The cooling unit was placed directly on top of the saturator. . . . .	189

B.7	Temperature measurement of CPC saturator used to determine the heat transfer coefficient between the saturator and the environment and the exponential time constant for changes in the saturator temperature. . . .	190
B.8	CPC measurement system at the Riverside Market St field site. . . . .	193
B.9	Schematic of data logger. . . . .	195

# List of Tables

3.1	Comparison of direct and recirculating concentration measured in wind tunnel studies of street canyons. . . . .	80
3.2	Emission factors for $NO_x$ (using molecular weight of $NO_2$ ) [g/km]. . . . .	91
3.3	Overview of measurement locations. . . . .	109
3.4	Detailed instrument locations on 8th St. . . . .	115
3.5	Detailed instrument locations at 7th St and Broadway. . . . .	117
3.6	Detailed instrument locations at Temple City site. . . . .	119
3.7	Detailed instrument locations at Beverly Hills site. . . . .	121
3.8	Summary of area weighted building height, street width, and aspect ratio of all sites. . . . .	137
3.9	Instrument Locations in May 2015 Riverside, CA field study. . . . .	149
3.10	Parameters of the urban field site in Riverside, CA. . . . .	149
3.11	Observed and model estimate of magnification in Riverside. . . . .	158
B.1	Parameters used in equations (B.2) and (B.4). . . . .	192

# Chapter 1

## Motivation, Objectives, and Approach

### 1.1 Problem Statement

Motor vehicles are a vital component of modern transportation infrastructure. However, motor vehicles emit air pollutants that negatively impact human health. Air quality regulations and vehicle emission standards have significantly reduced vehicle emissions since the 1970s but because of the growing number of vehicles, combined with high density development in urban areas, elevated concentrations of vehicle emitted pollutants still cause health problems. Recently, several studies have shown association between living within several hundred meters of high-traffic roads and negative health effects such as asthma and other respiratory impacts, birth and developmental effects, premature mortality, cardiovascular effects, and cancer (Harrison et al., 1999; Brauer, 2002; Hoek et al., 2002; Finkelstein et al., 2004). Air quality measurements near major roads indicate that these health effects are associated with elevated concentrations, relative to urban back-

ground levels, of traffic-related air pollutants, including carbon monoxide ( $CO$ ), nitrogen oxides ( $NO_x$ ), coarse ( $PM_{10-2.5}$ ), fine ( $PM_{2.5}$ ), and ultrafine ( $PM_{0.1}$ ) particle mass, particle number, black carbon (BC), polycyclic aromatic hydrocarbons (PAHs), and benzene (Hitchins et al., 2000; Kim et al., 2002; Zhu et al., 2002b; Kittelson et al., 2004).

Due to the health impact of vehicle emissions, methods to mitigate elevated near road concentrations may be required. Recently, several mitigation methods that use roadway design, such as elevated and depressed roads and barriers next to the road, have been suggested. Tracer and wind tunnel measurements show that these designs can be effective at reducing near road concentrations (Finn et al., 2010; Heist et al., 2009). These methods are unique because they use the design of the urban environment to alter dispersion of vehicle emissions at short distances, 10s to 100s of meters, from the road. Their use highlights the more general question of how the urban built environment alters near road concentrations of vehicle emissions at these spatial scales. There is concern that certain built environments may result in pollutant hot spots with significantly elevated concentrations. High population density in urban areas gives weight to this concern, because many people are potentially exposed to elevated concentrations of emissions from heavily trafficked urban roads due to their close proximity to the road. It is important to investigate the potential ways that the urban microenvironment design can adversely affect near road pollutant concentrations and also how it can be used to mitigate elevated near road concentrations. In order to develop effective policies and mitigation methods we must understand the processes that govern near-road pollutant concentrations in urban environments.

The link between traffic emissions and concentrations is determined through models of the atmospheric dispersion that dilutes pollutant emissions. Early research on dispersion of traffic emissions focused on idealized cases of homogeneous flat terrain. Research since

the 1970s has investigated the effect of the presence of buildings and other structures on dispersion. Field and wind tunnel studies have shown that certain building morphologies and structures can significantly alter dispersion at scales of 10s to 100s of meters from the road (Finn et al., 2010; Heist et al., 2009). While we have a fairly good understanding of dispersion in some urban configurations, there is still a need to improve our understanding of dispersion within cities in certain types of built environments.

In this thesis, I develop methods to estimate traffic related pollutant concentrations in several common types of built environments at scales of 10s to 100s of meters from the road. The thesis is focused on development of semi-empirical dispersion models. Semi-empirical models seek to explain the dispersion process using only a small number of important governing variables and include only the essential physics. These models are useful for studies of health effects due to traffic emissions as well as for the design of urban environments to minimize exposure to elevated pollutant concentrations. Semi-empirical models can be contrasted with more comprehensive models such as computational fluid dynamics (CFD) models. CFD models are designed to be general purpose because they solve the governing equations directly and can be adapted to a broad range of problems. However, they are very cumbersome to use and do not provide the insight that models based on only the essential physics provide.

The dispersion models developed in this research are applicable to the following topics:

1. Assessment of the variables governing dispersion of traffic emissions in transit oriented developments with nonuniform building height
2. Evaluation of the effectiveness of solid barriers next to roads to reduce near road pollutant concentrations

## **1.2 Background**

### **1.2.1 Assessment of the variables governing dispersion of traffic emissions in transit oriented developments with nonuniform building height**

In large cities, transit oriented development (TOD), urban design where high density housing is located in close proximity to shops and transportation infrastructure, results in increased population density near large roads (Boarnet & Crane, 2007). TODs are desirable because they promote walking, cycling, and use of public transportation, all of which reduce use of motor vehicles and the associated pollutant emissions. However, there is concern that the TOD residents living or working in close proximity to heavily trafficked urban streets may be exposed to elevated concentrations of vehicle emitted pollutants. This concern arises because the processes that dilute pollutants may be less effective in high density built environments.

Most models of dispersion in cities are designed for cases where the building height is uniform and the buildings are spatially homogeneous. There is a need to assess what variables primarily govern dispersion in real world cities with nonuniform building height and spatial inhomogeneity. This is done by developing semi-empirical dispersion models that link traffic emissions and a few characteristic features of the built environment morphology with near road pollutant concentrations. The work in this thesis is concerned with the class of microscale dispersion models that predict concentrations at distances of 10s to 100s of meters from the road.

Some of the earliest studies of dispersion in cities were performed in the 1970 and 1971 measurements of traffic emitted pollutants in San Jose, California, and St Louis, Missouri (Dabberdt et al., 1973). The studies resulted in a semi-empirical dispersion

model based on the Gaussian plume model formulation (Stockie, 2011) along with a "submodel" that accounts for the microscale features of the dispersion within the urban street. The plume spreads for the Gaussian plume model were determined from tracer release field measurements in a study conducted in St Louis between 1963 and 1965 (James L McElroy & Francis Pooler, Jr., 1968; James L McElroy, 1969).

The microscale model of (Dabberdt et al., 1973) and most semi-empirical urban dispersion models are based on the physical picture of the "street canyon", a street with uniform height buildings on either side, a prototypical building block of the urban environment. The ideal street canyon has buildings all the same height and no gaps between the buildings. Depending on the aspect ratio, the ratio of the height of buildings to the street width, and the rooftop wind speed and direction, a recirculating vortex flow can develop within the street (Oke, 1988). The physical picture of the dispersion within street canyons typically includes a model of the vortex flow. This model primarily determines the relationship between the near-road concentration and the governing meteorological variables.

There are several problems with applying semi-empirical street canyon dispersion models to model dispersion in real world cities. One problem with dispersion models based on the vortex flow concept is that it is not clear that they are applicable to real world urban streets with significant building height variability and spatial inhomogeneity. Well known street canyon dispersion models have been evaluated mostly with data collected in European cities, where medium density urban streets tend to closely approximate the ideal street canyon. Dense urban cores within the United States have significant spatial and building height variability, putting into question the applicability of the street canyon dispersion models for these urban environments. One of the primary objectives of this work is

to test the applicability of various dispersion models to estimate near road concentrations in cities with the characteristics of the urban cores in U.S. cities.

A further problem with urban dispersion models in general is that there is no consensus on the important meteorological variables that govern near road concentrations. The STREET model of Johnson et al. (1973), which is similar to the model of Dabberdt et al. (1973), parameterizes the concentration in terms of the near surface wind speed within the street, which is linearly related to the rooftop wind speed in the model. Nicholson (1975) developed a model that parameterizes concentrations in terms of the average vertical velocity near the top of the street canyon when the wind is perpendicular to the street. For parallel winds the average horizontal wind speed within the canyon is used. For conditions of low within-canyon wind speeds, the canyon plume box model (CPBM) of Yamartino & Wiegand (1986) parameterizes pollutant transport using a Gaussian plume model with plume spreads determined by the average vertical and horizontal turbulent velocities within the street canyon. The operational street pollution model (OSPM) (Berkowicz et al., 1997) relates the surface concentration with both the vertical turbulent velocity near the surface and the roof of the canyon. These turbulent velocities are determined from the rooftop wind speed through a model of the urban micrometeorology. It is not clear which meteorological variables primarily govern near-road concentrations. To determine the performance of these various parameterizations, part of the work in this thesis evaluates the performance of models with different relationships between the concentrations and meteorological variables such as wind speed and the vertical turbulent velocity.

Vortex flow within a street canyon may result in higher concentrations on one side of the street than the other. Most street canyon models describe the spatial variation of concentrations within the street by accounting for the vortex flow advecting emissions from the street toward the leeward side (Johnson et al., 1973; Yamartino & Wiegand,

1986; Berkowicz et al., 1997). These models typically include a parameterization of the "recirculating" contribution, which affects the concentration on both the windward and leeward sides of the street, and is due to the vortex flow trapping pollutants within the canyon, and the "direct" contribution, which impacts on the leeward side of the street, due to direct emissions advected across the street. Other models such as that of Nicholson (1975) only parameterize the average concentration within the canyon. As mentioned previously, the vortex flow model may not be appropriate for cities with significant spatial inhomogeneity. I examine the value of this aspect of the vortex flow concept as part of the dispersion model evaluation.

A significant challenge to the application of dispersion models to urban environments is the lack of measurements of the required meteorological data inputs. Because of this, models rely on assumptions about the relationships between available data and the required model inputs. The street canyon model of Dabberdt et al. (1973) parameterizes the concentration in terms of the rooftop wind speed. The rooftop wind speed used in the model is estimated from the wind speed measured at a nearby airport. This simple parameterization results from the need to use routinely measured wind speed as model inputs. Normally, only measurements of mean wind speed and direction are made at rural locations such as airports. Turbulence data is not routinely measured, and even mean wind speed and direction data is usually not available within dense urban centers. For this reason, all of the urban dispersion models require such parameterizations to be applicable in real world situations. The semi-empirical models that I describe in chapter 3 are developed with the requirement that they only depend on meteorological data that is readily available or can be determined through semi-empirical models that relate the wind speed measured at the "rural" airport site with that at the urban site of interest.

### **1.2.2 Evaluating the effectiveness of solid barriers next to roads to reduce near-road pollutant concentrations**

Several approaches have recently been suggested to mitigate the near road impact of vehicle emissions. They include:

1. More stringent vehicle emission standards
2. Noise barriers with a variety of shapes and coatings
3. Roadside vegetation
4. Roadway design such as elevated and depressed roads
5. Road canopies in combination with methods to treat the pollutants trapped in the canopies (McCrae, 2010)
6. Dynamic traffic management based on forecasts of conditions that might lead to poor air quality (McCrae, 2010)

Road canopies can confine pollutants within the road, but the trapped pollutants have to be treated or released at heights that reduce ground-level concentrations. The construction of canopies, stacks, and the removal of pollutants using methods such as electrostatic precipitation of particles are expensive. Catalytic coating on barriers to absorb or convert pollutants such as NO<sub>2</sub> has not been effective because the contact time between the pollutants and the coated surface is not large enough. Dynamic traffic management, which is reducing traffic flows when the meteorology is conducive to high air pollution levels, is difficult to implement even if adverse meteorological conditions could be forecast accurately. The most practical and potentially successful short-term mitigation

strategy is based on physical barriers. These barriers enhance vertical dispersion, thereby reducing near road concentrations of vehicle emissions. Vegetation barriers have been investigated as a method to filter particulates from the roadway. However, they must be very dense for a significant amount of particulate matter to be deposited. They may be effective at reducing concentrations, but only when they are so dense that they are essentially solid walls, and the method of reducing concentrations is by enhancing dispersion and not by filtration. In some cases vegetation can reduce wind speed and turbulence downwind, thereby reducing dispersion and increasing near-road concentrations. Elevated or depressed roadways can also reduce near-road air pollution, but not to the same degree as is possible with solid barriers (Heist et al., 2009).

For these reasons, there has recently been significant interest in the use of solid barriers to mitigate elevated near-road concentrations of traffic emissions. Highways and large roads are often designed with noise barriers next to the road to reduce traffic noise, and since roadside barriers already exist in many places, their use to mitigate elevated near road concentrations is very attractive.

There are several models that describe concentrations associated with emissions near bluff bodies (Huber & Snyder, 1982) and buildings (Huber, 1984, 1988; Huber & Snyder, 1982; Wilson & Britter, 1982; Schulman et al., 2000), which in principle can be applied to estimate the impact of barriers on dispersion. However, these models are specialized for narrow buildings and thus cannot be readily adapted to describe flow and dispersion behind long barriers next to roads. Additionally, these models focus on the effect of buildings on dispersion of emissions from point sources such as elevated stacks rather than dispersion from line sources such as roadways.

A few authors have developed dispersion models to explain the effect of barriers on near-road concentrations. Heist et al. (2009) explained data collected in a wind tunnel

study conducted by the EPA using a modified Gaussian plume model. The barrier effect was explained by shifting the roadway emission source upwind by a distance of several barrier heights, and increasing the turbulence that dilutes the emissions by some amount dependent on the barrier height. However, the shift distance and increased turbulence were not specified, only that they are related to barrier height and roadway configuration. Ultimately, a practical model should relate the important parameters such as barrier height with concentration reduction next to the road.

A further problem with current models of the effect of barriers on dispersion is that they are only representative of neutral stability conditions, while the real world conditions that are often of interest are stable periods during early morning commutes and unstable periods during daytime and evening commutes. For this reason, the data from a tracer study (Finn et al., 2010), conducted at the Idaho National Lab, is very useful because it contains conditions of neutral, unstable, and stable atmospheric stability. No dispersion models have directly explained the effect of atmospheric stability on the barrier's effectiveness at diluting roadway emissions. Therefore, part of my work has dealt with developing semi-empirical dispersion models that can be used to understand the effect of solid barriers on near road concentrations and account for atmospheric stability and important variables such as barrier height. This work is shown in chapter 2.

Several studies have modeled the effect of barriers on dispersion using CFD (Hagler et al., 2011; Steffens et al., 2013) and other numerical models such as quick urban industrial complex (QUIC) (Bowker et al., 2007). These studies support the findings of the other experimental studies and the semi-empirical models. The work in this thesis is focused on semi-empirical dispersion models rather than CFD.

## 1.3 Objectives

The objective of my research is to develop methods to estimate traffic related pollutant concentrations in urban areas. The models developed in this research are applicable to the following topics:

1. Evaluating the effectiveness of solid barriers next to roads to reduce near-road pollutant concentrations
  - (a) Used data from a wind tunnel study Heist et al. (2009) and a tracer study Finn et al. (2010) to formulate and evaluate semi-empirical dispersion models that account for the effect of barrier height and atmospheric stability on near-road concentrations.
  - (b) Conducted sensitivity studies of dispersion models to give guidance on the effect of atmospheric stability and barrier height on near road concentrations.
2. Assessment of the variables governing dispersion of traffic emissions in transit oriented developments with nonuniform building height
  - (a) Performed field measurements of ultrafine particle concentrations and the variables that govern dispersion at several field sites in Los Angeles and Riverside, CA.
  - (b) Formulated and evaluated semi-empirical dispersion models to estimate concentrations within urban environments with inhomogeneous building height.

## **1.4 Structure of the Dissertation**

Chapter 2 describes methods to estimate near-road pollutant concentrations when there is a barrier next to the road. Chapter 3 describes the field measurements and model development to estimate concentrations within urban environments with inhomogeneous building height.

## **Chapter 2**

# **Effect of Solid Barriers on Dispersion from Roads**

### **2.1 Introduction**

The primary objective of the research described in this chapter is to develop and evaluate dispersion models that can be used to evaluate how near road barriers might reduce the exposure to traffic emissions of people living next to large roads. The second objective of this study is to conduct sensitivity studies with the dispersion models to examine the effects of 1) barrier dimensions, 2) wind speed and direction, 3) atmospheric stability, and 4) road dimensions on near road concentrations in the presence of barriers.

In section 2.2 I provide a review of the studies conducted to date that deal with the impact of physical barriers on near road dispersion of roadway emissions. Section 2.3 describes three models of roadside barriers and shows the evaluation of the models with data from wind tunnel and field studies. Finally I use these models to examine the sensitivity of near road concentrations to changes in barrier height in section 2.4.

## 2.2 Background

Solid barriers affect concentrations associated with vehicle emissions by modifying the flow field and turbulence in the vicinity of the barrier. The mean flow pattern around a typical solid barrier is shown in Figure 2.1. The the wind direction is perpendicular to the barrier the pollutant plumes from vehicles are carried over the barrier by the mean flow that is deflected upward by the barrier. A recirculating region forms behind the barrier, in which the near surface flow is opposite to that in the mean flow aloft. Above the recirculating cavity, the flow is deflected downward. Turbulence levels are enhanced in a vertically expanding wake whose effects extend to a distance of about 10-20 times the height of the barrier. Figure 2.2 shows the increase in turbulent kinetic energy (TKE) in the presence of a barrier relative to that with no barrier present at different distances from the barrier. Initially the increase in TKE is largest near the top of the barrier. Farther downwind the increased TKE becomes mixed over a larger height as the wake grows in size. At 102 m from the barrier we see that the increased TKE is mixed over a height larger than the barrier.

The upward flow deflection caused by solid barriers effectively raises the height of roadway emissions from near ground level to approximately the height of the barrier. A fraction of these elevated emissions is entrained into the recirculating cavity and then re-emitted into the wake region of the flow. To a first approximation, the material entrained into the cavity acts as a ground level source with an initial vertical spread proportional to

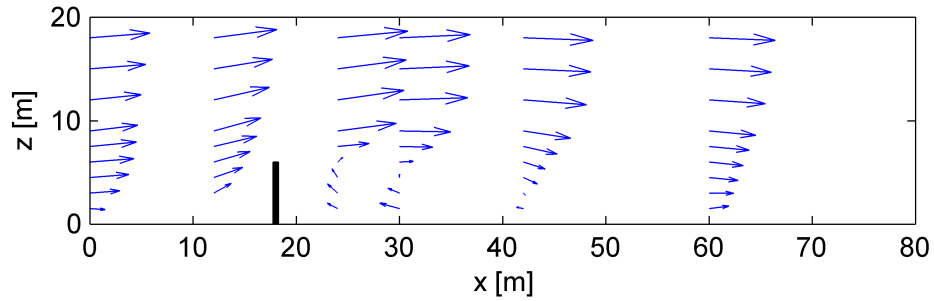


Figure 2.1: Flow induced by a solid barrier. The mean wind direction upwind of the barrier is along the x axis. Arrows represent wind direction vectors. The black rectangle represents the barrier location. Data from EPA wind tunnel study (Heist et al., 2009).

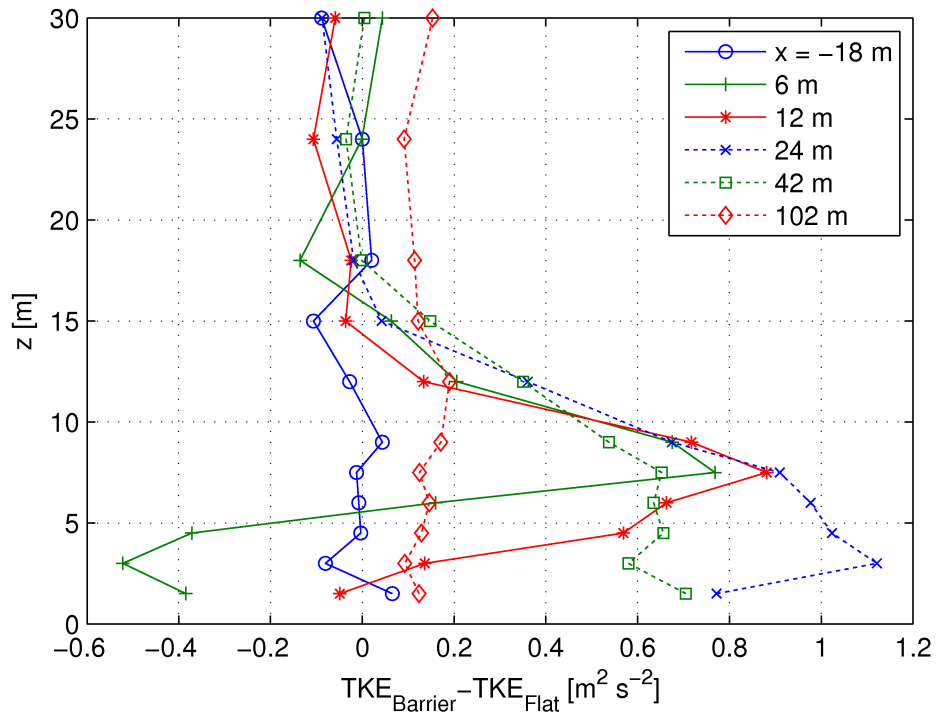


Figure 2.2: Increase in turbulent kinetic energy (TKE) in the presence of a solid barrier at different distances from the 6 m tall (full scale) barrier. The increased TKE is the difference between the TKE measured in the presence of a barrier and the TKE with no barrier present. Data from EPA wind tunnel study (Heist et al., 2009).

the barrier height. In general, the combination of all these barrier induced effects leads to a reduction in concentrations relative to those without the barrier.

The mean wind speed downwind of the barrier's recirculating cavity is an important variable that influences the concentration within the cavity. This can be seen by considering a simple box model of the cavity. Just downwind of the barrier, within the recirculating cavity, the mean horizontal velocity, averaged over the height of the barrier, is near zero. In this region material is rapidly mixed horizontally and vertically by the recirculating vortex flow, resulting in nearly uniform concentration between the ground and the height of the barrier. The mean horizontal wind speed downwind of the recirculating cavity primarily determines the flux of pollutants out of the cavity. The flux of pollutants into the cavity is determined by the turbulent exchange near the top of the barrier. If we assume that a constant fraction of the emission source strength is entrained into the cavity, then the outward flux, determined by the mean horizontal wind speed downwind of the cavity, governs concentrations within the cavity. For this reason it is important to accurately model the mean wind speed downwind of the barrier.

Downwash near buildings has the potential to bring elevated plumes down toward the surface, which may increase ground level concentrations of emissions from an elevated source. The mean flow downwind of the barrier induces downwash, raising concern that this reduces the effectiveness of the barrier or even increases concentrations downwind of the barrier relative to those that would be observed with no barrier present. However, this is not a concern for the application of reducing concentrations next to roadways because the road emission source is near ground level. The vertical lofting and subsequent downwash induced by the barrier does not increase ground level concentrations relative to the concentration next to the road with no barrier present. Only if the road was elevated would the downwash potentially cause an increase in ground level concentrations. For a ground level source, the increased vertical mixing of the emissions entrained into the barrier wake will result in a reduction in concentrations. We can be confident that the

presence of a barrier can only reduce near road concentrations of traffic emissions released near the surface.

Major experimental studies on the effects of barriers on dispersion include a wind tunnel study (Heist et al., 2009), a tracer study (Finn et al., 2010), and three field studies, one in Raleigh North Carolina (Bowker et al., 2007; Baldauf et al., 2008) one in Southern California (Ning et al., 2010), and one in Putten, The Netherlands (Hoogwerff et al., 2010). In addition to barriers, the wind tunnel study also investigated elevated and depressed roadways. The Raleigh study investigated the effects of barriers and barriers combined with vegetation.

Most of these studies focused on dispersion of inert gases, while the Raleigh, NC, Southern California, and Putten field studies also investigated the dispersion of particulate matter (PM). In the Raleigh study, total particle number and 20 nm and 75 nm concentrations were measured. The Southern California study measured particle number and mass distributions between 6-523 nm.

The Idaho Falls tracer study (Finn et al., 2010) evaluated the effect of atmospheric stability on the reduction of concentrations behind barriers. The wind tunnel study (Heist et al., 2009) investigated the effect of boundary layer surface roughness on dispersion behind the barrier. This study also examined the combined impact of roadside barriers along with several road configurations, including elevated and depressed roadways. I use data collected in these two studies to evaluate the semi-empirical dispersion models in section 2.3.

One study (Hagler et al., 2011) used  $k - \epsilon$  CFD models to examine the air quality impact of barriers with varying heights. Another study modeled roadside barriers using large eddy simulation and  $k - \epsilon$  models (Steffens et al., 2013).

In the measurement studies, the concentration immediately behind the barrier was 15-50% lower than the concentration with no barrier present when the wind direction was close to perpendicular to the barrier, although the Idaho Falls tracer study found some concentration deficits greater than 50%. The effect of the barrier persisted up to about 50 times the barrier height in all studies, after which the concentration approached the value that would occur without the barrier. The wind tunnel and CFD studies found that elevated or depressed roadways and barriers placed upwind or downwind of the road caused reduced downwind concentrations compared to flat roads with no barriers.

The evidence from all field studies generally shows that concentrations downwind of the barrier are never increased relative to those without a barrier present. The Idaho Falls tracer, CFD, and wind tunnel studies found reduced concentrations at all downwind distances for all atmospheric stabilities. The field studies in Raleigh and Southern California found some instances where larger concentrations occurred downwind of a barrier than in the no-barrier case. This effect was most evident in the Southern California study, where reduced concentrations were found immediately behind the barrier followed by a surge of concentrations about 80-100 m downwind. This is shown in Figure 2.3 for particle number and mass concentrations. A similar result was found for gaseous pollutants. One possible explanation for this is that traffic activity on small roads near the freeways contributed to these high concentrations. The Raleigh study also observed some high concentrations at large distances from the road, and the conclusion was that traffic on small roads downwind of the barrier was responsible for these anomalous concentrations.

The Raleigh study found that the presence of vegetation further decreased concentrations compared to only a solid barrier. The noise barrier reduced 20 nm PM number concentrations up to a distance of about 100 m from the road. The presence of both

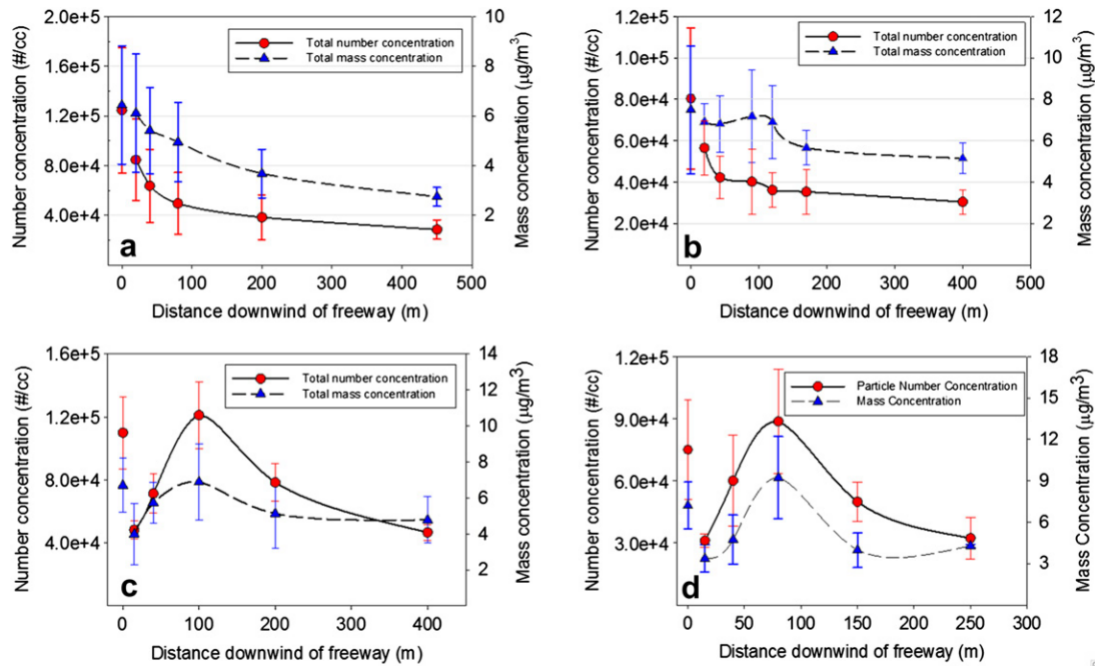


Figure 2.3: Particle number and mass concentrations at different distance downwind of the freeway (a) I-710 no noise barrier (b) I-5 no noise barrier; (c) I-710 with noise barrier; (d) I-5 with noise barrier. Note: The total particle number and mass concentrations at  $X = 0$  are derived from SMPS (10-225 nm) data at stationary sampling station; the concentrations at  $X > 0$  are derived from FMPS (6-523 nm) data. From Ning et al. (2010).

a barrier and vegetation caused greater reductions in both 20 nm and 75 nm particle number concentrations. This study also measured barrier edge effects and found that concentrations did not decrease significantly compared with the open field until about 40 m from the barrier edge.

Most barrier studies have focused on "standard" barriers, which are simple walls. Exceptions to this include a study conducted in Putten, the Netherlands (Hooghwerff et al., 2010), and the EU-LIFE Sound and Particle Absorbing System (SPAS, Magistrat Klagenfurt, 2011) project. The Putten study examined variations in the shape of the barrier top, porous barriers, catalytic coatings (to reduce  $NO_2$ ), and barriers with vegetation. The SPAS project investigated barriers with built-in particulate filters (Rodler & Henn,

2009; Iser & Scharl, 2009). Figure 2.4 shows an example of the filters used in the study installed on a noise barrier. The SPAS study found that, based on field measurements, filters installed in noise barriers can sometimes reduce concentrations of PM<sub>10</sub>. However, this effect depends on wind direction (Rodler & Henn, 2009). The study found that pressure due to wind is not sufficient to overcome the filter resistance (Iser & Scharl, 2009). Passing trucks generated sufficient pressure to overcome the filter resistance and cause some removal of PM, but passenger cars did not generate the required pressure increase.



Figure 2.4: Filter panel installed on a noise barrier for the SPAS study. (Magistrat Klagenfurt, 2011)

The Putten study found that the variations in the shape of the barrier top, porous barriers, catalytic coatings, and vegetated barriers did not reduce the concentration more than a simple 4 m tall wall. There has been criticism of the study and this result is questionable (McCrae 2010). Further research on "optimized" barriers is needed.

I next provide details of field and numerical studies that are most relevant to the objectives of this research, and which are used to develop the semi-empirical dispersion models.

### 2.2.1 Wind Tunnel Study

The wind tunnel study measured dispersion of roadway emissions in a 1:150 scale model of a 6 lane divided highway. Figure 2.5 shows the 12 configurations used in the study. They were one with flat terrain with no barrier, six with flat terrain and upwind or downwind barriers, one with an elevated roadway, three with depressed roadways, and one with a depressed roadway with both upwind and downwind barriers. Barriers with full scale heights corresponding to 6 m and 9 m were placed both upwind and downwind of the road as shown in Figure 2.5.

A simulated atmospheric boundary layer was created within the wind tunnel using Irwin spires at the tunnel inlet and roughness blocks arranged on the tunnel floor. This created a logarithmic approach flow profile of the form:

$$U = \frac{u_*}{\kappa} \ln \left( \frac{z - d}{z_0} \right) \quad (2.1)$$

where  $z$  is the height from the ground,  $u_*$  is the surface friction velocity,  $z_0$  is the surface roughness length,  $d$  is the displacement height, and  $\kappa$  is the Von-Karman constant. The profile in the wind tunnel was characterized by a surface roughness length,  $z_0$  of 5.2 mm, a displacement height,  $d$ , of 54 mm, and a surface friction velocity,  $u_*$  of 0.3 m/s. The experiments were repeated with smaller roughness elements to generate a profile with  $z_0 = 1.8mm$ , and  $d = 0$ .

Ethane was released from a simulated six lane highway. The ethane was released through many holes arranged in lines, with 12 mm tall roughness elements upwind of the holes to provide initial vertical mixing of the ethane. Vertical concentration profiles and ground level concentrations downwind of the source were measured using flame ionization detectors.

Vertical profiles of mean and turbulent velocities were measured at several distances from the road using laser doppler velocimetry.

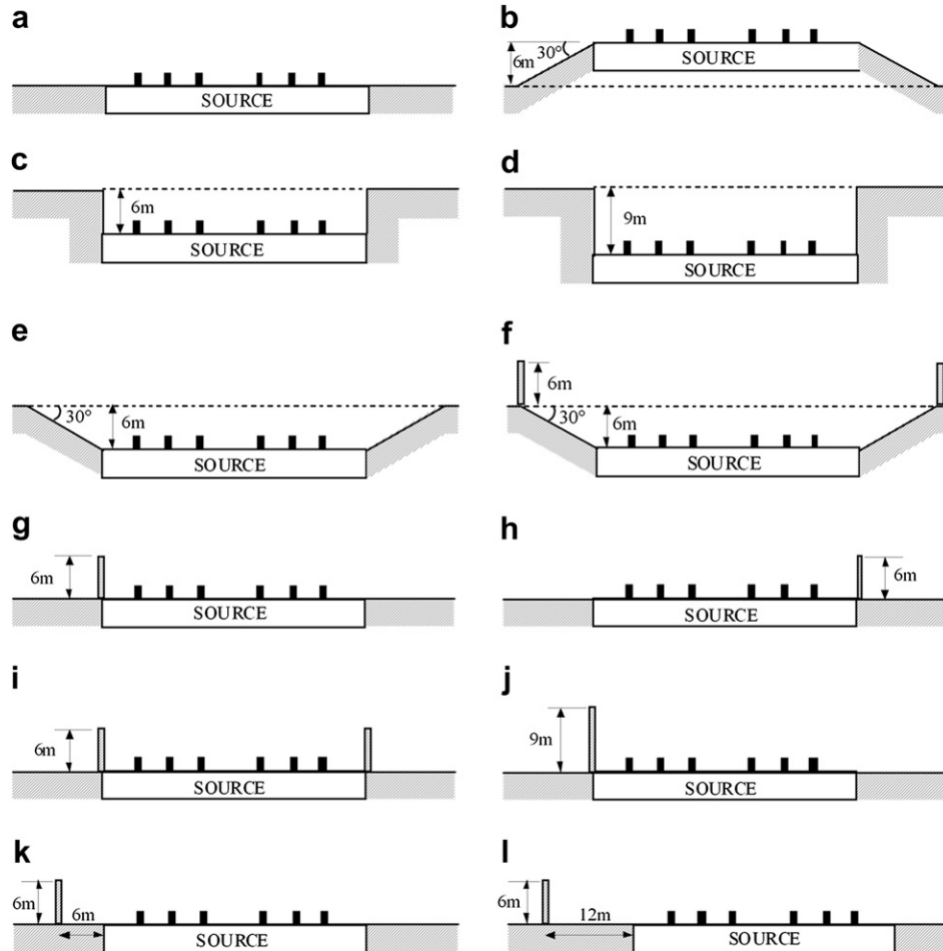


Figure 2.5: Elevation view showing cross sections through the various roadway configurations studied (cases A through L corresponding to figure lettering). Flow is from left to right. Dashed line in (b) through (f) represents at-grade elevation. From (Heist et al., 2009)

Barriers or depressed roadways with vertical walls created recirculation zones. When both upwind and downwind barriers were present, the downwind barrier recirculation zone length was reduced from 5 to 3 times the barrier height. Turbulent kinetic energy (TKE) calculated based on velocity measurements showed that the greatest increases in TKE were caused by the shear at the top of the barriers.

All of the configurations reduced downwind concentrations relative to the flat terrain case. The elevated roadway showed the least difference relative to the flat terrain case. Vertical concentration profiles indicated that the barriers and elevated roadway shifted peak concentrations vertically upward, as found in the CFD study (Hagler et al., 2011). The lowest downwind concentration occurred for the case when the depressed roadway was combined with upwind and downwind barriers. The effect of barrier placement, upwind or downwind and distance from road, was much smaller than the effects of the presence of barrier and the elevation of the road.

The study found that the ground level concentrations beyond a distance of about 10 times the height of the barrier could be modeled as a ground level source with two modifications: 1) the source is shifted upwind, and 2) the effective rate of vertical plume spread, the entrainment velocity,  $w_e$ , relative to the friction velocity,  $u_*$ , is increased in the presence of a barrier. The upwind shift in source location depends on road geometry, with larger shifts necessary when multiple physical effects are combined. Figure 2.6 shows that the concentrations associated with three roadway configurations can be described by shifting the flat terrain curve upwind by prescribed distances. They also found that the entrainment velocity depends on the surface friction velocity and the road geometry, with larger entrainment velocities occurring for cases with barriers rather than flat terrain

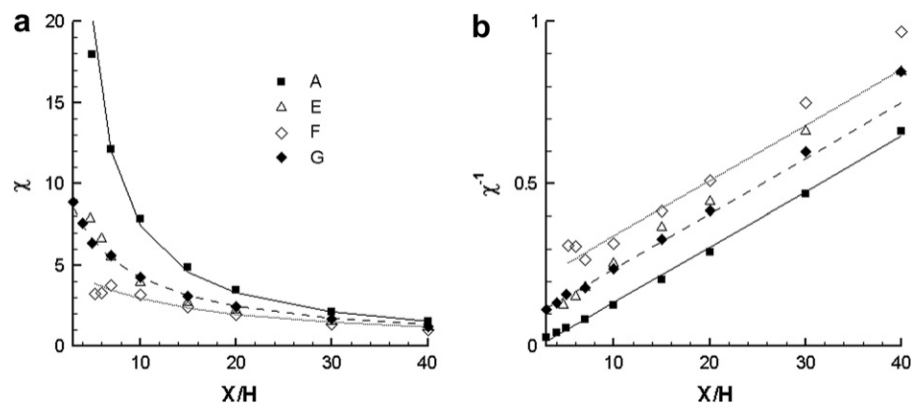


Figure 2.6: (a) Ground-level concentration as a function of downwind distance. (b) Inverse ground-level concentration as a function of downwind distance. Solid line is a straight-line fit to flat terrain data. Other lines show the effect of shifting source location for flat case a distance of 6H (dashed) and 11H (dotted) upwind. (A = flat terrain; E = depressed roadway, sloped walls; F = depressed roadway, sloped wall, and noise barriers; G = noise barrier at  $x/H = 3$ ). From (Heist et al., 2009)

and for rougher boundary layers with greater surface friction velocities. This is shown in Figure 2.7.

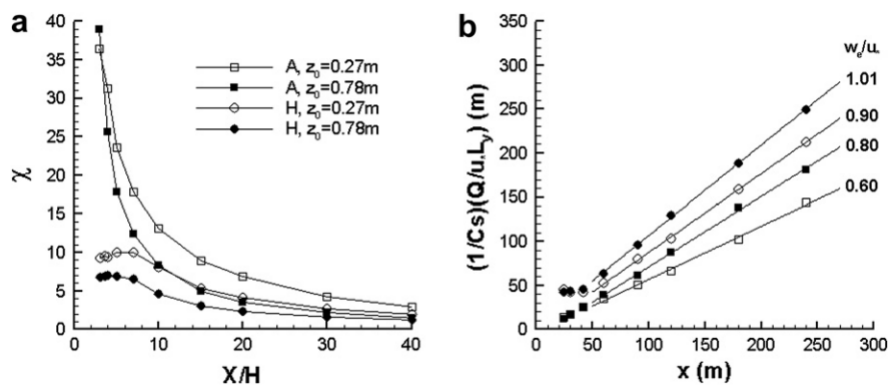


Figure 2.7: (a) Ground-level concentration versus downwind distance for two boundary layer wind profiles with different roughness lengths and for two different roadway configurations (Cases A and H). (b) Inverse ground-level concentration for the same cases, scaled to yield  $w_e/u_*$  as slope of best-fit line (axes units are full-scale meters). (A = flat terrain; H = noise barrier at  $x/H = 3$ ). From (Heist et al., 2009)

## 2.2.2 Tracer Study

The field study was conducted near NOAA's Grid 3 diffusion grid at the Department of Energy's Idaho National Laboratory (INL), which is located across a broad, relatively flat plain on the western edge of the Snake River Plain in southeast Idaho. A 90 m long by 6 m high straw bale stack represented a roadway barrier for the primary experiment (Figure 2.8). The primary and reference control experiments both had a 54 m long sulfur hexafluoride tracer line source release positioned 1 m above ground level (AGL) representing pollution sources from a roadway. In the primary experiment, the line source was positioned 6 meters upwind of the 6 m high barrier with a gridded array of 58 bag samplers downwind of the line source and barrier for measuring mean 15-min concentrations. The control experiments, conducted at an adjacent location and simultaneous to the primary, include identical source and concentration sampling but without the barrier in the array. An array of six 3-d sonic anemometers was deployed for making wind and turbulence measurements, 5 on the primary experiment and 1 on the control experiment.

Five tests were conducted during the study, each spanning a 3 hour period broken into 15 minute tracer sampling intervals. One test was conducted in unstable conditions, one in neutral conditions, and three in stable conditions. One of the days is not included in the model evaluation because wind directions were often not perpendicular to the source.

This study found several important results. The presence of the barrier always decreased concentrations downwind of the barrier compared to those in the open field, but increased concentrations upwind of the barrier. Increasing atmospheric stability increased downwind concentrations. The barrier enhanced both lateral as well as vertical dispersion (Finn et al., 2010).



Figure 2.8: Mock straw bale sound barrier, 6 m high and 90 m long. From (Finn et al., 2010)

The average crosswind maximum concentration measurements for four trials from the tracer study are shown in Figure 2.9. This figure demonstrates that reduced concentrations relative to the flat terrain case are found at all downwind distances downwind of the barrier. Concentration reductions were found up to about 20 times the barrier height downwind for neutral and unstable conditions (day 1 and day 2), and further downwind for stable conditions (day 3 and day 5). Concentrations were typically less than about 50% of the non-barrier concentrations in the wake zone of the barrier, although in some cases concentrations were as low as 20% of the non-barrier concentrations. This is similar to the concentration reduction found by the wind tunnel study conducted by Heist et al. (2009).

Figure 2.10 shows contour plots of the ratio of barrier to non-barrier concentrations. This figure demonstrates that a concentration deficit exists near the center of the barrier,

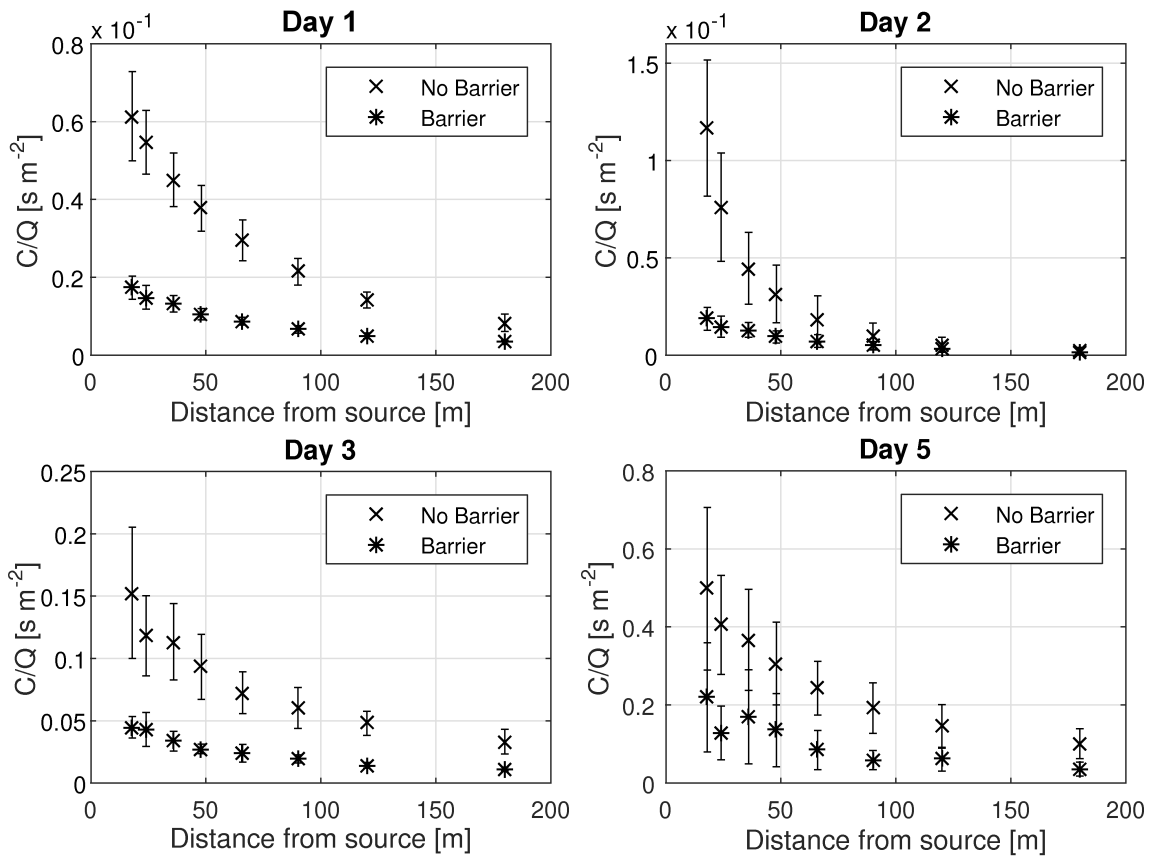


Figure 2.9: Average crosswind maximum concentration measurements from the Idaho Falls tracer study on day 1 (neutral), day 2 (unstable), day 3 (stable), and day 5 (stable). Error bars represent one standard deviation of the observations at each downwind distance.

with increased concentrations along the barrier edges. The large concentration ratio at the edges is due to the increased lateral plume spread and also possibly due to barrier edge effects. The magnitude of the concentration at the barrier edges is only a few tens of ppb, compared with thousands of ppb at the center, so the large ratios do not represent significant concentrations.

Increases in concentrations were found upwind of the barrier in some trials, especially in case d, which was conducted in the most stable conditions of the study. Low wind speeds

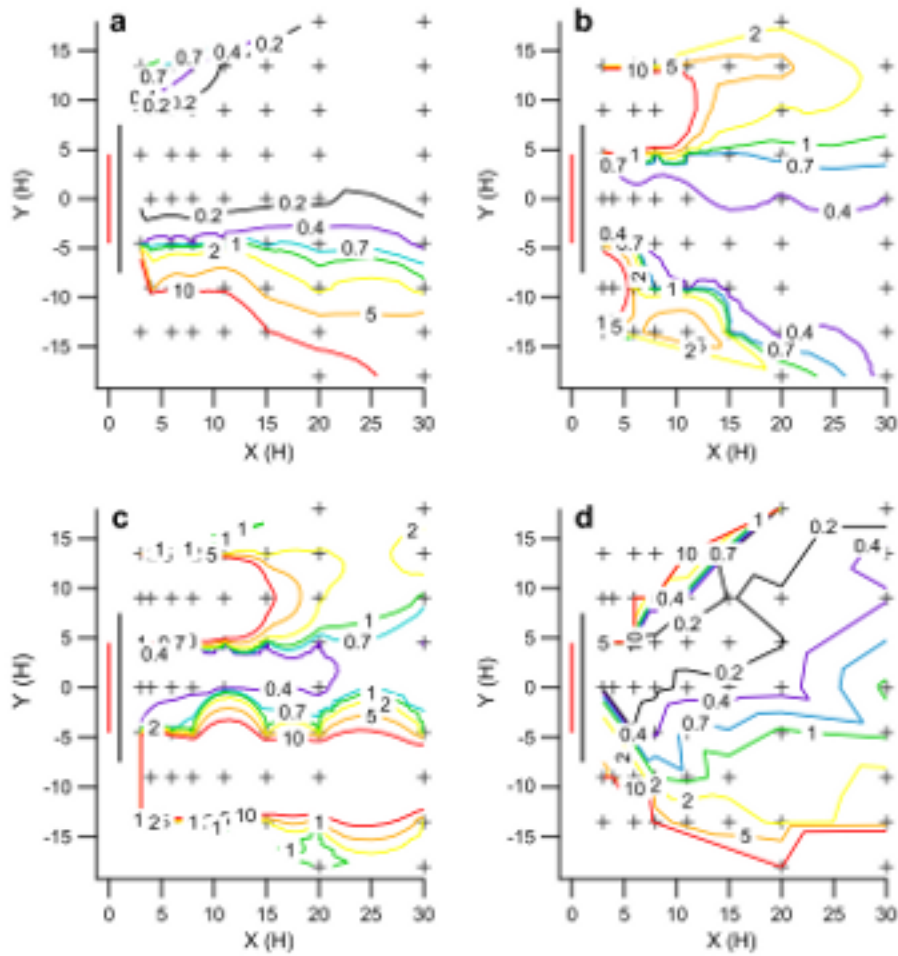


Figure 2.10: Contour maps of the ratio between barrier and non-barrier tracer concentrations at corresponding grid locations for the selected (a) unstable, (b) neutral, (c) weakly stable, and (d) stable cases. Tracer release line (bright red) and barrier (bold black) are shown for reference. From (Finn et al., 2010)

and high atmospheric stability in general tended to trap tracer upwind of the barrier to create high upwind concentrations.

## 2.3 Model Evaluation

In this section I show the development and evaluation of three dispersion models with data collected in the wind tunnel study (Heist et al., 2009) and the tracer study (Finn et al., 2010) (see section 2.2 for details of these studies).

Section 2.2 described the findings of the major experimental studies of the effect of barriers on near road concentrations. In summary, the major effects of barriers on concentrations are: 1) the concentration is well-mixed in a zone extending from the ground to the barrier height, and several barrier heights downwind, 2) the turbulence spreading the plume is increased downwind of the barrier, 3) the pollutant is lofted above the top of the barrier, which increases the concentration near the top of the barrier.

Three dispersion models are developed to account for these effects on near-road concentrations:

1. Source Shift model: Heist et al. (2009) made two modifications to the basic Gaussian plume model for ground level concentrations: 1) the source is shifted upwind, and 2) the effective rate of vertical plume spread, the entrainment velocity,  $w_e$ , relative to the friction velocity,  $u_*$ , is increased in the presence of a barrier (see section 2.2). However, this model is incomplete without specification of the source shift distance and increase in entrainment velocity. Heist et al. (2009) only specify that these parameters depend on barrier height and roadway configuration. The source shift model extends the model of Heist et al. (2009) to include parameterizations of the shift distance and the entrainment velocity.
2. Mixed Wake model: This model describes the rapid mixing within the barrier wake by modifying the vertical concentration profile used in the Gaussian plume dispersion

model. The vertical plume spread equation is also modified downwind of the barrier to account for the increased rate of plume spread in the presence of a barrier.

3. Puttock Hunt model: This model describes the vertical lofting over the top and subsequent downward flow behind the barrier in addition to the vertical mixing within the cavity behind the barrier. The model is based on the work of Puttock & Hunt (1979) in modeling dispersion around obstacles with separated wakes.

The source-shift and mixed-wake models proposed here are based on the Gaussian plume formulation for a point source, which gives the concentration as:

$$C(x, y, z) = \frac{Q}{\sqrt{2\pi}U(\bar{z})\sigma_y(x)} \exp\left(-\frac{y^2}{2\sigma_y(x)^2}\right) F_z(x, z) \quad (2.2)$$

$$F_z(x, z) = \frac{1}{\sqrt{2\pi}\sigma_z(x)} \left[ \exp\left(-\frac{(z-h)^2}{2\sigma_z(x)^2}\right) + \exp\left(-\frac{(z+h)^2}{2\sigma_z(x)^2}\right) \right] \quad (2.3)$$

where  $x$ ,  $y$ , and  $z$  are the downwind distance from the source, crosswind distance, and height of the receptor,  $h$  is the source height,  $Q$  is the emission rate,  $\sigma_y$  is the horizontal plume spread,  $\sigma_z$  is the vertical plume spread, and  $U(\bar{z})$  is the wind speed evaluated at the effective plume centerline height,  $\bar{z}$ , defined by:

$$\bar{z} = \frac{\int_0^\infty zC^y(x, z)dz}{\int_0^\infty C^y(x, z)dz} \quad (2.4)$$

where  $C^y$  is the crosswind integrated concentration. The expression for  $\bar{z}$  when the source height is zero is  $\bar{z} = \sqrt{\frac{2}{\pi}}\sigma_z$ .

The concentration from an infinitesimal segment of the line source aligned along the  $y$  axis is equal to  $C(x, y, z)dy$ , where the emission rate  $Q$  is replaced by the emission rate per unit length of the source. The total concentration from the source is calculated

by integrating this expression along the length of the source. The integral cannot be evaluated in closed form when the wind direction is not perpendicular to the source, but we use an analytical approximation to the integral (Venkatram & Horst, 2006) which results in:

$$C(x, z) = \frac{q}{2U \cos(\theta)} [erf(t_1) - erf(t_2)] F_z(x^{eff}, z) \quad (2.5)$$

where  $t_i = \frac{(y-y_i)\cos(\theta)-x\sin(\theta)}{\sqrt{2}\sigma_y(x_i)}$ , the subscripts refer to the two ends of the source,  $y_i$  is the y-coordinate of the two ends of the source,  $\theta$  is the angle between the wind direction and the perpendicular to the line source, and  $q$  is the line source emission rate per unit length. The vertical distribution function has been evaluated at the effective downwind distance (Venkatram & Horst, 2006):

$$x^{eff} = x/\cos(\theta) \quad (2.6)$$

This expression performs well for all wind directions, with errors less than 1% except when  $\theta = \pm 90^\circ$  or when the concentration is small (Venkatram & Horst, 2006).

We limit our analysis to conditions where the wind direction is close to perpendicular to the road because we expect the primary effects of the barrier, vertical mixing, increased turbulence that spreads the plume vertically, and vertical lofting, to be largest during perpendicular flow conditions, and because the two primary experimental data sets from the Idaho Falls (Finn et al., 2010) and wind tunnel (Heist et al., 2009) experiments focused on perpendicular wind conditions. Under parallel flow conditions the effect of the barrier on lateral plume spread could alter the near road concentration from that when the barrier is absent.

The plume spreads are calculated using new plume spread formulations (Venkatram et al., 2013) derived from the concentrations measured at the open terrain site during the Idaho Falls study (Finn et al., 2010). They are given by equations (2.7) and (2.8).

$$\sigma_z(x) = \begin{cases} a * 0.57 \frac{u_*}{U(\bar{z})} x \frac{1}{1+3 \frac{u_*}{U(\bar{z})} (\frac{x}{L})^{2/3}} & L > 0 \\ a * 0.57 \frac{u_*}{U(\bar{z})} x (1 + 2 \frac{u_*}{U(\bar{z})} \frac{x}{L}) & L < 0 \end{cases} \quad (2.7)$$

$$\sigma_y(x) = \begin{cases} 1.6 \frac{\sigma_v}{u_*} \sigma_z (1 + 1.5 \frac{\sigma_z}{L}) & L > 0 \\ 1.6 \frac{\sigma_v}{u_*} \sigma_z (1 + 0.5 \frac{\sigma_z}{|L|})^{-1/3} & L < 0 \end{cases} \quad (2.8)$$

where  $\sigma_v$  is the standard deviation of horizontal velocity fluctuations,  $L$  is the Monin-Obukhov length, and we include the factor  $a$ , which accounts for the increased rate of plume spread in the barrier models. The wind speed at the plume centerline,  $U(\bar{z})$  is given by the Monin-Obukhov similarity profile:

$$U(z) = \frac{u_*}{\kappa} \left[ \ln \left( \frac{z-d}{z_0} \right) + \psi_M \left( \frac{z_0}{L} \right) - \psi_M \left( \frac{z-d}{L} \right) \right] \quad (2.9)$$

where the integrated form of the non-dimensional wind shear,  $\psi_M$ , is given by (Paulson, 1970):

$$\psi_M(y) = \begin{cases} -4.7y & y < 0 \\ 2 \ln \left( \frac{1+x}{2} \right) + \ln \left( \frac{1+x^2}{2} \right) - 2 \tan^{-1}(x) + \pi/2 & y > 0 \end{cases} \quad (2.10)$$

where  $x = (1 - 16y)^{1/4}$ . The plume spreads and wind speed at  $\bar{z}$  are interdependent and must be evaluated simultaneously within this formulation.

Before proceeding to the description and evaluation of the barrier models, the basic Gaussian plume model formulation of equations (2.5) and (2.6), using equations (2.7) and (2.9) to calculate the vertical plume spread and wind speed, was validated with the

observed concentrations in the control experiments, without a barrier present, in both the tracer and wind tunnel studies.

The performance of the dispersion models is expressed quantitatively by the geometric mean and standard deviation of the residuals between the logarithm of the observations and predictions, by the fraction of data points that are within a factor of two of the observations, *fact2*, and by the correlation coefficient between the data,  $r^2$ . The geometric mean,  $m_g$ , and standard deviation,  $s_g$ , are defined as:

$$\ln(m_g) = \sum_i \epsilon_i / N \quad (2.11)$$

$$\ln(s_g) = \left[ \sum_i (\epsilon_i - \ln(m_g))^2 / (N - 1) \right]^{1/2} \quad (2.12)$$

where  $\epsilon_i = \ln(C_{oi}) - \ln(C_{pi})$  is the residual between the  $i_{th}$  observed concentration,  $C_{oi}$ , and the predicted concentration,  $C_{pi}$ , and  $N$  is the number of data points. A perfect correspondence between observations and predictions will produce  $m_g$  and  $s_g$  equal to 1. If  $m_g$  is less than 1 the observations are on average smaller than the model predictions. The 95% confidence interval of the ratio of the observed to predicted concentrations is approximately given by  $[m_g s_g^{-2} \ m_g s_g^2]$ .

Figure 2.11 shows a comparison of the measurements made in the control experiments in the wind tunnel with the model described above, where the factor  $a$  in the vertical plume spread, equation (2.7), is set to 1. The wind tunnel simulated a finite length source 48 cm long (72 m full scale). However, the concentration data can be adjusted to derive the concentration that would be observed if the source was infinitely long (Heist et al., 2009). The model comparison is made with the infinite source concentration that has been adjusted in this way. The model shows almost no bias and has very good

correlation with observations. The basic model formulation is clearly adequate to describe the concentration measurements in the wind tunnel data set.

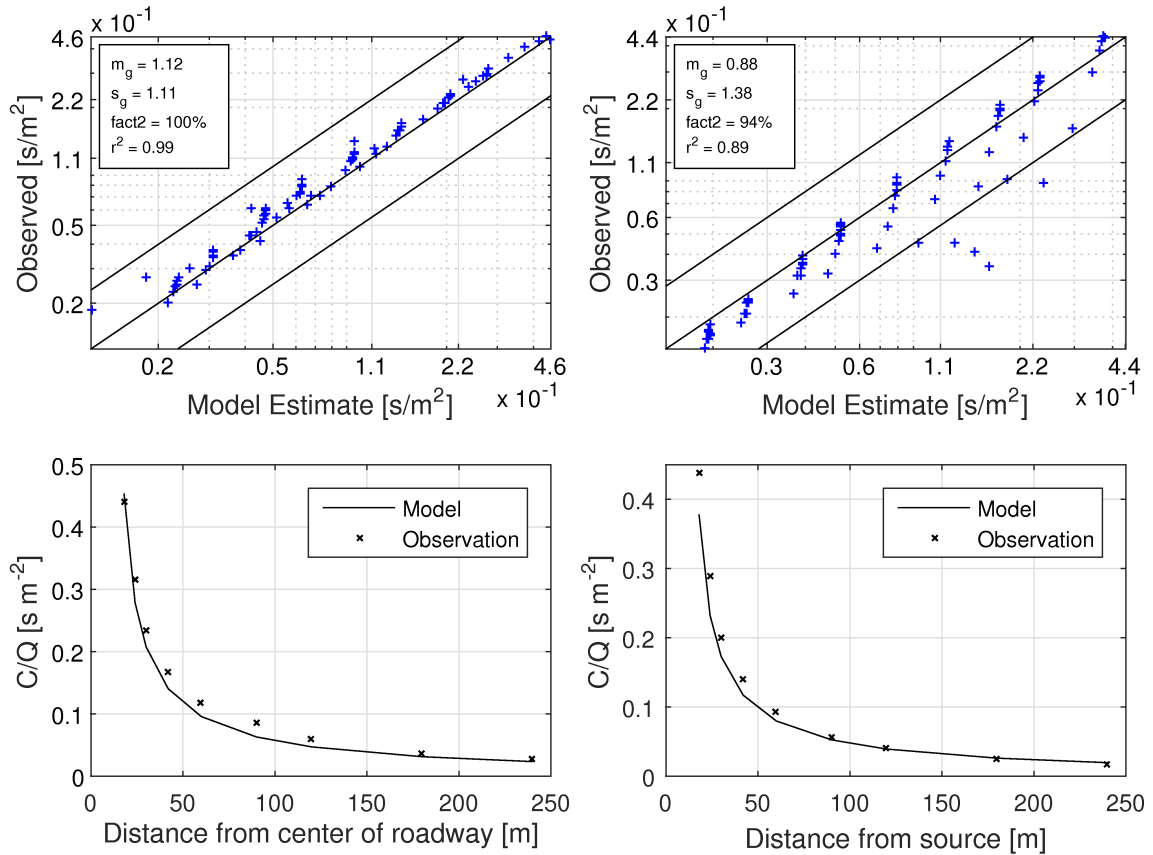


Figure 2.11: Comparison of Gaussian plume dispersion model with wind tunnel infinite source concentration during the control experiments (no barrier present) for receptors below a height of 6 m. Center black lines correspond to 1 to 1 lines and observations within outer two lines are within a factor of two of model estimates. Bottom figures show modeled and observed ground level concentrations as a function of distance from the road. The smooth approach flow wind tunnel case ( $z_0 = 0.27 \text{ m}$ ,  $u_* = 0.25 \text{ m/s}$ ) is on the left and the rough approach flow wind tunnel case ( $z_0 = 0.78 \text{ m}$ ,  $u_* = 0.3 \text{ m/s}$ , displacement height = 8.1 m) is on the right.

Figure 2.12 shows scatter plots comparing the model described above with the measurements made in the control experiments in the tracer study. The factor  $a$  in the vertical plume spread, equation (2.7), is set to 1. The model is nearly unbiased and correlates well with most of the data. Almost all of the data is within a factor of two of the ob-

servations. Even during very stable conditions, observed during day 5, most of the data points are within a factor of two the model, indicating that the model adequately describes the observations. During the stable conditions of day 3 and day 5 the model tends to overestimate by about 10%.

Figure 2.13 compares the modeled and observed variation with distance from the source. There is a tendency for the model to underestimate concentrations at large distances from the source for measurements made during day 1. However, the underestimation is very small and the observations remain within a factor of two of the model estimates. Overall there is very little bias in the model and very good correlation. We conclude that the formulation is adequate for estimating the concentrations in the control experiments.

### **2.3.1 Source Shift Model**

We extend the source-shift model, proposed by Heist et al. (2009), by including a formulation for the source shift distance based on the barrier height. The source shift model estimates concentrations using the Gaussian plume formulation, where the source is moved upwind by some distance,  $s$ , to account for the barrier. Figure 2.14 shows a schematic of the concept behind the source shift. To account for the barrier we place the source at some point upwind of the physical source, indicated in red, and predict concentrations using the Gaussian plume formulation where  $x$  is now the distance from the shifted source location to the receptor. This effectively increases the vertical plume spread at a given distance from the source.

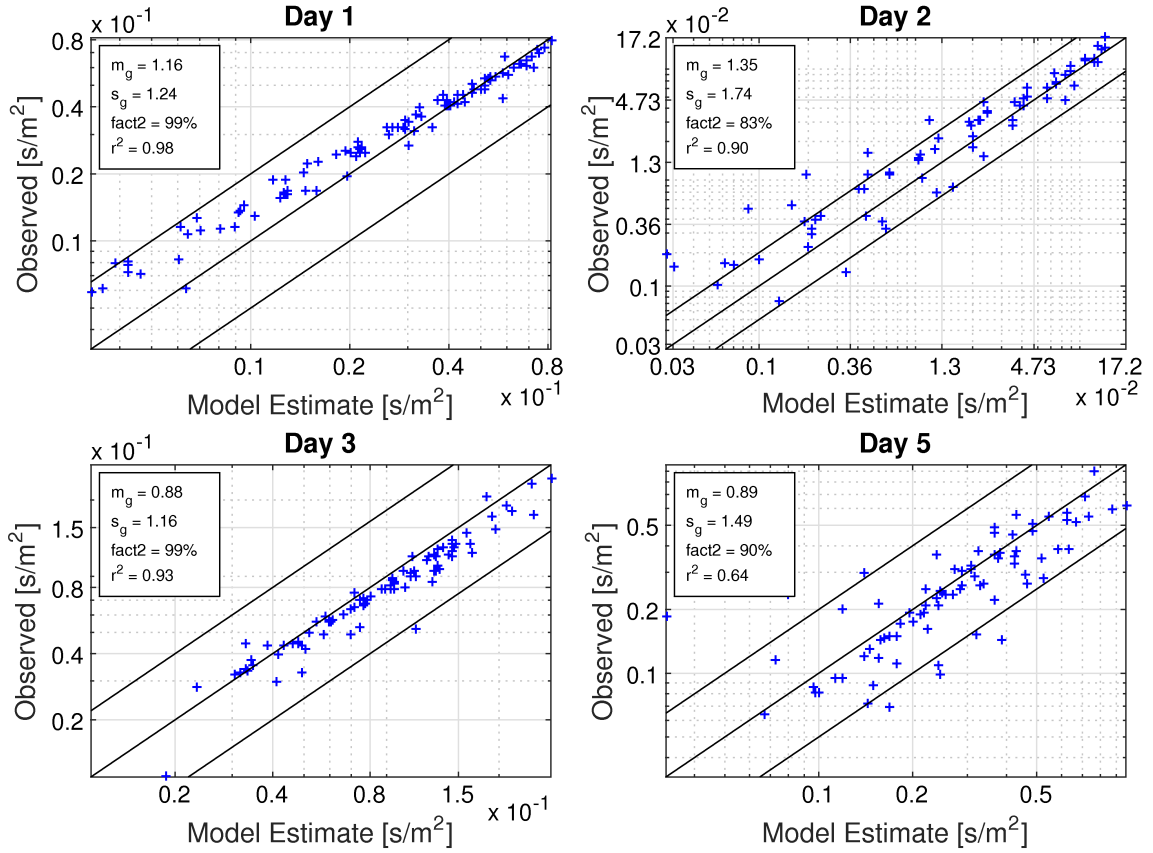


Figure 2.12: Comparison of Gaussian plume dispersion model with crosswind maximum concentrations observed during Idaho Falls control experiments (no barrier present). Center black lines correspond to 1 to 1 lines and observations within outer two lines are within a factor of two of model estimates. The 4 days of the Idaho Falls study represent measurements during atmospheric stability conditions that are: neutral - day 1, unstable - day 2, stable - day 3, and very stable - day 5.

One way to parameterize the source shift distance is to enforce the condition that the concentration downwind of the barrier is well mixed over the height of the barrier. Then, the vertical plume spread at the location of the barrier is proportional to the barrier height. Based on this assumption we can write the shift distance as:

$$\sigma_z \left( \frac{s + x_b}{\beta \cos(\theta)} \right) = \sqrt{\frac{2}{\pi}} H \quad (2.13)$$

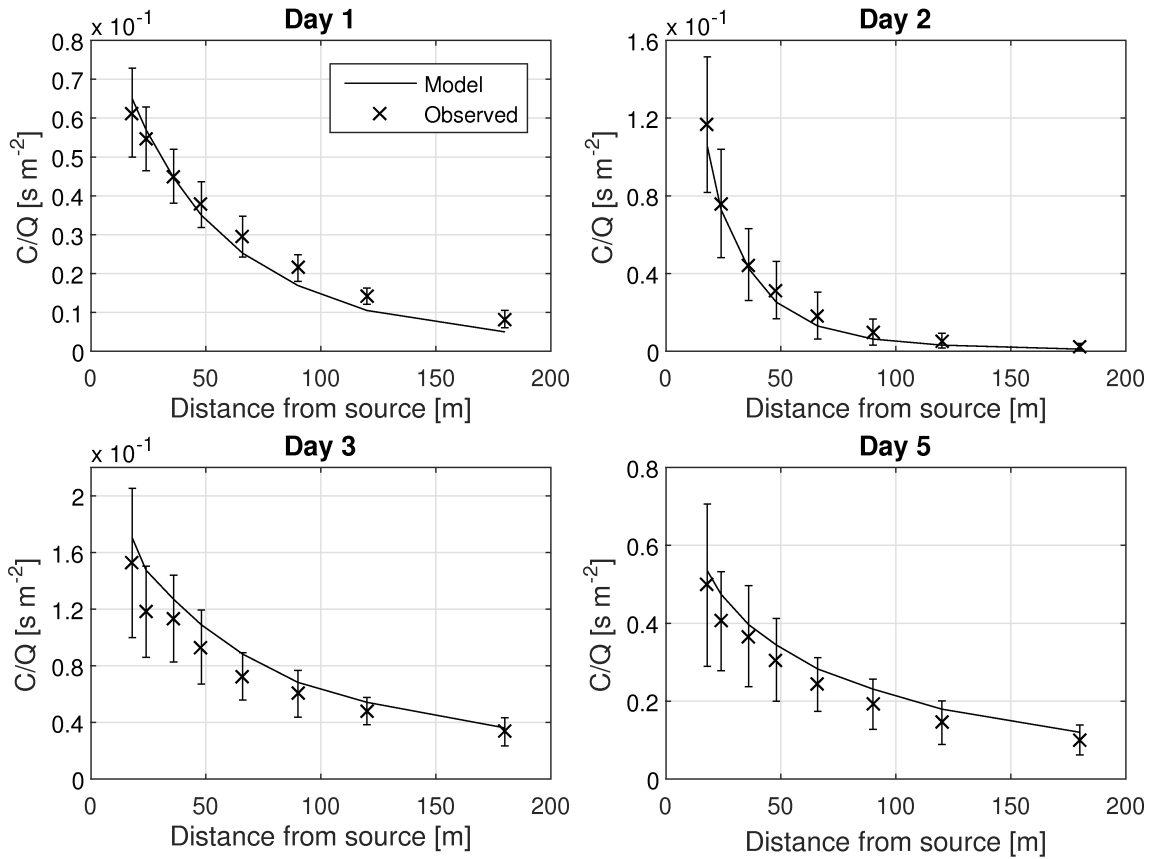


Figure 2.13: Downwind variation of Gaussian plume dispersion model and crosswind maximum concentration of Idaho Falls observations during the control experiments (no barrier present) . Error bars show standard deviation of observations. The 4 days of the Idaho Falls study represent measurements during atmospheric stability conditions that are: neutral - day 1, unstable - day 2, stable - day 3, and very stable - day 5.

where  $H$  is the barrier height,  $x_b$  is the distance from the physical source to the barrier,  $\theta$  is the angle between the mean wind direction and the normal to the barrier, and  $\beta$  is an empirical correction factor, which we include to calibrate the model. Equation (2.13) is only valid if the source is near the barrier, where  $s$  is positive; otherwise we set  $s = 0$ .

The rate of growth of the vertical plume spread is enhanced in the presence of the barrier. This effect is accounted for in the source shift model through the factor  $a$  in equation (2.7). The physical basis for the factor  $a$  is that the turbulence that spreads the plume is increased in the barrier wake. This is caused by the production of turbulence due

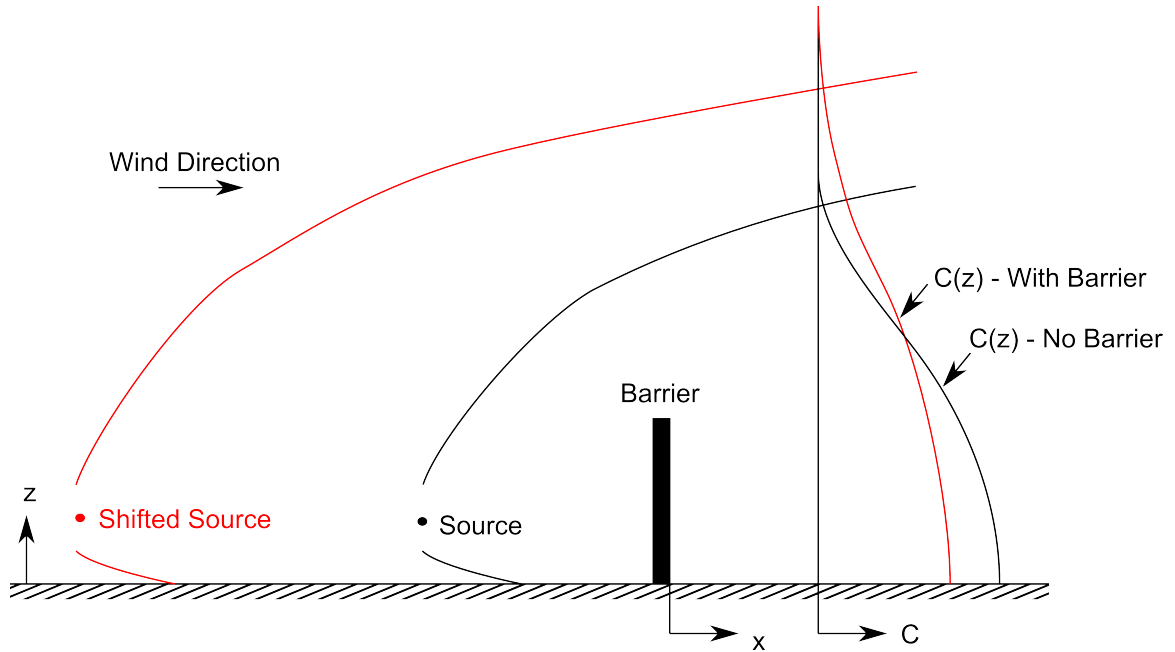


Figure 2.14: Schematic of the source-shift model. The physical source is indicated in black. If the source is shifted upwind the plume spread at some distance from the source is increased.

to the shear stress near the top of the barrier. Thus the factor  $a$  depends on the relative magnitudes of barrier produced turbulence and atmospheric turbulence that exists upwind of the barrier. The magnitude of the turbulent kinetic energy produced by the barrier is determined by equating the turbulence production and dissipation rates. The turbulent kinetic energy produced by the barrier is equal to the energy removed from the mean flow. Thus, using the expression for the drag force on a blunt obstacle, the rate of production of TKE is given by  $P_{barrier} = 1/2C_dU(H)^3/H$ , where  $C_d$  is the barrier drag coefficient and  $U(H)$  is the wind speed at the barrier height. The rate of turbulent production due to the shear stress on the ground is  $u_*^2 dU/dz \sim \frac{u_*^3}{\kappa z} \phi_M(z/L)$ . The turbulent dissipation rate is given by  $\epsilon = c \frac{k^{3/2}}{l}$ , where  $k$  is the TKE and  $l$  is the length scale of the large eddies. The ratio of the resulting TKE in the presence of the barrier to that without the barrier present is given by:

$$a_0 = \left( 1 + \frac{1}{2} \frac{\alpha C_d \kappa}{\phi_M(z/L)} \left( \frac{U(H)}{u_*} \right)^3 \right)^{2/3} \quad (2.14)$$

where  $\alpha$  is an empirical constant. With  $C_d = 0.5$ , we set  $\alpha = 0.0035$  by fitting the dispersion models with observations.

The turbulence in the wake of an infinitely long obstacle decays with distance as  $\sigma_w \sim x^{-1/2}$  (Tennekes & Lumley, 1972). Because of this, we allow the factor  $a$  to vary with distance from the barrier as:

$$a = 1 + (a_0 - 1) \left( 1 + \frac{x}{L_w} \right)^{-1/2} \quad (2.15)$$

where  $L_w$  is a length scale that characterises the length of the barrier's wake. We set  $L_w = 20H$  by fitting the models with observations.

Figure 2.15 shows a comparison of the source shift model predictions with observations during the Idaho Falls tracer study. Observations are the crosswind-maximum concentrations, the maximum concentration of the group of receptors at each perpendicular distance from the source. Only data where the wind direction is within  $40^\circ$  of perpendicular to the line source, 75% of the data, is included. Meteorological inputs required for the model were derived from measurements made at the sonic anemometer placed 9.6 m upwind of the source. The value of the calibration constant,  $\beta$ , was 0.4.

The model performs best during neutral and slightly stable conditions and worst during very stable conditions. During day 1 and day 3,  $s_g$  is less than 1.25 and there is good correlation between model and observations. The model is unbiased during day 1, with  $m_g$  equal to 0.9.

During day 2, the model overestimates near the barrier and  $s_g$  is large. Day 2 corresponds with very unstable, light wind conditions, where the average wind speed at 3 m

above ground level is 2 m/s, compared with 7.7 m/s of day 1 and 3.5 m/s of day 3. The model estimate of the concentration directly downwind of the barrier is inversely proportional to the wind speed, resulting in large predicted concentrations during day 2. The model could be overestimating concentrations near the barrier during unstable conditions because the effective wind speed given by equation (2.9) does not adequately estimate the actual wind speed downwind of the barrier. Since the wind speed is reduced in the barrier wake relative to that upstream, a possible way to improve the model performance for unstable conditions is to reduce the behind barrier wind speed relative to equation (2.9). This would increase concentrations for all stabilities, which implies that along with the change in wind speed, the turbulence should be increased by modifying the factor  $\alpha$  so that the model estimates the correct magnitude of concentrations.

During day 5, the model underestimates concentrations, especially near the barrier where the spread of the data is large. The comparison during day 5 may be misleading, because during very stable atmospheric conditions, tracer moved around the edges of the barrier rather than over the top of the barrier and mixed back into the middle, causing large observed concentrations. Thus the comparison for day 5 does not indicate poor model performance.

Figure 2.16 compares the downwind variation of the source shift model predictions with observations from Idaho Falls. The modeled and observed variations are similar during neutral and slightly stable conditions. However, during slightly stable conditions the observed plume spread increases more rapidly than the model predicts up to a distance of about  $20H$  from the barrier. The comparison for unstable conditions implies that the modeled plume spread grows much more rapidly with distance from the barrier than the observations show.

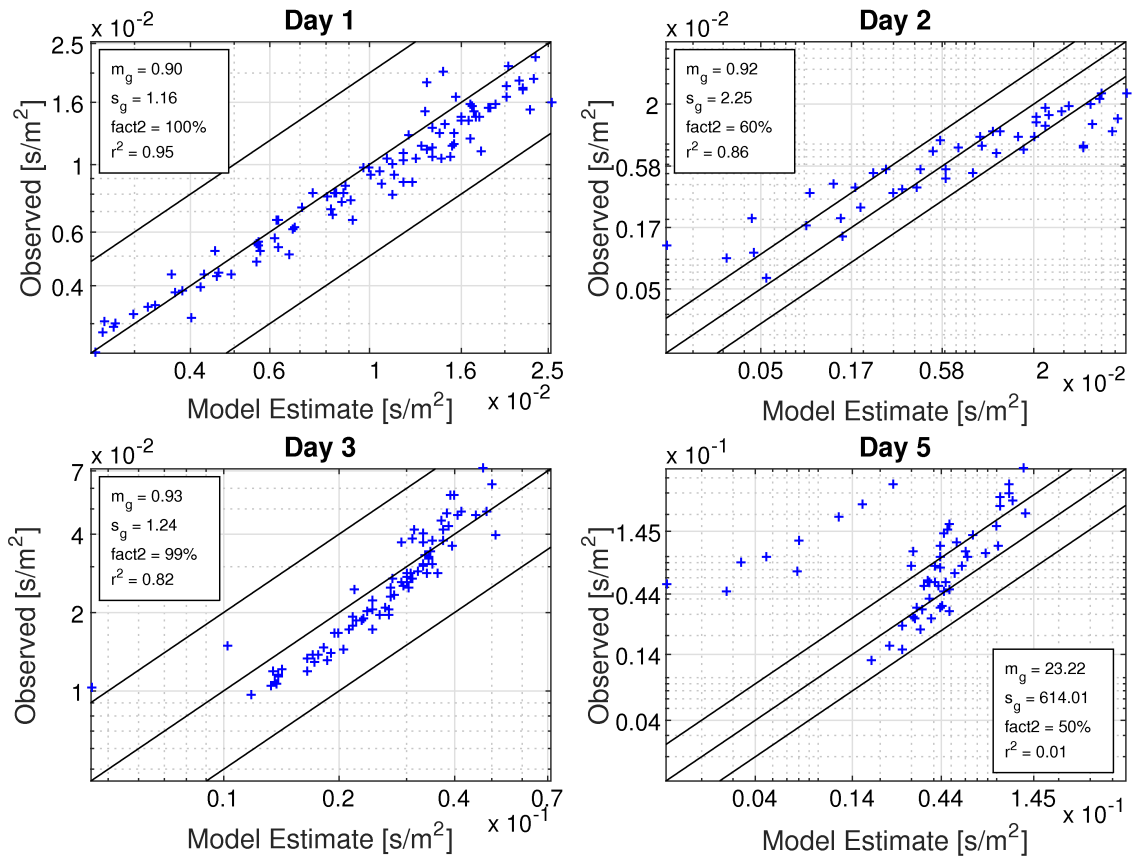


Figure 2.15: Comparison of the source-shift model with crosswind maximum concentrations observed during Idaho Falls. Center black lines correspond to 1 to 1 lines and observations within outer two lines are within a factor of two of model estimates. The 4 days of the Idaho Falls study represent measurements during atmospheric stability conditions that are: neutral - day 1, unstable - day 2, stable - day 3, and very stable - day 5. The model was run with  $\beta = 0.4$ .

I next show the performance of the source shift model at explaining concentrations measured in the wind tunnel study. The observed concentration has been adjusted to represent an infinitely long emission source as described previously. Two wind tunnel simulations were conducted with a barrier downwind of the road, one with a smooth approach flow and one with a rough approach flow. The smooth approach flow has a boundary layer with parameters  $z_0 = 0.18 \text{ cm}$  (0.27 m full scale) and  $u_* = 0.25 \text{ m/s}$ , while the rough approach flow has a boundary layer with a displacement height of 5.4

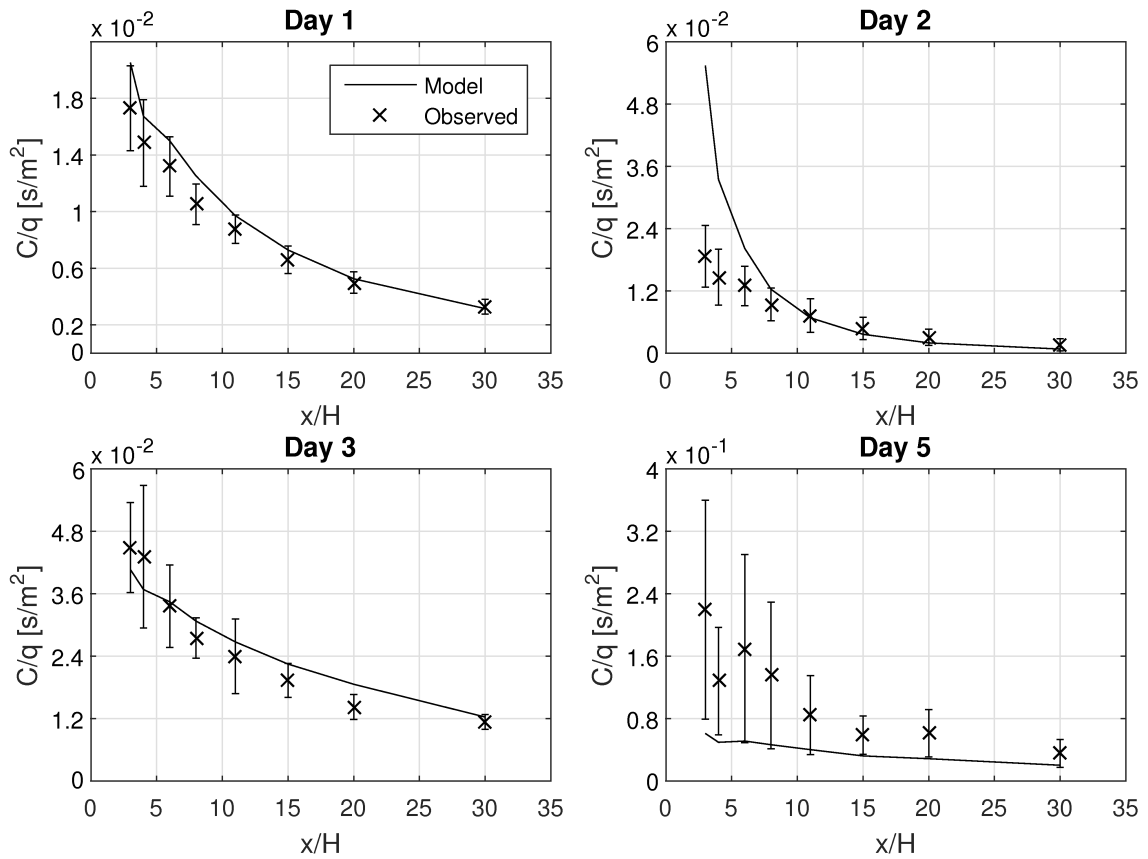


Figure 2.16: Downwind variation of source-shift model and crosswind maximum concentration of Idaho Falls observations. Error bars show standard deviation of observations. The 4 days of the Idaho Falls study represent measurements during atmospheric stability conditions that are: neutral - day 1, unstable - day 2, stable - day 3, and very stable - day 5. The model was run with  $\beta = 0.4$ .

cm (8.1 m full scale) and  $z_0 = 0.52$  cm (0.78 m full scale) and  $u_* = 0.3$  m/s. The comparisons between model estimates and infinite source observations for the smooth and rough cases are shown on the left and right, respectively of Figure 2.17.

The receptors where the observed concentrations are nearly constant correspond to the near wake of the barrier, where the concentration is well mixed by the recirculating cavity. The model overestimates concentrations in this region. Outside the near wake, the source shift model explains the data very well for the smooth approach flow: the model is well correlated with the data and is unbiased outside the near wake. For the rough approach

flow the correlation is also very good but the model overestimates by about 50%. The observed concentrations in the smooth and rough cases are very similar, while the model predicts significantly larger concentrations in the rough case. There is uncertainty in the magnitude of the wind speed downwind of the barrier, and it is likely that the wind speed has not been specified correctly. The large roughness elements in the rough case create an urban canopy layer in which the wind profile may be better described by an exponential profile (MacDonald, 2000) than the similarity profile that was used in the model. It is unclear how the presence of the barrier alters the wind profile. This is discussed further in the evaluation of the mixed wake model.

### 2.3.2 Mixed wake Model

The mixed wake model is based on the Gaussian plume formulation, where the vertical concentration distribution,  $F_z$  is modified to account for the effect of the barrier. Figure 2.18 shows a schematic of the model. In the presence of a barrier, we assume that the concentration is well mixed between the surface and the barrier height to mimic the effect of the recirculating zone behind the barrier. The concentration above the barrier follows a Gaussian distribution.

The vertical concentration profile downwind of the barrier is then given by:

$$F_z = \begin{cases} \frac{C_s}{q} & z < H \\ \frac{C_s}{q} \exp\left(-\frac{(z-H)^2}{2\sigma_z(x)^2}\right) & z > H \end{cases} \quad (2.16)$$

where the surface concentration  $C_s$  is given by:

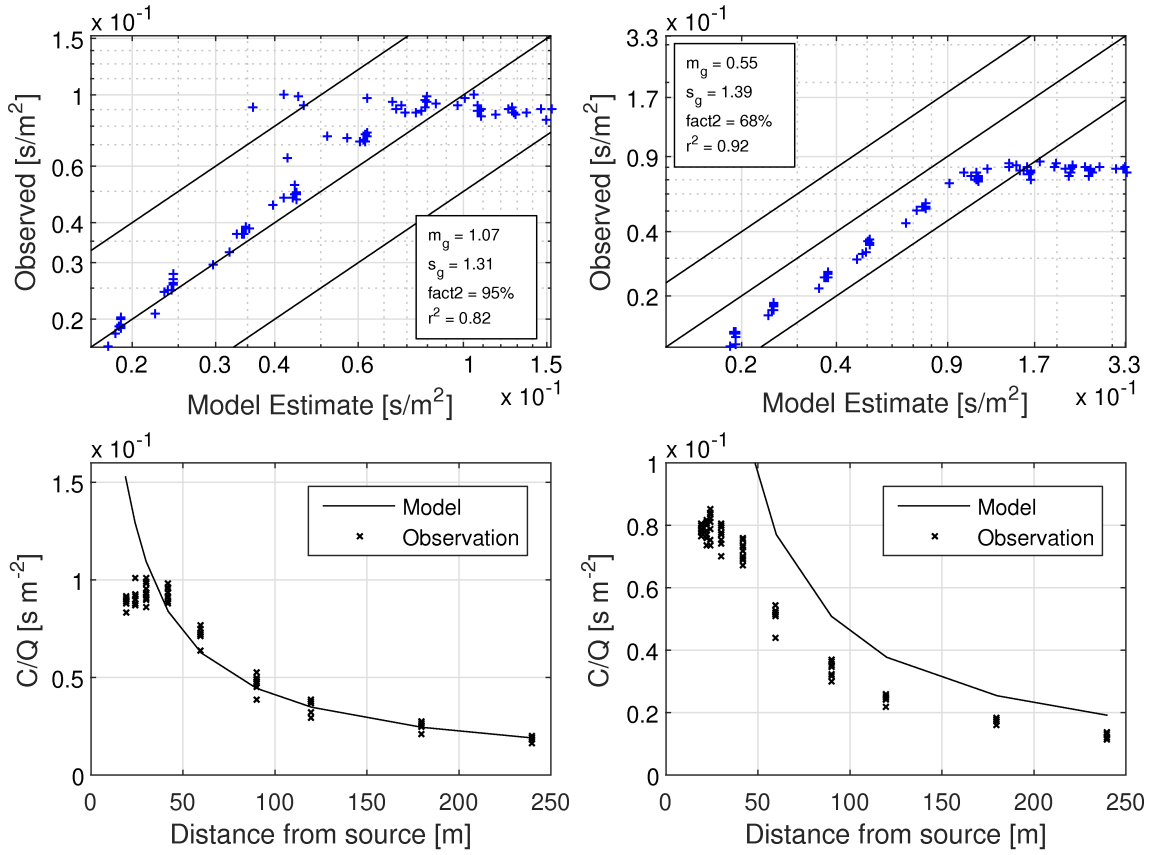


Figure 2.17: Comparison of source-shift model with wind tunnel infinite source concentration for receptors below a height of  $1H$ . Center black lines correspond to 1 to 1 lines and observations within outer two lines are within a factor of two of model estimates. The smooth approach flow wind tunnel case ( $z_0 = 0.27 \text{ m}$ ,  $u_* = 0.25 \text{ m/s}$ ) is on the left and the rough approach flow wind tunnel case ( $z_0 = 0.78 \text{ m}$ ,  $u_* = 0.3 \text{ m/s}$ , displacement height =  $8.1 \text{ m}$ ) is on the right. The model was run with  $\beta = 0.4$ .

$$\frac{C_s}{q} = \frac{1}{U(H/2)H + U(\bar{z})\sqrt{\frac{\pi}{2}}\sigma_z(x)} \quad (2.17)$$

The physical source height does not enter into the mixed wake model equations if it is smaller than the barrier height. The equation is not valid if the source is elevated far above the barrier height, but in this situation the barrier would have little effect on the concentration.

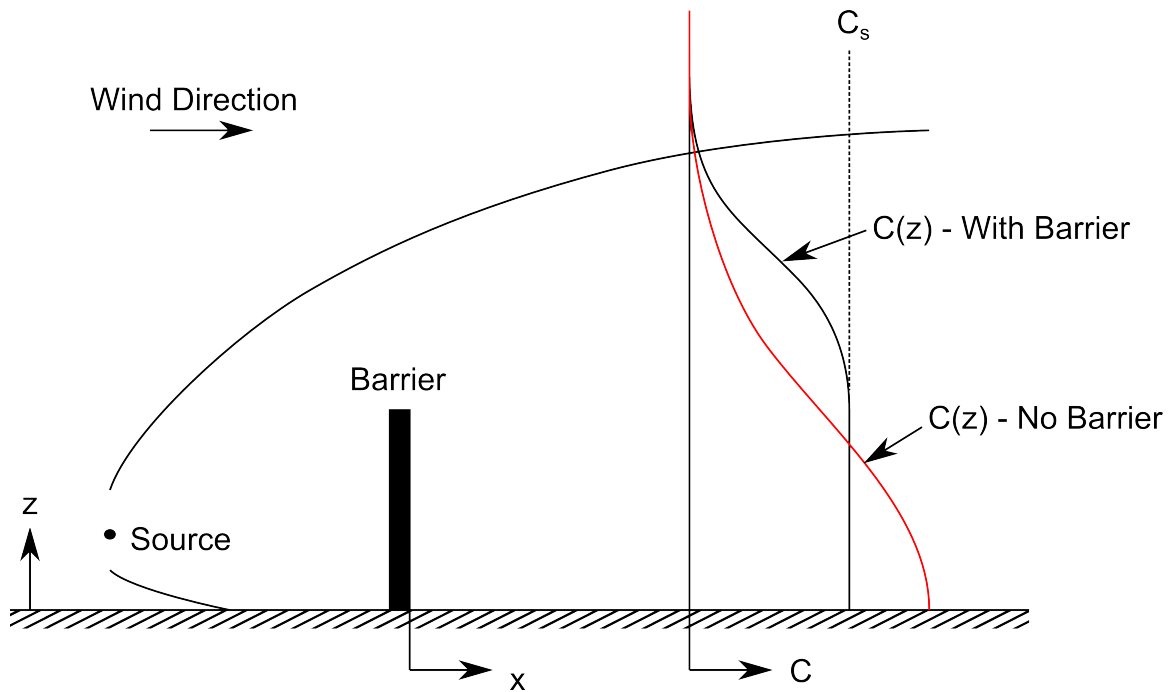


Figure 2.18: Schematic of the mixed-wake model. The pollutant mass is well-mixed below the barrier height in the mixed-wake model and then follows a Gaussian profile above the barrier height.

There are two important wind speeds in this formulation (which are included in equation 2.17: the wind speed at half the barrier height and the wind speed at the effective plume centerline height. The pollutant mass that is mixed below the barrier height is advected with the wind speed at half the barrier height, and the rest of the plume is advected with the wind speed at the effective plume centerline height.

Figure 2.19 shows scatter plots comparing the mixed wake model with crosswind maximum concentrations measured at Idaho Falls. The model performance is similar to that of the source shift model, except that during very stable conditions (day 5) the model does not underestimate as much as the source shift model. The spread of the data is smaller than that of the source shift during all stabilities. The mixed wake model

performs best during neutral and slightly stable atmospheric conditions, and overestimates concentrations near the barrier during unstable conditions.

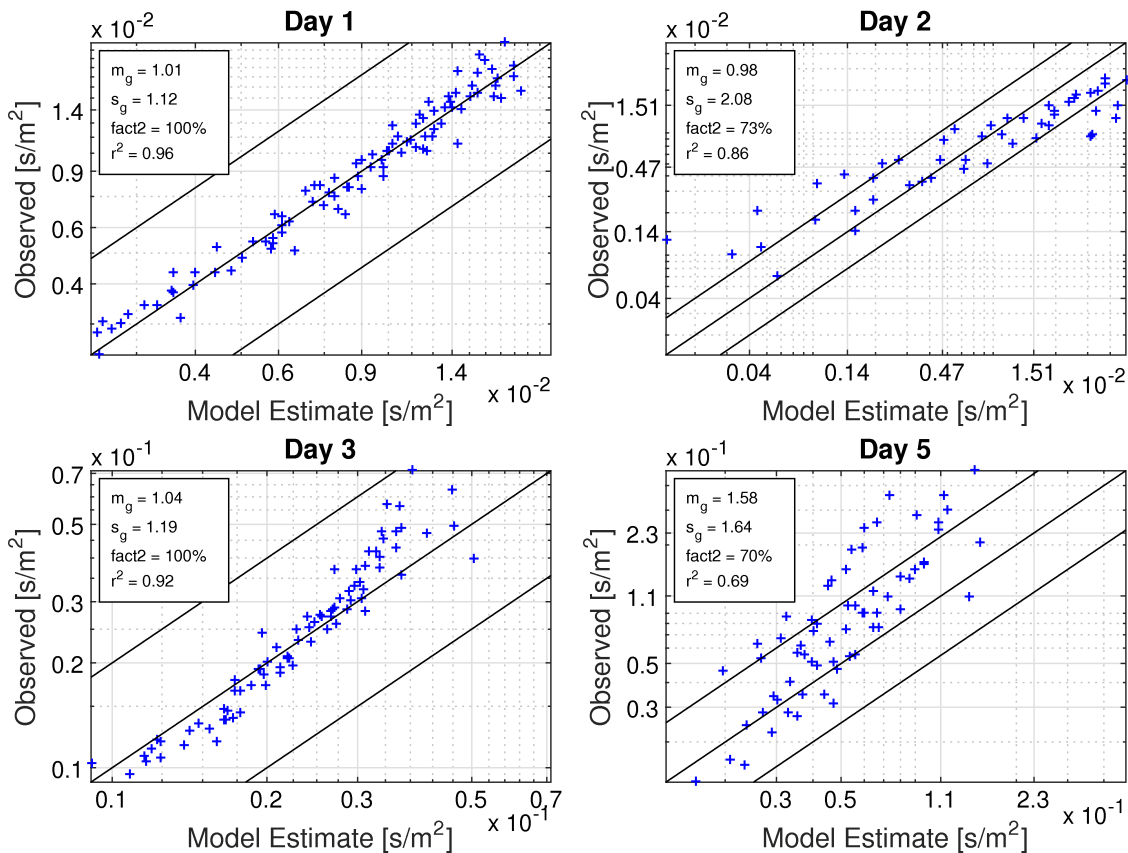


Figure 2.19: Comparison of the mixed wake model with crosswind maximum concentrations observed during Idaho Falls. Center black lines correspond to 1 to 1 lines and observations within outer two lines are within a factor of two of model estimates. The 4 days of the Idaho Falls study represent measurements during atmospheric stability conditions that are: neutral - day 1, unstable - day 2, stable - day 3, and very stable - day 5.

The downwind variations of the mixed wake model predictions and observed concentrations are shown in Figure 2.20. The results are similar to those of the source shift model.

Figure 2.21 shows a comparison of the mixed wake model predictions with the wind tunnel concentrations. The comparisons for the smooth and rough wind tunnel cases are

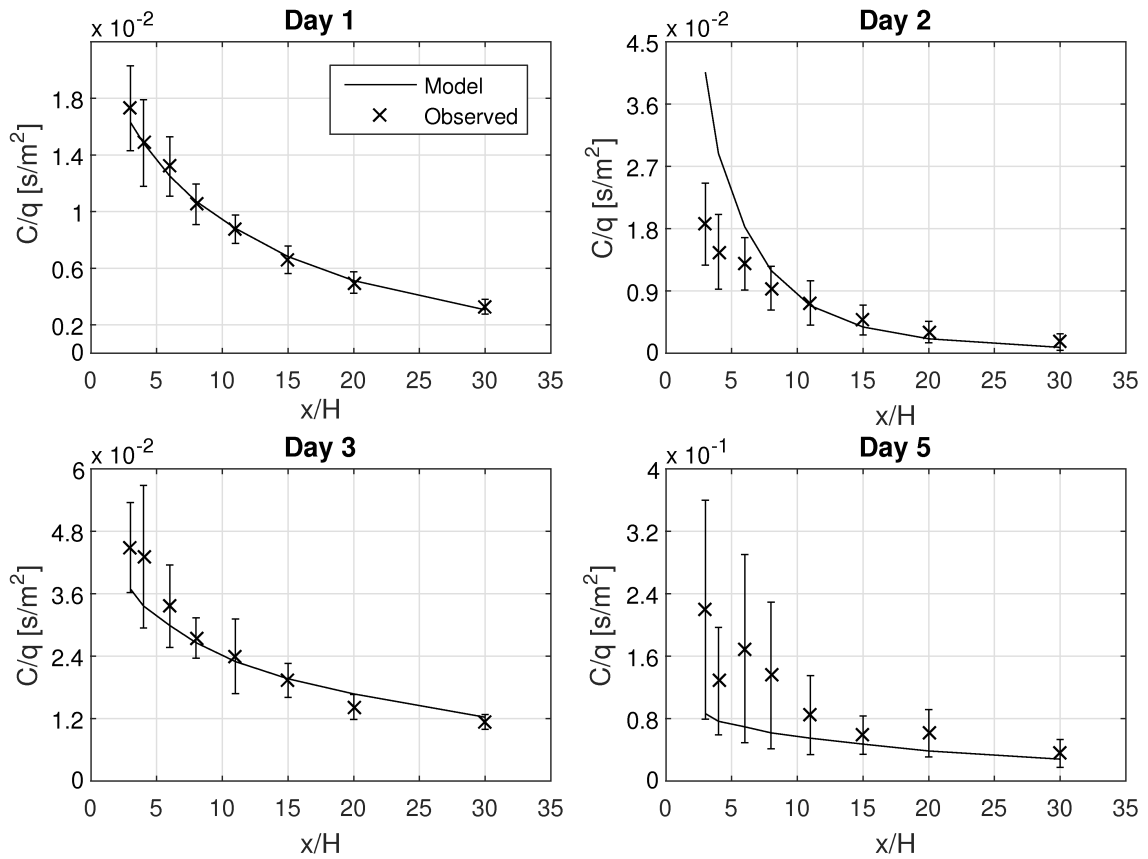


Figure 2.20: Downwind variation of mixed wake model and crosswind maximum concentration of Idaho Falls observations. Error bars show standard deviation of observations. The 4 days of the Idaho Falls study represent measurements during atmospheric stability conditions that are: neutral - day 1, unstable - day 2, stable - day 3, and very stable - day 5.

on the left and right, respectively. The model tends to underestimate concentrations near the barrier in the smooth boundary layer case. The correlation with the rough wind tunnel data is very good, but the model overestimates by about 50% far from the barrier.

Both the source shift and mixed wake models predict larger concentrations in the rough approach flow case than in the smooth case because the modeled wind speed is smaller in the rough case. However, the observations tend to be slightly larger in the smooth case. The models are more sensitive to changes in surface roughness length than the observations suggest. The large roughness elements of the rough case create an urban

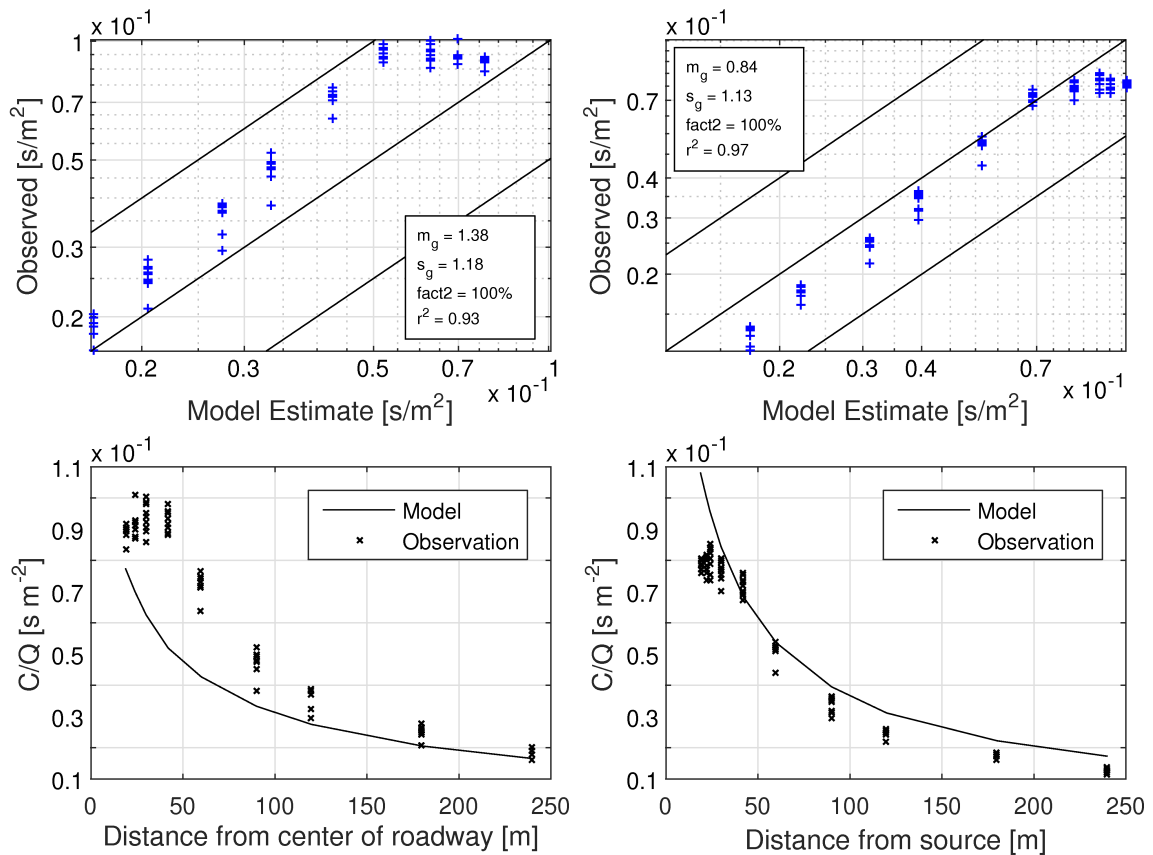


Figure 2.21: Comparison of mixed wake model with wind tunnel infinite source concentration for receptors below a height of  $1H$ . Center black lines correspond to 1 to 1 lines and observations within outer two lines are within a factor of two of model estimates. The smooth approach flow wind tunnel case ( $z_0 = 0.27 \text{ m}$ ,  $u_* = 0.25 \text{ m/s}$ ) is on the left and the rough approach flow wind tunnel case ( $z_0 = 0.78 \text{ m}$ ,  $u_* = 0.3 \text{ m/s}$ , displacement height =  $8.1 \text{ m}$ ) is on the right.

canopy, resulting in significant uncertainty in how to specify the wind profile. It is unclear how the barrier alters the wind profile within the urban canopy. This highlights the need to better understand the wind speed downwind of the barrier and the effect of surface roughness on the wind speed to more accurately model the concentration.

### 2.3.3 Puttock-Hunt Model

Puttock & Hunt (1979) developed a model that describes diffusion near objects with separated wakes. The model is based on the two-dimensional advection diffusion equation

using the eddy diffusivity model along with the following assumptions: 1) the concentration within the separated wake is constant, 2) the net concentration flux across the separation streamline is zero, 3) the mean flow outside the separated wake is potential flow, and 4) the eddy diffusivity is constant. They develop an analytical expression for the concentration and state that the solution is still a good approximation even if assumptions 3 and 4 are not satisfied. We solve the governing equation numerically and specify a form of the eddy diffusivity specific to flow over a sound wall instead of the constant eddy diffusivity specified by assumption 4.

Assumption 3 deserves some more explanation. Potential flow is by definition incompressible and irrotational. This type of flow can be expressed in terms of the scalar velocity potential,  $\phi$ , and stream function,  $\psi$ , which satisfy  $\nabla^2\phi = 0$  and  $\nabla^2\psi = 0$  and which are related to the velocity as follows:

$$(U, V) = \left( \frac{\partial\phi}{\partial x}, \frac{\partial\phi}{\partial z} \right) = \left( -\frac{\partial\psi}{\partial z}, \frac{\partial\psi}{\partial x} \right) \quad (2.18)$$

where  $U$  and  $V$  are the horizontal and vertical components of the wind speed. For two-dimensional flow, the potential and stream function are scalar fields. In the Puttock-Hunt model the velocity potential and stream function are model parameters that are specified to match the flow over a sound wall. We describe how these parameters are specified below.

The governing equation, modified for non-constant wind speed and eddy diffusivity, is:

$$\frac{\partial C}{\partial\phi} = \frac{\partial}{\partial\psi} \left( K_z(\phi, \psi) \frac{\partial C}{\partial\psi} \right) \quad (2.19)$$

where  $C$  is the concentration, and  $K_z(\psi)$  is the vertical eddy diffusivity. Equation 2.19 is derived by writing the turbulent advection diffusion equation, where the turbulent fluxes are given by the eddy diffusivity hypothesis, in terms of the velocity potential and stream function, assuming that the horizontal and vertical diffusivities are equal, and then neglecting the downwind diffusion term.

The boundary condition on the ground is the zero flux condition. In terms of the velocity potential and stream function:

$$\left. \frac{\partial C}{\partial \psi} \right|_{\psi=\psi_0} = 0, \phi < \phi_1, \phi > \phi_2 \quad (2.20)$$

where  $\psi_0$  is the value of the stream function at the ground, and  $\phi_1$  and  $\phi_2$  are the upwind and downwind limits of the separated wake.

On the surface of the separated wake the concentration is equal to the constant wake concentration (by assumption 1):

$$C(\phi_1 < \phi < \phi_2, \psi = 0) = C_w \quad (2.21)$$

where  $C_w$  is the concentration within the wake. In addition to the condition of (2.21), the net flux through the separation streamline is zero (assumption 2):

$$\int_{\phi_1}^{\phi_2} \left. \frac{\partial C}{\partial \psi} \right|_{\psi=\psi_0} d\phi = 0 \quad (2.22)$$

This provides the condition to determine the wake concentration,  $C_w$ .

Far from the source the concentration goes to zero:

$$C \rightarrow 0 \text{ as } |\phi| \rightarrow \text{inf} \quad C \rightarrow 0 \text{ as } |\psi| \rightarrow \text{inf} \quad (2.23)$$

Equation (2.19) is solved using a finite difference method and then the resulting concentrations are transformed to the physical ( $x$ - $z$ ) domain using the specified stream function and velocity potential. If the approach flow velocity profile is a constant independent of height from the ground, a solution for the potential in the upper half plane (bounded by the  $x$ -axis and extending to infinity) is  $\phi = U_0x$  and the stream function is  $\psi = -U_0z$  where  $U_0$  is the approach flow velocity. The potential and stream function satisfy the Laplace equation, which is invariant under a conformal transformation, and (2.18) so we can determine the potential and stream function in the physical domain using a conformal transformation from the upper half plane to the physical domain. The conformal transformation is defined by the shape of the boundary in the physical domain. With this in mind, it is convenient to define the boundary of the sound wall recirculation zone by a polygon because any polygon can be mapped conformally to the upper half plane using the Schwarz-Christoffel transformation (Walker, 1964). We define the approach flow velocity,  $U_0$ , as the velocity predicted by Monin-Obukhov similarity theory at the sound wall height.

The specific transformation we use is defined by Figure 2.22. The potential flow region extends to infinity in the  $z$ -direction and is bounded by the ground at  $z=0$  and by the hypotenuse of two triangles which define the separated wake downwind of the wall and an upwind displacement zone where the flow is also separated. The barrier height is  $H$ , the downwind separation streamline touches the ground at  $x = w_d$ , and the displacement zone begins at  $x = -w_u$ . With these parameters specified the velocity potential and stream function are fully defined. The shape of the separated wake is somewhat arbitrary - we chose the simplest shape possible - but it turns out that the predicted concentrations

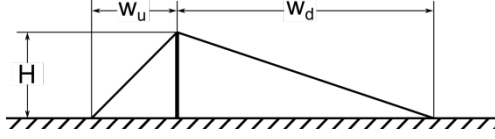


Figure 2.22: Schematic defining the boundary of the potential flow region. The variables are:  $H$ , the barrier height,  $w_d$ , the distance from the wall where the separation streamline touches the ground, and  $w_u$ , the upwind distance where the displacement zone begins.

are not very sensitive to the shape of the separation streamline, and are effected much more by the wall height and downwind extent of the wake.

The eddy diffusivity is calculated using an empirically determined expression for the standard deviation of vertical velocity fluctuations developed by Weil (1996). This formulation is the same as that used in the PRIME model (Schulman et al., 2000). We assume that the vertical eddy diffusivity can be related with the standard deviation of vertical velocity fluctuations by:

$$K_z = \frac{\sigma_w^2 l}{U} \quad (2.24)$$

where  $l$  is the turbulence length scale. The standard deviation of vertical velocity fluctuations is calculated using the following equation developed by Weil (1996):

$$\sigma_w = \sigma_{w0} + (1.7\sigma_{wN} - \sigma_{w0}) \left( \frac{x + R}{R} \right)^{-2/3} \quad (2.25)$$

where  $x$  is downwind distance from the barrier, the subscript  $N$  refers to a value typical of neutrally stable atmospheric conditions, and the subscript  $0$  refers to the ambient value. The diffusion length scale  $R$  is equal to  $2H$  for a long wall. Solving (2.24) for  $\sigma_w$ , plugging this into (2.25), and assuming the velocities and turbulence length scales are equal for the ambient, typical neutral, and behind-wall turbulence, results in the following expression for the eddy diffusivity downwind of the wall:

$$K_z^{0.5} = K_{z0}^{0.5} + (1.7K_{zN}^{0.5} - K_{z0}^{0.5}) \left( \frac{x+R}{R} \right)^{-2/3} \quad (2.26)$$

We substitute the similarity profile of eddy diffusivity for the ambient and neutral diffusivities:

$$K_z(z) = \frac{\kappa u_* z}{\phi_H(z/L)} \quad (2.27)$$

where  $\phi_H$  is the non-dimensional temperature gradient, given by (Businger et al., 1971):

$$\phi_H(y) = \begin{cases} ((1/0.74)^2 - 16y)^{-1/2} & y < 0 \\ 0.74 + 4.7y & y > 0 \end{cases} \quad (2.28)$$

The Puttock-Hunt model as described above assumes that the source and sound wall are infinitely long and that the wind direction is perpendicular to the roadway, but the model can be extended to account for finite sources and small angles between the wind direction and the normal to the roadway. The idea behind the extension of the model is to multiply the concentrations by a Gaussian horizontal distribution function:

$$C(x, y, z) = C_{PH}(x, z) \frac{1}{\sqrt{2\pi}\sigma_y(x)} \exp\left(-\frac{y^2}{2\sigma_y(x)}\right) \quad (2.29)$$

where  $C_{PH}$  is the Puttock-Hunt model solution. By integrating (2.29) along the line source using the method of (Venkatram & Horst, 2006) to evaluate the integral we obtain:

$$C(x, z) = \frac{C_{PH}(x^{eff}, z)}{\cos(\theta)} 0.5[erf(t_1) - erf(t_2)] \quad (2.30)$$

where  $t_i$  and  $x^{eff}$  are described in the discussion of (2.5). Using (2.30) we can determine the effect of wind direction and finite length source on the concentration.

Figure 2.23 shows scatter plots comparing the Puttock Hunt model with crosswind maximum concentrations measured at Idaho Falls. The model performance is quite similar to those of the source shift and mixed wake models. The model overestimates concentrations near the barrier during unstable conditions by more than a factor of two. This overestimation is also present in the source shift and mixed wake models. It is likely due to improper specification of the wind speed downwind of the barrier.

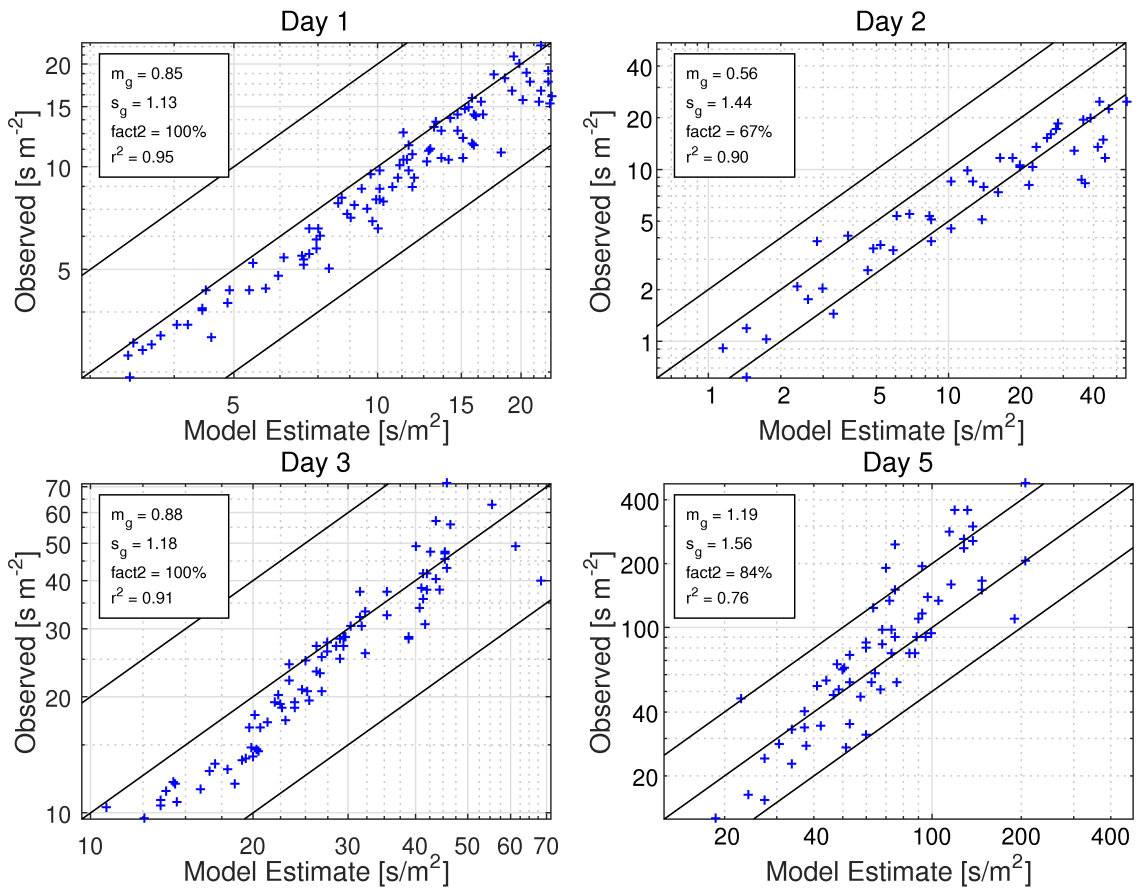


Figure 2.23: Comparison of the Puttock Hunt model with crosswind maximum concentrations observed during Idaho Falls. Center black lines correspond to 1 to 1 lines and observations within outer two lines are within a factor of two of model estimates. The 4 days of the Idaho Falls study represent measurements during atmospheric stability conditions that are: neutral - day 1, unstable - day 2, stable - day 3, and very stable - day 5.

The downwind variations of the Puttock Hunt model predictions and observed concentrations are shown in Figure 2.24. The results are similar to those of the mixed wake model.

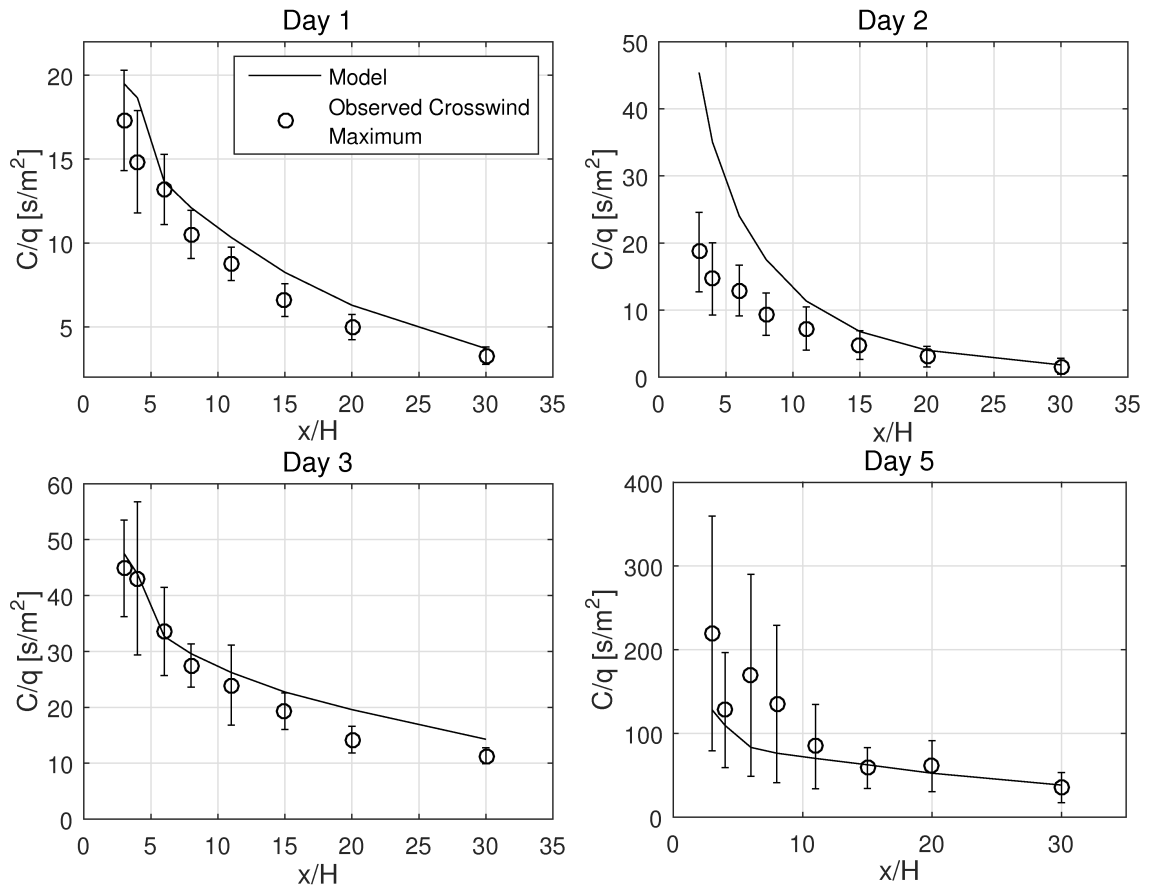


Figure 2.24: Downwind variation of Puttock Hunt model and crosswind maximum concentration of Idaho Falls observations. Error bars show standard deviation of observations. The 4 days of the Idaho Falls study represent measurements during atmospheric stability conditions that are: neutral - day 1, unstable - day 2, stable - day 3, and very stable - day 5.

Figure 2.25 shows a comparison of the Puttock Hunt model predictions with the wind tunnel concentrations. The model tends to underestimate concentrations near the barrier in the rough boundary layer case. The correlation with both the smooth and rough wind tunnel data is very good and most of the data is within a factor of two of model estimates.

The Puttock Hunt model captures a significant feature of the concentration: the concentration is nearly constant with downwind distance within a distance of about 50 m from the source. This constant concentration occurs due to the rapid mixing within the barrier's near wake. The Puttock Hunt model explicitly accounts for this effect using the boundary condition of equation (2.21). This comparison supports the assumption that the concentration within the wake is constant due to rapid mixing.

The model underestimates concentrations for the rough case. However, the model shows the correct trend of smaller concentrations in the rough case than the smooth case, while the source shift and mixed wake models predict larger concentrations in the rough case. This could be because the Puttock Hunt model attempts to capture the characteristics of the mean flow over the barrier, resulting in more accurate estimates of the wind speed downwind of the barrier and the concentration there than the other two models.

Based on the evaluation of the three dispersion models we can draw some conclusions about the effect of roadside barriers on near road concentrations of vehicle emissions. The good performance of the mixed wake model during neutral stability conditions indicates that the primary effect of the barrier is to increase the vertical mixing by an amount proportional to the barrier height. The source shift model also compares well with the neutral data. The good performance of the source shift described by (2.13) is consistent with the conclusion that the primary effect of the barrier is to increase the vertical mixing by an amount proportional to the barrier height.

Poor performance of the models during unstable conditions is likely due to overestimation of the wind speed downwind of the barrier. We have not accounted for the reduction in wind speed in the mixed wake and source shift models. In the Puttock-Hunt model

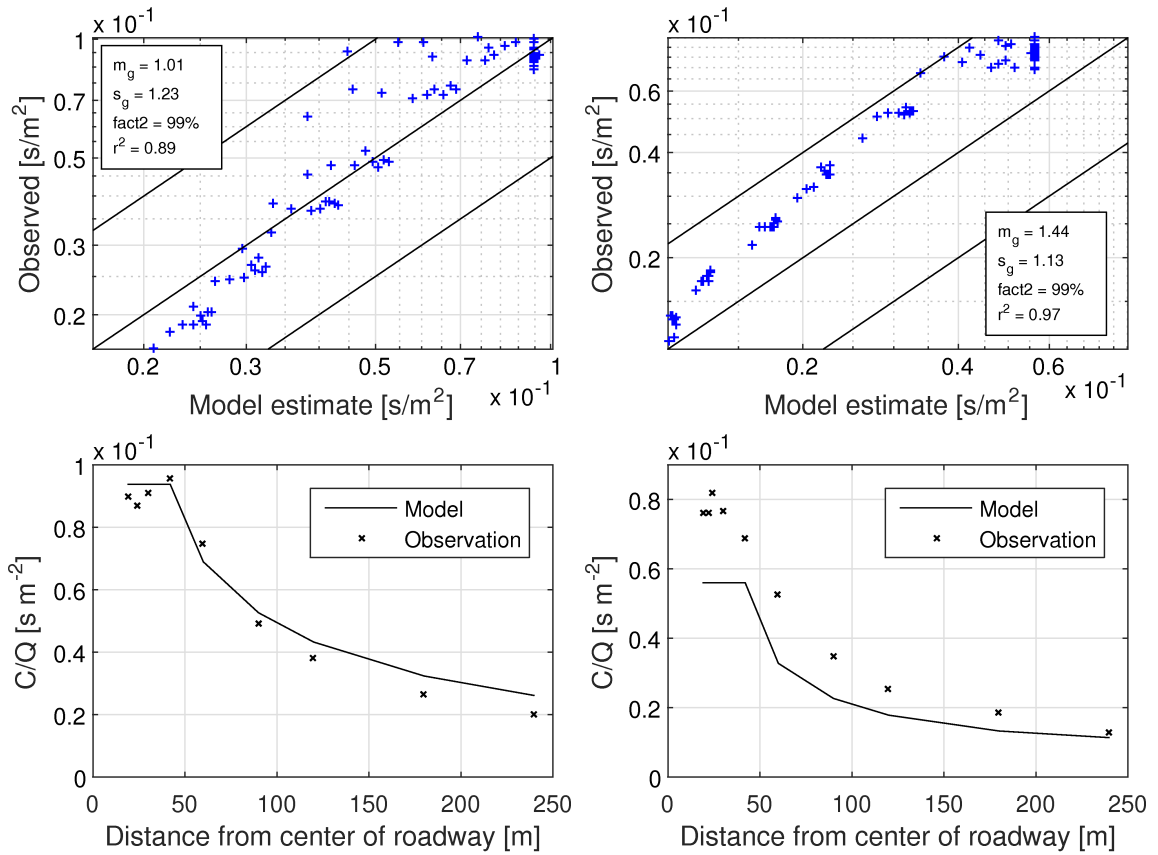


Figure 2.25: Comparison of Puttock Hunt model with wind tunnel infinite source concentration for receptors below a height of  $1H$ . Center black lines correspond to 1 to 1 lines and observations within outer two lines are within a factor of two of model estimates. The smooth approach flow wind tunnel case ( $z_0 = 0.27m$ ,  $u_* = 0.25m/s$ ) is on the left and the rough approach flow wind tunnel case ( $z_0 = 0.78m$ ,  $u_* = 0.3m/s$ , displacement height =  $8.1m$ ) is on the right.

the wind speed is determined from the potential flow model, which may overestimate the wind speed in the barrier wake.

All of the models tend to be too sensitive to changes in surface roughness. We suspect that this is due to under or over estimation of the wind speed during the large roughness case of the wind tunnel study. The rough case simulates an urban canopy. There is some uncertainty about how the wind profile should be specified for an urban canopy, and it is not clear how the barrier alters the wind flow in the canopy.

### 2.3.4 Modification of Mean Wind Profile Downwind of the Barrier

We speculated that the model overestimation during unstable conditions is due to an improper specification of the wind speed and turbulence downwind of the barrier. We tested this idea by developing a modified form of the mixed wake model that accounts for reduced wind speed in the wake of the barrier. In the modified model, the wind speed at half the barrier height in (2.17) is given by the similarity profile of (2.9) multiplied by an empirical function given by:

$$f = 1 + \frac{f_{max} - 1}{1 + (x/L_w)^{1/2}} \quad (2.31)$$

where  $f_{max}$  is an empirical constant that gives the maximum wind speed reduction. The factor of  $x^{-1/2}$  used in (2.31) was chosen to be consistent with the observed variation of the wind speed in the wake of two dimensional obstacles (Tennekes & Lumley, 1972). We settled on a value of  $f_{max} = 0.3$  by comparing the model with observations. The constant  $\alpha$  in (2.14) was also set equal to 0.02, effectively increasing the turbulence and vertical plume spread behind the barrier relative to the unmodified model.

Figure 2.26 shows the comparison of the modified form of the mixed wake model with observations in Idaho Falls. The model predictions are much closer to observations under unstable conditions for the receptors close to the barrier. For neutral and stable conditions the model performance is similar to that of the unmodified model. This supports the idea that the wind speed reduction in the barrier's wake should be taken into account in the dispersion model to accurately predict concentrations within the near wake. The modified form of the mixed wake model tends to underestimate concentrations at large distances from the barrier for the neutral conditions of day 1 and the unstable conditions of day

2. However, the overall performance of the model is much better, especially at short distances from the barrier.

In the next section, we use the dispersion models developed here to investigate the effectiveness of roadside barriers for the purpose of reducing near road concentrations of vehicle emissions.

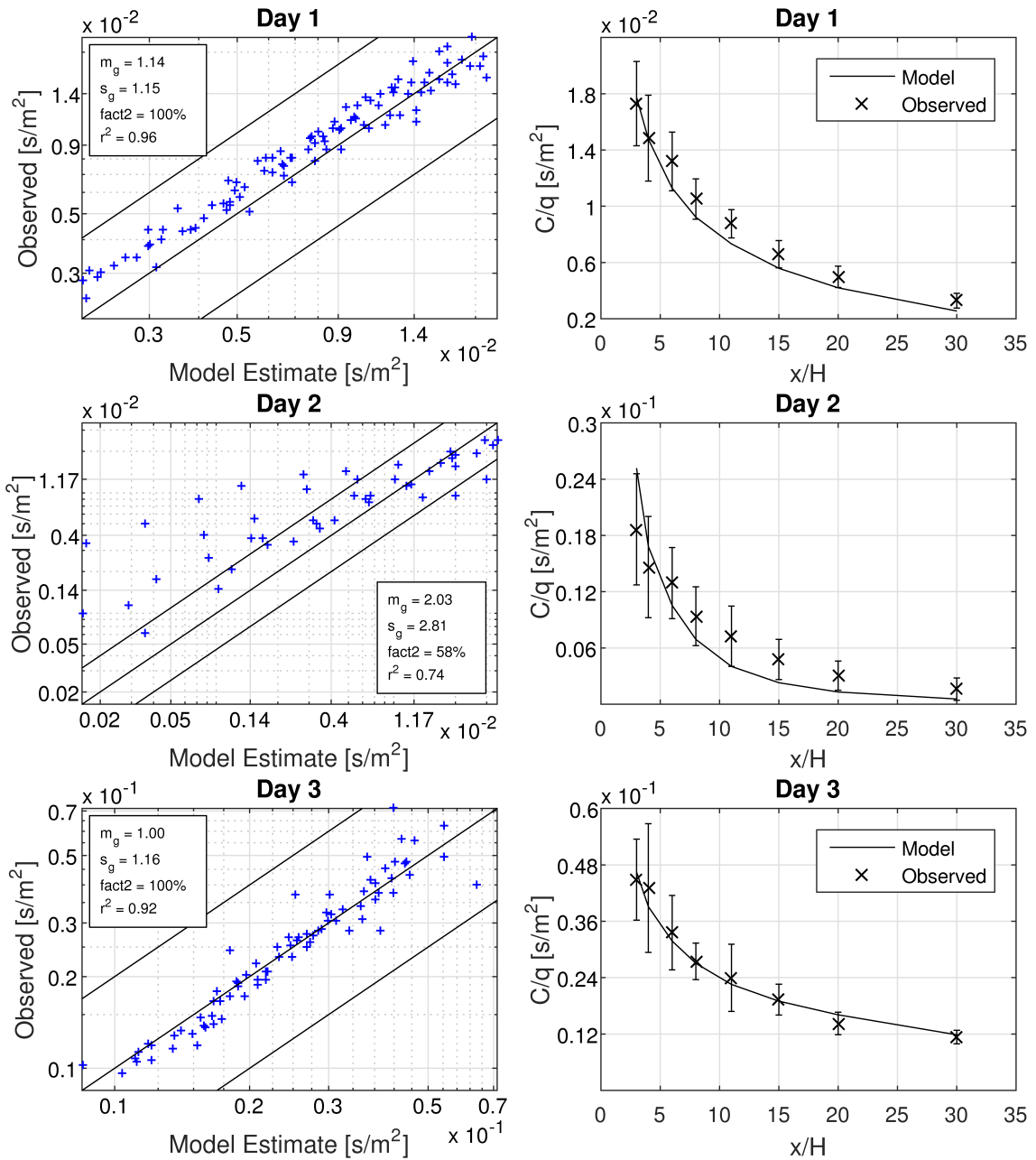


Figure 2.26: Comparison of the modified mixed wake model with crosswind maximum concentrations observed during Idaho Falls. Center black lines correspond to 1 to 1 lines and observations within outer two lines are within a factor of two of model estimates. Error bars on downwind variation figures show standard deviation of observations. The 3 days of the Idaho Falls study included in the figure represent measurements during atmospheric stability conditions that are: neutral - day 1, unstable - day 2, stable - day 3.

## 2.4 Effectiveness of Roadside Barriers to Reduce Near-Road Concentrations of Vehicle Emissions

Previous sections have shown that solid roadside barriers enhance dispersion, thereby reducing near-road concentrations of vehicle emissions. This section uses the dispersion models developed for roadside barriers to evaluate the effect of several important variables on the concentration reduction. The effect of barrier height, meteorological conditions, surface roughness, and road width on the near road concentration reduction and the downwind extent of the concentration reduction are studied. This study is important because it allows us to make conclusions about how varying road configurations and meteorological conditions impact the roadside barrier effectiveness.

It is anticipated that the barrier's effectiveness under stable conditions characteristic of early morning rush hours and under unstable conditions characteristic of afternoon rush hours can be very different. Since roadway emission rates are high during these times of the day, it is important to characterise the concentration reduction obtained under both conditions. The mixed wake model using the modified form of the wind speed profile in (2.31) is used to perform the sensitivity study since this model has the least bias for all meteorological conditions. The source shift produces similar results to the mixed wake model so the results of the sensitivity study are not included. The Puttock-Hunt model was also not used because the model is biased under unstable conditions.

Two types of simulations were performed. First, a barrier was located 10 m downwind of a simulated roadway consisting of one line source. The concentration at a ground level receptor located 10 m downwind of the barrier was compared with the simulated concentration with no barrier present. The concentration ratio, the ratio of concentration with a barrier present to that with no barrier present, was evaluated to determine the

barrier's effectiveness. Next, the concentration ratio at varying distances from the road was determined from a similar simulation. Finally, to study the effect of road width, a five lane highway was simulated by placing emission sources at 2 m intervals between 2 m to 10 m upwind of the barrier. The concentration ratio at the ground level receptor 10 m downwind of the barrier was calculated and compared with the concentration ratio for the simulation of a single lane 10 m upwind of the barrier.

Figure 2.27 shows the concentration ratio at the receptor 10 m downwind of the barrier as a function of barrier height and for different surface roughness lengths and atmospheric stabilities. In the simulation, one line source was placed 10 m upwind of the barrier. The model was run with a fixed surface friction velocity of 0.3 m/s while the Monin-Obukhov length and surface roughness length took values of  $\infty$ , -20 m, 20 m, and 0.05 m, 0.2 m, and 0.5 m, respectively.

The concentration ratio decreases with increasing barrier height as expected. Decreasing the surface roughness length causes the concentration ratio for a given barrier height to decrease. This occurs because the wind speed at half the barrier height is increased when the surface roughness length is decreased, resulting in smaller concentration predictions near the barrier. The non-barrier concentration on the other hand does not depend on the surface roughness length because the wind speed factor cancels out with the vertical plume spread. The concentration ratio is significantly affected by atmospheric stability, with the smallest ratios occurring during stable conditions,  $L = 20m$ , and the largest during unstable conditions,  $L = -20m$ . Stable conditions occurring during early morning rush hour traffic or nighttime are usually associated with the largest near road concentrations. It is therefore beneficial for the barrier effect to be large during stable conditions.

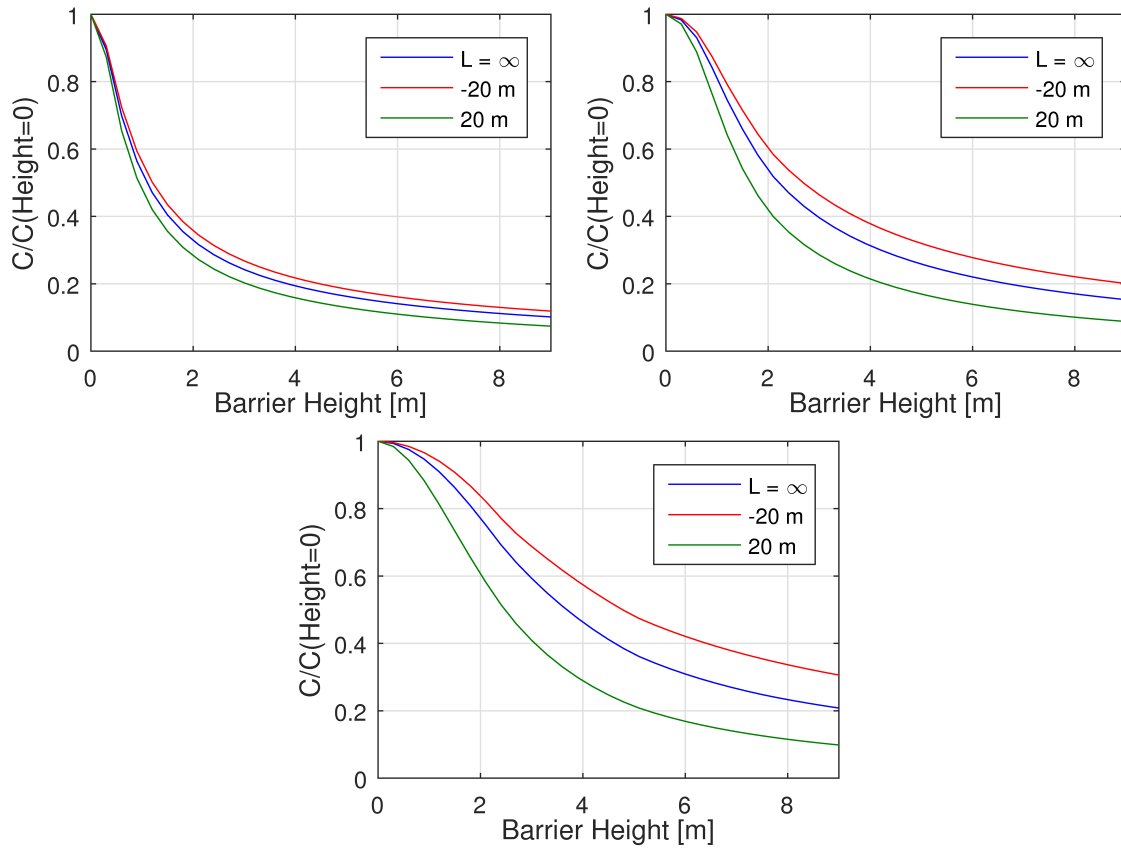


Figure 2.27: Sensitivity of concentration at a receptor 10 m from the barrier to barrier height and meteorological conditions for  $z_0$  of (top left) 0.005 m, (top right) 0.02 m, (bottom) 0.05 m.

Figure 2.28 shows the effect of changing the road width on the concentration ratio. In this case, a simulation was performed for a 5 lane highway and the ratio of the concentration ratio to the concentration ratio of the previous 1 lane highway simulation was plotted. We see that the concentration ratio of the 5 lane highway is smaller than that of the single lane road. This is because the 5 lane highway has more of the source located near the barrier than the single lane road. The barrier induced plume spread has a relatively larger effect on the concentration in this case because the atmospheric turbulence generated plume spread is smaller.

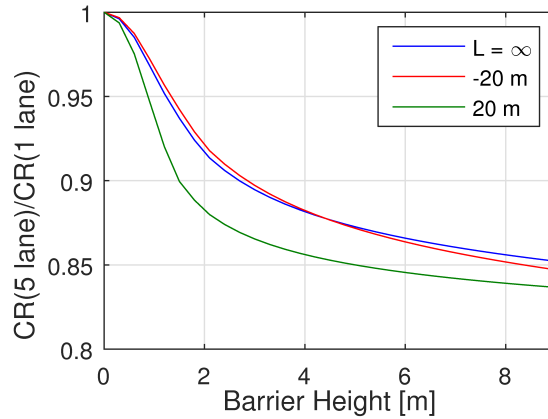


Figure 2.28: Sensitivity of concentration at a receptor 10 m from the barrier to road width. The surface roughness length is 0.2 m.

The variation of the concentration ratio with distance from the barrier and for different atmospheric stabilities is shown in Figure 2.29. The model was run with a fixed surface friction velocity of 0.3 m/s while the Monin-Obukhov length took values of  $\infty$ , -20 m, and 20 m. The surface roughness length was 0.02 m. The smallest concentration ratios occur during stable atmospheric conditions ( $L = 20 \text{ m}$ ), while the largest occur during unstable conditions ( $L = -20 \text{ m}$ ). During stable conditions the concentration reduction persists to larger distances from the barrier than during neutral and unstable conditions. Thus, the barrier is most effective at reducing concentrations during early morning and nighttime stable periods, when concentrations tend to be largest.

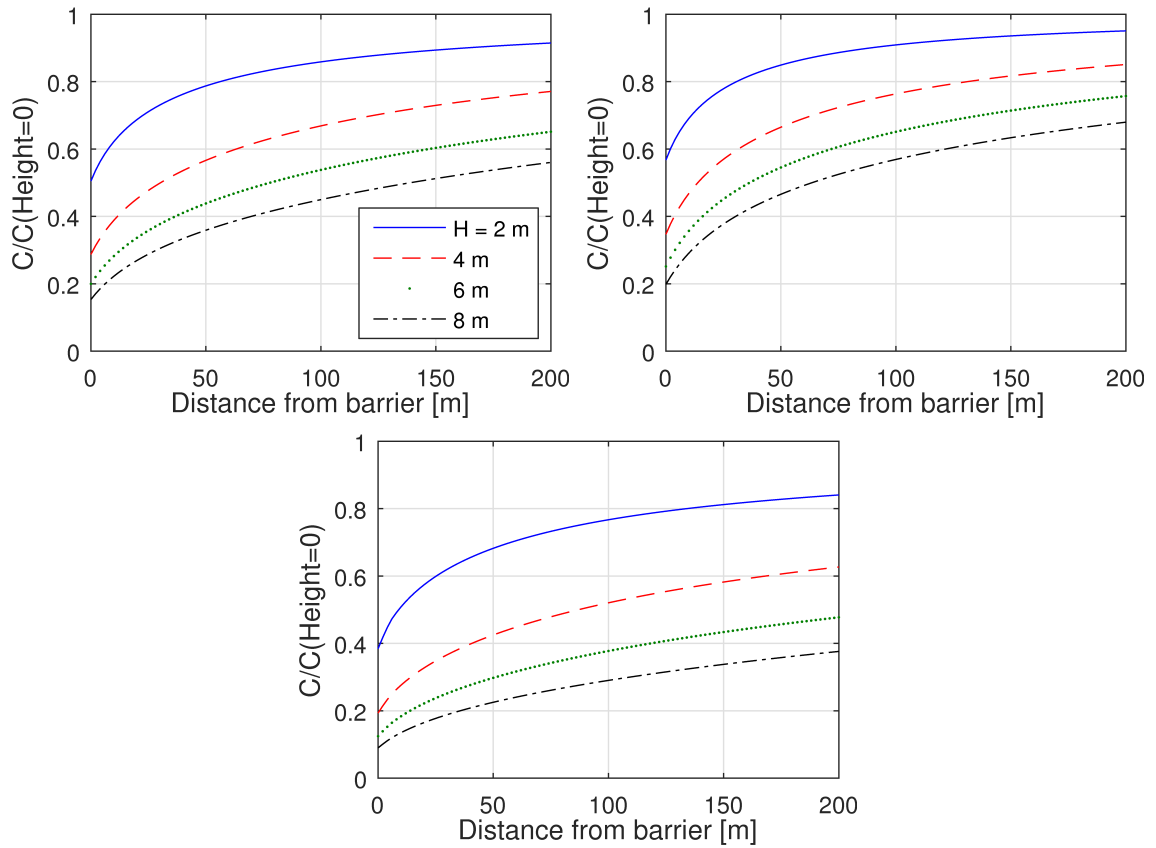


Figure 2.29: Concentration ratio at various distances from the barrier for different barrier heights and Monin-Obukhov lengths. Monin-Obukhov length has values of (top left)  $\infty$ , (top right) -20 m, (bottom) 20 m.

## 2.5 Conclusions

Three models of the effect of roadside barriers on dispersion of roadway emissions were developed and evaluated with data collected in a field study and a wind tunnel study. The field study specifically focused on examining the barrier effect under different atmospheric stabilities. The evaluation of the models shows that they account for the primary effects of barriers on dispersion. These effects are: 1) Pollutants are lofted over the top of the barrier, 2) The pollutants are well-mixed over the height of the barrier within the recirculating vortex, 3) The rate of plume spread downwind of the barrier is increased.

The source shift model accounts for the increased vertical plume spread by shifting the emission source upwind by some amount that depends on the barrier height and meteorology. The increased rate of plume spread is accounted for by increasing the surface friction velocity by an amount determined through an empirical function of the barrier height. The mixed wake model accounts for the barrier effects through a modified form of the vertical concentration distribution. The empirical modification of the behind-barrier surface friction velocity is also used. The Puttock-Hunt model assumes potential flow and uses a numerical solution of the advection diffusion equation with the eddy diffusivity model. Special boundary conditions for the recirculating cavity are used to account for the rapid mixing within the cavity. The eddy diffusivity is enhanced within the barrier wake to simulate the increased plume spread.

All three models adequately describe the effect of roadside barriers on the near road concentration during neutral and slightly stable atmospheric conditions. The geometric standard deviation of the residual of the log transformed concentrations is usually less than 1.5 in all but the very stable conditions of the field study. The data is nearly always within a factor of two of model estimates. The bias in the models as measured by the geometric mean of the residuals is less than about 15%. The comparison of models with data from the wind tunnel study and for unstable cases of the field study shows larger model bias and larger scatter in the data.

Some of the discrepancy between model and observations for the wind tunnel and unstable field study data is explained by the inadequate parameterization of the wind speed in the barrier's wake. This can be seen for the comparison of model estimates with the data from the smooth and rough cases of the wind tunnel study. The models have a large sensitivity to the surface roughness length, while the observed concentrations are very similar for the two different surface roughnesses tested. In the models, the wind

speed downwind of the barrier is determined using the Monin-Obukhov similarity profile, where the upwind meteorology is used as inputs, while the true wind speed downwind of a barrier is likely reduced due to sheltering. Using a more realistic estimate of the wind speed will likely reduce model bias for the wind tunnel study.

The comparison of models with data from the unstable cases of the field study shows that the models significantly overestimate concentrations in the near wake of the barrier. This is related to the specification of the wind speed profile downwind of the barrier. A modified form of the mixed wake model that uses an empirical function to reduce the wind speed in the barrier wake relative to that predicted by the Monin-Obukhov similarity profile has less bias in estimating concentrations during unstable conditions. This modified model also has good performance during neutral and stable conditions. This shows that the wind speed reduction in the barrier wake significantly alters the dispersion of vehicle emissions and that this effect should be included in the dispersion models.

After evaluating the three dispersion models, the mixed wake model, including the modified form of the behind-barrier wind speed, was used to evaluate the effectiveness of roadside barriers at reducing near road concentrations of vehicle emissions. This was done by simulating the concentration next to a roadway in several different configurations. The barrier height, road width, meteorological conditions, and surface roughness length were varied and the concentration ratio, the ratio of concentration with barrier to that without a barrier, was evaluated to determine the barrier's effectiveness. The sensitivity study shows that barriers are most effective during stable atmospheric conditions. The concentration ratio under stable conditions was smaller than that under neutral and unstable conditions, and also remained smaller for the largest distance from the barrier. Thus roadside barriers are most effective, during early morning rush hours and nighttime, when concentrations are usually largest. Concentration ratios were found to decrease as surface roughness

length decreased. Thus roadside barriers are more effective in rural areas than in urban areas characterized by large surface roughness length.

## **Chapter 3**

# **Assessment of the variables governing dispersion of traffic emissions in transit oriented developments with nonuniform building height**

### **3.1 Introduction**

Transit oriented developments (TODs) are built environments in which high density residential developments are located nearby public transportation and local businesses. TOD design helps improve environmental sustainability by reducing emissions associated with transportation, and promotes healthy activities such as walking and cycling (Boarnet & Crane, 2007). However, there is concern that the TOD residents living or working in close proximity to heavily trafficked urban streets may be exposed to elevated concentrations of vehicle emitted pollutants. The processes that dilute pollutants may be less effective in high density built environments, and thus it is important to consider the effect of increased population density and building density on human exposure to traffic emis-

sions in TODs. The primary goal of the research described in this chapter is to develop models that explain how the built environment affects exposure to traffic emissions. This is done by developing semi-empirical models that describe near-road pollutant concentrations and account for the essential built environment and meteorological variables that govern dispersion in cities. The models are designed to estimate near road concentrations of vehicle emissions in cities with significant building height variability. To achieve our goal we have conducted field measurements of concentrations and the variables that govern dispersion in several urban environments that have different building morphologies.

Section 3.2 gives an overview of our knowledge of dispersion in urban environments. Section 3.3 describes the analysis of near road concentration data collected at an urban site in Hannover, Germany using several semi-empirical dispersion models. The analysis provides insight on which meteorological variables primarily govern dispersion in an urban built environment. This gives motivation for our study of dispersion in environments with nonuniform building height and spatial inhomogeneity, and also motivates the need for the field measurements that we conducted. Section 3.4 describes the measurements of concentrations and variables governing dispersion within Los Angeles county, California, USA. Section 3.5 shows the evaluation of the dispersion models with data collected in the field measurements conducted in Los Angeles. Additional field measurements were conducted in Riverside county, California, USA. These measurements and the analysis of the resulting data is described in section 3.6. I give conclusions of this work in section 3.7. I also provide some guidance on the design of TODs to minimize exposure.

## 3.2 Background

The issue of whether the built environment increases near road concentrations of vehicle emissions, and if so to what degree, is very important, and has been addressed by many research studies over the past 40 years, including field, wind tunnel and water channel observations, and numerical simulation.

Much research has analyzed the “street canyon” (Figure 3.1) as a prototype of the urban built environment. The street canyon is a long street with uniform buildings on both sides, forming a canyon. When the above rooftop wind blows close to perpendicular to the canyon, one or multiple vortices form within the canyon. A single vortex results in the wind direction at street level pointing in the opposite direction of that at the rooftop, from the windward side to the leeward side. When the rooftop wind is at an angle, a helical vortex forms within the canyon.

The existence of a vortex within the street canyon depends on the aspect ratio, the ratio of building height to street width. When the aspect ratio is small, no consistent vortex forms within the canyon, and when the aspect ratio is large, multiple vortices may form. Oke (1988) groups the flow regime within building arrays into the following classes based on the canyon aspect ratio (Figure 3.2): isolated roughness flow – the wakes downwind of individual obstacles do not interfere with each other, wake interference flow – the wakes behind obstacles are the same size as the distance between obstacles and begin to interfere with each other, skimming flow – a stable circulation forms within the canyon and the bulk of the flow does not enter the canyon.

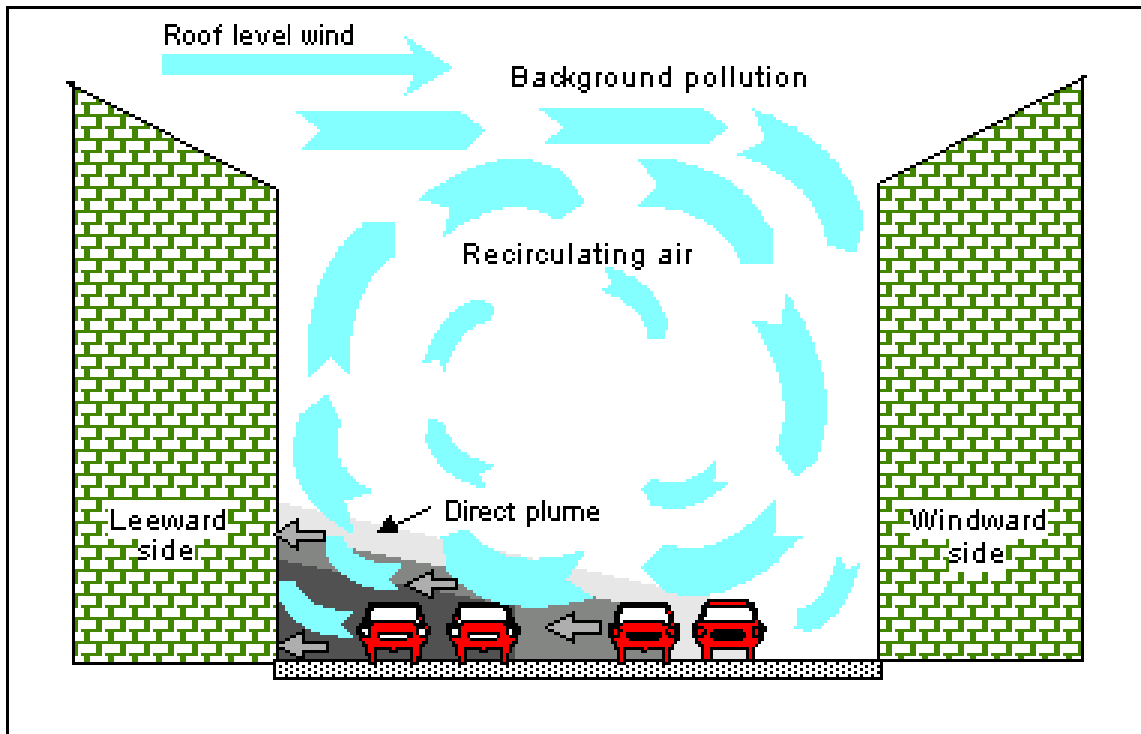


Figure 3.1: Street Canyon Schematic. From Berkowicz et al. (1997)

For a long street canyon, the change from isolated roughness to wake interference flow occurs around an aspect ratio of 0.3, and the change from wake interference to skimming flow occurs around an aspect ratio of 0.75.

The street canyon vortex may disappear under low ambient wind speeds. DePaul & Sheih (1986) verified the existence of a vortex flow using neutrally buoyant balloons as tracers. They found that the vortex disappears when the ambient wind speed is less than 1.5-2 m/s. However, Caton et al. (2003) state that this disappearance is not observed in numerical models or wind tunnels. DePaul & Sheih (1986) found the within-canyon velocity was about 0.6 of the rooftop velocity. Nakamura & Oke (1988) found that the wind speeds within and above a street canyon were linearly related, and the within-canyon velocity was 0.7 of that at the roof.

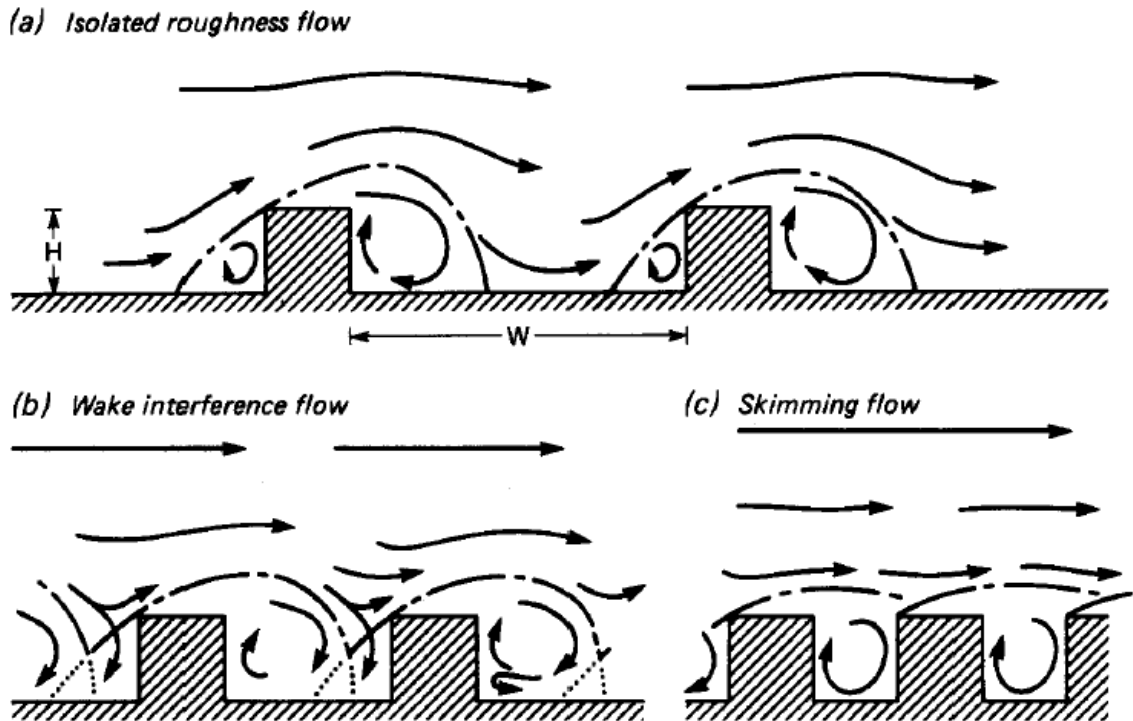


Figure 3.2: Building array flow regimes. (Oke, 1988)

One early field study was conducted in a street canyon in San Jose, CA in 1973 (Johnson et al., 1973). Carbon monoxide concentrations and wind speed were measured at several locations and at 5 different heights within the canyon. The researchers found that the concentrations at the leeward side of the canyon were 3 to 4 ppm (33% - 66%) larger than those at the windward side when the wind blows perpendicular to the canyon, while under parallel flow the concentrations are similar at both sides. The vertical concentration gradient is smaller at the windward side. The authors show that the ground level concentration at the leeward side is related to the rooftop wind speed, traffic count, and street geometry as follows:

$$C_L = C_b + \frac{0.07N}{(U + 0.5)(2 + x)} \quad (3.1)$$

where  $C_b$  is the background concentration,  $N$  is the traffic count,  $x$  is the distance from the traffic lane to the receptor, and  $U$  is the wind speed. A similar form holds for the windward side, with  $2 + x$  replaced by the street width. The factor of 0.5 in the denominator accounts for the effect of vehicle induced turbulence. This model indicates that changes in building height do not directly alter the concentration, and only the street width and rooftop wind speed determine the dispersion.

A useful method to characterize dispersion in street canyons is to measure the time that it takes for a local release of a puff of tracer gas to disperse and the concentration to approach background level. This method was used by DePaul & Sheih (1985), who released sulfur hexafluoride gas in a street canyon in Chicago with an aspect ratio (height/width) of 1.5. They measured the tracer gas concentration decay along with wind speed and turbulence data (DePaul & Sheih, 1986). The concentration decay is due to vertical transport of  $SF_6$  from the canyon by mean vertical velocities or turbulence; thus the decay time,  $\tau$ , can be related to the canyon height,  $H$ , and the vertical entrainment velocity, the rate at which clean air is mixed into the canyon and polluted air is mixed out,  $w_e$ , as  $\tau = H/w_e$ . It was found that the wind speed 3 m above the rooftop was strongly related to the vertical transport, as  $w_e = 0.16U(H + 3)$ . This again shows the importance of the rooftop wind speed in determining near road concentrations.

Nicholson (Nicholson, 1975) presented a model that accounts for both vertical transport and horizontal transport from the street canyon. By considering a box model of the canyon, where the concentration,  $C$ , is uniform within the canyon we obtain:

$$\frac{dC}{dt} = \frac{Q}{H} - \frac{\bar{U}C}{L} - \frac{\bar{w}C}{H} \quad (3.2)$$

where  $Q$  is the emission rate,  $\bar{U}$  is the height averaged horizontal velocity along the canyon axis,  $\bar{w}$  is an average vertical transport velocity, and  $L$  is the street length. Nicholson also gives models for  $\bar{U}$  and  $\bar{w}$  (Nicholson, 1975). The horizontal velocity is described by an exponential power law (MacDonald, 2000):

$$U(z) = U_H e^{(z-H)/l} \quad (3.3)$$

where  $U_H$  is the velocity at the building height and  $l$  is a length scale that determines how deep the rooftop wind penetrates into the urban canopy.

Wind tunnel models of street canyons have shown the same relationship between wind speed and pollutant dilution as was found in the previously mentioned field studies. Meroney et al. (1996) found that the concentration was inversely related to the approach wind speed, as in equation (3.1). Barlow & Belcher (2002) found that the entrainment velocity that mixes pollutants vertically is proportional to the wind speed above the canyon. They also found a dependence on flow regime, with the largest entrainment velocity occurring in the wake interference regime (see Figure 3.3).

Both studies tested the effect of increasing the surface roughness upstream of the canyon to simulate real urban conditions. Meroney et al. (1996) found that the presence of upstream buildings creates a displacement of the incoming velocity profile, which causes the formation of a shear layer at the top of the canyon and results in a permanent recirculating eddy within the canyon (with aspect ratio 1), while the small upstream roughness case shows an intermittent eddy for the same canyon. The presence of upstream buildings thus results in trapping of pollutants within the permanent recirculating eddy, resulting in larger concentrations. For smaller aspect ratios the presence of upstream buildings is less important (see Figure 12 and 14 in Meroney et al. (1996)). Barlow &

Belcher (2002) found that increasing the upstream surface roughness reduces the effect of changing the aspect ratio. They also found that the recirculation is strengthened when upstream roughness increases.

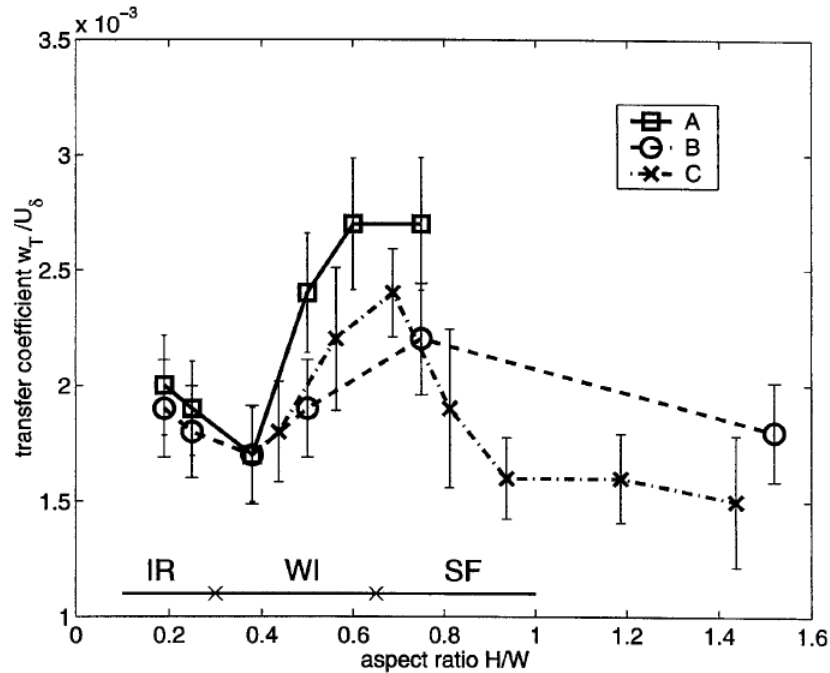


Figure 3.3: Transfer velocity normalized by approach wind speed as a function of canyon aspect ratio measured by Barlow & Belcher (2002). IR, WI, and SF represent the individual roughness, wake interference, and skimming flow regimes (Oke, 1988).

Street canyons can be “step-up” or “step-down” if the windward side buildings are taller or shorter than the leeward side, respectively. Hoydysh & Dabberdt (1988) conducted a wind tunnel study of winds and dispersion in asymmetric street canyons. They found concentrations lower by a factor of two in the step-up canyon compared with equal height or step-down canyons.

The previously mentioned studies show the importance of the rooftop wind speed in determining dispersion in street canyons. Other studies indicate that the vertical pollutant transport occurs due to an unstable shear layer that develops at the top of the canyon

(Louka et al., 2000). The unsteady fluctuations of the shear layer cause intermittent recirculation in the canyon, thus intermittently flushing pollutants out of the canyon. The street canyon studied by Louka et al. (2000) was mostly isolated, with only three buildings upwind of the canyon. The reason for the very intermittent vortex flow in this experiment may be similar to that for the Meroney et al. (1996) wind tunnel study, where the isolated street canyon had a more unsteady vortex than the canyon surrounded by urban roughness.

Nakamura & Oke (1988) measured temperatures within a 17 m tall street canyon. They found that the temperature difference between roof and canyon floor was usually less than  $0.5\text{ }^{\circ}\text{C}$ . During the day the floor was warmer than the roof and during the night the floor was cooler. The temperature differences are very small, a fact that is attributed to rapid mixing within the canyon. The air is unstable or near neutral within the canyon, even during the night. During the day the vertical canyon surfaces provide large surface area to absorb solar radiation. The building material stores heat, with the result that during the night the canyon can remain warm. In the context of an entire urban area this is known as the urban heat island. The implication for dispersion is that the turbulence is likely larger within the urban area during nighttime than outside the urban area, and thus dispersion is also likely larger in the urban area than in a rural area at night.

The existing work on modelling street canyons is summarized by Vardoulakis et al. (2003). Existing models can be classified as: empirical regression models, semi-empirical box models, semi-empirical Gaussian plume models, Lagrangian particle models, unsteady Gaussian puff models, and CFD models. We are most interested in the semi-empirical box and Gaussian plume models because they require only easily measured input variables and capture only the essential mechanisms of dispersion in cities. CFD models are capable

of simulating dispersion in cities but they do not provide clear insight into the important mechanisms and thus do not help us suggest TOD designs to minimize exposure.

We have already described some examples of the semi-empirical Gaussian and box models: the STREET model (Johnson et al., 1973), and the model of Nicholson (Nicholson, 1975). Additional models are the Canyon Plume Box Model (CPBM) (Yamartino & Wiegand, 1986), and the Operational Street Pollution Model (OSPM) (Berkowicz, 2000). OSPM is widely used, so we use it as a basis for our measurement design.

### 3.2.1 Operational Street Pollution Model (OSPM)

OSPM combines a street canyon box model with a model of the dispersion of the direct emissions from the road. The recirculating vortex flow advects emissions from the road toward the leeward side of the street. The emissions are then mixed vertically, and are trapped within the canyon by the vortex flow. To model these features of the dispersion, OSPM separates the concentration into two components: the recirculating component and the direct component (see Figure 3.1).

For the direct component, the vertical plume spread,  $\sigma_z$ , is given by  $\sigma_z = h_0 + \sigma_w x / U_s$ , where  $\sigma_w$  is the vertical turbulent velocity at the bottom of the canyon,  $U_s$  is the wind speed at the bottom of the canyon, and  $h_0$  is the initial vertical plume spread. By modeling the road as an area source, the concentration at a distance  $w$  from the edge of the road is given by:

$$C_{direct} = \sqrt{\frac{2}{\pi}} \frac{q}{W \sigma_w} \ln \left( 1 + \frac{\sigma_w W}{h_0 U_s + \sigma_w w} \right) \quad (3.4)$$

where  $q$  is the emission rate per unit length of road,  $\sigma_w$  and  $U_s$  are the vertical turbulent velocity and the wind speed at the bottom of the canyon, and  $W$  is the street width. The direct contribution used in OSPM is determined by setting  $w = 0$  (Berkowicz, 2000):

$$C_{direct} = \sqrt{\frac{2}{\pi}} \frac{q}{W\sigma_w} \ln \left( 1 + \frac{\sigma_w W}{h_0 U_s} \right) \quad (3.5)$$

The initial vertical spread,  $h_0$ , is due to the mixing produced by motion of the vehicles, and is of the order of the vehicle height.

The recirculating contribution is determined by considering the canyon as a box model. Emissions enter the box at the bottom and are transported out of the box at the top by the vertical turbulent velocity at the top of the box. For the case of  $H \geq W$ , the concentration in the box is:

$$C_{recirc} = \frac{q}{W\sigma_{wr}} \quad (3.6)$$

where  $\sigma_{wr}$  is the vertical turbulent velocity at the top of the canyon.

OSPM determines the wind speed at the bottom of the canyon from that at the rooftop by assuming a logarithmic velocity profile (equation (2.1)) within the canyon, with zero displacement height and a surface roughness length of 0.1 m. The vertical turbulent velocity is calculated as  $\sigma_w = 0.1U$ , where  $U$  is the wind speed at the surface or rooftop.

The relative magnitudes of the direct and recirculating components depend on the canyon aspect ratio. Table 3.1 summarizes the magnitudes of the recirculating and direct contributions of several wind tunnel studies of Kastner-Klein & Plate (1999), Meroney et al. (1996), and Hoydysh & Dabberdt (1988). These studies measured concentrations in street canyons with aspect ratio from about 1.2 to 0.125. The background concentration

Table 3.1: Comparison of direct and recirculating concentration measured in wind tunnel studies of street canyons.

Study	Aspect Ratio	Leeward	Windward	Direct/ Recirculating
(Hoydysh & Dabberdt, 1988) Figure 12	1.2	11400	5390	1.1
(Kastner-Klein & Plate, 1999) Figure 2	1	40-80	10	4-8
	1	126	41.8	2.0
	0.5	43.2	11.6	2.7
(Meroney et al., 1996) Figure 14	0.33	28.7	6.17	3.7
	0.25	25.4	3.43	6.4
	0.125	7.07	1.79	–

in these studies is small. The studies found that the recirculating contribution has the same order of magnitude as the direct contribution, with increasing recirculating contribution as the aspect ratio increases. The direct contribution is between 1.1 to 8 times the recirculating, depending on the aspect ratio.

So far I have focused on describing dispersion models used for urban environments. However, these models are linked with models of the relationship between near surface meteorology within the urban area and that at upwind rural locations or above the rooftop. Section 3.2.2 gives background information on the models used to relate meteorology within urban areas to that at upwind rural areas.

### 3.2.2 Urban Canopy Models

Figure 3.4 is a schematic of the various length scales and processes active in the urban boundary layer (UBL) (Fisher et al., 2006). As the air enters the urban area from the

upwind rural area, the increase in surface roughness causes the development of an internal boundary layer (IBL) (Garratt, 1990) where the wind speed adjusts to the new boundary condition. The IBL height grows with distance from the rural-urban boundary. The wind that has adjusted to the urban surface roughness conditions is the UBL. The UBL can be divided into regions based on height from the ground, where different physical processes dominate. The near-surface UBL flow is described by the roughness sublayer and the inertial sublayer, similar to the description of flow over a rural surface. The roughness sublayer is the region, up to a few building heights from the ground, where the dominant length scale is the building height, and the flow is dominated by the effects of the buildings. Above the roughness sublayer is the inertial sublayer, where the dominant length scale is the height from the ground, and Monin-Obukhov similarity theory can be considered valid.

Approximately below the building height is the urban canopy layer (UCL), where the flow is dominated by the effect of individual buildings. The UCL contains the vortices that characterize dispersion in street canyons. Dispersion models such as OSPM require the wind speed and turbulence near the bottom of the UCL as inputs to the dispersion equations, so it is important to understand how the wind speed near the urban surface is affected by the presence of the buildings.

There are several simplifying models that can be used to estimate near surface micrometeorology in urban areas. One approach to model the UCL is to treat the urban area in a manner similar to a forest canopy. The effect of the buildings is treated as a distributed drag force on the flow, and the models are design to estimate the spatially averaged wind profile rather than the wind around any one given building. The resulting model predicts an exponential variation of the wind speed with height (MacDonald, 2000). Urban canopy

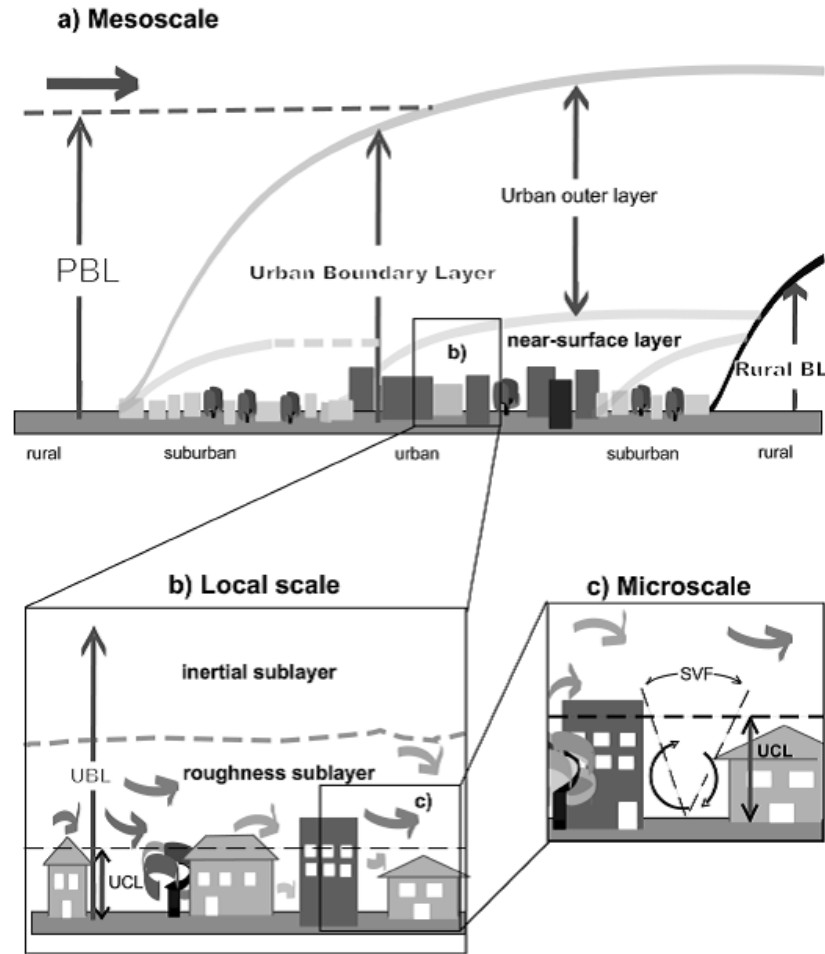


Figure 3.4: Schematic of an urban boundary layer. From Fisher et al. (2006)

wind models typically parameterize the average characteristics of the urban area in terms of the frontal area fraction,  $\lambda_f = A_f/A_d$ , and plan area fraction,  $\lambda_p = A_p/A_d$ , where, for regular obstacle arrays,  $A_f$  is the frontal area of one obstacle exposed to the wind,  $A_d$  is the area of the ground per obstacle, and  $A_p$  is the plan area of the obstacle viewed from above.

Another approach is to assume the velocity does not vary with height within the urban canopy. Bentham & Britter (2003) developed a model that relates a constant spatially

averaged canopy velocity,  $U_c$ , with the surface friction velocity of the inertial sublayer above the urban area,  $u_*$ , and the frontal area fraction:

$$\frac{U_c}{u_*} = \left( \frac{2}{\lambda_f} \right)^{1/2} \quad (3.7)$$

Another approach is to use simple empirical relationships between street and roof wind speed and turbulence. Several field experiments have provided data for this approach (Allwine et al., 2002; Arnold et al., 2004; Rotach et al., 2005; Hanna et al., 2007). Data on the change in wind speed and turbulence between rooftop and surface within urban environments is given in section 3.5.

For practical application of the urban dispersion models described in section 3.2, the rooftop wind speed, and sometimes the turbulence above the street canyon rooftop, must be known. Since micrometeorological measurements are not routinely made in urban areas, these variables must usually be estimated from measurements at an upwind rural location. Models to estimate rooftop wind speed in an urban area based on measurements at upwind rural locations have been developed (Belcher et al., 2003; Bentham & Britter, 2003; Coceal & Belcher, 2004). In these models, an internal boundary layer model is used to estimate the development of turbulence and wind speed in the inertial layer above the roughness sublayer as the air travels from the rural area to the urban area.

The internal boundary layer is defined by the reduction in wind speed that occurs due to increased surface roughness. The vertical extent where the velocity deficit is greater than some cutoff value is called the internal boundary layer. In order to develop models of the IBL, the growth rate of the height of the IBL is assumed to be proportional to the vertical turbulent velocity Garratt (1990):

$$\frac{dh}{dx} \sim \sigma_w/u(h) \sim u_*/u(h) \sim \kappa/\ln(h/z_0) \quad (3.8)$$

where  $h$  is the IBL height.

This equation is integrated from the rural to the urban area to obtain:

$$(h/z_{0u})(\ln(h/z_{0u}) - 1) + 1 = Ax/z_{0u} \quad (3.9)$$

where  $z_{0u}$  is the urban surface roughness length and  $A$  is an empirical constant of order 1.

Since the wind speed above the top of the IBL retains its upwind rural value, Equation (3.9) can be used to determine the change in the surface friction velocity in the urban area by equating the wind speed from the upwind rural profile and the urban profile at  $h$ :

$$u_{*r}\ln(h/z_{0r}) = u_{*u}\ln(h/z_{0u}) \quad (3.10)$$

where  $r$  and  $u$  refer to the rural and urban values. These expressions along with the exponential velocity profile allow us to estimate wind speeds in an urban area based on measurements of wind speed at an upwind rural location. This allows us to generate model inputs required for dispersion models such as OSPM.

MacDonald et al. (1998) gives expressions for the surface roughness length and displacement height as a function of the frontal and plan area fraction:

$$d = H_b \left( 1 + \frac{\lambda_p - 1}{4.43\lambda_p} \right) \quad (3.11)$$

$$z_0 = H_b \left( 1 - \frac{d}{H_b} \right) \exp \left[ - \left( 0.5 \frac{C_d}{\kappa^2} (1 - d/H_b) \lambda_f \right)^{-0.5} \right] \quad (3.12)$$

where  $d$  is the displacement height and  $H_b$  is the building height.

Based on the models described in this section we can get a basic understanding of how the built environment affects dispersion of vehicle emissions in an urban area. To do this, we conducted a study of the sensitivity of the OSPM predicted concentration to the building height. We assume constant values of  $u_{*r} = 0.2m/s$ , and  $z_{0r} = 0.01m$ , and use the internal boundary layer and urban canopy models along with a simple model of the building layout of an urban area to compute the meteorological inputs required for OSPM. OSPM is used to compute the concentration magnification, the ratio of the near road concentration in the presence of buildings to that with no buildings next to the road. Equation (3.5) is used to calculate the concentration in the absence of buildings, the denominator for the concentration ratio. The urban concentration is taken to be the maximum of the leeward and windward concentration estimates.

We assume that the urban area consists of rectangular buildings with width  $W_b$  and height  $H$ , resulting in the relationship  $\lambda_f = \lambda_p \frac{H}{W_b}$ . We set the plan area fraction to 0.5 and the street width and building width are taken to be 20 m. The surface roughness length and displacement height of the urban area are determined from equations (3.11) and (3.12). Equations (3.9) and (3.10) are then used to compute the surface friction velocity above the urban area. The logarithmic velocity profile is then used to compute the wind speed at the top of the buildings for use in OSPM. The OSPM equations are solved for the surface concentration at the leeward and windward side of the street.

Figure 3.5 shows the variation of the magnification with building height. The magnification is always greater than 1 and increases with increasing building height. For a canyon aspect ratio of 2.0, the magnification is about 7.25, and for a relatively short canyon with aspect ratio of 0.5 the magnification is about 2.5. Thus, OSPM predicts

significantly increased concentrations in urban areas and a relatively large sensitivity to building height.

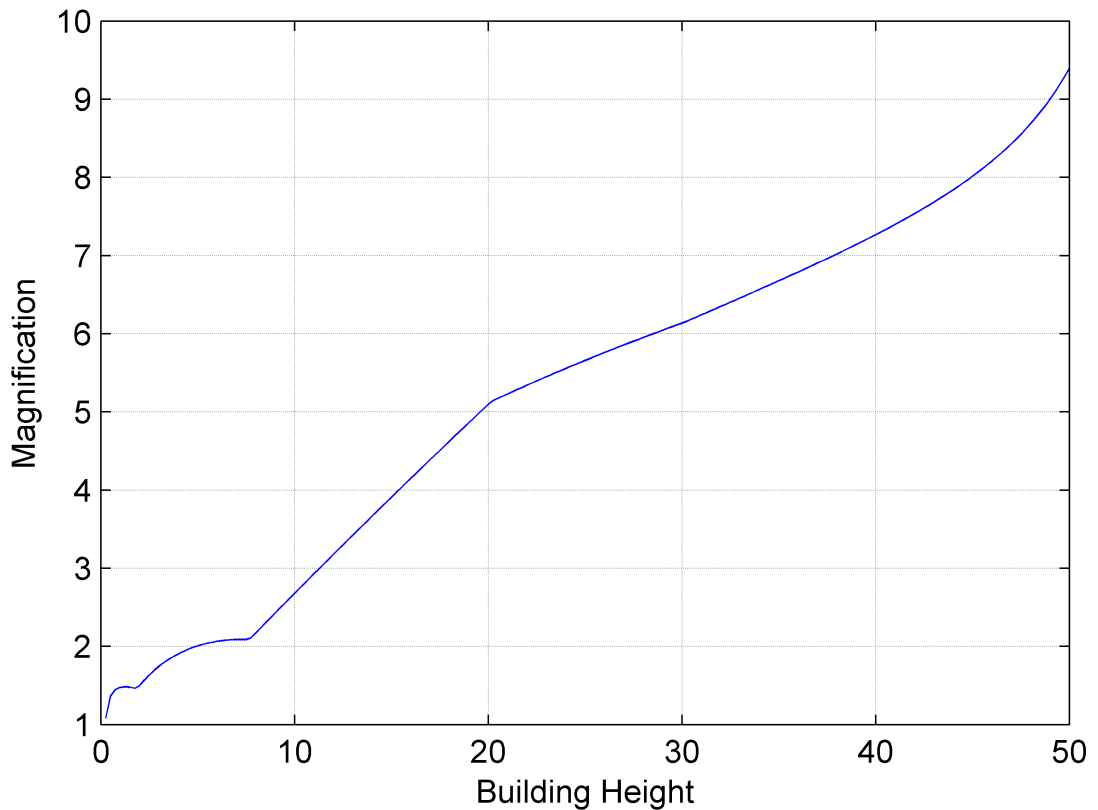


Figure 3.5: Concentration magnification predicted using OSPM.

OSPM is widely used to estimate concentrations of traffic emissions in cities and can be considered a prototype of the type of semi-empirical dispersion models that we use to understand dispersion of vehicle emissions in urban areas. OSPM has been evaluated with data collected in European cities (Berkowicz et al., 1997; Berkowicz, 2000; Kukkonen et al., 2003), which are characterized by uniform building heights and spatial homogeneity. However, it has not been shown that the concepts used in OSPM are useful for estimating near road concentrations of vehicle emissions in cities characterized by nonuniform building

heights and spatial inhomogeneity, such as those found in urban cores within the United States. Thus it is necessary to develop semi-empirical dispersion models that are applicable to these types of cities.

There are several issues with current urban dispersion models that we hope to address. First, the street canyon dispersion model is primarily designed for cities with uniform building heights. We hope to evaluate the applicability of this type of model for estimating near road concentrations within cities with varying building heights. Second, it is not clear which variables primarily govern near road concentrations in urban areas. Since OSPM assumes a logarithmic velocity profile within the urban canopy and a constant turbulent intensity to derive the near surface and rooftop turbulent velocities from the mean rooftop wind speed, the primary variables governing concentrations in OSPM are the canyon aspect ratio and the rooftop wind speed. The assumption that the mean wind speed is the primary meteorological variable determining the magnitude of the dispersion should be tested. Other variables such as the rooftop and near surface vertical turbulent velocities or the average rooftop vertical velocity may prove to better explain near road concentrations in urban environments. Additionally, the assumption of a constant turbulent intensity of 0.1, used to estimate the near surface turbulence from the wind speed, is questionable based on observations of much larger turbulent intensities in field measurements in Oklahoma city and Manhattan (Hanna et al., 2007).

In the next section I describe the analysis of near road concentration data collected in Hannover, Germany. The data is used to evaluate several dispersion models in order to determine the meteorological variables that primarily govern dispersion in the urban area of Hannover. This analysis provides evidence on what mechanisms predominantly determine near road concentrations within cities. This gives insight that is important in developing

the semi-empirical dispersion models and designing field experiments in Los Angeles that are used to examine dispersion in cities with significant building height variability.

### **3.3 Analysis of Long Term Measurements of Near Road Concentrations of Vehicle Emissions to Determine the Primary Variables Governing Dispersion in Urban Streets**

The operational street pollution model (OSPM), described in section 3.2 represents the current state of knowledge of dispersion of vehicle emissions in cities. However, OSPM has primarily been evaluated with data collected in European Cities characterized by uniform building heights and spatial homogeneity (Berkowicz et al., 1997; Berkowicz, 2000; Kukkonen et al., 2003). Several assumptions used in OSPM may not be useful for estimating near road concentrations in cities with significant inhomogeneity. OSPM uses the rooftop wind speed as the primary meteorological variable controlling concentrations. However, it is not clear what meteorological variables primarily govern dispersion in cities at the street scale (distances of about 100 m from the road). In this section we analyze the assumption that the rooftop wind speed governs dispersion of vehicle emissions. We use data collected in continuous field measurements by the German Niederschsisches Ministerium für Umwelt, Energie und Klimaschutz in Hannover, Germany between 2003 and 2007. This data set is ideal because it included measurements of turbulence data. We analyze the near road concentration data in the framework of several dispersion mod-

els to understand the variables that primarily govern near road concentrations in urban environments.

### 3.3.1 Data Set

The German Niedersächsisches Ministerium für Umwelt, Energie und Klimaschutz runs a pollution monitoring network throughout Germany. We obtained data from two monitoring sites that record gaseous pollutants,  $PM_{2.5}$ , and  $PM_{10}$  concentrations as well as meteorological data. The two sites, HRSW and HRVS, are located in Hannover on Göttinger Strasse. See Figure 3.6 for a map of the buildings and site locations. The sites are positioned at two heights, one (HRVS) near ground level within the urban canopy and one (HRSW) on a building roof 34 m above the street site. Concentration measurements were made at 1.5 m AGL and 35.5 m AGL. The buildings adjacent to Göttinger Strasse are 20 m tall and have almost no gaps between them, thereby forming a 20 m tall, 25 m wide and 200 m long street canyon. Göttinger Strasse runs along a line that points 17 degrees west of north. The street level HRVS site was instrumented with a sonic anemometer at 10 m AGL to measure 30 minute average wind speed, temperature, turbulent fluxes of momentum and heat, and vertical and horizontal turbulent velocity. The roof level HRSW site measured 30 minute average wind speed, wind direction, solar radiation, temperature, humidity, pressure, and precipitation at 42 m AGL. Automatic traffic counts classified into passenger cars and trucks were made. Data was obtained from January 1, 2003 through December 31, 2007.

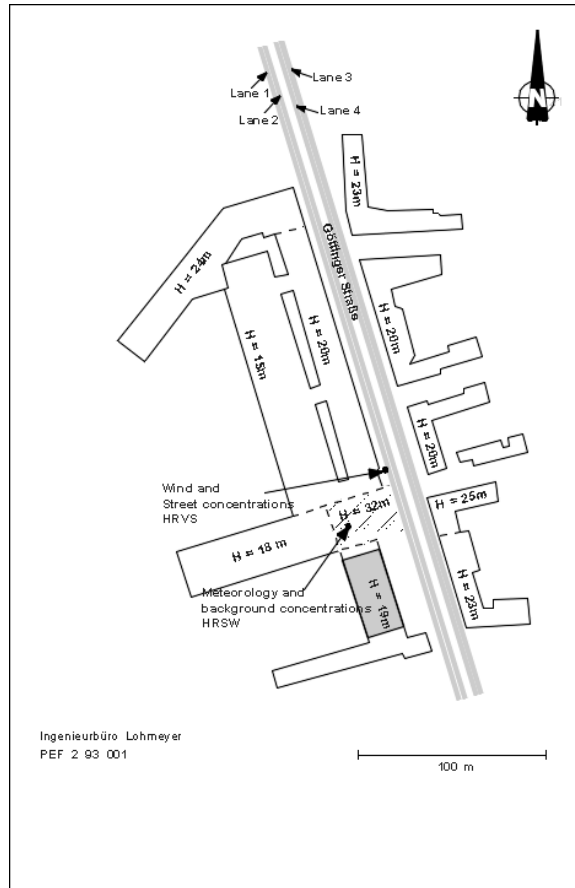


Figure 3.6: Map of Göttinger Strasse showing locations of concentration and micro meteorology stations and building heights.

### 3.3.2 Method

We use the Göttinger Strasse data to evaluate several alternative dispersion models with different dependence on the surface and rooftop  $\sigma_w$  and wind speed. We treat the rooftop concentration as the urban background, so the difference between street and roof concentrations is the local contribution described by the models.

We used the  $NO_x$  concentration measurements for model comparison because  $NO_x$  emission factors are well known. The emission factors for  $NO_x$  were determined using the EPA Emfac 2007 emission model (CARB, 2015b). We used the average emission factors

Table 3.2: Emission factors for  $NO_x$  (using molecular weight of  $NO_2$ ) [g/km].

Year	Light Duty Vehicles	Trucks
2003	0.465	6.18
2004	0.415	5.89
2005	0.358	5.99
2006	0.319	5.74
2007	0.287	5.40

for light and heavy duty trucks for the truck portion of the traffic and that for light duty vehicles for the passenger car portion. The emission factors are shown in Table 3.2.

One of the models analyzed with the data is the expression for the OSPM direct contribution concentration, given by equation (3.4). We develop alternative dispersion models by modifying this expression. If the plume spread is negligible relative to the initial vertical dispersion due to turbulence generate by motion of the vehicles,  $\sigma_{ws}W/U_s h_0 \ll 1$ , then the direct contribution is given by (Venkatram et al., 2007):

$$C_{direct} = \sqrt{\frac{2}{\pi}} \frac{q}{h_0 U_s} \quad (3.13)$$

Conversely, if the initial vertical plume spread is negligible compared with the plume spread only due to atmospheric turbulence at the position of the receptor, then the direct concentration becomes:

$$C_{direct} = \sqrt{\frac{2}{\pi}} \frac{q}{W \sigma_w} \ln \left( 1 + \frac{W}{w} \right) \quad (3.14)$$

This expression is valid if  $\sigma_{ws}w/U_s h_0 \gg 1$ . Note that the dependence on  $W/w$  in equation (3.14) is not physically realistic because it allows the concentration to approach infinity if the receptor is right next to the road. This is because the plume spread of the

segment of the road at the position of the receptor would be zero, resulting in infinite concentrations. In order to apply equation (3.14) we neglect the log term. This can be justified if the receptor is elevated, as described in section 3.3.5.

The model performance is quantified by calculating the geometric mean,  $m_g$  and standard deviation  $s_g$  of the residuals as well as the correlation coefficient,  $r^2$  and the fraction of data within a factor of two of model estimates,  $fact2$ . The definition of the geometric mean and standard deviation are given in section 2.3.

### 3.3.3 Results

Plots comparing equation (3.4) with observations are shown in Figure 3.7. The model is run with  $h_0 = 2m$ . From the scatter plot we see that the model overestimates by a factor of two, and there is not a strong correlation between model estimates and observations. The other panels of Figure 3.7 show the variation of the modeled and observed concentrations, normalized by emission rate, with 10 m wind speed, standard deviation of vertical velocity fluctuations, and wind direction. The variation of the observations is generated by binning data based on the variables on the x-axes and computing the average value in each bin. Error bars show standard deviations of the data within each bin. These figures show that the model systematically overestimates when the wind speed is less than about 1 m/s. In the figure of concentration against  $1/\sigma_w$  we see that the observations show a linear relationship between normalized concentration and  $1/\sigma_w$ . The model shows a similar sensitivity to  $1/\sigma_w$ , except for very small values of  $\sigma_w$  where the model underestimates concentrations. The bottom right panel of figure 3.7 shows that the model predicts the correct magnitude of concentrations when the wind direction is parallel to the street, and overestimates when the wind direction is perpendicular to the

street. The reason the model produces larger concentrations when the wind direction is perpendicular to the street is because the wind speed is smaller during these conditions.

The model approximately reproduces the observed concentration variation with wind direction even though the model equations are independent of wind direction. However, the model may be overestimating during perpendicular winds because we have not accounted for the effect of wind direction in the model. This can be seen by considering two opposing effects on the concentration of changes in wind direction: change in street level wind speed and change in the effective emission source. When the wind becomes parallel to the street the width of the street,  $W$ , in the log term in equation (3.4) should be replaced with the length of the street. Physically this means that during parallel winds there is a larger section of road upwind of the receptor and the larger emission source produces larger concentrations. The opposing physical effect is that when the wind is parallel to the street the wind speed tends to be larger, which produces smaller concentrations relative to perpendicular flow.

Figure 3.8 shows the comparison of the model given by equation (3.14), where the log term has been neglected, with observations in 2003. The model bias is smaller than that of equation (3.4), with an  $m_g$  of 1.02. The correlation coefficient of  $r^2 = 0.62$  is also better than that of the equation (3.4). The fraction of data within a factor of two of observations is 72%, which indicates that this model performs very well in estimating concentrations. The plot of concentration against  $1/\sigma_w$  in the bottom left panel of Figure 3.8 shows that the model has the same sensitivity to  $\sigma_w$  as the observations, although it tends to underestimate while equation (3.4) is unbiased except for very small values of  $\sigma_w$ . The top right panel of Figure 3.8 shows that equation (3.14) also has the correct sensitivity to wind speed, and has less bias than equation (3.4) when the wind speed is less

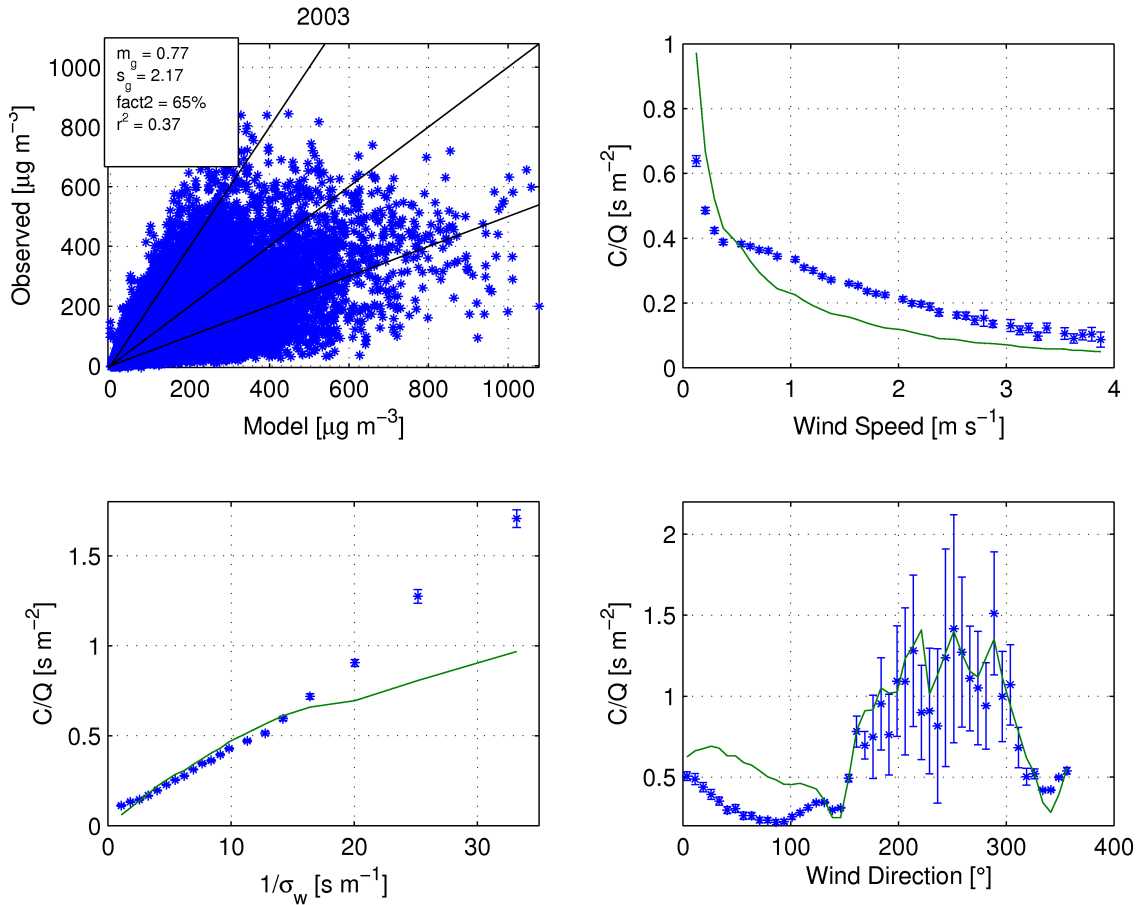


Figure 3.7: Comparison of equation (3.4) with observations during 2003. Top left shows scatter plot. Top right shows variation of observations (blue) and model (green) with wind speed. Bottom left shows variation with  $1/\sigma_w$ . Bottom right shows variation with wind direction. Wind directions parallel to the street are 163 and 343 degrees,

than 1 m/s. We conclude that equation (3.14) performs better than equation (3.4) under low wind speed conditions. The improved performance under low wind speed conditions is also seen on the bottom right panel of Figure 3.8, which shows concentration plotted against wind direction. In the figure we see that equation (3.14) overestimates less than equation (3.4) during perpendicular flow conditions, when the wind speed is smallest.

We have seen that equation (3.14) predicts the correct magnitude of concentrations. We expect the predictions of equation (3.13) to overestimate concentrations because this

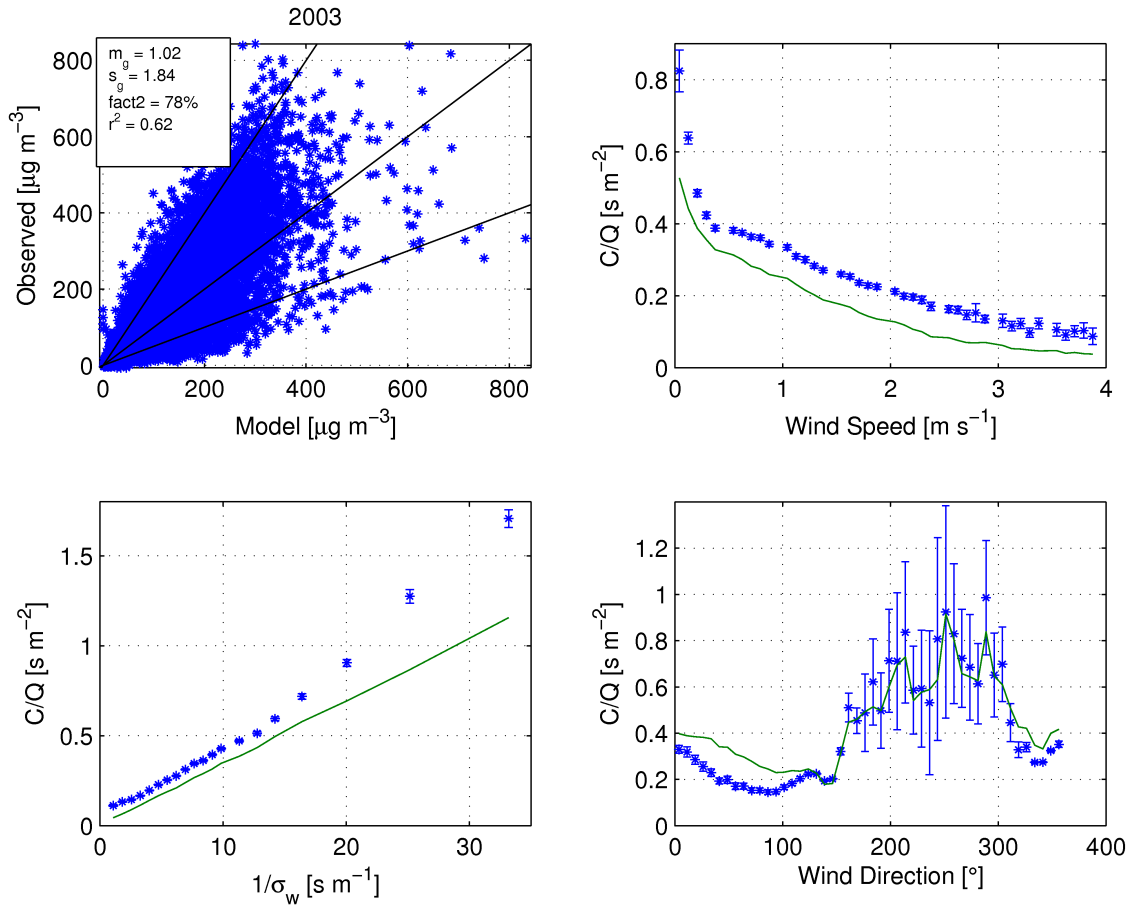


Figure 3.8: Comparison of equation (3.14) with observations during 2003. Top left shows scatter plot. Top right shows variation of observations (blue) and model (green) with wind speed. Bottom left shows variation with  $1/\sigma_w$ . Bottom right shows variation with wind direction.

equation neglects the atmospheric plume spread. We see in Figure 3.9 that equation (3.13) overestimates by a factor of five. There is also nearly zero correlation between model and observations. This indicates that the wind speed alone is not a good predictor of the near road concentration.

Based on this comparison we conclude that the vertical turbulent velocity explains the observed concentrations well, while the wind speed is not well-correlated with observations and including the wind speed in the model does not improve predictions of near

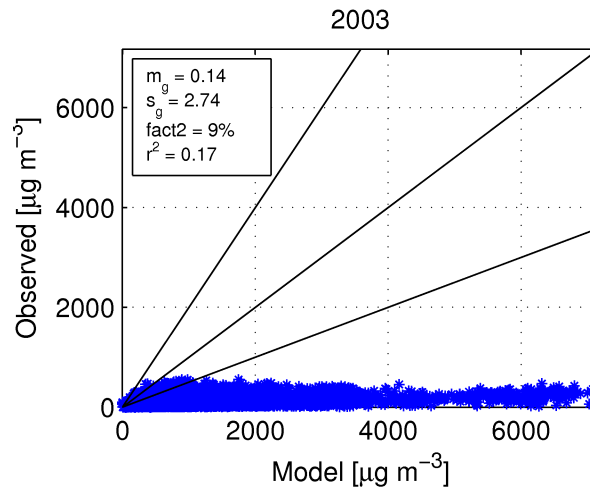


Figure 3.9: Scatterplot comparing model assuming plume spread is dominated by the initial vertical dispersion with observations.

road concentrations. The importance of the vertical turbulent velocity and insensitivity to wind speed was observed previously in near road concentrations of vehicle emitted *NO* (Venkatram et al., 2007). It is somewhat surprising that the near road concentration is not more strongly correlated with the street level wind speed since the standard deviation of vertical velocity fluctuations is normally strongly correlated with wind speed. However, in urban environments where mean wind speeds are small the horizontal turbulent velocities are usually very large relative to the mean wind speed, and the mean wind varies significantly depending on the nearby buildings (Hanna et al., 2007). The result is that horizontal motion is better characterized as a turbulent dispersion rather than advection by a strong mean flow. Thus the concentrations are primarily determined by turbulent transport in the vertical direction. This view of urban dispersion is somewhat inconsistent with the street canyon picture of a strong recirculating vortex flow. We now examine the concentrations and semi-empirical models further to better determine why the vertical turbulent velocity plays such a dominant role in determining near road concentrations.

### 3.3.4 Effect of Initial Vertical Mixing

The model of the initial vertical mixing in equation (3.4) produces a strong dependence on wind speed, while the observations do not show such a large dependence on wind speed. The dependence on wind speed arises through the initial vertical spread term in equation (3.4). The model is sensitive to the initial vertical spread because a large portion of the modeled concentration originates from sources located close to the receptor, where the plume spread is dominated by the initial vertical spread. To examine the influence of the initial vertical mixing, we developed a modified the model with a different model of the initial vertical spread. The modified model assume that the concentration is well-mixed below the height  $h_0$ , and follows a Gaussian shape above  $h_0$ . Then the concentration near the surface becomes:

$$C = \sqrt{\frac{2}{\pi}} \frac{q}{\sigma_{ws} W} \left( 1 + \sqrt{\frac{2}{\pi}} \frac{h_0 U_s}{L \sigma_{ws}} \right)^{-1} \quad (3.15)$$

where  $L$  is the length of the street upwind of the receptor. This model essentially enhances the vertical plume spread due to atmospheric turbulence for the part of the street located near the receptor, thereby reducing the importance of the initial vertical spread and the wind speed.

Figure 3.10 shows the performance of equation (3.15). The bottom right panel of Figure 3.10 shows that the model does not overestimate concentrations when the wind direction is perpendicular to the street, while the other models of equations (3.4) and (3.14) do. Equation (3.15) has a similar correlation with the data as equation (3.14). The model bias is slightly larger, although this could be explained by a small bias in the emission estimates.

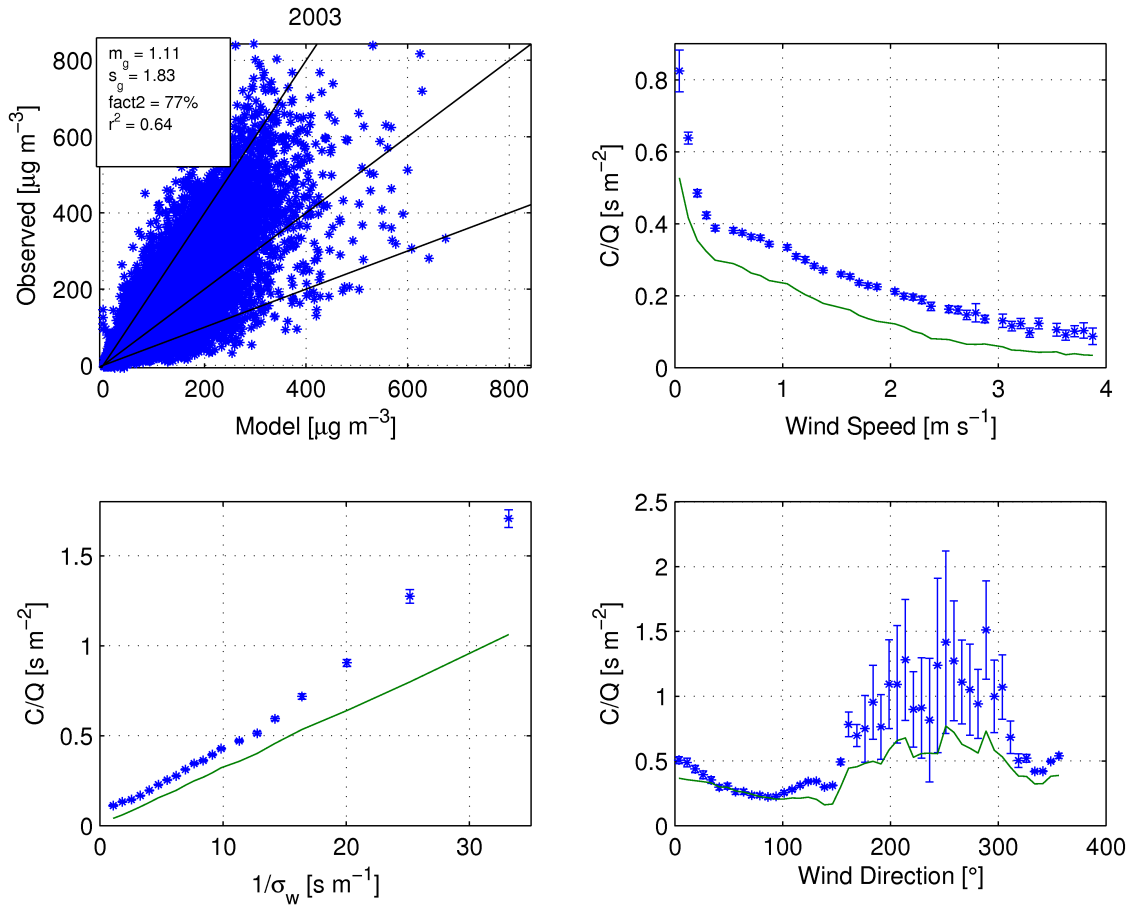


Figure 3.10: Comparison of equation (3.15) with observations during 2003. Top left shows scatter plot. Top right shows variation of observations (blue) and model (green) with wind speed. Bottom left shows variation with  $1/\sigma_w$ . Bottom right shows variation with wind direction.

This evaluation provides evidence that equation (3.4) is more sensitive to the wind speed than the observations because the formulation of the initial vertical plume spread is not appropriate for dispersion in urban environments. The model that enhances vertical mixing due to atmospheric turbulence for sources located near the receptor, equation (3.15), performs better. This indicates that strong vertical mixing occurs within the street, resulting in dominance of the vertical mixing over the initial plume spread and low sensitivity of observed concentrations to the wind speed.

### 3.3.5 Influence of Receptor Height

We see from the wind roses in Figure 3.11 that the within street wind direction is usually parallel to the street even though the rooftop wind direction is often perpendicular to the street. This indicates that channeling of the flow within the street is the dominant mean flow pattern, and that recirculating vortex flow is rare. Dispersion models show that the concentration difference between street and roof level does not depend on the mean wind speed when the flow is parallel to the street. We can see this by writing the equations for a dispersion model that accounts for the height of the receptor. If the receptor is elevated, using a Gaussian model for the vertical concentration profile, equation (3.4) becomes:

$$C_{direct} = \frac{q}{\sqrt{2\pi}\sigma_{ws}W} \left[ Ei \left( 0.5 \frac{z^2}{(h_0 + \sigma_w(w + W)/U)^2} \right) - Ei \left( 0.5 \frac{z^2}{(h_0 + \sigma_w w/U)^2} \right) \right] \quad (3.16)$$

where  $Ei$  is the exponential integral and  $z$  is the receptor height. When the wind is parallel to the street the street width,  $W$ , within the  $Ei$  term is replaced with the street length,  $L$ , and the distance of the receptor from the edge of the street,  $w$ , is set equal to zero. This substitution can be made by assuming the concentration is mixed over the width of the street and instead of integrating over the street width in the derivation of equation (3.4), we integrate over the length of the street.

Since we are taking the difference between the street and roof level concentration to remove the background concentration, we also apply equation (3.16) by taking the difference between the two levels. When the wind is parallel to the street and the street is very long so that  $\frac{HU}{\sigma_w L} \ll 1$  and  $H \gg z_r \gg h_0$ , the difference in concentration becomes:

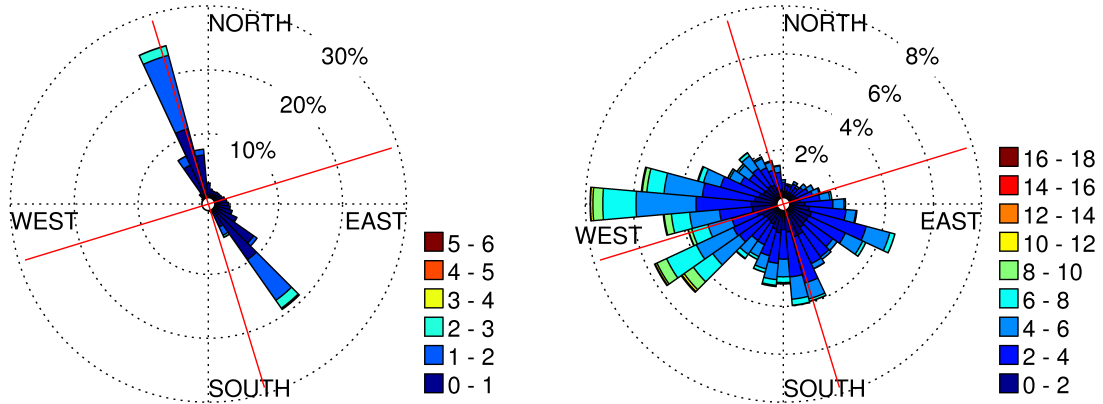


Figure 3.11: Wind roses for the 10 m (left) and rooftop (right) anemometers in the Göttinger Strasse data.

$$C_{direct} = \frac{q}{\sqrt{2\pi}\sigma_{ws}W} \ln\left(\frac{H}{z_r}\right) \quad (3.17)$$

where  $z_r$  is the height of the near surface receptor.

This expression is independent of the wind speed and initial vertical plume spread. This provides additional evidence for why the mean wind speed does not play much of a role in determining near road concentrations within urban areas. Due to frequent channeling of the flow, the wind direction is often parallel to the street, and thus equation (3.17) shows that the wind speed does not influence the difference in concentration between the surface and rooftop.

Figure 3.12 shows that equation (3.16) is much less sensitive to the wind speed than equation (3.4) ( $z=0$  m). The figure also shows that the street does not need to be very long for equation (3.17) to be applicable. A 100 m street length and 20 m building height were used to generate the figure. Even for this short street length, changes in receptor height have a much larger influence on the concentration difference than changes in the wind speed.

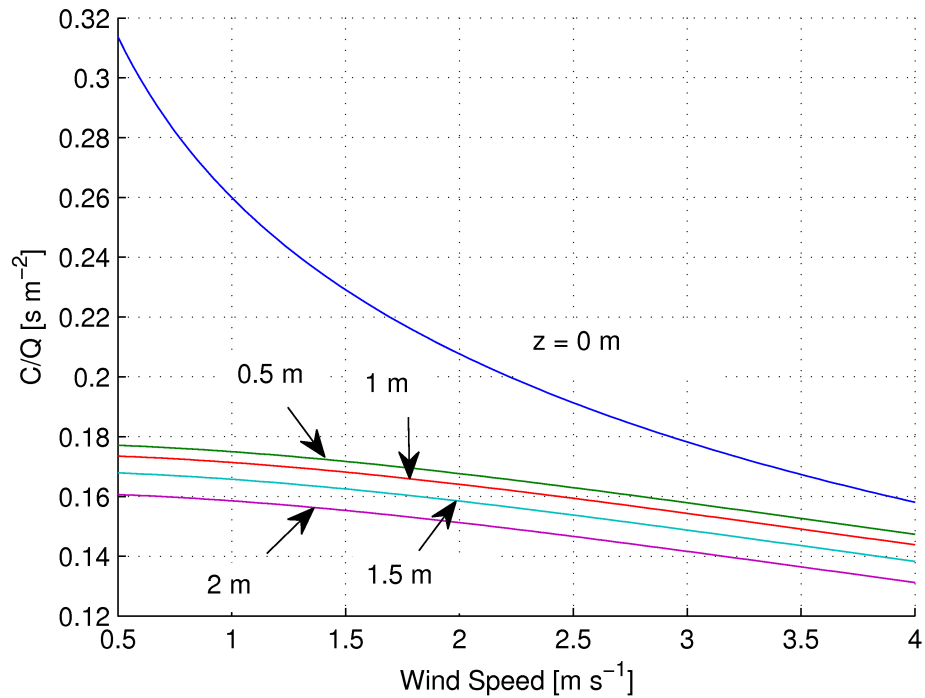


Figure 3.12: Difference between a receptor at height  $z$  and a receptor at 20 m AGL calculated with equation (3.16) for parallel flow. The model is run with a street length of 100 m, width of 20 m, and with  $\sigma_w = 0.5 \text{ m s}^{-1}$ . Note that  $z = 0 \text{ m}$  corresponds to equation (3.4).

The assumptions underlying equation (3.17) break down when the wind is perpendicular to the street and the street width is not much larger than the building height. We do see that equation (3.14), and thereby equation (3.17) since it is only different by a constant, performs worse under perpendicular flow than when the wind is parallel to the street. This provides additional evidence that the arguments leading to the derivation of equation (3.17) give a good explanation of why vertical turbulent transport primarily determines near road concentrations in urban areas.

The sensitivity of equation (3.16) to initial vertical spread and receptor height is shown in Figure 3.13. If the receptor height is much larger than the initial vertical plume spread,  $z/h_0 \gg 1$ , then the concentration becomes insensitive to the initial vertical

plume spread. This corresponds with the case where the second exponential integral term in equation (3.16) approaches zero. Equation (3.16) justifies the removal of the log term from equation (3.14). The log term is not physically realistic because it allows the concentration to become very large when the receptor is located directly next to the street, while in reality the maximum concentration is limited by the initial vertical plume spread.

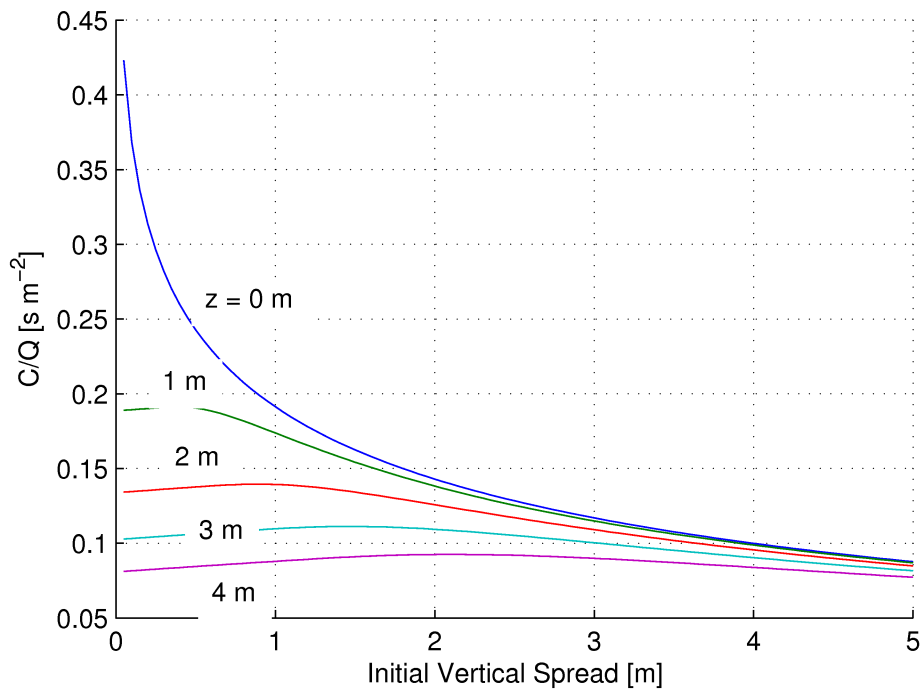


Figure 3.13: Sensitivity of dispersion model of equation (3.4) ( $z = 0 \text{ m}$ ) and equation (3.16) to initial vertical spread and receptor height.

The performance of equation (3.16), where the model is applied by taking the difference between the concentration at the street and roof receptors, is shown in Figure 3.14. The figure shows that equation (3.16) is nearly unbiased and shows good correlation with observations. The sensitivity to wind speed and turbulence is similar to the

observed sensitivity, and the model shows the correct concentration magnitude under both perpendicular and parallel flow conditions.

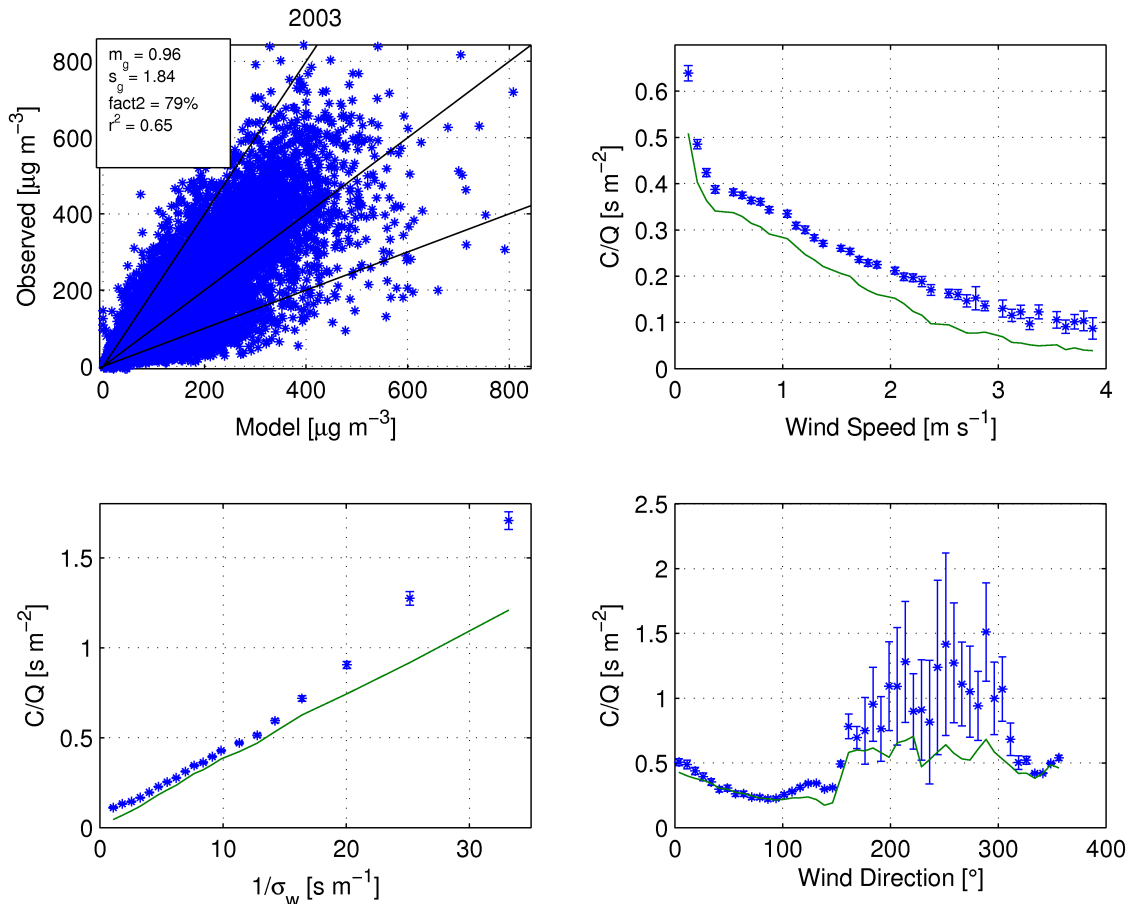


Figure 3.14: Comparison of equation (3.16) with observations during 2003. Top left shows scatter plot. Top right shows variation of observations (blue) and model (green) with wind speed. Bottom left shows variation with  $1/\sigma_w$ . Bottom right shows variation with wind direction.

The frequent occurrence of parallel winds in the measurements provides additional evidence that the street canyon vortex flow model used in OSPM is often not appropriate for modeling dispersion in cities with nonuniform building heights. Recirculating vortex flow is not often observed in the measurements in Göttinger Strasse. In our field measurements in Los Angeles, described in section 3.4, we also usually observe channeling

flow rather than vortex flow even when the rooftop wind direction is perpendicular to the street. The good performance of equation (3.16) at explaining the difference between near surface and rooftop concentrations in Göttinger Strasse indicates that frequent occurrence of channeling flow causes the pollutant dispersion to be dominated by vertical turbulent transport. Thus concentrations are insensitive to the mean wind speed, and the vertical turbulent velocity primarily governs near road concentrations of vehicle emissions.

### **3.3.6 Discussion**

The comparison of several alternative dispersion models shows that the dispersion models of equations (3.14), (3.16), and (3.15) are suitable for estimating near road concentrations in urban environments. The models indicate that the street level vertical turbulent velocity is the dominant variable controlling dispersion within a street. The mean wind speed only has a small effect on the difference in concentration between the receptors located at street and roof level, which can be explained through two alternative dispersion models. The low sensitivity of the concentration difference to wind speed is justified by equation (3.16) if the near surface wind direction is often parallel to the street. Measurements in Göttinger Strasse and the Los Angeles field study, described in section 3.4, show that winds predominantly channel within the street rather than forming recirculating vortices, thus supporting this explanation for the low sensitivity to wind speed. An alternative explanation is that the direct contribution model used by OSPM (equation (3.4)) possibly does not account for the initial vertical mixing correctly and is too sensitive to the section of the road located directly next to the receptor, resulting in a greater sensitivity to the wind speed than observations indicate. A modified model which mixes pollutants more rapidly shows a better correlation with data, especially under low

wind speed conditions, indicating that the initial vertical mixing is more rapid than that used in the OSPM model.

### **3.4 Design of Field Measurements in Los Angeles**

In section 3.3 we analyzed measurements of near road concentrations of vehicle emissions in Göttinger Strasse, Hannover, Germany to determine the primary meteorological variable governing dispersion of vehicle emissions in urban environments. However, it remains to be seen how the dispersion models described in section 3.3 perform for cities with significant building height variability and spatial inhomogeneity. To evaluate the performance of the dispersion models for cities with these characteristics, we conducted field measurements of near road concentrations of vehicle emissions along with the meteorological variables governing dispersion in several cities in Los Angeles and Riverside counties, California, USA. The design of the experiments is based on the knowledge gained from the analysis of the dispersion models in section 3.3. This section describes the field measurements.

Equation (3.14) best explained the variation of the near road concentrations observed in Göttinger Strasse. This model shows that the standard deviation of vertical velocity fluctuations measured at approximately half the building height is the primary variable governing the near road concentrations. Thus, our field study includes measurements of the near surface and rooftop turbulent velocities. The field study also includes measurements of mean wind speed and wind direction in order to evaluate the performance of other dispersion models such as OSPM. OSPM estimates the near road concentration as the sum of the direct plume contribution from the road and the recirculating contribution,

due to trapping of pollutants within the street canyon. The recirculating contribution is governed by the rooftop standard deviation of vertical velocity fluctuations. Within the OSPM framework, see section 3.2 for details, the rooftop turbulence and surface wind speed and turbulent quantities are estimated from the rooftop mean wind speed. Thus, our field study included measurements of the turbulence and mean winds at the urban rooftop as well as at the surface.

For most practical applications the rooftop wind speed and direction within the urban area must be determined from measurements of wind speed at a nearby local monitoring station, most likely located at a nearby airport. This is because meteorological variables are not routinely measured in urban areas. The wind speed and turbulence from the upwind rural area are modified by the built environment as the air passes from an upwind monitoring station to the urban site of interest. The wind speed at the urban rooftop, and therefore the turbulence and near surface mean wind as well, are thus a function of the overall built environment characteristics between the rural reference location and the urban site. The modification of the meteorological variables between the reference and urban sites is explained by the internal boundary layer (IBL) model described in section 3.2.2. Our field study included measurements of the mean wind and turbulent quantities at a rural reference location upwind of the urban field sites in order to evaluate the IBL model.

We use ultrafine particle number (UFP) as the primary vehicle emitted pollutant to evaluate the dispersion models. This is done for two reasons. First, UFP is linked with negative health effects (Knibbs et al., 2011). Second, we have access to several TSI3022A condensation particle counters that provide high resolution measurements of UFP.

Concentrations of UFP were measured at multiple fixed locations at each field site. The fixed locations were chosen based on several considerations. The primary consideration

for the instrument locations was based on the need to separate the contribution of local vehicle traffic from the total measured at a given monitor. Concentrations at multiple sites can be combined to better separate the local contribution from background sources not associated with the street of interest. For the purpose of evaluating OSPM we can easily separate the direct contribution from the recirculating contribution and the background by taking the difference in concentration between two locations on opposite sides of the street. This method is effective when a recirculating vortex exists within the canyon, which advects the direct plume contribution to one side of the street. The method we use to isolate the OSPM recirculating contribution is to take the difference between the surface concentration and that measured with a monitor placed on a nearby rooftop. The concentration used to evaluate equation (3.14) is also based on the difference between the surface and rooftop concentrations. Thus, most of the field measurement designs included rooftop measurements of concentrations as well as measurements on opposite sides of the street at each chosen location.

The second consideration for locating the concentration monitors is based on the need to resolve the effect of the built environment on near road concentrations. Field measurements pose significant challenges to isolating the effect of one variable on the concentration because variability in uncontrolled factors such as traffic emission rate can overwhelm the signal due to the presence of buildings. The local vehicle emission rate must be known to evaluate the dispersion models but emissions can be difficult to determine in practice. Individual vehicle emission rates can vary significantly, and during congested driving conditions, characteristic of urban environments, the local traffic within a street is often accelerating or idling, increasing uncertainty of the emission rates (Smit et al., 2008). Emission models of gaseous pollutants and particle mass are usually accurate to about a factor of two or three (Smit et al., 2010). Ultrafine particle number (UFP), which

we use as the primary measured pollutant in the field study, has emission factors that vary by about an order of magnitude (Kumar et al., 2011). Because of the uncertainty in the emission estimates, when possible the experiments were designed so that UFP concentration measurements were made at two sections on the same street: one section with tall buildings adjacent to the street, and another where there are no buildings or very short buildings adjacent. This design ensures that local vehicle emissions are similar at the two locations, allowing us to directly compare concentrations at the open and building sections to isolate the building effect.

Our strategy for estimating traffic emissions is to make manual counts of light and heavy duty vehicles and then to apply average emission factors to the traffic counts. Since the particle number concentration emission factor is very uncertain we foresee that determining accurate emission estimates may pose a challenge in evaluating the models.

This forms a broad outline of the necessary measurements for the field study. The experiment design conducted in practice has depended on availability of instruments, and the overall design has evolved as we gained knowledge from previous experiments. The data used in this thesis was collected during two primary measurement campaigns. The first was conducted in several cities in Los Angeles County, CA, USA between September 2013 and July 2014. Table 3.3 gives an overview of the building morphology of the various field locations in this campaign. In the following sections we describe the instrumentation used at each of the field sites and the details of each experiment. Analysis of the data from the Los Angeles study is given in section 3.5. The second campaign was conducted in Riverside, CA, USA in September and August, 2015. Description of the Riverside field study and results of data analysis for are given in section 3.6.

Table 3.3: Overview of measurement locations.

Location	Dates	Building Morphology
8th St., Los Angeles	UFP 5/7/14 and 5/9/14 Micrometeorology 4/22/14 - 5/13/14	Street canyon 50 m tall, 20 m wide street at one location. Parking lot at another loca- tion
Wilshire Blvd., Beverly Hills	UFP 5/30/14 Micrometeorol- ogy 5/19/14 - 7/1/14	Variable building height up to 50 m, 30 m wide street
Temple City Blvd., Temple City	UFP 1/15, 1/16, 1/17/14 Micrometeorology 1/13/14- 2/14/14	6 m tall uniform buildings, 30 m wide street
7th St./Broadway, Los Angeles	9/20/14	Step up street canyon from 25 to 50 m

### 3.4.1 Instrumentation

We use Campbell Scientific CSAT3 3D sonic anemometers (Figure 3.15) to record the three components of wind speed and the sonic temperature at a sampling frequency of 10 Hz. The data is processed using the method described in Kaimal & Finnigan (1994) to yield the 30 or 60 minute averaged values of the turbulent heat flux, surface friction velocity, standard deviation of the vertical and horizontal turbulent velocities, wind speed, wind direction, temperature, and Monin-Obukhov Length.

TSI 3022A condensation particle counters (Figure 3.16) are used to record ultrafine particle number concentrations at a sampling rate of 1 Hz. Samples are drawn through a copper and tygon tube with the tube sampling inlet set at 1 m above ground level. The instruments measure the concentration of particles with diameters greater than 10 nm (50% detection efficiency is 10 nm). The inlet flow rate is  $25 \text{ cm}^3 \text{ s}^{-1}$  and the flow rate through the detector is  $5 \text{ cm}^3 \text{ s}^{-1}$ . Power is supplied by 12 V 100 A hr lead acid deep cycle batteries through 12 V to 120 V AC power inverters. Data loggers were constructed

to record data from the serial port and store it on SD cards. Details of the data logger system is given in appendix B.

AQMesh five gas concentration monitors were used to measure concentrations of carbon monoxide, nitrogen oxide, nitrogen dioxide, ozone, and sulfur dioxide at the 8th St and Temple City field sites.



Figure 3.15: Campbell scientific CSAT3 sonic anemometer.

### **3.4.2 Los Angeles - 8th St, April 23 - May 13 2014**

Measurements were made near the 8th and Hill St intersection in Los Angeles between April 23 and May 13, 2014. An overview of the experiment is shown in Figure 3.18. The site was chosen because 8th St has a section where there are no buildings next to the



Figure 3.16: Condensation particle counter.

road, the “parking lot” site, and a section where there are tall buildings directly next to the road, the “building” site. This design helps remove the effect of emission variation: because the open and building sites have very similar traffic we can directly compare the concentrations at the site to determine the effect of the buildings at the “building” section on the concentration. Sonic anemometers were placed at an upwind rural location near LAX airport, at a rooftop location on the 50 m tall Union Lofts building, located at the 8th and Hill St intersection, at the parking lot and building sites, and at the mid-section between the two sites.

The upwind rural sonic anemometer was mounted on a tripod at 3.15 m above ground level (AGL). Figure 3.15 shows a photo of this anemometer, looking downwind. There were no buildings upwind of the sonic essentially all the way to the pacific ocean several



Figure 3.17: AQMesh concentration monitor (at top of photo).

kilometers to the west. The street level sonic anemometers were mounted to light poles next to 8th St at about 4 m AGL (Figure 3.19). See Figure 3.21 and Table 3.4 for detailed instrument locations. The sonics were attached to 2 foot long beams attached to the poles and oriented with the sensor pointed toward the street, except for the sonic next to the parking lot, which was oriented southwest because the predominant wind direction is southwesterly. We attempted to place the sonics away from major obstructions. However, 8th St has several large trees next to the road, and the instrument at location 1 (Table 3.4) was placed about 10 m downwind of a tree, and instrument location 2 was at a section of road where there were trees upwind and downwind. Locations 3 and 4, the locations of the primary sonic anemometer measurements, were far from any trees or other obstacles.

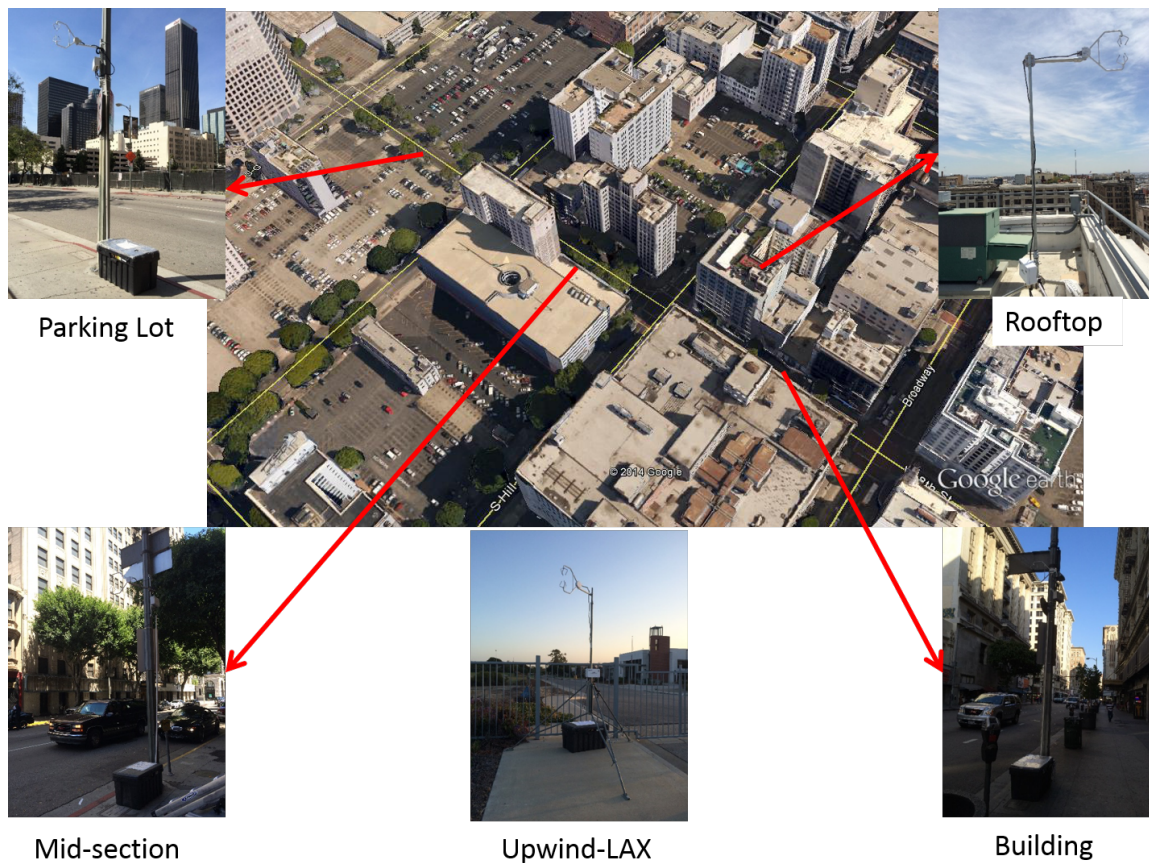


Figure 3.18: Overview of 8th St field study.

Condensation particle counters were placed at the locations shown in Figure 3.21. The CPCs were placed on May 7th and May 9th between about 8:00 and 18:00 PDT, but no rooftop CPC (number 360) was used on May 7th because the instrument was not available. The CPCs were co-located (Figure 3.20) for 30 minutes before the start of measurements on both May 7th and 9th to derive inter-instrument calibration factors used to adjust the data. The results of the calibration are shown in Appendix A.



Figure 3.19: Sonic anemometer and AQMesh monitor mounted to light pole next to 8th St.



Figure 3.20: Co-location of CPCs before start of measurements on 8th St.

Traffic data for 8th St was obtained from automatic traffic detectors run by city of LA. The traffic was recorded at the 8th St and Olive St intersection located midway between the open and building sites.

Table 3.4: Detailed instrument locations on 8th St.

ID	Instrument	Location	Latitude	Longitude	Heading ( $\circ$ from north)	Height (inches)	Dates (month/day/year)
1	Sonic 0984	Building Region	34.04413	-118.25533	19	146	4/23 – 5/1
2	Sonic 0984	Middle region	34.04482	-118.256503	190	157	5/1 – 5/13
3	Sonic 0245	Building Region	34.04403	-118.25541	204	160	4/23 – 5/13
4	Sonic 1055	Parking lot	34.04523	-118.25713	37	155	4/22 – 5/13
5	Sonic 2564	Upwind LAX airport	33.95494	-118.40472	36	124	5/7 – 5/13
6	Sonic	8th St. roof of union lofts	34.044285	-118.255326	18	95	5/1 – 5/13
1	AQMesh 82150	Building region				152	5/1 – 5/9
3	AQMesh 89150	Building region				166	5/1 – 5/9
A	CPC 483	Near sonic 0245	34.04403	-118.25541		59	5/7 and 5/9
B	CPC 498	Across street from sonic 0245	34.044213	-118.255361		59	5/7 and 5/9
C	CPC 494	Near sonic 1055	34.045406	-118.25738		59	5/7 and 5/9
D	CPC 502	Across street from sonic 1055	34.045506	-118.257285		59	5/7 and 5/9
E	CPC 360	Roof of union lofts building	34.044398	-118.255464		59	5/9

### **3.4.3 Los Angeles - 7th St and Broadway, September 20, 2013**

Figure 3.22 shows an overhead view of the locations of measurements made in Los Angeles on September 20. Table 3.5 shows the detailed locations of the instruments. Four sonic anemometers were mounted on tripods at several locations: one on a tripod about 3 m above the top of the 55 m tall Van Nuys apartment building next to 7th St, one at 2.4 m AGL on the southwest side of 7th St, one at 2.4 m AGL on the northwest side of Broadway, and one at 2.4 m AGL at a park, Rancho Cienega Recreation center, approximately 10 km west (upwind) of the 7th St site. The upwind sonic was placed as far from buildings and trees as possible on a flat baseball field. The buildings surrounding the park were 1 or 2 stories tall. The rooftop sonic was placed on a section of the rooftop about 10 m higher than the rest of the roof near the edge of the building (Figure 3.23). A small structure stands about 7 m to the east of the sonic.

Three TSI 3022A CPCs and two Matter Aerosol DiSCminis were used to measure concentrations of ultrafine particle number. Two CPCs were placed on opposite sides of Broadway, and one on top of the 55 m tall Van Nuys apartment building. The two DiSCminis were placed on opposite sides of 7th St. The CPCs and DiSCminis were calibrated relative to each other by co-locating the instruments for about 30 minutes and adjusting the data using the resulting calibration factors. Appendix A shows the calibration plots along with the regression coefficients for each instrument.

Traffic at the 7th St and Broadway intersection was recorded using a camera attached to a tripod on the roof of the Van Nuys building. Additionally, traffic data was obtained from the city of LA's automatic traffic counting system. The traffic data for 7th St was obtained from detectors located at 7th St and San Pedro intersection, and for Broadway

Table 3.5: Detailed instrument locations at 7th St and Broadway.

ID	Instrument	Location	Latitude	Longitude	Heading ( $^{\circ}$ from north)	Height (m)
1	Sonic	Roof	34.044645	-118.252957	83	57.4
2	Sonic	7th St	34.04495	-118.253129	210	2.4
3	Sonic	Broadway	34.044639	-118.253956	322	2.4
2	DiscMini 2	7th St South	34.044888	-118.253035		1
3	CPC 483	Broadway West	34.044719	-118.253955		1
4	CPC 481	Roof	34.044623	-118.252775		56
5	DiscMini 1	7th St North	34.045004	-118.252914		1
6	CPC 360	Broadway East	34.044634	-118.253786		1
	Sonic	Upwind Park	34.023285	-118.35091	75	2.4

from detectors at Broadway and Pico St. The manual and automatic counts were compared, and the automatic counts were adjusted to match the magnitude of the manual counts.

#### **3.4.4 Temple City - Las Tunas Dr and Temple City Blvd**

This site is characterized by fairly uniform single story buildings. Measurements of particle concentrations and turbulence were made between January 13 and February 13, 2014 in Temple City at the Las Tunas Dr and Temple City Blvd intersection. Figure 3.24 shows the locations of the CPCs and sonic anemometers at the site. One anemometer was placed on the roof of a 6.1 m tall building near the intersection and another was mounted to a light post at the south side of the street near mid-block. An additional sonic was placed at a rural upwind site at Rose Hill Park. CPCs were placed at the four corners of the block and on both sides of the street near mid-block on January 15, 16, and 17. The CPCs were co-located to derive calibration factors. Results are given in Appendix A. Traffic was counted using a video camera near mid-block. Table 3.6 gives a summary of the instrument locations.

The sonic anemometer at Rose Hill Park was located on top of a 50 m tall, 300 m wide hill. This is not an ideal location for the sonic because the wind speed is increased at the top of the hill relative to the surrounding area, but there were no other open areas that can be used as a rural reference location available. We can account for the wind speed up at the top of the hill using a model developed by Jackson & Hunt (1975). The surface roughness length of the park is determined by the observed wind speed and surface friction velocity to be 3.67 cm. Using equation 2.11b in (Jackson & Hunt, 1975) we estimate the inner layer height,  $l$ , to be 18 m. The sonic on the hilltop is 2.9 m AGL.

Table 3.6: Detailed instrument locations at Temple City site.

ID	Instrument	Location	Latitude	Longitude	Heading ( $^{\circ}$ from north)	Height (m)	Dates (month/day/year)
1	Sonic	South Center	34.106693	-118.060151	88	2.4	1/13/14 – 2/13/14
2	Sonic	Roof	34.1069	-118.060712	354	8.4	1/13/14 – 2/13/14
1	CPC 502	South Center	34.106693	-118.060151		1	1/15/14, 1/16/14, 1/17/14
2	CPC 498	Roof	34.106874	-118.060758		7	1/15/14, 1/16/14, 1/17/14
6	CPC 499	South West	34.10662	-118.060669		1	1/15/14, 1/16/14, 1/17/14
7	CPC 480	South East	34.106761	-118.059658		1	1/15/14, 1/16/14, 1/17/14
8	CPC 497	North East	34.106975	-118.059708		1	1/15/14, 1/16/14, 1/17/14
9	CPC 494	North Center	34.106903	-118.060259		1	1/15/14, 1/16/14, 1/17/14
10	CPC 483	North West	34.106834	-118.060711		1	1/15/14, 1/16/14, 1/17/14

Using this height, table 3 (Jackson & Hunt, 1975) results in a fractional speed up ratio of 0.48. This is consistent with the observed 50% increase in wind speed relative to the measurements made in September at the Montecito Heights Recreation center baseball field about 1 km north of Ascot Hills park.

### **3.4.5 Beverly Hills - Wilshire Blvd**

The measurements on Wilshire Blvd, Beverly Hills were similar to those made on 8th St, except no rooftop measurements were made. Figure 3.25 shows an aerial view of the site, showing CPC locations near the “parking lot” and “building” locations, which have only short buildings and 50 m tall buildings directly next to the road, respectively. Sonic anemometers were placed next to the street at the “parking lot” and “building” locations, and at the same upwind LAX site used in the Los Angeles 8th St field study. Four CPCs were placed at the location shown in Figure 3.25. Table 3.7 gives details of the instrument locations.

The next section shows the analysis of the data collected from the field measurements described in this section.

Table 3.7: Detailed instrument locations at Beverly Hills site.

ID	Instrument	Location	Latitude	Longitude	Heading ( $^{\circ}$ from north)	Height (m)	Dates (month/day/year)
1	Sonic 0245	Building Region North	34.067162	-118.390488	50	4.14	5/19/14 - 7/1/14
3	Sonic 0984	Open Region South	34.06696	-118.3923	95	4.06	5/19/14 - 7/1/14
1	CPC 494	Building Region North	34.067162	-118.390488		1	5/30/14
2	CPC 483	Building Region South	34.066954	-118.390392		1	5/30/14
3	CPC 498	Open Region South	34.06696	-118.3923		1	5/30/14
4	CPC 502	Open Region North	34.067162	-118.392417		1	5/30/14
	Sonic 1055	Upwind near LAX	33.95494	-118.40472		3.15	5/19/14 - 7/1/14



Figure 3.21: Instrument locations on 8th St. See Table 3.4 for symbol definitions.



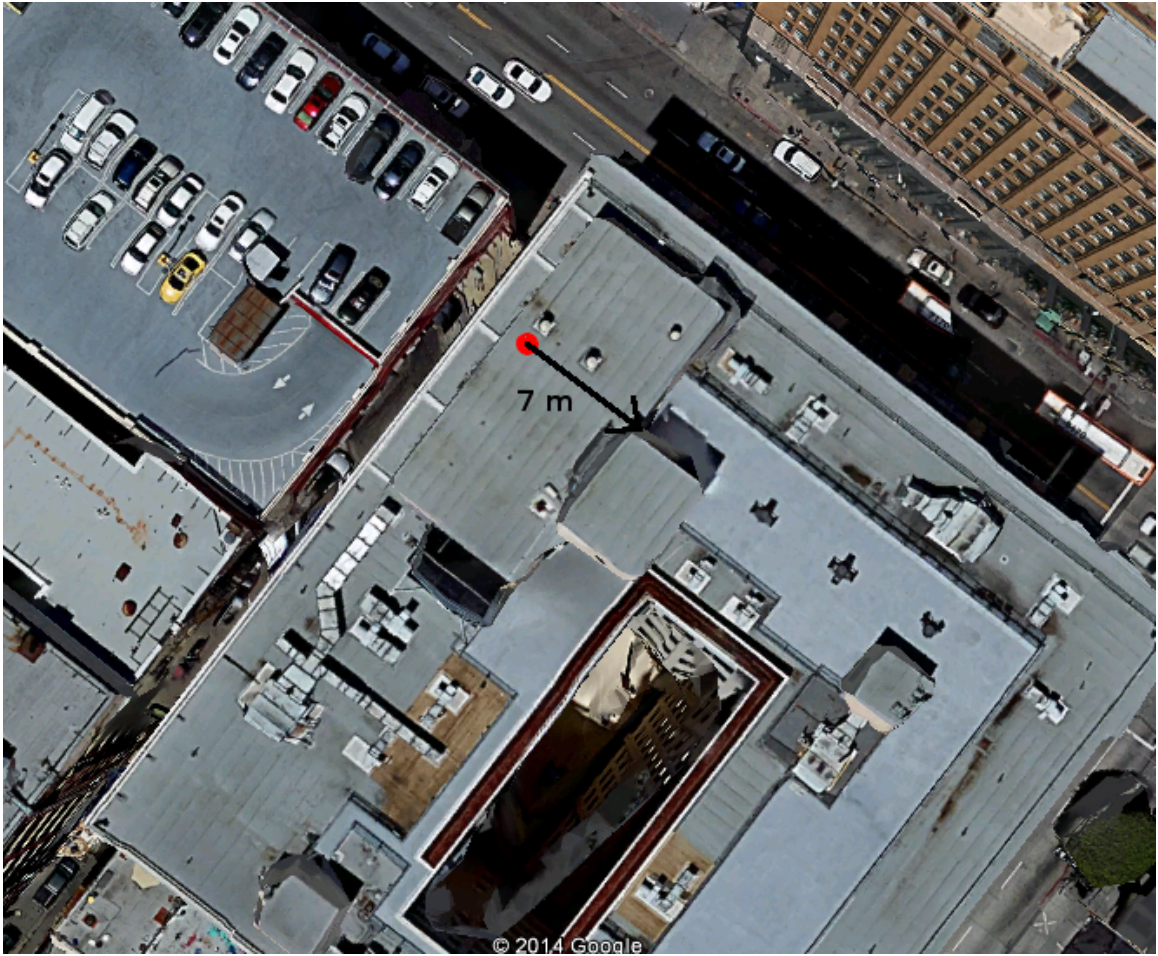


Figure 3.23: Location of rooftop sonic anemometer near the edge of a section of roof about 10 m above the rest of the roof. A small structure sites about 7 m to the east of the sonic.



Figure 3.24: Temple City experiment site. For marker definitions see table 3.6.

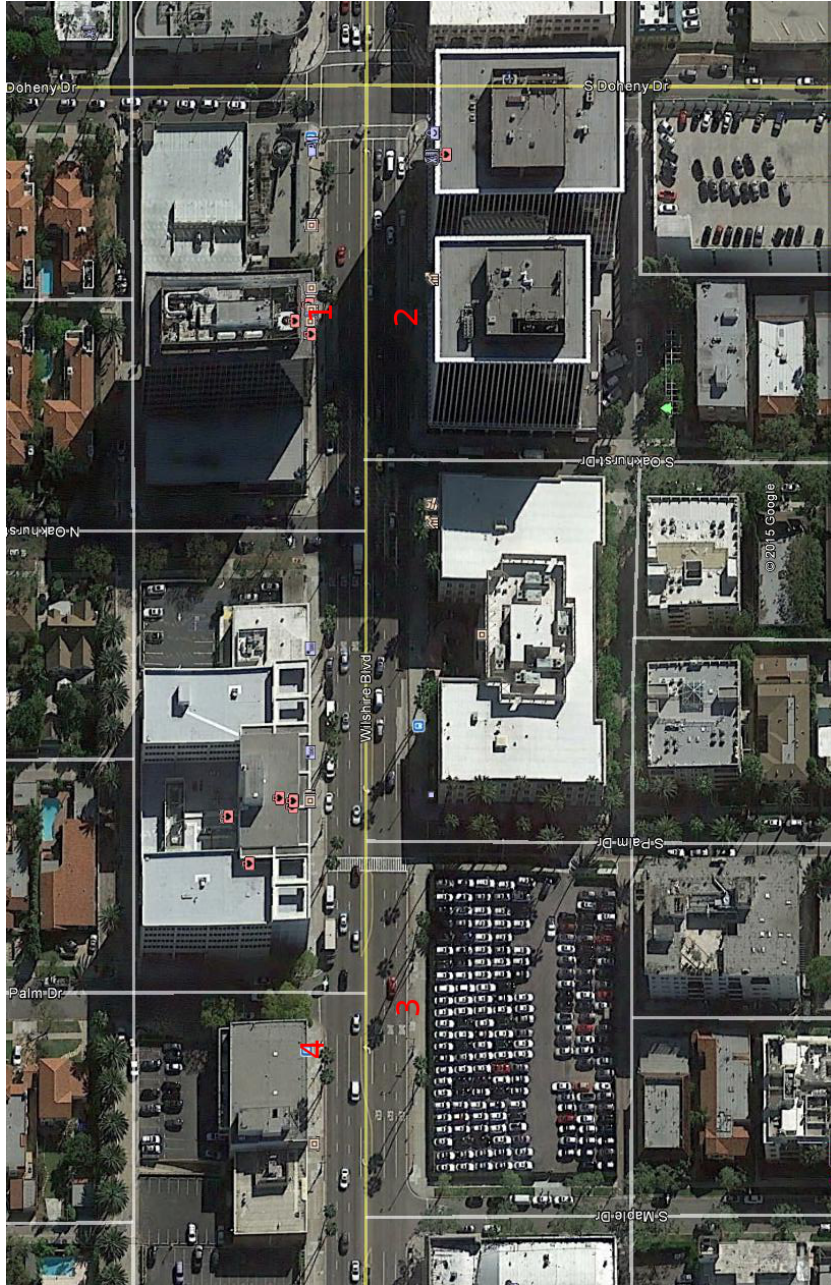


Figure 3.25: View of Wilshire Blvd field site. For marker definitions see table 3.7.

### 3.5 Interpretation of Ultrafine Particle Concentration Data From the Los Angeles Field Study Using Several Dispersion Models

In this section I analyze the UFP concentration data collected in the Los Angeles field measurements using several semi-empirical dispersion models. First I evaluate the OSPM recirculating contribution model, described in section 3.2, with observations of near road concentrations in the Los Angeles field study. The recirculating contribution model is evaluated by comparing the model with the difference between the average concentration of the two receptors located on opposite sides of the street and the rooftop concentration.

The data collected on 8th St is analyzed first. Wind roses of data collected at the building and open near surface anemometers, shown in Figure 3.26, indicate that winds are often parallel to the street at the building section and perpendicular to the street at the open section. Thus the evidence points toward channeling flow existing in the street canyon rather than a coherent street canyon type vortex flow.

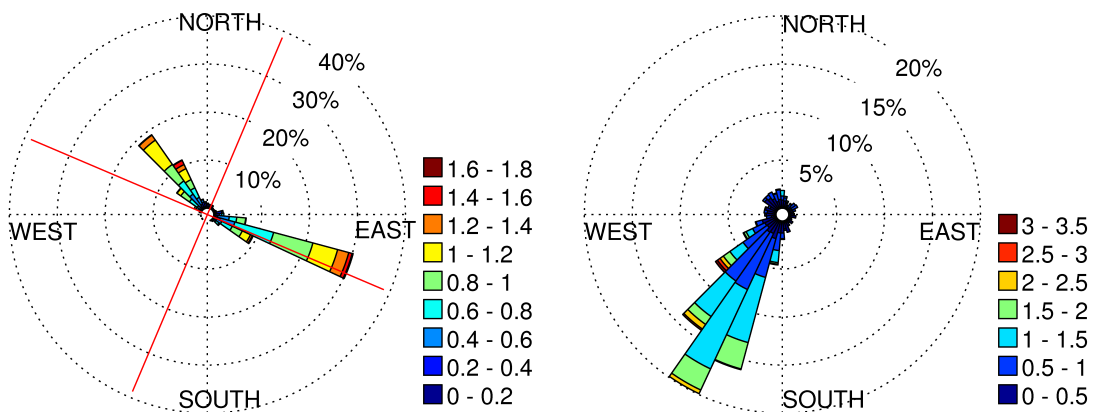


Figure 3.26: Wind roses for the LA 8th St building (left) and open (right) locations.

Figure 3.27 shows the comparison of the OSPM recirculation contribution model with the vertical concentration difference at the building and open sections of 8th St on May 9th, 2014. The rooftop value of the standard deviation of vertical velocity fluctuations, the required meteorological input variable in equation (3.6), is equal to 0.1 of the rooftop wind speed as specified in the standard OSPM formulation. The concentration has been normalized by the emission rate calculated by assuming a constant UFP emission factor of  $10^{14} \text{ veh}^{-1} \text{ km}^{-1}$ , equal to the order of magnitude of UFP emission factors under real world driving conditions (Ketzler et al., 2003).

The building section shows some correlation between the data, while the open section shows no correlation. This is expected because the street canyon model predicts that there is no vortex flow at the open section, and thus the recirculating contribution should be zero. The magnitude of the vertical concentration difference indicates that the emission factor is near  $6.5 \times 10^{14} \text{ veh}^{-1} \text{ km}^{-1}$ , about four times larger than expected based on previous emission estimates (Ketzler et al., 2003). There is only a very weak correlation between model estimates and observations.

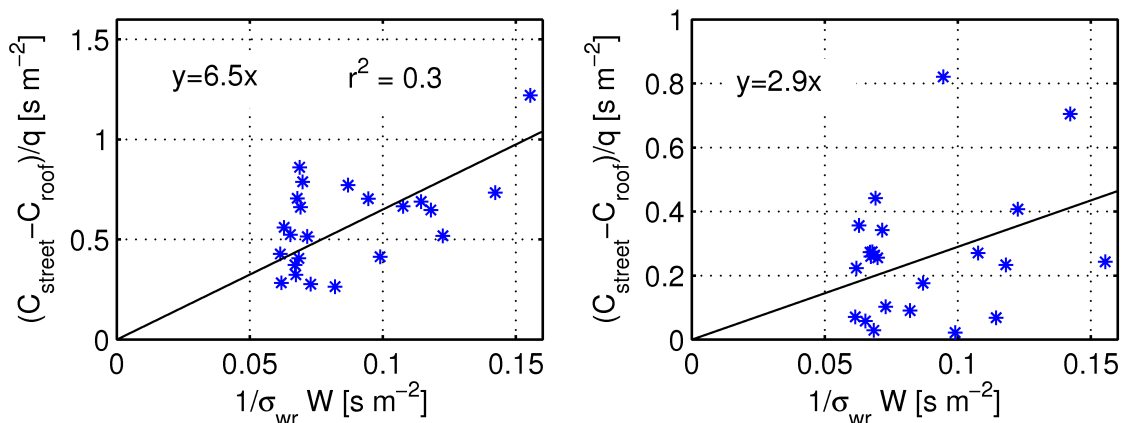


Figure 3.27: Evaluation of OSPM recirculating contribution model with data collected on 8th St, LA. The comparison with building section data is on the left and that with open section data is on right. The concentration has been normalized by the 30 minute average emission rate assuming an emission factor of  $10^{14} \text{ veh}^{-1} \text{ km}^{-1}$ .

The UFP emission rate could be extremely variable under real world congested urban driving conditions (Smit et al., 2010). This is because acceleration and deceleration result in significantly different emissions than those during free flow constant speed driving. We have assumed that the emission rate is proportional to traffic flow rate by a constant factor, but this model may not yield adequate emission estimates in view of the large uncertainty in estimating emissions in urban driving conditions. Figure 3.28 shows the same comparison as the previous figure, except the emission rate used to normalize the concentration is the daily average value rather than that based on the 30 minute traffic count. The figure shows a better correlation between model and observation than the previous comparison, indicating that the UFP emission rate is not proportional to the local traffic flow rate.

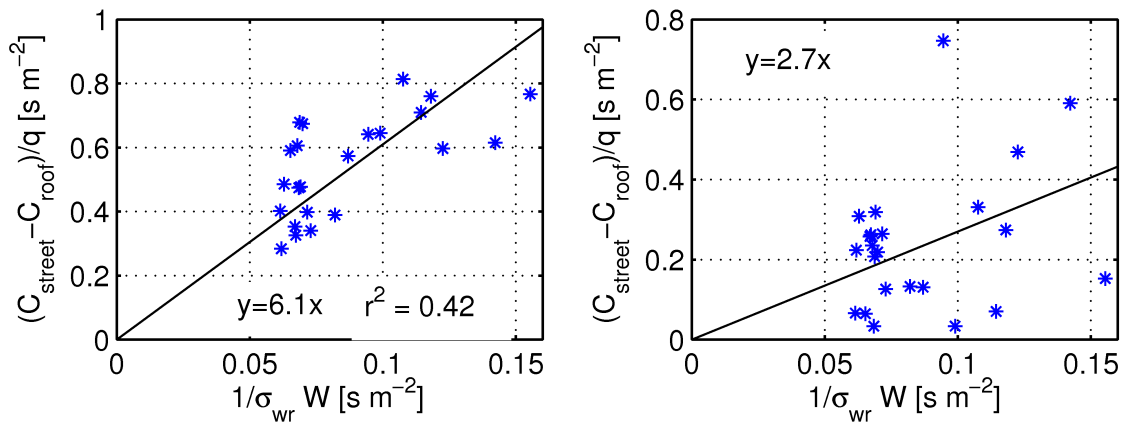


Figure 3.28: Evaluation of OSPM recirculating contribution model with data collected on 8th St, LA. The comparison with building section data is on the left and that with open section data is on right. The concentration has been normalized by the daily average emission rate assuming an emission factor of  $10^{14} veh^{-1} km^{-1}$ .

It is surprising that the local UFP emission rate is not related to the traffic flow rate. This indicates that the effects of stop and go traffic under urban driving conditions significantly alters emissions. Another explanation is that emissions from surrounding

streets influence the local UFP concentration. This makes sense because the time scale for material to be transported to the roof,  $\tau_{vert} \sim H^2/K$ , is on the order of minutes for the 50 m tall buildings next to 8th St. Thus, there is sufficient time for emissions from adjacent streets to be advected into the local street by the mean near surface wind before these emissions are mixed vertically through the urban canopy. If this is the case, the vertical transport model must characterize the average vertical concentration difference over a large area. The horizontal size of this area,  $L$ , can be determined by equating the vertical transport time scale with the horizontal transport time scale within the urban canopy,  $\tau_{horiz} \sim L/U_c$ , where  $U_c$  is the mean canopy wind speed, resulting in  $L \sim \frac{HU_c}{s_w}(1 + H/w)$ . For 8th St the horizontal length scale is about 300 m, equivalent to about three city blocks. Thus the emissions within the approximately three block area surrounding the field site influence the difference between the observed surface and rooftop concentrations.

Still, the area averaged traffic flow rate should have a similar trend with that recorded on 8th St, and thus the emission rate averaged over the three block area should be similar to that estimated using the traffic flow rate on 8th St. Thus we assume that urban driving conditions produce large uncertainty in emission rates and cause poor correlation of UFP emissions with local traffic counts. Throughout the rest of this section we use the daily average traffic with a constant emission factor rather than the 30 minute traffic counts to estimate UFP emissions.

We have so far evaluated the OSPM recirculating contribution model with observations at the 8th St field site. Comparison of the model with observations at other sites with different building morphology will indicate the usefulness of the model in estimating near road concentrations in cities with nonuniform building heights. Figure 3.29 shows a comparison of the OSPM recirculating contribution model with observations of the vertical

concentration difference at all sites in the Los Angeles field study where rooftop concentration measurements were made. The correlation between the model and observations is essentially zero. The OSPM recirculating contribution model tends to underestimate the concentration at the 7th and Broadway sites, and overestimates concentrations at the 8th St open site. There is also significant scatter of data measured at each site.

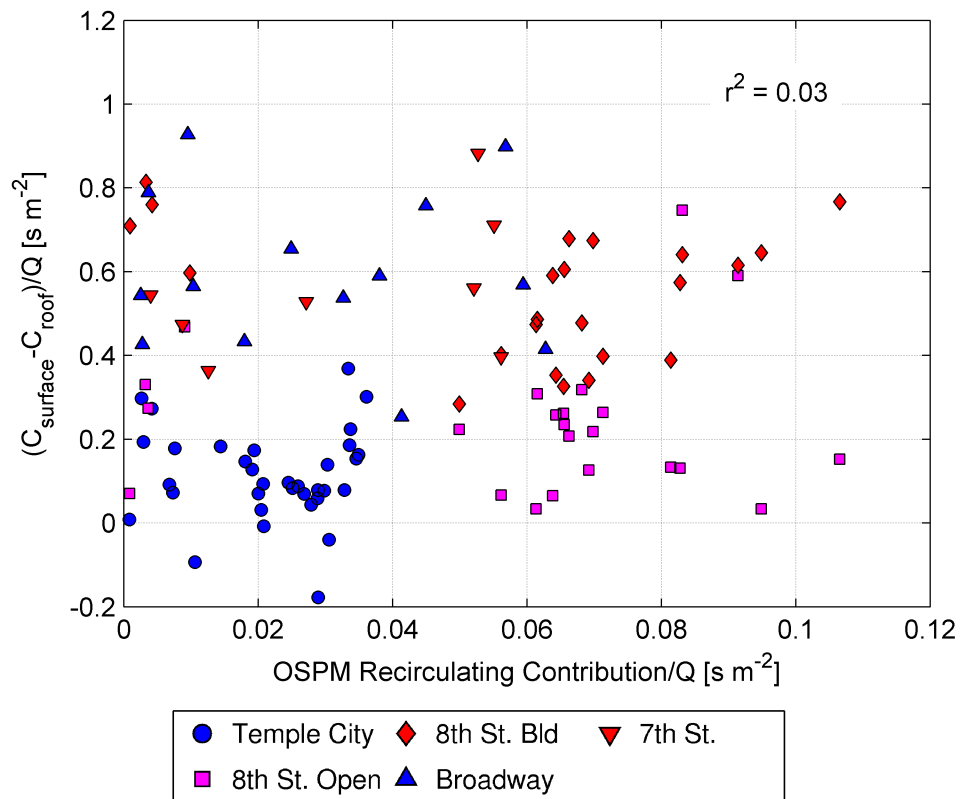


Figure 3.29: Evaluation of OSPM recirculating contribution model with data collected in the LA field study at 8th St, Temple City Blvd, Broadway, and Seventh St. The concentration has been normalized by the daily average emission rate assuming an emission factor of  $10^{14} \text{ veh}^{-1} \text{ km}^{-1}$ .

The OSPM recirculating contribution model is not adequate for estimating near road concentrations of vehicle emissions for the data collected in the Los Angeles field study.

We next describe the development of a semi-empirical dispersion model to address the issues in the OSPM formulation.

### 3.5.1 Vertical Dispersion Model

The OSPM formulation uses the rooftop wind speed as the primary meteorological input variable governing near road concentrations. However, the analysis of the data collected in Hannover, Germany, shown in section 3.3, showed that the model including only the standard deviation of vertical velocity fluctuations measured at a height of approximately half the building height performed the best at explaining the near road concentrations. This indicates that near road concentrations are governed by vertical turbulent pollutant transport within the street canyon. Thus, the next step in developing a model of the near road concentrations was to examine the role of vertical turbulent transport for the data collected in Los Angeles.

We derive a model for the vertical turbulent transport using the eddy diffusivity hypothesis. The flux of pollutants near the street surface is equated with the vertical turbulent pollutant flux:

$$K_z \frac{C_s - C_r}{H} \sim \frac{Q}{W} \quad (3.18)$$

where  $K_z$  is the vertical eddy diffusivity,  $H$  and  $W$  are the building height and street width,  $C_s$  is the horizontally averaged concentration in the street canyon,  $C_r$  is the rooftop (at  $H$ ) concentration, and  $Q$  is the emission rate per unit length of the street.

The eddy diffusivity is written as the product of the mixing length,  $l$ , and the standard deviation of vertical velocity fluctuations averaged over the height of the buildings,  $\sigma_w$ :

$$K_z = l\sigma_w \quad (3.19)$$

The vertical average  $\sigma_w$  is estimated from the measured surface  $\sigma_{ws}$  and roof  $\sigma_{wr}$  values through:

$$\frac{1}{\sigma_w} = \frac{1}{2} \left( \frac{1}{\sigma_{wr}} + \frac{1}{\sigma_{ws}} \right) \quad (3.20)$$

If we assume that the size of the large turbulent eddies dominating vertical mixing is limited by the smaller of the street width and building height, then the mixing length is proportional to the smaller of  $H$  and  $W$ :

$$l \sim \left( h_0 + \frac{HW}{H+W} \right) \quad (3.21)$$

where  $h_0$  is the mixing length associated with the initial vertical mixing caused by the motion of the vehicles, and  $\beta$  is an empirical constant included to calibrate the model. Equations (3.18) through (3.21) are combined to yield an expression for the surface concentration:

$$C_s = \frac{Q}{\beta\sigma_w W} \left( \frac{1 + a_r}{1 + \frac{h_0}{H}(1 + a_r)} \right) + C_r \quad (3.22)$$

where  $a_r = H/W$  is the aspect ratio. Equation (3.22) has the same form as equation (3.14), except for the aspect ratio term. Comparing the two equations, plugging in the building height and street width of Gottinger Str, and accounting for the best fit slope of equation (3.14) with observations determined in section 3.3, the value of  $\beta$  works out to be equal to 1.7. The parameter  $\beta$  combines the proportionality constants implied in equations (3.18) and (3.21).

If measurements of the rooftop concentration are not available,  $C_r$  can be estimated by assuming that local emissions are matched by vertical transport at roof level:

$$\gamma C_r W \sigma_{wr} = Q \quad (3.23)$$

where  $\gamma$  is an empirical constant used to calibrate the model. The value of  $\gamma$  is determined by fitting the model with observations in the Los Angeles study.

Substituting equation (3.23) into (3.22) yields:

$$C_s = \frac{Q}{\gamma \sigma_w W} \left[ 1 + \frac{\gamma \sigma_{wr}}{\beta \sigma_w} \frac{1 + a_r}{1 + \frac{h_0}{H}(1 + a_r)} \right] \quad (3.24)$$

Equations (3.22) and (3.24) are referred to as the vertical dispersion model (VDM). Equation (3.22) can be used if  $\sigma_w$  and  $C_r$  are known. In the field studies conducted in Los Angeles measurements at roof level were not available at several of the sites. Thus it was necessary to estimate  $\sigma_{wr}$  for use in equation (3.24).

We estimate  $\sigma_{wr}$  by assuming that turbulent kinetic energy produced at roof level, per unit length of street,  $u_{*r}^2 U_r W$ , is dissipated over the volume of the street:

$$u_{*r}^2 U_r W \sim \sigma_{wr}^3 W \sim \frac{\sigma_w^3}{l} W H \quad (3.25)$$

where  $l$  is the length scale of the large turbulent eddies within the canyon, and  $u_{*r}^2$  and  $U_r$  are the shear stress and the mean wind speed at roof level, both of which are correlated with  $\sigma_{wr}$ . If  $l$  is similar to the form given by equation (3.21), we can write the semi-empirical expression:

$$\sigma_{wr} = \sigma_w (1 + \eta a_r)^{1/3} \quad (3.26)$$

where  $\eta = 0.4$  provides the best fit with the data as shown in a later section. The ratio of rooftop and average  $\sigma_w$  is nearly constant because the  $1/3$  power in equation (3.26) results in low sensitivity to the aspect ratio.

At most of the field sites in Los Angeles the buildings lining these streets varied substantially in height. So the application of the dispersion model depended on defining an effective building height,  $H$ . We found that the following definition worked the best:

$$H = \frac{1}{L} \sum_i H_i B_i \quad (3.27)$$

where  $L$  is the street length,  $H_i$  and  $B_i$  are the height and width (along the street) of building  $i$ , and the sum is taken over all the buildings on one side of the street. Equation (3.27) can be interpreted as the area-weighted building height: the sum of the frontal area of the buildings divided by the street length. Then, the equivalent building height used in equation (3.22) is the average over both sides of the street.

We assume that the modelled concentration represents an average over the street canyon within one city block. For the effective building height to be consistent with the model, it is calculated from the geometry of all the buildings bordering the street canyon within one city block. The use of the block length for defining the scale for horizontal inhomogeneity is somewhat arbitrary, but the assumption of horizontal homogeneity within one city block has been used in models such as SIRANE (Soulhac et al., 2011), and comparisons with observations indicate that this is a useful assumption.

Figure 3.30 shows the evaluation of equation (3.22) with data collected at 8th St. Using the value of  $\beta = 1.7$  and accounting for the building height and street width terms in equation (3.22), the slope of 5.2 in the left panel of Figure 3.30 corresponds with a UFP emission factor of  $3.2 \times 10^{14} \text{ veh}^{-1} \text{ km}^{-1}$ , which is about twice the value

quoted by (Ketzel et al., 2003), and is more reasonable than the estimate of  $6.5 \times 10^{14} \text{ veh}^{-1} \text{ km}^{-1}$  derived from the evaluation of the OSPM recirculating contribution model. Since emission factors vary significantly depending on driving conditions this indicates that the concentration estimated using equation (3.22) has the correct order of magnitude. The vertical dispersion model has a good correlation with the vertical concentration difference and gives the right order of magnitude of the concentration.

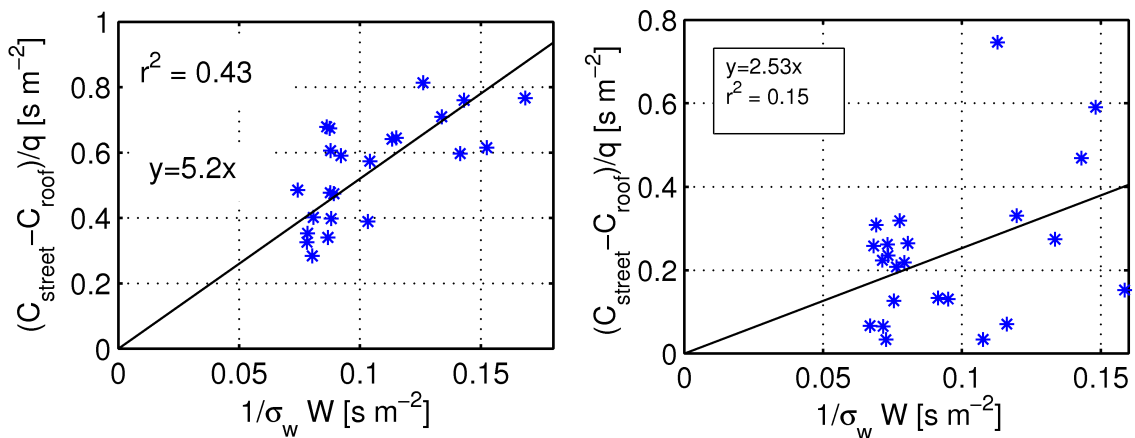


Figure 3.30: VDM model prediction compared with data in the LA 8th St building section (left) and open section (right). The concentration has been normalized by the daily average emission rate assuming an emission factor of  $10^{14} \text{ veh}^{-1} \text{ km}^{-1}$ .

We obtained building height and outline information from the Los Angeles Count GIS data portal (Los Angeles County, 2008), which we used to calculate the built environment parameters shown in Table 3.8 for the sites at which data was collected in the field studies.

Figure 3.31 shows the evaluation of equation (3.22) with the vertical concentration difference at all sites in the Los Angeles field study where rooftop concentration measurements were made. The VDM has less bias for the 7th St, Broadway, and 8th St open sites than the OSPM recirculating contribution model. The model underestimates

Table 3.8: Summary of area weighted building height, street width, and aspect ratio of all sites.

Site	Area weighted building height (m)	Street width (m)	Aspect ratio
8th St Building Section	43.25	20.0	2.16
8th St Mid Section	34.5	20.0	1.73
Broadway	35.90	26.0	1.38
7th St	45.80	25.0	1.83
Temple City	6.00	30.0	0.20
Wilshire Blvd Building	36.0	30	1.20
Wilshire Blvd Open	8.25	30	0.28

concentrations for the 8th St open site somewhat. Overall the comparison of the VDM with observations is good.

### 3.5.2 Evaluation of VDM With the Local Contribution

A limitation of the method used to evaluate the vertical dispersion model is that the rooftop concentration may be unknown. Moreover, the "open" sites have no well-defined rooftop concentration since there is no building height at which to measure the concentration. For this reason we developed an alternative method to analyze the data that does not rely on measurements of the roof concentration. Instead of using the vertical concentration difference to evaluate equation (3.22), we determine the contribution of local emissions to the total concentration observed at the surface monitors, and compare only this "local contribution" with equation (3.24).

The UFP concentration time series contains information about the local vehicle emissions in the form of large amplitude short lived spikes superimposed on the slowly varying

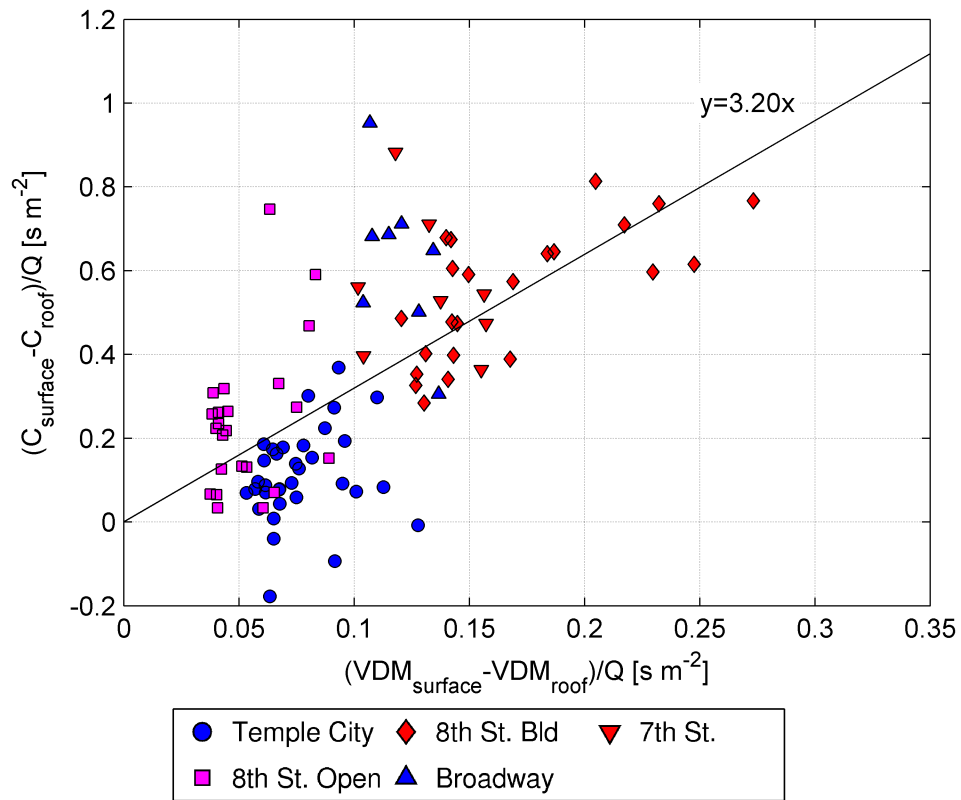


Figure 3.31: Evaluation of VDM model with data collected in the Los Angeles field studies. The concentration has been normalized by the daily average emission rate assuming an emission factor of  $10^{14} \text{ veh}^{-1} \text{ km}^{-1}$ .

baseline. This occurs because the UFP emission factor varies by several orders of magnitude, and so local emission events from high emitting vehicles produce large concentration spikes that can be separated from the total concentration. We filter the signal to separate the slowly varying component from the spikes, which contain information about local emissions. A moving average filter with a window size larger than the time scale of the spikes does not adequately separate the two components because the concentration distribution is highly skewed, making the average an inadequate measure of the baseline concentration. Instead of the moving average, we use a windowed percentile to separate the components. We define the baseline as the concentration that is below a chosen

percentile of the concentration distribution. Then, within each time window of a chosen length, each data point is classified as either baseline or spike if the concentration is below or above the percentile cutoff of the window. The baseline is then constructed by linearly interpolating between the points that are classified as baseline, and the spikes are separated by subtracting the baseline from the total. This type of analysis is common for analysing UFP time series, especially in analysis of mobile monitoring data Bukowiecki et al. (2002).

Figure 3.32 shows the result of this procedure with the baseline at the 10th percentile for several hours of data collected in 8th St on May 9th, 2014. The window size is taken to be 10 minutes, since the window size should be larger than the length of time the spikes last, which is about 1 minute. This procedure shows a good separation of the peak and baseline concentrations.

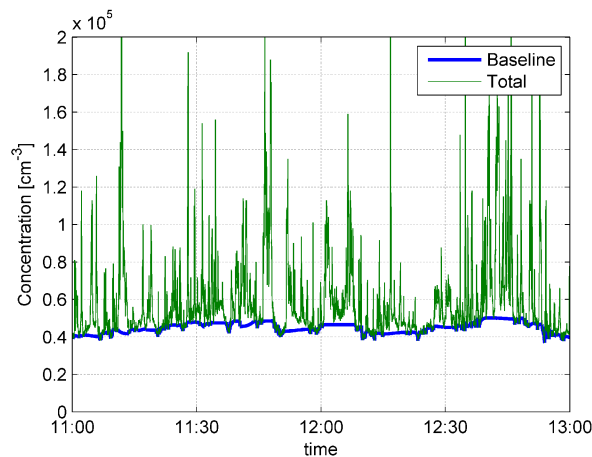


Figure 3.32: Baseline and total concentration.

A windows size of 10 minutes results in an adequate separation of the concentration signals, but can be considered to be somewhat arbitrary. We calculated the 30 minute average of the baseline concentration for window sizes of 5, 10, and 15 minutes, and found

no significant difference in the results. This is shown in Figure 3.33 for data collected at 8th St. The cutoff percentile is also a somewhat arbitrary choice, so we chose different cutoff percentiles and compared the resulting 30 minute average baselines. Figure 3.34 shows that the baseline is affected by the choice of cutoff, with larger cutoffs producing larger baselines. The spikes are also sensitive to the choice of cutoff. However, this does not affect the analysis significantly because different cutoffs only result in a shift of the concentrations by a constant amount. The important feature of this procedure is that it removes the variability caused by variation in the baseline.

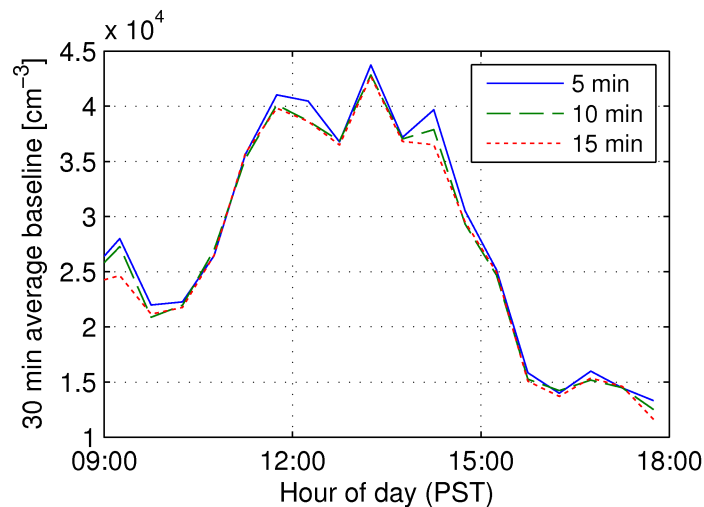


Figure 3.33: Sensitivity of calculated baseline to window size.

The VDM was applied to the data from the field studies using the best fit parameters  $h_0 = 2m$ ,  $\gamma = 5.3$ , and  $\beta = 1.7$ . The value of  $\beta$  corresponds with the value determined from the best fit of equation (3.14) to the Gottinger Str data. The value of  $\gamma$  was determined by matching the observed and modelled concentrations from the Los Angeles data. Figure 3.35 indicates that the model provides a good description of the measured

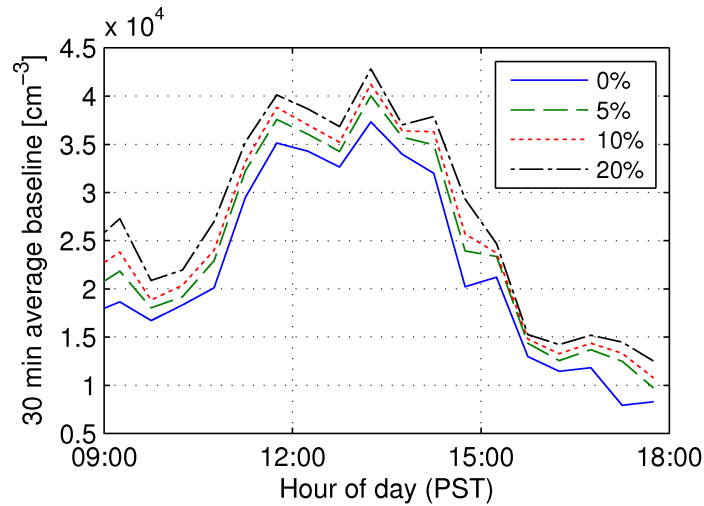


Figure 3.34: Sensitivity of calculated baseline to cutoff percentile.

local contributions of UFP at most of the sites. This implies that local contributions are primarily governed by the ratio of equivalent building height to street width and the standard deviation of the vertical velocity fluctuations. The slope of the fit line is consistent with an emission factor of  $3 \times 10^{14} \text{ veh}^{-1} \text{ km}^{-1}$ . This value is within the range reported by (Ketzler et al., 2003).

The observed local contribution at the 8th St open site is much larger than that predicted by the model. We suspect that the measurements are affected by emissions from the adjoining parking lot and building areas that we have not accounted for. The emissions must be approximately 5 times larger than we have estimated based on the traffic flow rate on 8th St to account for the model underestimation.

If emissions from adjacent streets influence the concentration at the open site, then it follows that the VDM represents the concentration averaged over an area larger than a single street, and the effective building height for the open site should encompass the buildings within a larger area than the region directly adjacent to the street. However,

the definition of effective building height is somewhat arbitrary and it is not clear how the building height should be defined for the open area.

Figure 3.36 shows the comparison of the VDM with observations except that the building height of the 8th St open section has been changed from 0 to the value of the 8th St building section area weighted building height. The figure shows that the model has almost no bias for the 8th St open site using this building height. Thus the model underestimation for the open site is likely due to underestimation of the effective building height.

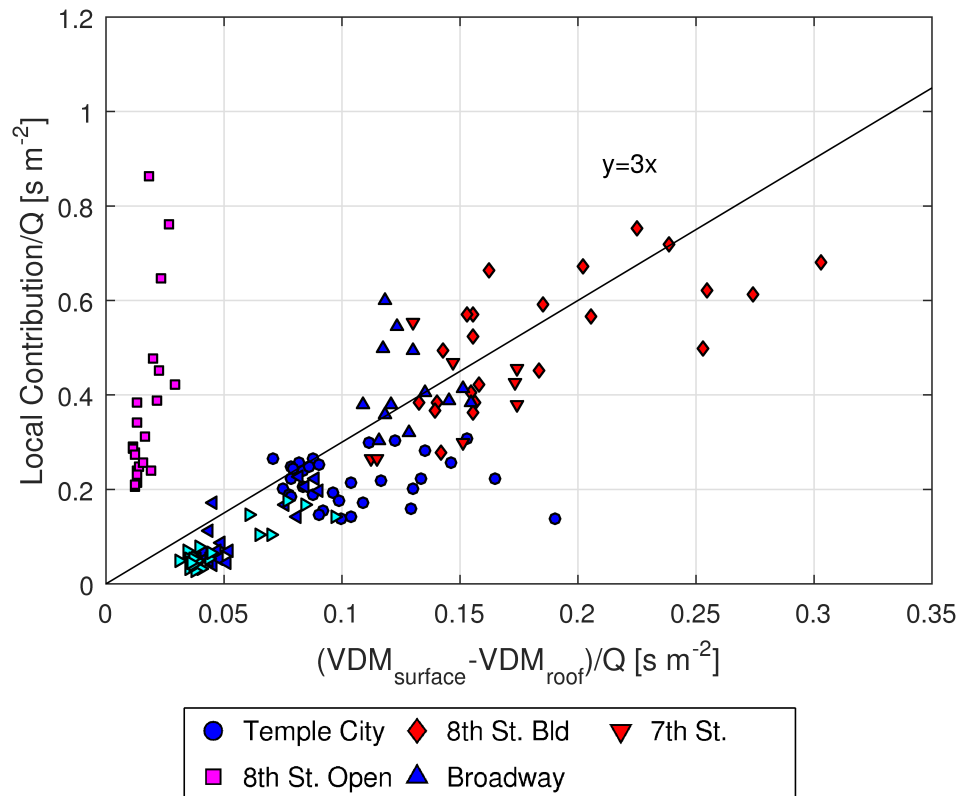


Figure 3.35: Comparison of vertical dispersion model with 30 minute averaged local contribution. Concentration is normalized by daily average emission rate, assuming an emission factor of  $10^{14} \text{ veh}^{-1} \text{ km}^{-1}$ .

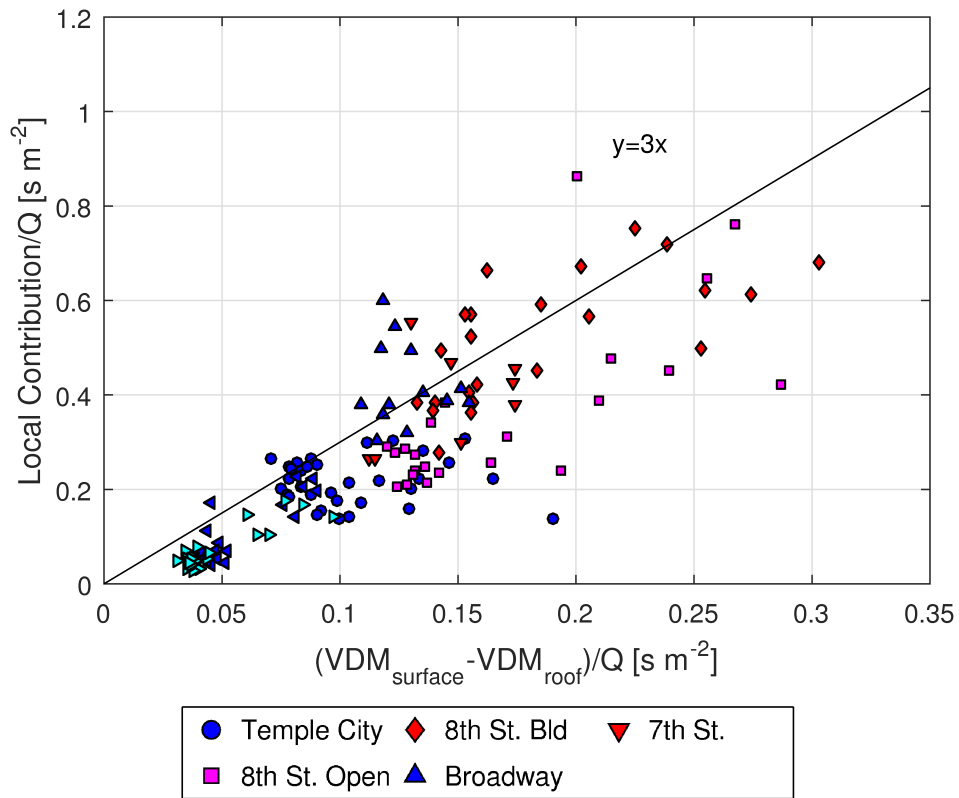


Figure 3.36: Comparison of vertical dispersion model with 30 minute averaged local contribution. Concentration is normalized by daily average emission rate, assuming an emission factor of  $10^{14} \text{ veh}^{-1} \text{ km}^{-1}$ . The building height of the 8th St open section has been set equal to that of the 8th St building section.

### 3.5.3 Discussion

Our analysis of data from field studies conducted in urban areas suggests that vertical mixing governs near surface concentrations within the urban canopy. This conclusion is supported by observations analysed in (Hanna et al., 2014), which show that data from field studies conducted in Manhattan, NY, indicate rapid vertical mixing in the presence of buildings.

We show that modeling the air quality impact of vehicular emissions reduces to estimating the effective aspect ratio of the street, and the roof level  $\sigma_w$ . The effective aspect

ratio plays the major role in magnifying concentrations relative to those that would have been measured in the absence of buildings.

Concentrations are relatively insensitive to the mean wind speed at the rooftop or surface. Evaluation of the OSPM recirculating contribution model, which uses the mean rooftop wind speed as the primary meteorological variable governing near road concentrations, shows no correlation between model estimates and observations at the various field sites in the Los Angeles study. This supports the conclusion that vertical turbulent transport rather than advection by the mean wind dominates dispersion in cities.

We have shown that urban areas with significant building height variability can be characterized for dispersion applications by the mean street width and the area weighted building height.

In this analysis we have used data from seven different field sites to evaluate the performance of the model. However, the amount of data collected at each field site was limited to only about eight hours per study day, and measurements were only repeated for a few days at each site. Thus it is desirable to evaluate the VDM with much more data. The next section describes field measurements conducted in Riverside, CA over a period of about a month. The data is used to provide further evaluation of the performance of the VDM.

### **3.6 Evaluation of Vertical Dispersion Model with Measurements in Riverside**

The goal of the work in this chapter is to extend the evaluation of the VDM beyond what has been done with the Los Angeles study described in chapter 3.5. This is done

for several reasons. First, the original analysis used only about 40 hours of concentration data collected at seven urban sites. Ideally we would make measurements for a much longer time period with varying meteorological conditions to better determine the effect of meteorological variables such as wind speed and vertical turbulent velocity on dispersion. The original study also showed significant scatter among the data points that may be removed by using longer time averages or by combining data with similar meteorological conditions. Second, the aspect ratios of the field sites investigated in the Los Angeles study are mostly greater than 1.2 or less than 0.3. Evaluation of the model with additional data at sites with intermediate aspect ratios would be extremely useful to better understand the effect on concentration magnification of the street aspect ratio, which primarily determines the magnification in the VDM. Finally, the study relied on measurements of ultrafine particle concentrations, the emissions of which are highly uncertain. The uncertainty in emission rates hindered model evaluation so one of the goals in this work is to evaluate the model with concentration data of a pollutant with well known emission factor, such as carbon monoxide or  $NO_x$ . It is hoped that this will allow better calibration of the empirical constants within the VDM.

To meet these goals, measurements of near-road concentrations along with the meteorology used as inputs to the VDM and traffic counts were measured in an urban area in Riverside, CA. The data was used to evaluate the performance of the VDM and to examine the effect of the governing variables on near-road concentrations. The measurements are described in section 3.6.1.

### **3.6.1 Description of Field Measurements in Riverside, CA**

The VDM model equations are derived in section 3.5. The VDM relates the concentration averaged over a street,  $C$ , with the standard deviation of vertical velocity fluctuations,

$\sigma_w$ , area-weighted building height,  $H$ , defined in section 3.5, and street width,  $W$ , through equation (3.22). The rooftop concentration can be determined using equation (3.23). The VDM model predicted concentration is sensitive to the street aspect ratio,  $a_r = H/W$  and the vertical average  $\sigma_w$  within the street,  $\overline{\sigma_w} = 2(1/\sigma_{wr} + 1/\sigma_{ws})^{-1}$ . The average is related to the rooftop value through equation (3.26).

The value of the two empirical constants in the model equations,  $\beta$  and  $\gamma$ , were determined to have values of 1.7 and 5.3, respectively, based on the Los Angeles field study and the data collected in Göttinger Strasse, Hannover. More details about the model calibration are found in section 3.5.

Equations (3.22), (3.23), and (3.26) show that the primary variables controlling the near-road concentrations are the area-weighted building height, street width, and the rooftop and surface  $\sigma_w$ . However, measurements of  $\sigma_w$  are not usually available at a given site, and most meteorological measurements are made in rural areas. Because of this the VDM is associated with a model that can predict the values of the rooftop, and urban surface  $\sigma_w$  through (3.26), from meteorological measurements made at an upwind rural area. The field study was designed to measure near-road concentrations within an urban area along with the input variables for the VDM given above and the meteorology at an upwind rural location.

As in the previous study conducted in Los Angeles, concentration measurements were made next to a busy road at two locations, one with tall buildings next to the road and one several blocks away with only short buildings next to the road. A site next to Market St in Riverside, CA was chosen to meet the requirements of the study. Figure 3.37 shows an overview of the site. The "building" section has an area weighted building height (equation (3.27)) of 14.37 m and a street width of 33 m, resulting in an aspect ratio of

0.44. The "open" section has area weighted building height of 2.14 m and street width of 30 m. The traffic on Market St is about 26000 vehicles per day.

Figure 3.37 and table 3.9 show the locations of the instruments that were used in the study. Campbell scientific CSAT3 sonic anemometers were used to measure the three components of wind speed and temperature at 10 Hz at both the building and open sites and on the roof of city hall, approximately 100 m from the building site. One additional sonic anemometer was placed at Riverside airport, about 7.8 km southwest of the "building" section. This anemometer was included to evaluate a model of the evolution of wind speed and turbulence from an upwind rural area to the urban area. The resulting turbulence data was processed to yield time average wind speeds, wind direction, turbulent velocities, and heat and momentum fluxes. The micrometeorological measurements were made continuously between July 30 and September 9, 2015.

Concentrations of ultrafine particles were measured using TSI 3022A condensation particle counters between about 7 am and 7 pm on 15 days in August and September, 2015, resulting in a total of about 150 hours of particle concentration data. Continuous measurements could not be made because the instruments were powered by batteries that needed to be recharged during the night. A total of five particle counters were used: one on each side of Market St at both the building and open sites and one on the city hall roof. The instruments provided 1-second average concentrations. The ultrafine particle concentration data was processed to yield the contribution of local vehicle traffic using the method described in 3.5.2.

Measurements of carbon monoxide (CO), nitrogen oxides (NO and NO<sub>2</sub>), ozone O<sub>3</sub>, and sulfur dioxide SO<sub>2</sub> were made using AQMesh five gas pollutant monitor "pods" between August 18 and September 9, 2015. The pods are ideally suited for long term measurements of concentrations of vehicle emissions. They use much less power than

the CPCs, the integrated battery holds enough charge to function for the entire study, enabling continuous concentration measurements. Three pods were used: one on each side of Market St at the "building" section, and one on the rooftop. Averaging time for the AQMesh monitors was 1 minute, and data was later aggregated into 60 minute averages for analysis. Only the carbon monoxide data was analyzed in this paper.

Street level instruments were mounted to the light pole nearest to the locations shown in figure 3.37. Sonic anemometers and AQMesh pods were mounted at a height of 4 m above ground level (AGL). CPCs mounted to light poles have inlets at a height of 1 m AGL. The rooftop sonic anemometer and AQMesh pod were attached to a tripod 3 m and 2m above the 25 m tall roof of city hall, respectively. The rooftop CPC inlet is 0.5 m above the rooftop.

Video of Market St was recorded during the particle concentration measurements, and traffic counts, separated into subgroups of passenger cars and large trucks were made from the video.

The resulting dataset was used to compare VDM estimates with observed concentrations of ultrafine particles and carbon monoxide. The micrometeorological measurements at the urban rooftop, surface, and at the airport were compared with an internal boundary layer (IBL) model (Garratt, 1990) which can be used to predict urban micrometeorology from upwind rural values, and with the micrometeorological models in (Schulte et al., 2015) that relate rural, rooftop, and surface  $\sigma_w$ .

Evaluation of the IBL model requires knowledge of the surface roughness length and displacement height of the urban area. These parameters can be determined using methods such as those of MacDonald et al. (1998), which relate the surface friction velocity and displacement height with the average building height,  $\overline{H}$ , of the urban area, and the

Table 3.9: Instrument Locations in May 2015 Riverside, CA field study.

Location	Latitude	Longitude	Instruments
West side of Market St between University Ave and Mission Inn Ave	33.982783	-117.375697	CPC 498, AQMesh 101, Sonic Anemometer
East side of Market St between University Ave and Mission Inn Ave	33.982815	-117.375362	CPC 481, AQMesh 103
West and side of Market St between 11th and 12th St	33.979262	-117.378055	CPC 497, Camera, Sonic anemometer
East side of Market St between 11th and 12th St	33.979302	-117.377717	CPC 504
Rooftop (25 m tall)	33.980874	-117.375699	CPC 499, AQMesh 104, Sonic Anemometer

plan,  $\lambda_p$  and frontal,  $\lambda_f$  area densities, the ratio of total plan and frontal area of the buildings, respectively, to the total lot area of the urban center. We characterized the height and outline of the buildings within a 500 m radius buffer zone around the urban field site and processed the data to yield the average building height and plan and frontal area densities. The method of MacDonald et al. (1998) was then used to determine the surface roughness length,  $z_0$  and displacement height,  $d$ . These parameters are summarized in table 3.10.

Table 3.10: Parameters of the urban field site in Riverside, CA.

Parameter	Value
$\bar{H}$	8.3 m
$\lambda_p$	0.27
$\lambda_f$	0.1
$z_0$	0.664 m
$d$	4.25 m

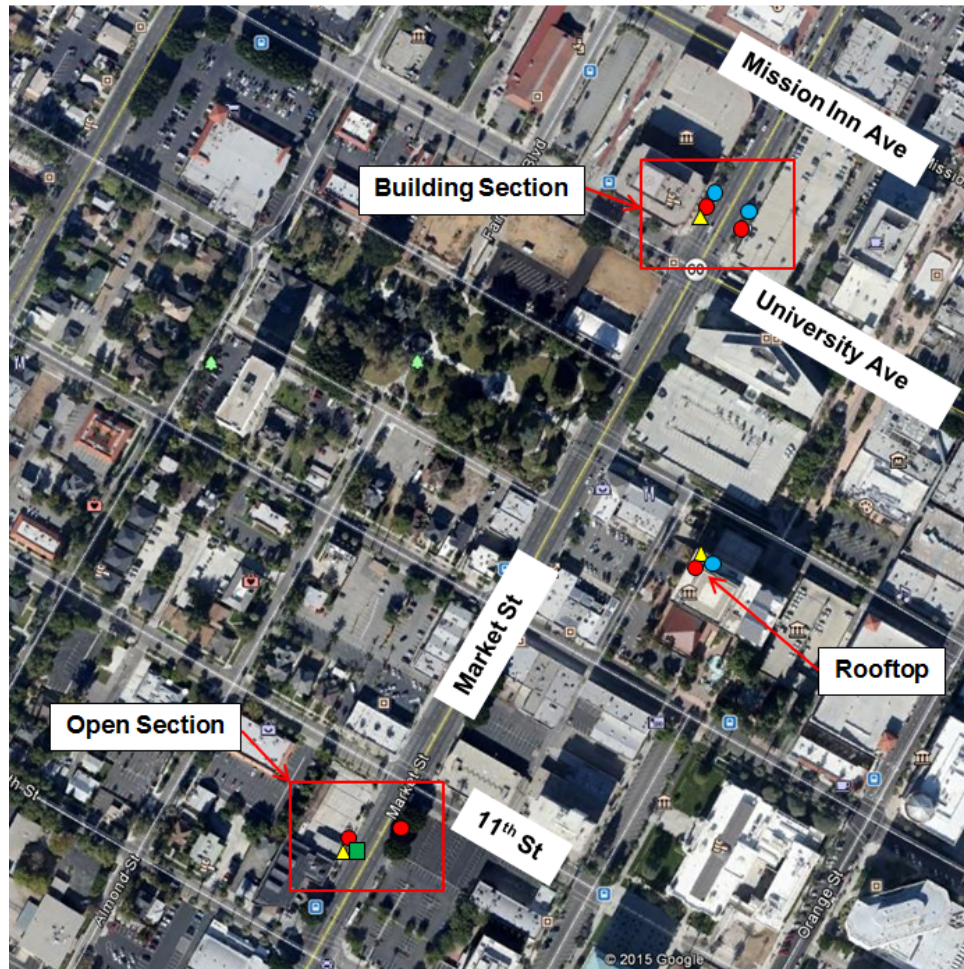


Figure 3.37: Location of instruments in May 2015 Riverside, CA field study. ● - Condensation Particle Counter (CPC) - AQMesh. ▲ - Sonic Anemometer. ■ - Camera. Map Data: Google

Prior to locating the AQMesh pods at the field site, they were co-located near the Riverside Rubidoux regional monitoring station operated by the South Coast Air Quality Management District. Further information about the site is available from CARB (CARB, 2015a). Co-located 1 minute average concentrations of  $NO$ ,  $NO_2$ ,  $O_3$ , and  $SO_2$  were made between August 6 and August 17, 2015. The 60 minute average  $CO$  concentration data was used to calibrate the AQMesh measurements. Several models were used to

perform the calibration. Initially a linear model was used to relate the concentration of one of the AQMesh pods with that of the regional station:

$$CO_{RivMag} = c_1 + c_2 CO_{101} + \epsilon \quad (3.28)$$

where  $CO$  and  $CO_{101}$  are the regional station and AQMesh pod 101 carbon monoxide concentrations, respectively,  $c_1$  and  $c_2$  are regression model constants, and  $\epsilon$  is the random error.

The residuals between observations and estimates of Equation (3.28), shown in Figure 3.38, contained a diurnal trend that needed to be removed to improve evaluation of the VDM. Because of this another model that included the temperature and rate of change of temperature was developed. The rate of change of temperature is represented using the finite difference  $\frac{dT}{dt} = \frac{T(t+\Delta t) - T(t)}{\Delta t}$ , where  $T$  is the temperature,  $t$  is the time, and  $\Delta t$  is the averaging time, resulting in:

$$CO_{101}(t) = c_1 + (c_2 + c_3 T(t)) CO_{RivMag}(t) + c_4 T(t) + c_5 T(t + \Delta t) + \epsilon \quad (3.29)$$

where  $c_1$  through  $c_5$  are regression model constants.

It is likely that the rate of change of temperature is a proxy variable for an unknown factor with similar diurnal variation, since there is no apparent reason for the rate of change of temperature to influence the measured concentration. The  $CO$  electrochemical cell is sensitive to other gas species, such as  $H_2$ ; diurnal variation in the concentration of these species may cause the trend in the residuals of (3.28). The residuals of (3.29) shows less trend with hour of day (Figure 3.38) or other important variables such as temperature. A similar model was used to calibrate the other two pods relative to pod 101. The RMS

error for AQMesh pod number 101 was 56 ppb, and the error in the calibration between pod 101 and pods 103 and 104 was 26 and 28 ppb, respectively. The errors are small enough to resolve the difference between the surface and rooftop concentrations of local vehicle emissions, which is on the order of 100 ppb. Thus, these errors are acceptable for evaluation of the VDM.

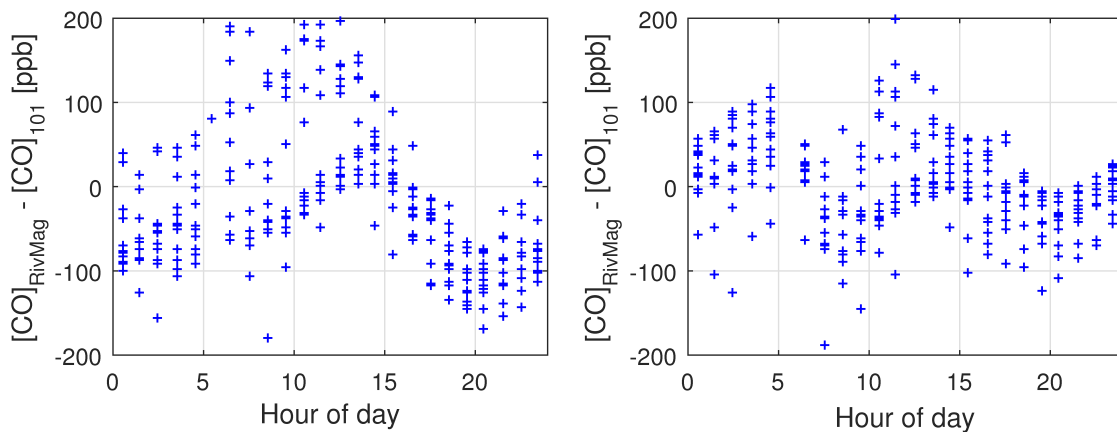


Figure 3.38: Residuals of AQMesh calibration models 1 (left) and 3 (right) vs hour of day.

Traffic counts taken on August 31 and September 3 and 4, 2015 were used to derive an empirical function describing the variation of traffic flow rate with time of day. The resulting daily variation in traffic, assumed to be the same for all measurement days, is shown in Figure 3.39. The flow rate of heavy duty vehicles is taken to be 5% of the light duty vehicles. Note that traffic counts were only taken between 7 am and 7 pm.

We next describe the results of the evaluation of the VDM with the observed concentrations of ultrafine particles and  $CO$ . The model is first calibrated using estimates of the  $CO$  emission factor. Next the performance of the model is evaluated and the hypothesis that dispersion is primarily determined by vertical turbulent transport is investigated.

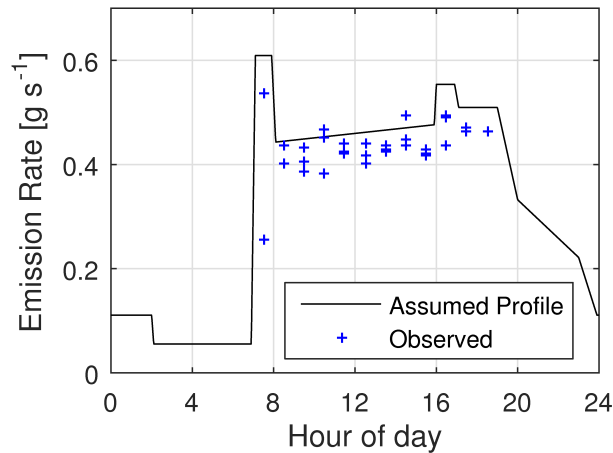


Figure 3.39: Assumed daily variation of vehicle traffic. Observed traffic flow rate for August 31 and September 3 and 4 are also shown.

### 3.6.2 Evaluation of the Vertical Dispersion Model

CO concentrations from the Riverside field measurements were used to calibrate the VDM. To carry out the calibration, model estimates of the vertical difference,  $C - C_{roof}$ , of the concentration were compared with the corresponding observed 2-hour averaged carbon monoxide concentrations. For the observations the surface concentration is the average of the concentration on the two sides of the street. An emission factor of  $1.5 \text{ g km}^{-1}$  for light duty vehicles was determined using EMFAC2011-LDV (CARB, 2015b). A value of  $15 \text{ g km}^{-1}$  was chosen for heavy duty vehicles.

Fitting the constant in (3.22) with observations resulted in a value of  $\beta = 0.43$ , 75% smaller than the value of 1.7 derived from the comparison of the model with concentrations of  $NO_x$  in Göttinger Str and UFP in Los Angeles(3.5). This implies that the emission factor of  $NO_x$  was overestimated for the Göttinger Str data, or the emission factor of CO was underestimated in the present study. A review of emission models found that CO and  $NO_x$  emission estimates are mostly within a factor of three and two, respectively, of observations (Smit et al., 2010). Emission models also tended to overestimate  $NO_x$

emissions (Smit et al., 2010). Due to the relatively large uncertainty in the emission estimates, our best estimate for  $\beta$  is that it lies in the range 0.85 - 1.3, the lower and upper limits being constrained by the likely uncertainty in the  $NO_x$  and CO emission factors, respectively. In this study we take the center of this range and set values of  $\beta = 1.0$  and  $\gamma = 3.1$ . The emission factor for CO that is consistent with these values is  $3.3 \text{ g km}^{-1}$  for light duty vehicles, about twice as large as the EMFAC predictions but within the factor of three interval that describes the likely variation of emission factors. Taking  $\beta = 1.0$  indicates that the emission factor of UFP in the Los Angeles measurements was  $1.76 \times 10^{14} \text{ veh}^{-1} \text{ km}^{-1}$ .

Figure 3.40 shows the comparison of the observed vertical difference of carbon monoxide concentrations with VDM predictions. Values where the vertical difference was less than or equal to  $2 \text{ } [\mu\text{g m}^{-3}]$ , about 10% of the data, were removed from the comparison. These values mostly occur during nighttime and early morning when the traffic flow rate is very low. Data on the traffic flow rate during night and early morning was not available in this study. Model estimates are determined using emission factors of  $3.3 \text{ g km}^{-1}$  for light duty vehicles and  $33 \text{ g km}^{-1}$  for heavy duty vehicles.

The performance of the model is expressed quantitatively by the geometric mean,  $m_g$ , and geometric standard deviation,  $s_g$ , of the residuals between the observations and predictions, by the fraction of data points that are within a factor of two of the observations,  $fact2$ , and by the correlation coefficient between the data,  $r^2$ . An  $m_g$  of 1 indicates zero model bias. The interval that contains 95% of the ratios of observed to predicted concentrations is approximately given by  $[m_g s_g^{-2} \text{ } m_g s_g^2]$ .

There is significant scatter between the observations and model estimates, indicated by the low correlation coefficient. However, 74% of the data are within a factor of two

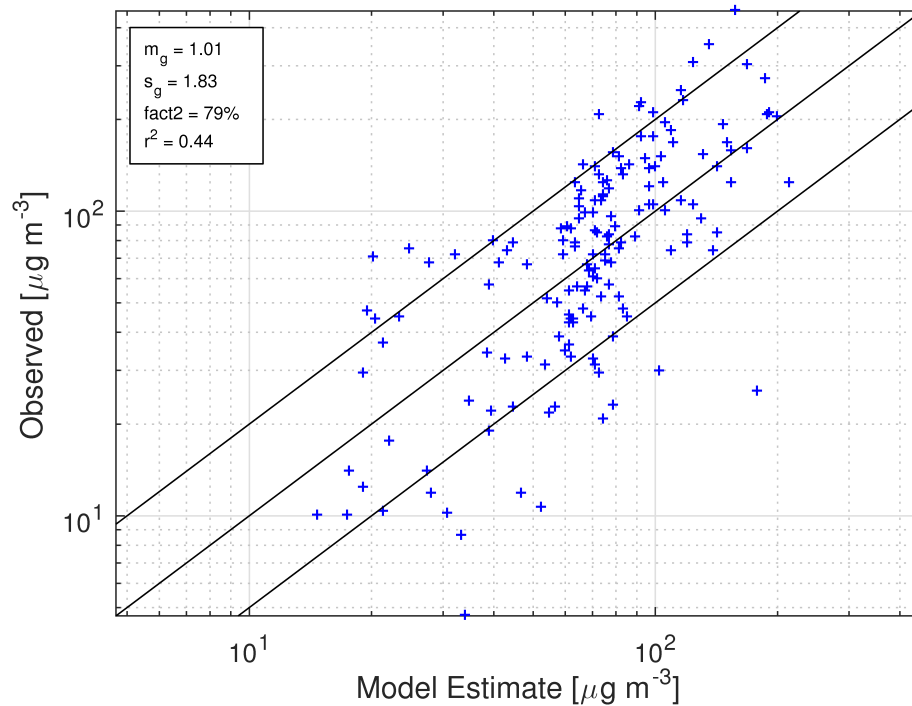


Figure 3.40: Comparison of Vertical Dispersion Model with vertical difference of 1-hour average carbon monoxide concentrations in Riverside, CA. Observations are normalized by the emission rate assuming an emission factor of  $3.3 \text{ g km}^{-1}$  for light duty vehicles and  $33 \text{ g km}^{-1}$  for heavy duty vehicles.

of model estimates. This indicates that the model performance is good, since dispersion models are considered to perform well when most of the data is within a factor of two of model estimates. Most of the discrepancy between observations and model estimates is due to cases where the observed vertical difference is small compared with model estimates. This usually occurs during night and early morning between about 1:00 am to 7:00 am, when the traffic flow rate and hence the emission rate is very small. We do not have a good estimate of the actual traffic flow rate during this time period. In particular, the comparison is somewhat sensitive to the assumption of when the morning rush hour traffic begins, since this determines the time of the morning spike in concentration.

There is little model bias since we derived the emission factor from the comparison of model with observations. The value of  $s_g$  indicates that 95% of the observations are within a factor of about 3.3 of the model estimates.

Figure 3.41 shows the variation of observations and model predictions with surface wind speed, rooftop  $\sigma_{wr}$ , and the wind direction relative to the normal direction to the street. Mean values were determined within five bins of equal width. For the wind direction, the bins were  $45^\circ$  sectors. A bootstrap method (Hanna, 1989) was applied to the observations within each bin to derive 95% confidence intervals for the mean values. For the bootstrap, 1000 resamples of the data were taken, the mean of each resample was calculated, and the confidence intervals were derived directly from the distribution of the means.

The data clearly shows that the model reproduces the variation of the observations with both  $\sigma_{wr}$  and surface wind speed. This indicates that the model adequately accounts for the variation of the meteorological variables. Since  $\sigma_{wr}$  is the only model input variable, this provides evidence that  $\sigma_{wr}$  governs dispersion in urban areas. The variation of concentrations with wind direction is also explained by the model. Concentrations tend to be largest when the wind is at  $135^\circ$  relative to the road normal, which occurs during nighttime when  $\sigma_{wr}$  is small.

Figure 3.42 shows the comparison of 1-hour averaged local contributions of ultrafine particles, normalized by emission rate, with predictions of the VDM. The model predictions are generated using the value of  $\sigma_w$  measured on the rooftop to estimate the surface  $\sigma_w$  model input. This yields better model predictions than using the measured surface  $\sigma_w$  directly.

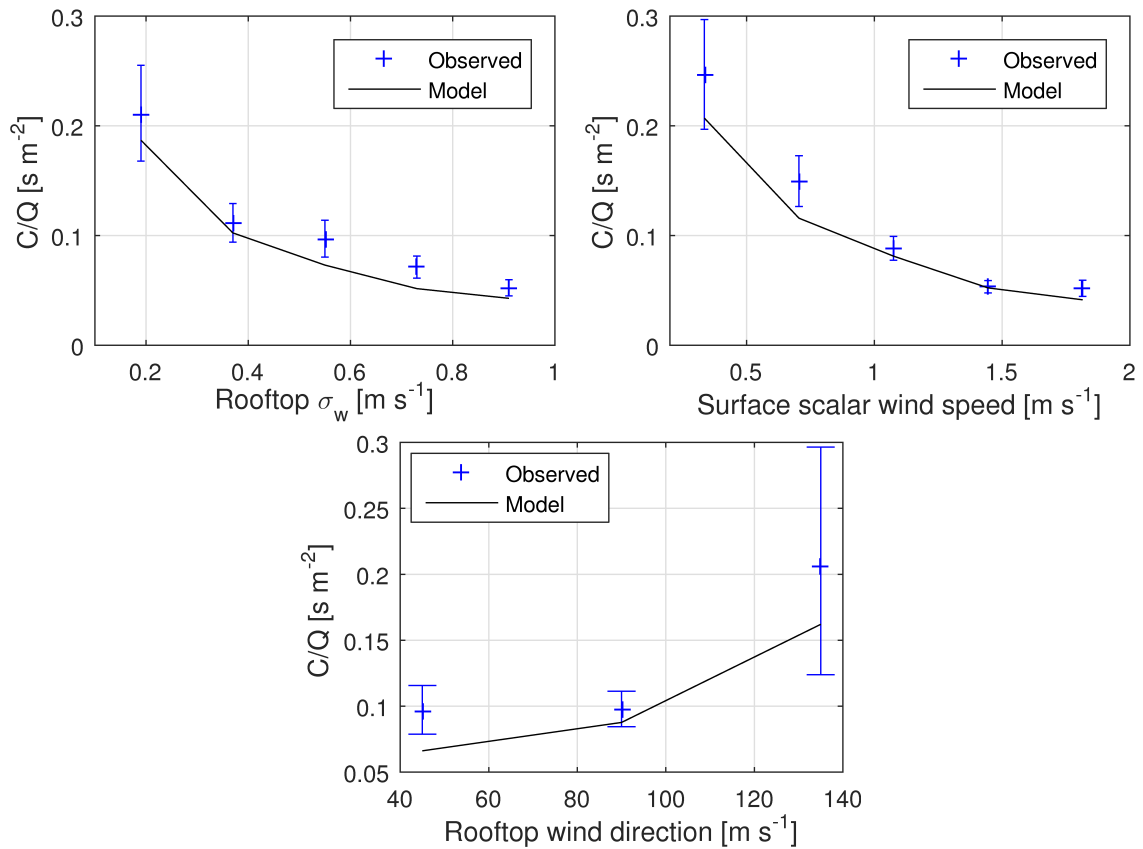


Figure 3.41: Variation of vertical difference of 2-hour average carbon monoxide concentrations with the rooftop  $\sigma_w$  (top left), the surface scalar wind speed (top right), and the wind direction relative to the normal to the road (bottom). Observations are normalized by the emission rate assuming an emission factor of  $3.3 \text{ g km}^{-1}$  for light duty vehicles and  $33 \text{ g km}^{-1}$  for heavy duty vehicles.

The emission rate is determined from the daily average traffic determined for September 3, 2015 and an emission factor of  $3.03 \times 10^{14} \text{ veh}^{-1} \text{ km}^{-1}$ . The emission factor was determined from a best fit line of the modeled and observed concentrations. This emission factor is about twice the emission factor of  $1.76 \times 10^{14} \text{ veh}^{-1} \text{ km}^{-1}$  determined from the study in Los Angeles.

We see a low correlation between model estimates and observations. However, the observations are mostly within a factor of two of the model estimates. Based on  $s_g$ , 95% of the observations are within a factor of 3.13 of the model estimates.

The VDM predicts the correct magnitude of the magnification, the ratio of the concentration at the building site to that at the open site. The bootstrap was used to calculate the mean and 95% confidence intervals of the mean observed magnification. Table 3.11 shows that the modeled magnification of 1.56 is within the 95% confidence interval of the observed magnification. If emission rates at the building and open sites are equal the magnification is independent of emission rate.

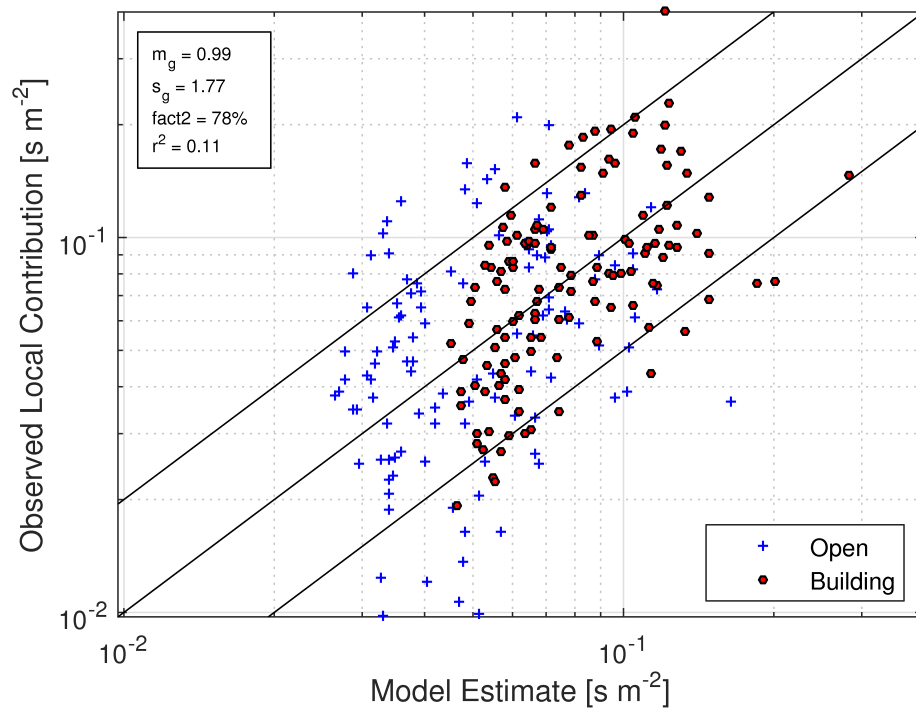


Figure 3.42: Comparison of Vertical Dispersion Model with measurements of ultrafine particle concentrations in Riverside, CA.

Table 3.11: Observed and model estimate of magnification in Riverside.

Observed Magnification	Model Estimate
1.61 [1.42 1.91]	1.56

Figures 3.43 and 3.44 show the variation of observations and model predictions with rooftop  $\sigma_w$  and surface wind speed, respectively. The bootstrap method was applied to estimate the mean value and 95% confidence intervals, shown as error bars, for bins of equal width. Comparison of the observed and modeled variation with  $\sigma_w$  indicates that the model formulation adequately accounts for the effect of  $\sigma_w$  on the dispersion. Almost all the model values are within the 95% confidence intervals of the observations. However, the comparison for the open section shows that for small values of  $\sigma_w$  the model overestimates concentrations. Figure 3.44 shows a similar trend: observed concentrations for small wind speeds tend to be lower than the model predicts. It is not clear what causes this overestimation. One possible explanation is that the UFP emission rate is overestimated during early morning. For larger wind speeds the VDM describes the observed concentration variation with scalar wind speed. This indicates that horizontal transport by the mean wind does not significantly affect near-road concentrations in urban areas. This result is consistent with the conclusions of the Los Angeles study, which showed that dispersion was primarily determined by vertical turbulent transport and not horizontal advection by the mean wind.

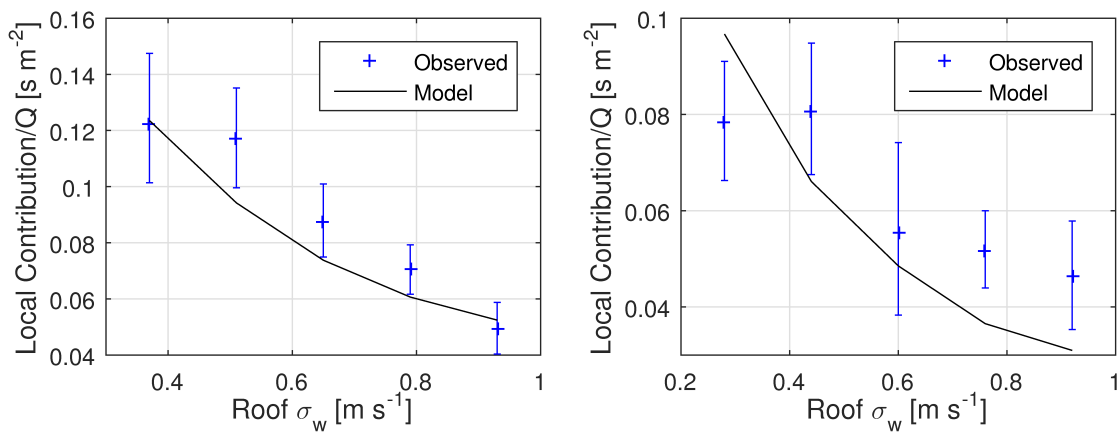


Figure 3.43: Variation of observed local contribution and VDM estimates with rooftop  $\sigma_w$ . (left) Building section. (right) Open section.

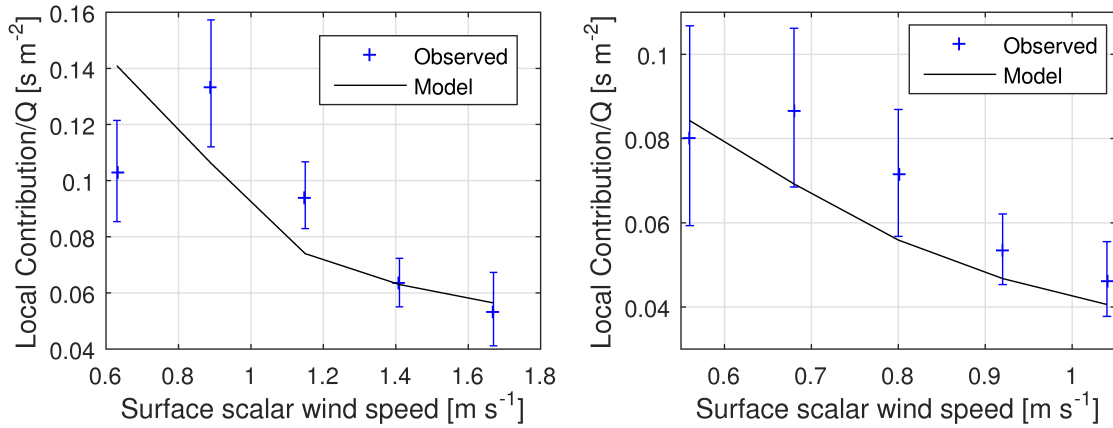


Figure 3.44: Variation of observed local contribution and VDM estimates with surface scalar wind speed. (left) Building section. (right) Open section.

The above comparisons show that the VDM adequately predicts near road concentrations within an urban area. To apply the model we need to determine the value of the meteorological input variables:  $\sigma_w$  at the urban rooftop and surface. Since measurements of  $\sigma_w$  are not routinely made in urban areas these variables must be determined from routine meteorological measurements, which are usually only made in rural areas such as airports. Section 3.6.3 describes the evaluation of a model that relates measured micrometeorology at a rural area to that at the urban rooftop and surface.

### 3.6.3 Evaluation of a Model to Estimate the Standard Deviation of Vertical Velocity Fluctuations in the Urban Area

The micrometeorology within an urban area is typically related to that at an upwind rural area using an internal boundary layer (IBL) model (Garratt, 1990). The height of the IBL is determined using equation (3.30) (Garratt, 1990):

$$\frac{dh}{dx} = A \frac{\sigma_w}{U_{urban}(h)} \quad (3.30)$$

where  $h$  is the IBL height,  $x$  is the distance the air mass has traveled from the rural area, and  $A$  is an empirical constant taken to be unity. The wind speed at the top of the IBL retains the value of the rural velocity profile. Since the velocity profile is continuous, matching the upwind rural wind speed profile,  $U_{rural}$ , with the urban wind speed profile,  $U_{urban}$ , at the top of the IBL,  $U_{urban}(h) = U_{rural}(h)$ , allows us to determine the surface friction velocity in the urban area. The wind speed in the urban and rural areas is given by the Monin-Obukhov similarity profile:

$$U(h) = \frac{u_*}{\kappa} \left[ \ln\left(\frac{h-d}{z_0}\right) + \psi_M\left(\frac{z_0}{L}\right) - \psi_M\left(\frac{z-d}{L}\right) \right] \quad (3.31)$$

where the appropriate rural or urban values of  $u_*$ , the surface friction velocity,  $z_0$ , the surface roughness length,  $d$ , the displacement height, and  $L$ , the Monin-Obukhov length, are used to evaluate the wind speed based on the rural or urban velocity profile.  $\psi_M$  is the integrated form of the dimensionless wind shear (Paulson, 1970).

We compared the IBL model with observations of the surface friction velocity measured at the urban rooftop location. The anemometer at this location was at 28 m AGL. Surrounding buildings within a 500 m radius buffer zone have an average height of 8.3 m. Thus, the rooftop anemometer is likely located within the inertial sublayer above the roughness sublayer, which typically extends up to 2 to 5 times the average building height (Grimmond & Oke, 1999). We can therefore compare the observations at this location directly with the IBL model without considering the reduction of surface friction velocity which occurs within the roughness sublayer.

The left panel of Figure 3.45 shows the comparison of the values of  $u_*$  estimated at the urban rooftop using the IBL model with observations. The comparison shows that the model underestimates the rooftop value by about 30% during unstable conditions.

During stable atmospheric conditions the model significantly underestimates the urban surface friction velocity. The right panel of Figure 3.45 shows the comparison of the model with observations, where the model is run assuming neutral atmospheric conditions. This improves the performance of the model for stable conditions. However, the model still significantly underestimates the urban surface friction velocity.

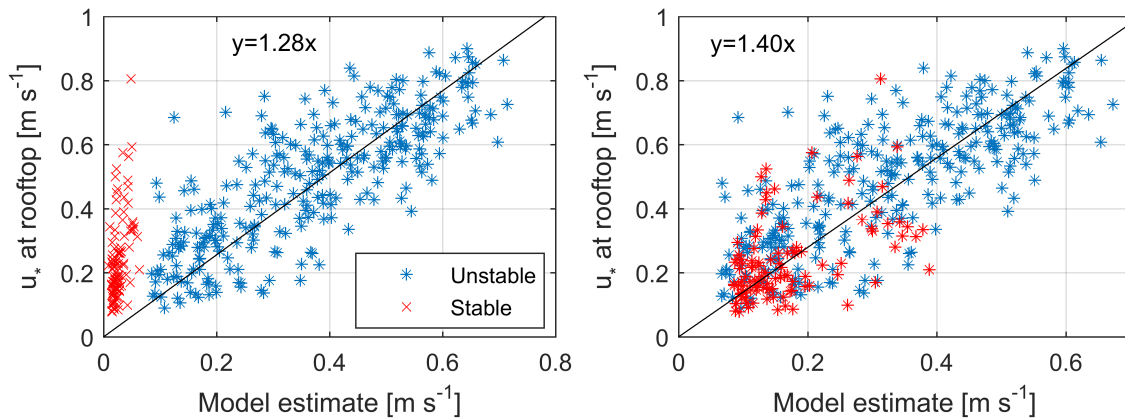


Figure 3.45: Comparison of modeled and observed rooftop  $u_*$ . (left) The model estimate is determined using the complete IBL model. (right) The model estimate assumes neutral atmospheric conditions (infinite Monin-Obukhov length).

A simplified form of the IBL model was evaluated in Schulte et al. (2015). This model was also recommended by Fisher et al. (2006) to estimate the value of the urban surface friction velocity from rural measurements. The basic form of the model is:

$$\frac{u_{*urban}}{u_{*rural}} = \left[ \frac{z_{0urban}}{z_{0rural}} \right]^\alpha \quad (3.32)$$

where  $\alpha$  is an empirical constant. Fisher et al. (2006) recommends a value of 0.0706. However, based on sensitivity studies of the IBL model we settled on a value of 0.14 for  $\alpha$ . Since for neutral conditions  $\sigma_w = 1.3u_*$  equation (3.32) also represents the ratio of  $\sigma_w$  at the rooftop to that at the airport.

Figure 3.46 shows the evaluation of (3.32) with observations. We see that the model performs as well as the complete IBL model, except that the simple model underestimates less. The right panel shows that the rooftop value of  $\sigma_w$ , the primary micrometeorological input variable for the VDM, is well predicted by equation (3.32) for unstable conditions. For stable conditions the model tends to underestimate the rooftop  $\sigma_w$ .

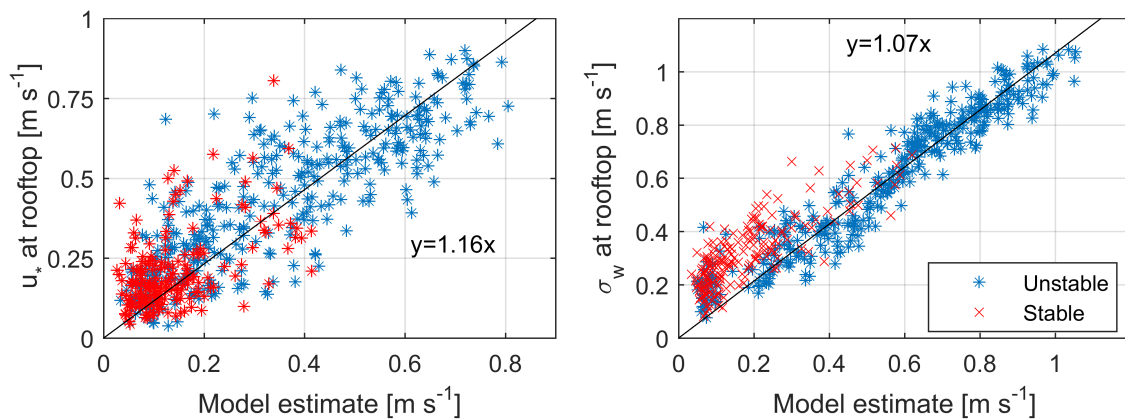


Figure 3.46: Comparison of  $u_*$  (left) and  $\sigma_w$  (right) predicted by the simple IBL model (equation (3.32)) with observations.

Once the rooftop value of  $\sigma_w$  is estimated from the upwind rural measurements using the IBL model, the surface  $\sigma_w$  can be estimated using (3.26). Figure 3.47 shows that the magnitude of the roof and surface  $\sigma_w$  are nearly equal at the building section, as predicted by the model, but at the open section the surface  $\sigma_w$  is about 50% smaller than that at the roof.

### 3.6.4 Discussion

The evaluation of the VDM supports the applicability of the model for estimating near-road concentrations within urban areas. Analysis of the difference between observations and model estimates indicates that the model shows the correct variation with  $\sigma_w$  and

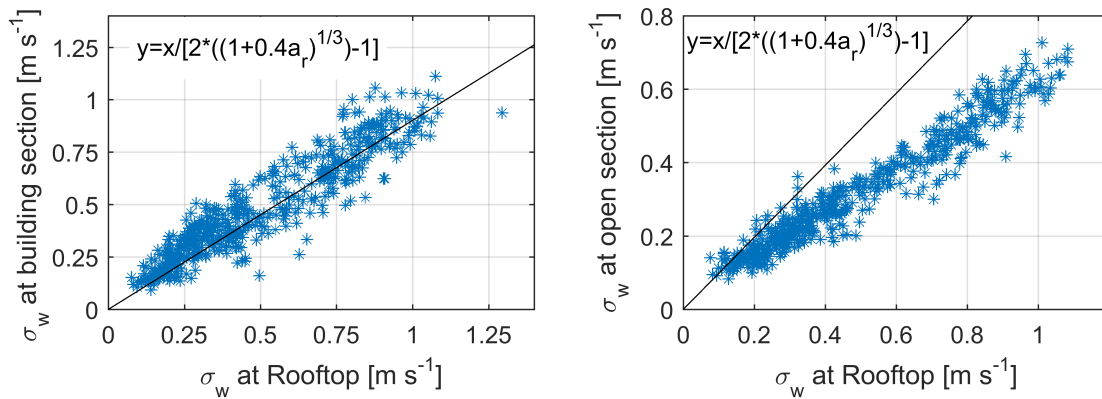


Figure 3.47: Comparison of  $\sigma_w$  at rooftop with the near surface  $\sigma_w$  at the building and open sections. The black line represents the model of (3.26)

wind speed, even though the only meteorological input variable is the rooftop  $\sigma_w$ . This shows that during low wind speed conditions, often observed in urban areas,  $\sigma_w$  controls dispersion. The mean wind speed likely plays a small role in dispersion in urban areas because the turbulent intensities are large, resulting in significant horizontal meandering of the pollutant plume. Measurements of mean winds and turbulence in Manhattan and Oklahoma city (Hanna et al., 2007; Hanna & Zhou, 2009) support the conclusion that strong vertical turbulent mixing governs dispersion in urban areas. Near surface winds in these studies were only about 1/3 of the rooftop value, and wind directions varied significantly (Hanna et al., 2007). This results in more horizontal meandering of pollutant plumes, creating conditions where vertical transport governs the near road concentrations.

For the VDM to be consistent with the data collected in the Los Angeles study as well as the Riverside measurements it was necessary to assume that the emission factors of  $NO_x$ ,  $CO$ , and UFP could vary by about a factor of two of the EMFAC2011 estimates. This assumption is supported by studies showing errors in emission models of up to a factor of three and two for  $CO$  and  $NO_x$ , respectively (Smit et al., 2010). Emission factors depend on the composition of the vehicle fleet and the type of driving conditions. Hence,

traffic flow conditions observed in the Riverside study may result in emission factors that are different from those predicted by average speed models such as EMFAC, and it may be necessary to estimate emissions by explicitly including the level of traffic congestion at the field site in the emission model (Smit et al., 2008). However, it may be difficult to obtain more accurate emission estimates even with more comprehensive models that include measures of congestion because it will be more difficult to obtain accurate estimates of the input data for these models. Considering the uncertainty in the emission rates, the value of the model calibration constant  $\beta$  is likely within about a factor of two of the value  $\beta = 1.0$  chosen in this study.

We have generally found that the rooftop and surface  $\sigma_w$  are very well correlated and are nearly equal in magnitude. The model of equation (3.26) explains this strong correspondence between the roof and surface values. The model works well for the measurements at the building section, but the open section shows much smaller surface  $\sigma_w$  than is expected based on the model. It is possible that the near-surface observation at one location within the urban area is not a good estimate of the  $\sigma_w$  averaged over the street, which is the quantity described by equation (3.26) and is also the value required for the VDM and other semi-empirical dispersion models. This could also explain why using equation (3.26) in the VDM evaluation to estimate the surface  $\sigma_w$  produced a better comparison with observations of UFP than using the surface measurements directly.

We found that the full IBL model of equation (3.30) tends to underestimate the  $u_*$  in the urban area. The IBL model performs best if we neglect the effect of atmospheric stability. If the effect of stability is included, the model significantly underestimates urban  $u_*$ . This could be due to the fact that the urban area tends to have a positive heat flux even during nighttime resulting in more neutral and unstable conditions than would be expected based on the rural heat flux measurements. Monin-Obukhov similarity theory,

which forms the basis of the velocity profiles used in the IBL model, is also likely not valid within the urban area during nighttime since the boundary layer height and roughness sublayer height are nearly equal, resulting in a nonexistent inertial sublayer. The simplified form of the model in equation (3.32) has a correlation that is just as good as the full IBL model, but has less bias. This model is likely the best choice for estimating urban  $\sigma_w$  from rural measurements for dispersion applications due to its good performance and simplicity.

Using (3.26) and either (3.30) or (3.32), all the meteorological inputs for the VDM can be determined from measurements of the surface friction velocity at an upwind rural location. However, often only mean wind data is routinely measured. In these cases, the value of the surface friction velocity at the rural location can be determined from measurements of mean wind speed and temperature at a single height using methods such as those in Holtslag & Van Ulden (1983).

## 3.7 Conclusions

Measurements of near road concentrations of  $NO_x$  along with meteorological variables conducted in an urban street in Hannover, Germany were used to determine what variables primarily govern dispersion of vehicle emissions in urban areas. The data analysis showed that the standard deviation of vertical velocity fluctuations primarily governs near road concentrations of vehicle emissions. This indicates that vertical turbulent pollutant transport is the primary mechanism that dilutes pollutants in urban areas. Semi-empirical dispersion models that account for rapid vertical mixing show good performance in predicting the near road concentrations.

Two field studies were conducted, one in Los Angeles county, CA and one in Riverside, CA, to analyze the effect of urban areas with variable building heights on the dispersion of vehicle emissions. Evaluation of the data collected in the Los Angeles field study showed that the ratio of area weighted building height to street width along with the vertical average of the standard deviation of vertical velocity fluctuations primarily govern near road concentrations. A dispersion model, the vertical dispersion model, which accounts for rapid vertical mixing, shows good performance with both the Los Angeles and Hannover data.

Measurements of near road concentrations of ultrafine particles and carbon monoxide conducted over several months in an urban area in Riverside, CA, were used to calibrate and further evaluate the VDM. The evaluation supports the conclusions of the previous evaluation with data collected in Los Angeles, CA, and shows that the VDM is adequate for its intended purpose of estimating near road concentrations of vehicle emissions in urban areas.

Dispersion in urban areas is primarily governed by vertical turbulent transport, and therefore the primary variable governing urban near-road concentrations are the ratio of area weighted building height to street width and the vertical turbulent velocity. This conclusion is supported by measurements of wind speeds and turbulence within cities, which indicate that mean wind speeds are typically low and turbulent velocities are large. The area weighted building height provides a useful measure to characterize dispersion in cities with significant building height variability.

Measurements of the turbulence at the urban rooftop and at an upwind rural location are consistent with an internal boundary layer model of the evolution of the flow from the rural to the urban area. This model can be used to estimate the meteorological

input variables for the dispersion model from measurements at an upwind rural location, a necessity for practical application of urban dispersion models.

The results of this study can inform the design of transit oriented developments, urban developments where urban densification strategies are used to reduce traffic emissions. Effective mitigation methods must account for the magnitudes of the background concentrations and the concentrations due to local emissions within the street. In the study at Los Angeles, 8th St, 50 m tall buildings next to the 20 m wide street are associated with a 50% increase in the UFP concentration due to local emissions, resulting in a 25% increase in the total concentration. In the Riverside urban area the, on average, 14 m tall buildings next to the road magnified the near road concentrations of ultrafine particles emitted by the road traffic by a factor of 1.6 relative to a section of road with short or no buildings. Considering the relatively high population density in cities, exposure to elevated near road concentrations may be significantly increased due to the presence of buildings.

Mitigation methods may significantly reduce the exposure concentration in urban areas with tall buildings. The vertical dispersion model suggests the following methods to mitigate exposure of pedestrians to high surface concentrations: 1) limiting vehicle traffic within streets with large aspect ratios when there is high pedestrian traffic, 2) limiting the street aspect ratio based on expected pedestrian exposure, and 3) in new developments, or where such design can be implemented, separate pedestrian and heavy vehicle traffic into different streets.

# Chapter 4

## Conclusion

Exposure to elevated concentrations of vehicle emissions causes asthma and other respiratory impacts, birth and developmental effects, premature mortality, cardiovascular effects, and cancer. The urban built environment significantly affects dispersion of vehicle emissions. Solid barriers next to roads can enhance dispersion, thereby mitigating elevated roadside concentrations. Tall buildings reduce dispersion, creating hot spots of vehicle emitted pollutants in urban areas and increasing exposure of city residents to elevated concentrations of vehicle emissions.

Simple models that can be used to estimate the impact of the built environment on near road concentrations of vehicle emissions are needed. The work in this thesis develops semi-empirical dispersion models that are useful for linking vehicle emissions with near road concentrations. First, models were developed to analyze the effectiveness of roadside barriers at mitigating elevated concentrations of vehicle emissions. Next, models of dispersion in cities with significant building height variability were developed.

## Roadside Barriers

The primary effect of roadside barriers on dispersion is that they enhance the vertical plume spread by an amount proportional to the barrier height. Barriers also increase the turbulence in the barrier's wake, resulting in a greater rate of increase of the size of the pollutant plume. Wind speeds in the barrier wake are reduced. The effect of the barrier persists up to a distance of about 10-20 times the barrier height. Enhanced plume spread due to the presence of the barrier significantly reduces near road concentrations of vehicle emissions. Field and wind tunnel studies show concentration reductions of about 50% directly downwind of a 6 m tall barrier.

Three dispersion models were developed which relate the near road concentration in the presence of the barrier with the meteorology measured upwind of the barrier and the barrier height. The source shift model moves the source upwind by a distance related to the barrier height and enhances the vertical plume spread by an empirical function of the barrier height and wind speed. The mixed wake model increases vertical mixing by an amount proportional to the barrier height by modifying the Gaussian plume model. This model also enhances the vertical plume spread using the empirical function developed for the source shift. The Puttock Hunt model numerically solves the advection diffusion equation using the eddy diffusivity model. The flow over the barrier is assumed to be potential flow. The solution is computed in a domain consisting of the upper half plane and then mapped back to the physical domain using a conformal map. The conformal map is defined by the boundary of the barrier's separated wake. Enhanced turbulence in the barrier wake is included in the model by modifying the eddy diffusivity using an empirical function.

All three models show adequate comparison with most of the observations collected in a field tracer study and a wind tunnel study. The models are unbiased for neutral and stable atmospheric conditions. However, the models overestimate concentrations directly downwind of the barrier by a factor of two during unstable atmospheric conditions. A modification of the mixed wake model shows that overestimation during unstable conditions is related to the specification of the wind speed in the wake of the barrier. The mixed wake model was modified using a semi-empirical function to reduce the wind speed in the barrier's wake relative to that upwind. The modified model gives unbiased concentration estimates for all atmospheric stabilities. Thus the reduction in wind speed downwind of the barrier is an important barrier effect that can significantly alter the dispersion of vehicle emissions and the resulting near road concentrations.

Sensitivity studies of the modified mixed wake model show that roadside barriers are most effective during stable atmospheric conditions. Thus barriers can be very effective at reducing near road concentrations during early morning rush hour and nighttime, when concentrations are often largest. Increasing surface roughness reduces the barrier effect. Thus roadside barriers in urban areas are less effective than those in rural areas. Roadside barrier effectiveness also decreases as the road width increases.

## **Dispersion in Cities with Variable Building Height**

Analysis of  $NO_x$  concentrations collected in a street canyon in Hannover, Germany shows that the primary meteorological variable influencing near road concentrations of vehicle emissions in cities is the standard deviation of vertical velocity fluctuations within the street. This indicates that vertical turbulent pollutant transport is the primary mechanism that dilutes pollutants in urban areas.

Wind direction measurements in Hannover show that the wind primarily channels in the street rather than forming street canyon type vortices. This indicates that street canyon models such as OSPM may not be appropriate for modeling dispersion in some cities. OSPM has primarily been evaluated with data collected in European cities, characterized by spatial homogeneity and uniform building height. Dispersion models must be evaluated with data collected in cities with significant building height variability.

A dispersion model, the vertical dispersion model, which accounts for rapid vertical mixing, shows good performance in estimating concentrations measured in Hannover and in a field study conducted in Los Angeles, CA. The Los Angeles study was designed to measure near road concentrations in several cities with significant building height variability. Evaluation of the data collected in the Los Angeles field study showed that the ratio of area weighted building height to street width along with the vertical average of the standard deviation of vertical velocity fluctuations primarily govern near road concentrations. This conclusion is supported by measurements of wind speeds and turbulence within cities, which indicate that mean wind speeds are typically low and turbulent velocities are large. The area weighted building height provides a useful measure to characterize dispersion in cities with significant building height variability.

Measurements of near road concentrations of ultrafine particles and carbon monoxide conducted over several months in an urban area in Riverside, CA, were used to calibrate and further evaluate the VDM. The evaluation supports the conclusions of the previous evaluation with data collected in Los Angeles, CA, and shows that the VDM is adequate for its intended purpose of estimating near road concentrations of vehicle emissions in urban areas.

Measurements of the turbulence at the urban rooftop and at an upwind rural location in the Riverside study are consistent with an internal boundary layer model of the evolution

of the flow from the rural to the urban area. This model can be used to estimate the meteorological input variables for the dispersion model from measurements at an upwind rural location, a necessity for practical application of urban dispersion models.

The models developed in this thesis are useful for evaluating exposure of city residents to elevated concentrations of vehicle emissions. This may be especially useful in designing Transit Oriented Developments (TODs), which are building developments where housing is located in close proximity to public transportation infrastructure. TODs increase building and population density, thereby potentially significantly increasing exposure of TOD residents to vehicle emissions.

The observed increase in near road concentrations of local vehicle emissions between the "building" and "open" locations at the Los Angeles, 8th St and Riverside sites, was 50% and 60%, respectively. The 60% increase at the Riverside site is due to an increase of the area weighted building height next to the 30 m wide street from 2 m to 14 m. For 8th St the increase in concentration is associated with the presence of 50 m tall buildings directly next to the 20 m wide street, compared with no buildings directly next to the street at the open section. The increase in concentrations due to the presence of 50 m tall buildings next to the street predicted by the VDM is much larger than the 50% observed increase in concentrations. The discrepancy is related to how the VDM is defined. The VDM is designed to predict the surface concentration averaged over a horizontal size of about one city block. However, this definition of the horizontal averaging scale is somewhat arbitrary. By considering the time required to mix pollutants vertically over the building height and the time required to advect pollutants along the street, we determined that the horizontal averaging length scale in 8th St should be on the order of 300 m, about 3 city blocks. Emissions from streets up to about 3 city blocks from the monitors affect the observed local contribution. Thus, the area weighted building

height should also be defined based on this 3 city block averaging scale rather than only over one block. By increasing the area weighted building height to reflect the average height within this larger region, we obtain better comparison between observations and model estimates. Thus, when the buildings are very tall, the VDM should only be used to estimate the concentration averaged over a scale of several city blocks.

Background emission sources represent about 50% of the total concentration at 8th St. Thus, the 50% increase in concentration of local emissions at 8th St represents an increase of about 25% in the total concentration between the open and building sites. The impact of background sources on exposure of TOD residents to vehicle emissions must be considered in order to implement effective methods to mitigate exposure to high surface concentrations.

We mentioned the following mitigation methods suggested by the vertical dispersion model: 1) limiting vehicle traffic within streets with large aspect ratios when there is high pedestrian traffic, 2) limiting the street aspect ratio based on expected pedestrian exposure, and 3) in new developments, or where such design can be implemented, separate pedestrian and heavy vehicle traffic into different streets. The second mitigation method conflicts with the requirements of high density TODs. Limiting the street aspect ratio effectively limits population density in cities but the goals of TOD require residents to live in more dense areas so that the need for transportation can be reduced. However, it is possible to plan developments so that high traffic roads are located outside of residential areas and away from pedestrian zones. This appears to be the most useful mitigation method but it requires detailed planning of the TOD. The VDM can guide the implementation of this type of mitigation method by providing designers with the tools needed to understand how changes in the TOD design and traffic flow ultimately result in changes in exposure to vehicle emissions.

## Appendix A

# Calibration of Condensation Particle Counters

On each day that measurements were made, prior to locating the TSI3022A condensation particle counters at field locations, the instruments were co-located at one location next to the street. The data collected during the co-location was used to derive inter-instrument calibration factors that were used to adjust the concentrations measured during the experiments.

Figure A.1 shows scatter plots comparing concentrations measured by three of the CPCs at the 8th St field site on May 7th, 2014 with one CPC used as the reference. Figure A.2 shows a similar comparison for May 9th, 2014. Figure A.3 shows scatter plots comparing concentrations measured by the four CPCs and one DiscMini at the Broadway field site on September 20, 2013. Figure A.4 shows the calibration plots for the CPCs used at the Temple City field site on January 16, 2014. Calibration plots for the CPCs used at the Wilshire Blvd site are shown in Figure A.5.

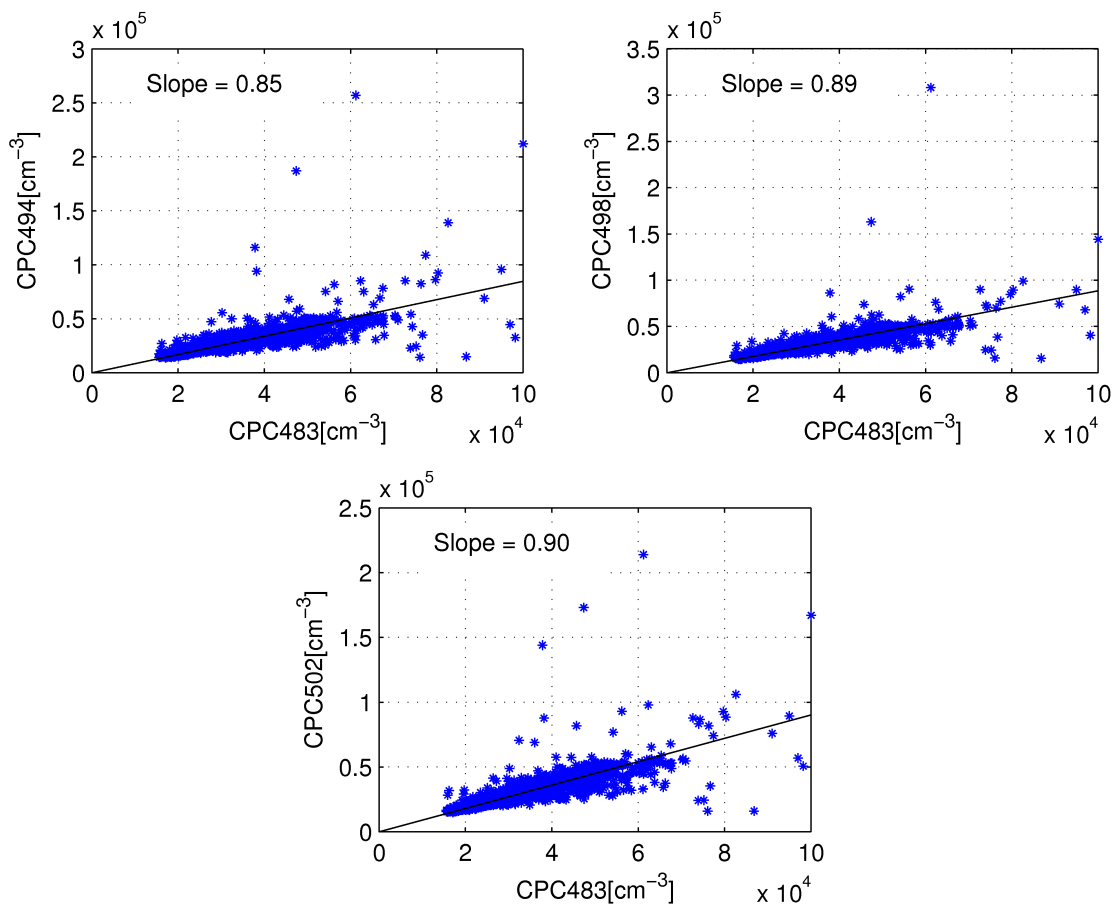


Figure A.1: Calibration derived from co-location of instruments next to 8th St on May 7th

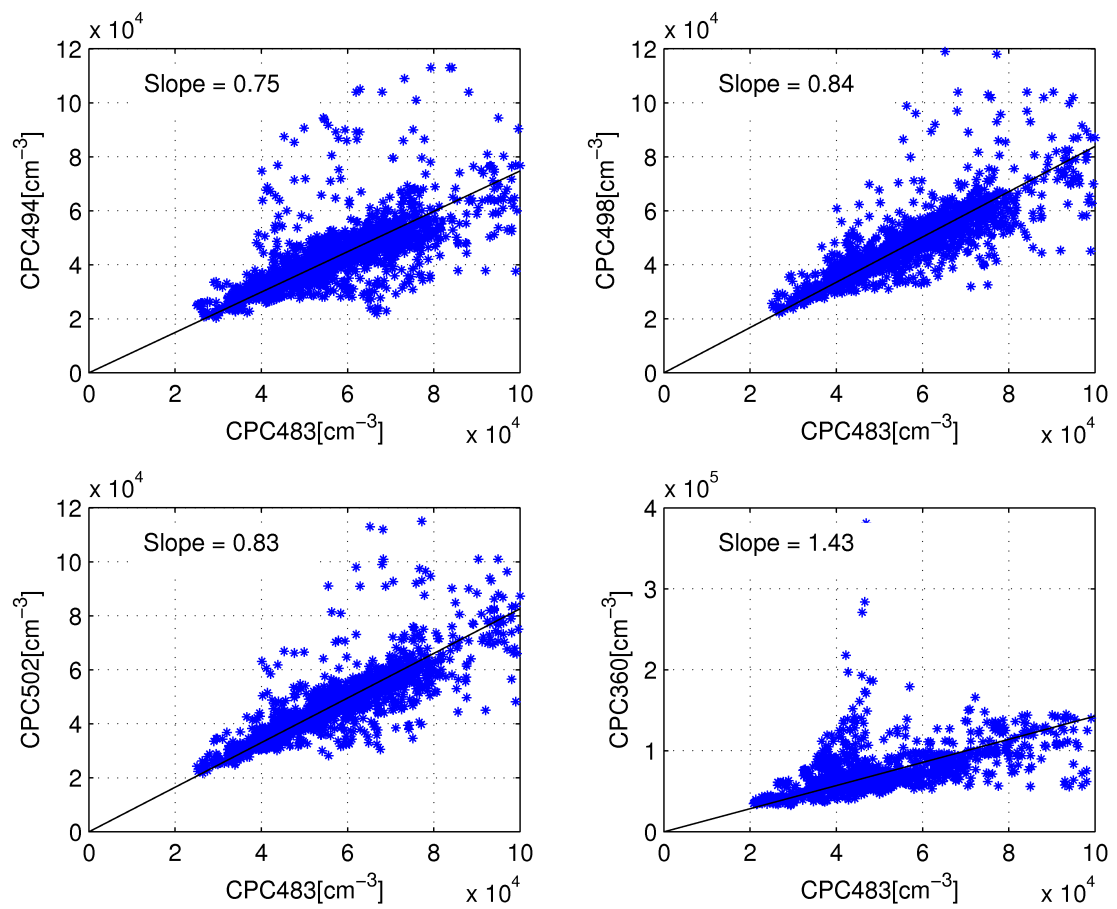


Figure A.2: Calibration derived from co-location of instruments next to 8th St on May 9th

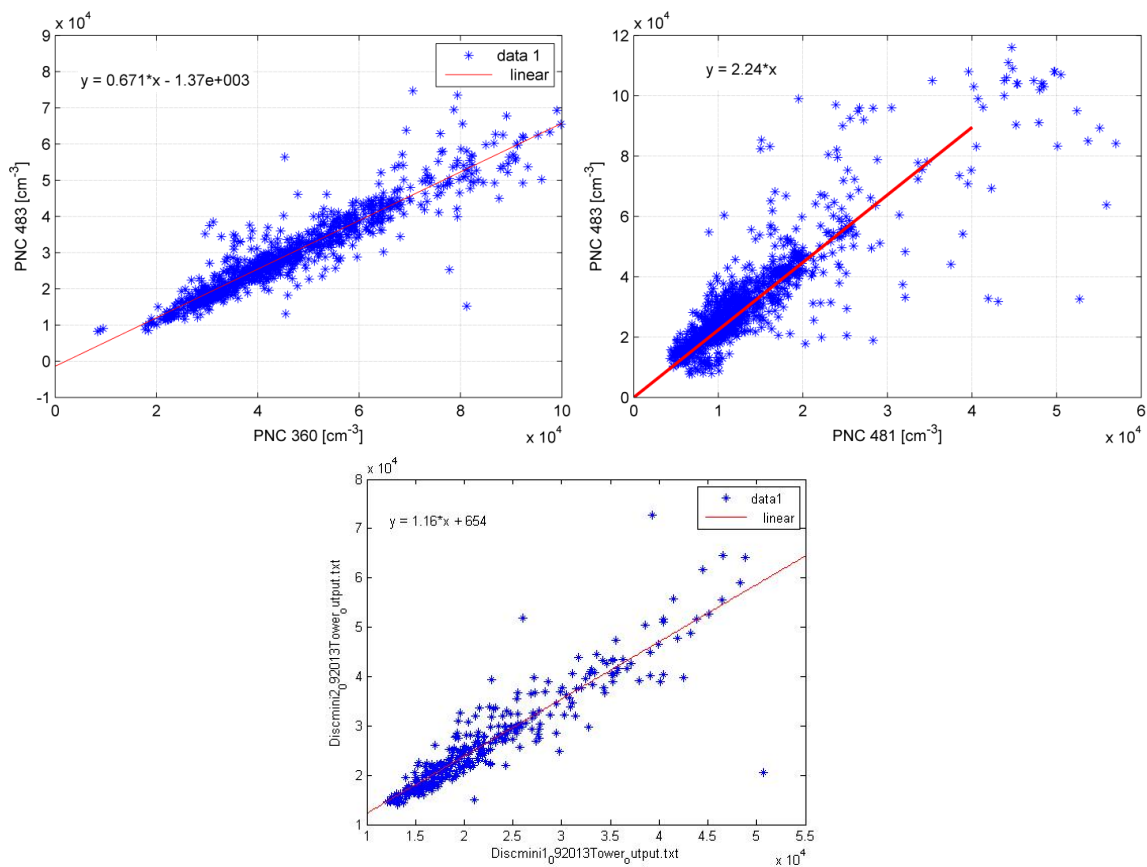


Figure A.3: Calibration derived from co-location of instruments next to Broadway on September 20th. The calibration factor between DiScmini 2 and CPC 483 was 1.34 (not shown).

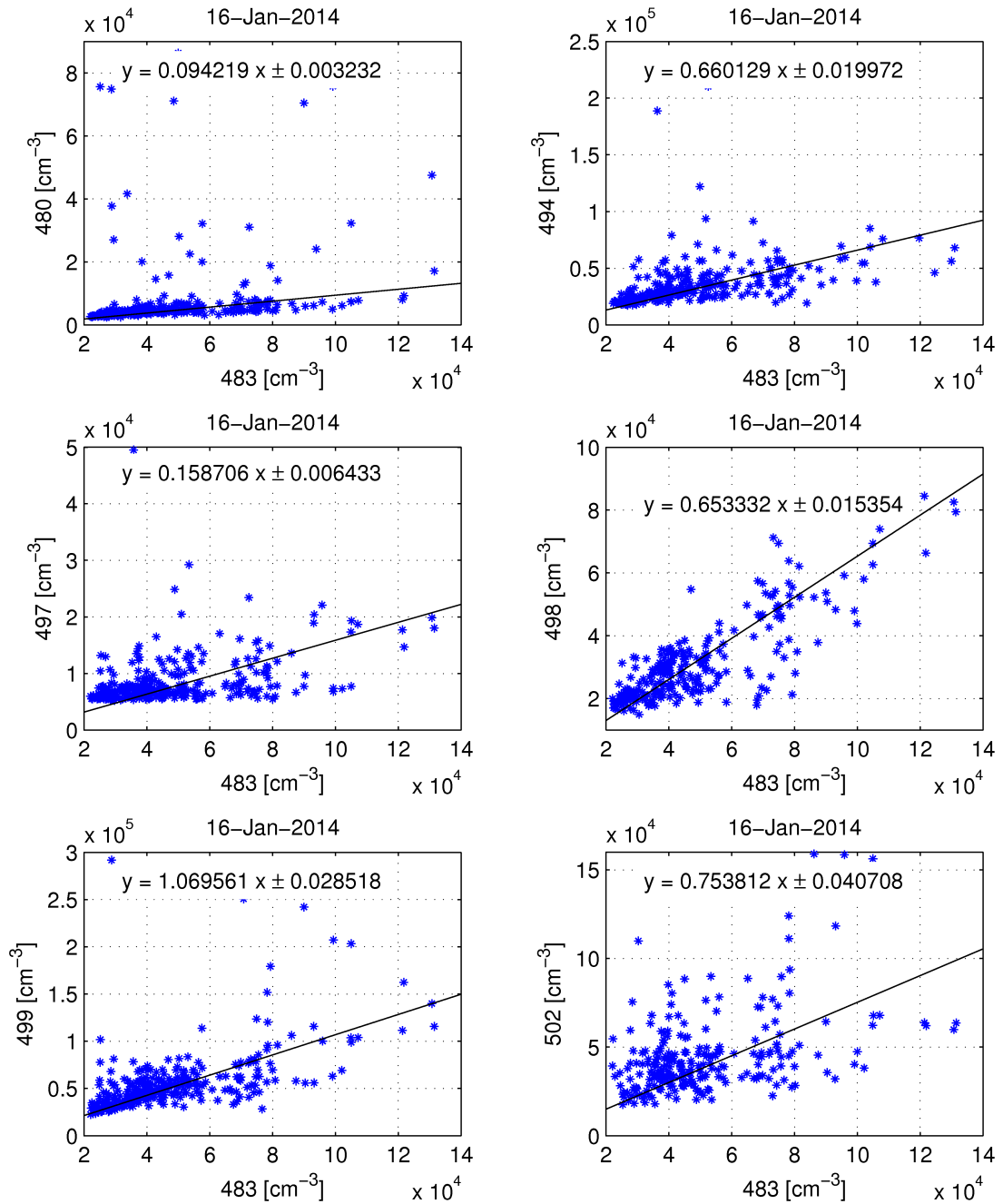


Figure A.4: Calibration derived from co-location of instruments next to Temple City Blvd on January 16, 2014.

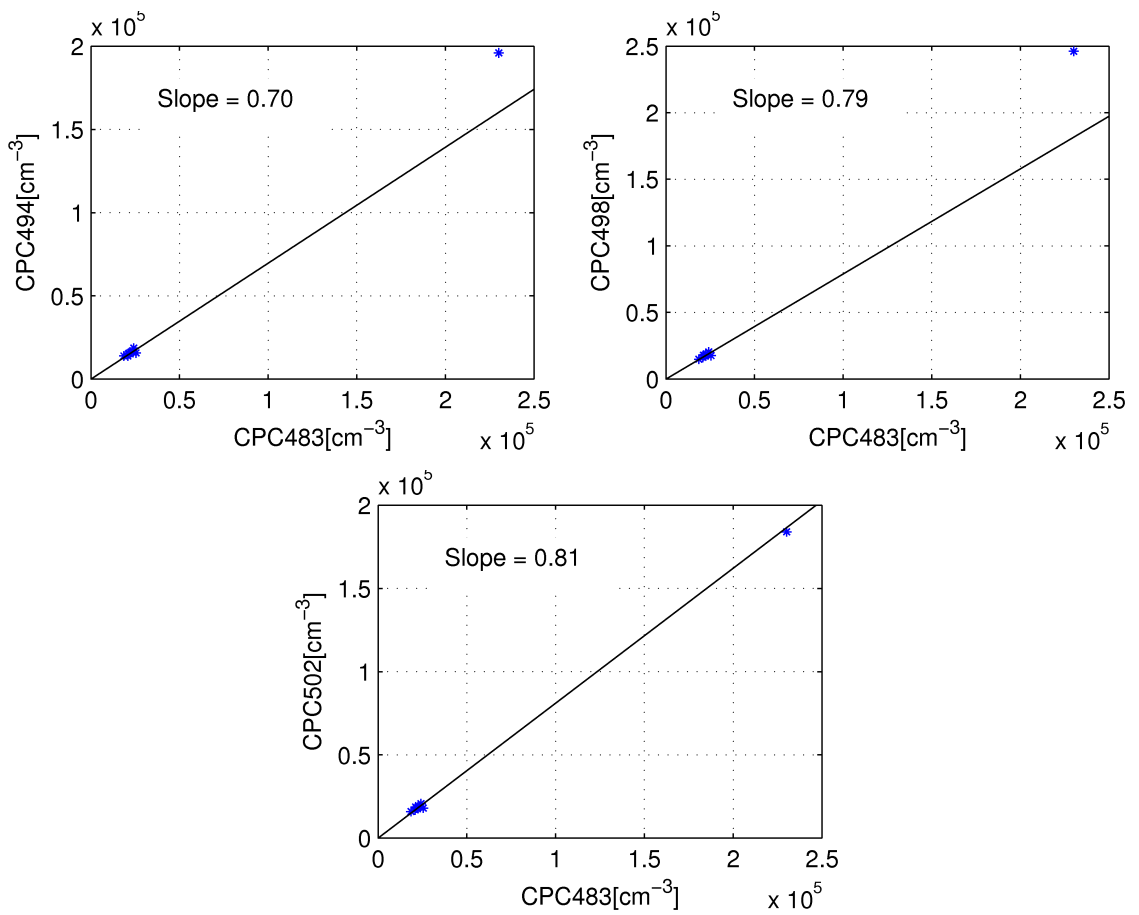


Figure A.5: Calibration derived from co-location of instruments next to Wilshire Blvd on May 30, 2014.

## **Appendix B**

# **Design of a System to Enable Long Term Measurements of Near Road UFP Concentrations Using TSI3022A Condensation Particle Counters**

This section describes the systems designed to allow long term measurements with TSI3022A condensation particle counters. The long term field measurements of particle concentrations with TSI3022A CPCs require support infrastructure to provide power, environmental protection, and data logging. The CPCs use AC line inputs for power and provide data output as a voltage signal and through a serial interface. In the Los Angeles and Riverside field studies, power outlets were not available at most instrument locations. We designed a system to provide power to the CPCs when no AC power is available. The CPCs have no data storage so data must be recorded on external memory. The CPCs cannot be exposed to rain, and do not function if the ambient temperature is above 37 degrees Celsius or below 10 degrees Celsius. We designed systems to shield the CPCs from rain, regulate the temperature, and to record data.

## B.1 System Design

Figure B.1 shows a photo of the CPC measurement system mounted to a tripod. The CPC, data logger, and CPC cooling system are contained within the top enclosure. Batteries located in a bottom enclosure power the CPC. An inverter within the bottom enclosure converts the 12 V DC battery power to 110 V AC power used as input for the CPC. The 110 V power cable connects the bottom and top enclosure. For long term field measurements the batteries are charged using photovoltaic panels. A SunSaver-20 charger controller is used to regulate the battery charging. Figure B.2 shows the data logging and support systems. A cellular modem is used to remotely receive data from the field and ensure the instruments are operating correctly. Remaining components are power supplies to supply 5 V DC and 12 V DC to the data logger and modem.

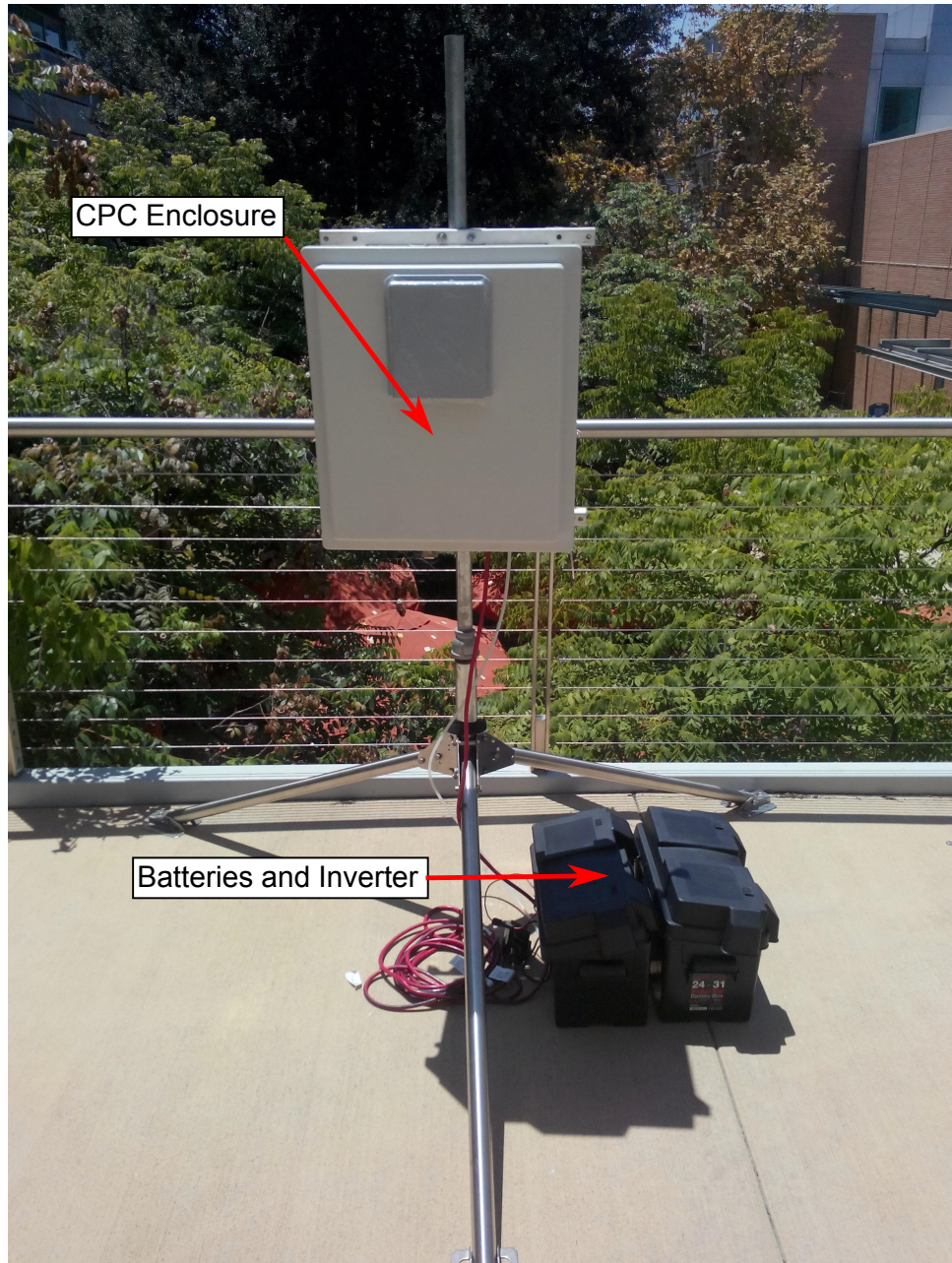


Figure B.1: CPC measurement system mounted to a tripod.

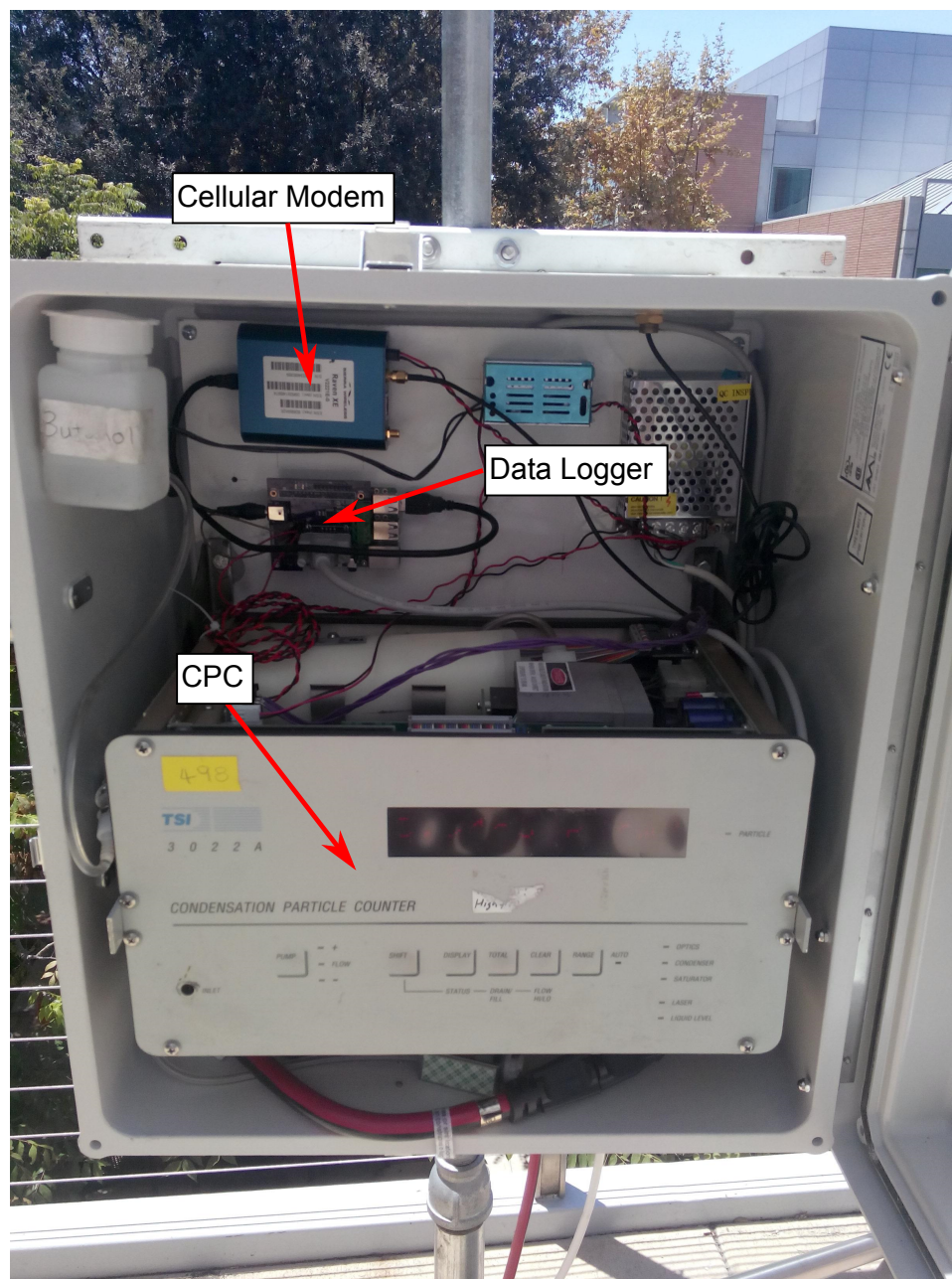


Figure B.2: CPC measurement system.

## B.2 Power Supply

The CPC and power inverter use about  $50\text{ W}$  of power during steady state operation. Thus, for one day of operation the CPC uses  $4.32\text{ MJ}$  of energy. Figure B.3 shows the energy available from a 15% efficient photovoltaic panel located near Riverside. The photovoltaic panel supplies power to the CPC and to the battery charger during the day. If we assume that there is a 25% loss of energy in the battery charge/discharge cycle, then, with a factor of safety of 10%, we need a solar panel with an area of  $1.7\text{m}^2$  to supply enough power to the CPC and battery for continuous operation. This corresponds to an approximately  $240\text{ W}$  rated panel.

A battery can power the CPC during the night when solar power is unavailable. This battery needs to supply at most  $2.6\text{MJ}$  between charges. This requires a lead acid deep cycle battery with a capacity greater than  $120\text{ A hr}$ . A smaller battery may be used if the CPC is turned off during part of the night. During field measurements in Riverside, the CPCs were only run for about 8 hours every day that measurements were made. The large solar panels needed to continuously power the CPCs could not be used in the Riverside urban area, and thus the equipment was turned off at night and the batteries were recharged in the lab.

Figure 5B.4 shows an electrical schematic of the solar power system. Two  $120\text{ W}$  panels are used because larger capacity panels cannot be easily used with a  $12\text{ V}$  battery system. The SunSaver-20 by Morningstar is used to regulate the battery charge. The CPC and data logger are powered from the Load terminals of the SunSaver-20. This system will shut down the CPC and data logger if the battery voltage becomes very low.

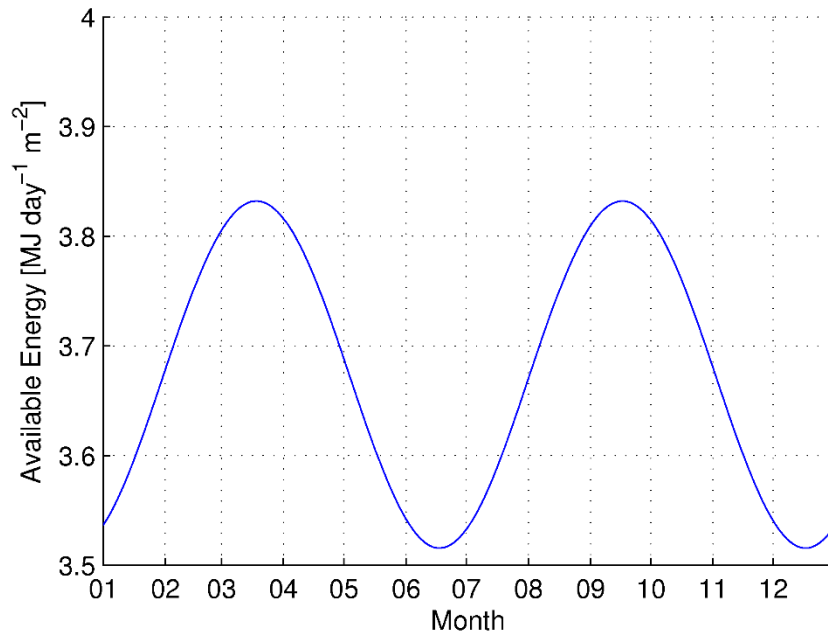


Figure B.3: Daily usable energy from a solar panel located at 34 degrees N, 117 degrees W facing south and tilted at 34 degrees and with an efficiency of 15%. Cloud cover is 50%.

The data and control signal between the data logger and CPC is also shown. This is used to collect data from the CPC and to send the temperature control feedback signal.

The solar panel needs to be mounted on a support to fix the angle at 34 degrees (for Riverside) from the horizontal.

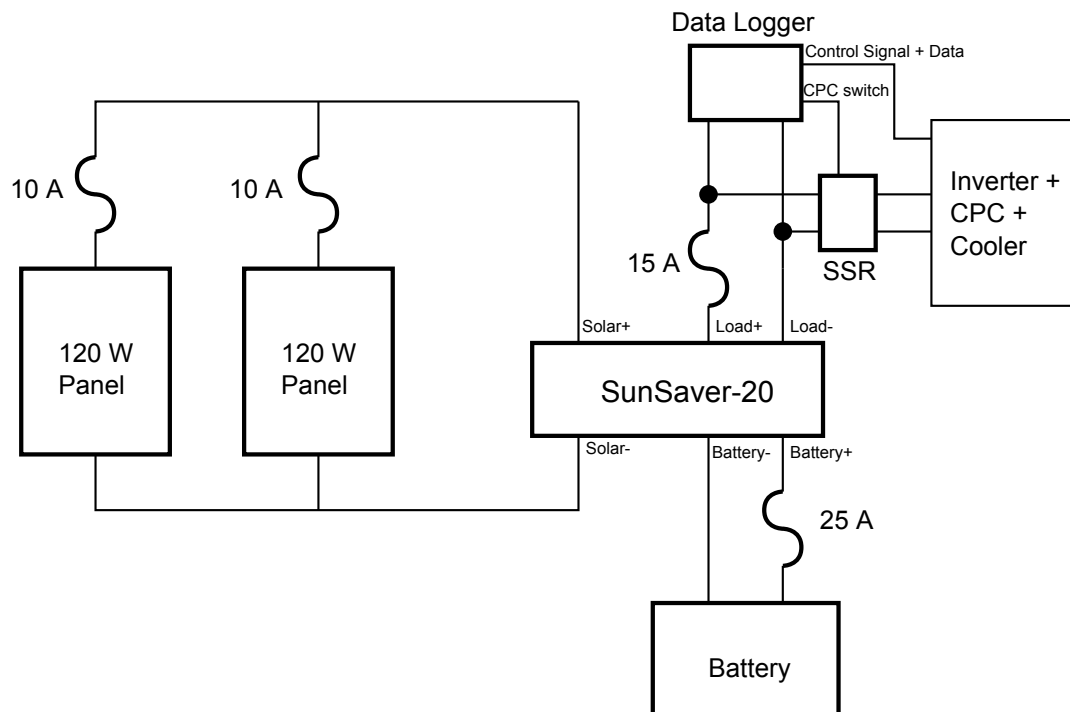


Figure B.4: Schematic of solar power system.

### B.3 Cooling System

The aerosol flow path within the CPC is shown in Figure B.5. Aerosol first mixes with saturated butanol vapor within the heated saturator tube. The flow then passes into the cooled condenser tube, where the butanol vapor becomes supersaturated and heterogeneous nucleation of butanol onto the aerosol particles occurs. The saturator and condenser are designed to operate at  $35^{\circ}\text{C}$  and  $10^{\circ}\text{C}$  respectively. When the ambient temperature exceeds  $35^{\circ}\text{C}$ , the temperature of the saturator is uncontrolled and the CPC operates out of specification. Ambient temperatures frequently exceed  $35^{\circ}\text{C}$  in Riverside during the summer, necessitating cooling of the saturator tube.

The cooling system for the saturator is based on a thermoelectric cooling element. The cold side of the thermoelectric cooler is placed directly on top of the metal block of

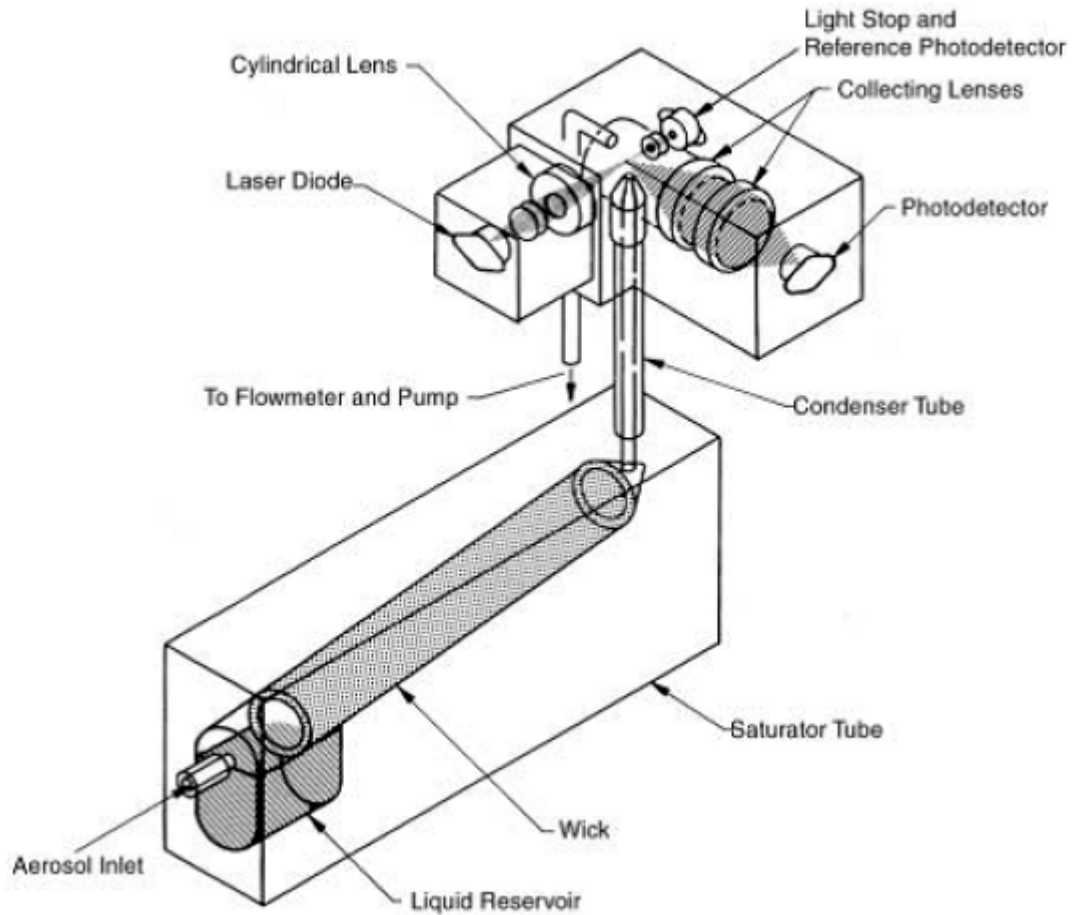


Figure B.5: Drawing of the CPC sensor. From TSI (2002)

the saturator with a heat sink and fan on the hot side of the cooler. Figure B.6 shows a photo of the saturator block with the top insulation removed prior to placing the cooler on top.

We determined the needed cooling capacity by estimating the heat transfer rate into the saturator from the environment. The required cooling heat flux,  $Q_c$ , is  $Q_c = hA(T_\infty - T_s)$ , where  $h$  is the heat transfer coefficient,  $A$  is the surface area of the saturator, and  $T_\infty$  and  $T_s$  are the ambient and saturator temperatures. We measured the heat transfer coefficient by applying a known power input to the resistive heater within the saturator

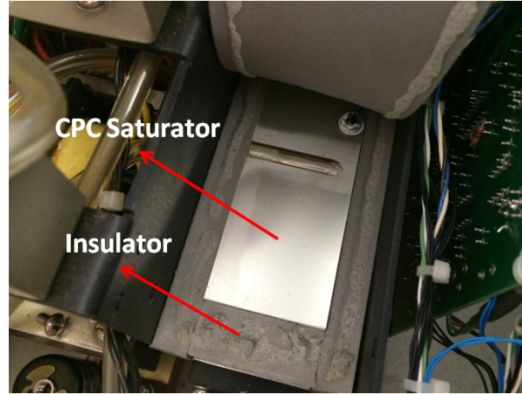


Figure B.6: Top view of the CPC saturator (model 3022A). The cooling unit was placed directly on top of the saturator.

and recording the final and ambient temperatures. We also measured the time constant for the system to reach equilibrium. The system response is given by:

$$T = T_{\infty} + (T_0 - T_{\infty})e^{-t/\tau} + \frac{Q}{hA}(1 - e^{-t/\tau}) \quad (\text{B.1})$$

where  $Q$  is the heater input,  $T_0$  is the initial temperature, and the exponential time constant is  $\tau = \frac{\rho V C_p}{hA}$ , where  $\rho$  and  $C_p$  are the density and specific heat capacity of the saturator metal, respectively, and  $V$  is the saturator volume. The steady state temperature when the heater was off was  $T_{\infty} = 23.4^{\circ}\text{C}$ . Figure B.7 shows the measured temperature time series along with the fitted model when a heat input of  $6.19\text{ W}$  was applied. The best fit for the exponential time scale was 20.7 minutes. The fitted heat transfer coefficient was  $hA = 0.97\text{ W K}^{-1}$ .

The system was designed to operate with a maximum ambient temperature of  $41^{\circ}\text{C}$ , the maximum temperature recorded at the Riverside-Rubidoux monitoring station in 2014. Using this temperature and the measured heat transfer coefficient we obtain a required cooling heat flux of  $5.82\text{ W}$ . The TEC1-12706 thermoelectric cooler was selected to meet this requirement. When run with an input voltage of  $5\text{ V}$  and hot and cold side

temperatures of  $70^{\circ}\text{C}$  and  $35^{\circ}\text{C}$  this module produces a cooling heat flux of about  $18.5\text{ W}$ . Under these conditions resistive heating within the module produces an additional  $8.2\text{ W}$  that must be removed by the heat sink.

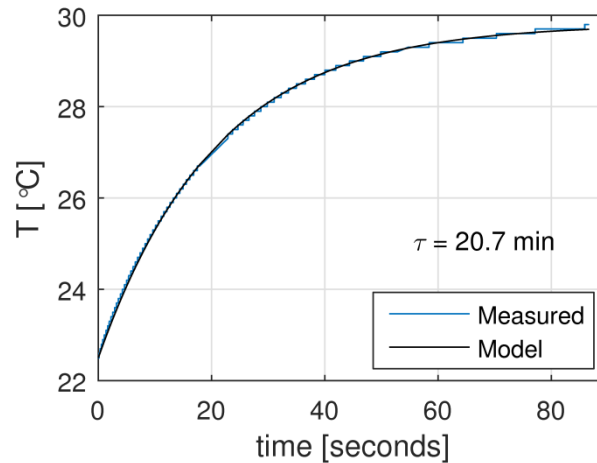


Figure B.7: Temperature measurement of CPC saturator used to determine the heat transfer coefficient between the saturator and the environment and the exponential time constant for changes in the saturator temperature.

A steady state model of the heat transfer was used to evaluate the performance of the cooling system. The temperature within the CPC enclosure is larger than the ambient temperature outside. Because of this we must consider the entire system of CPC and cooler along with the enclosure for the heat transfer calculations. Based on preliminary calculations it was determined that a ventilation fan for the enclosure is necessary to limit the interior temperature.

The system that is solved for the steady state temperatures is:

$$\begin{aligned}
0 &= \epsilon Q_{sol} - h_{be} A_b (T_b - T_\infty) - h_{bi} A_b (T_b - T_a) \\
0 &= h_{bi} A_b (T_b - T_a) - h A (T_a - T_s) + (T_{hs} - T_a)/R + Q_e - \rho_{air} C_{pair} \dot{V}_{air} (T_a - T_\infty) \\
0 &= h A (T_a - T_s) - Q_{cTEC} \\
0 &= Q_{cTEC} + Q_{pTEC} - (T_{hs} - T_a)/R
\end{aligned} \tag{B.2}$$

where  $T_b$ ,  $T_a$ , and  $T_{hs}$  are the enclosure, enclosure internal air, and heat sink temperatures, respectively,  $Q_{sol}$ ,  $Q_e$ ,  $Q_{cTEC}$ ,  $Q_{pTEC}$  are the heat flux into the enclosure due to solar heating, electrical power dissipated within the enclosure due to the electronics, and the cooling heat flux and resistive heating, respectively, generated by the thermoelectric cooler. The other parameters and their values are described in Table B.1.

The heat transfer coefficients on the exterior,  $h_{be}$ , and interior,  $h_{bi}$ , surfaces of the enclosure are calculated using (Incropera & DeWitt, 1996):

$$Nu = 0.68 + \frac{0.67 Ra^{1/4}}{(1 + (0.492/Pr)^{9/16})^{4/9}} \tag{B.3}$$

where  $Nu$ ,  $Ra$ , and  $Pr$  are the Nusselt, Rayleigh, and Prandtl numbers, respectively. The thermoelectric cooler heat fluxes are calculated using (Chein & Huang, 2004):

$$\begin{aligned}
Q_{cTEC} &= S_m T_s I - 0.5 R_m I^2 - K_m (T_{hs} - T_s) \\
Q_{pTEC} &= VI = V(V - S_m (T_{hs} - T_s))/R_m
\end{aligned} \tag{B.4}$$

where  $V$  and  $I$  are the TEC voltage and current and the other parameters are given in Table B.1.

Using these parameters we determined that a minimum ventilation flow rate of  $80 \text{ ft}^3 \text{ min}^{-1}$  and a maximum thermal resistance of the heat sink of  $1.0 \text{ K W}^{-1}$  are required. Thus a

Table B.1: Parameters used in equations (B.2) and (B.4).

Parameter	Description	Value
$\epsilon$	emissivity of the enclosure	0.2
$A_b$	surface area of the enclosure	$2.93 \text{ m}^2$
$R$	thermal resistance of the heat sink	
$\rho_{air}$	density of air	$1.2 \text{ kg m}^{-3}$
$C_{pair}$	specific heat capacity of air	$1000 \text{ J kg}^{-1} \text{ K}^{-1}$
$\dot{V}_{air}$	Ventilation flow rate through enclosure	
$Q_{sol}$	Solar heating	$787 \text{ W}$
$Q_e$	Electrical power dissipation in enclosure	$100 \text{ W}$
$S_m$	TEC module Seebeck coefficient	$0.0506 \text{ V K}^{-1}$
$R_m$	TEC module resistance	$1.97 \Omega$
$K_m$	TEC module thermal conductivity	$0.52 \text{ W K}^{-1}$

CPU cooler and fan combination was chosen to meet the required thermal resistance of the heat sink. A suitable fan was chosen for the enclosure ventilation.

Figure B.8 shows an overview of the CPC measurement system as it is used in the Riverside field study. All equipment was attached to light poles next to the road.

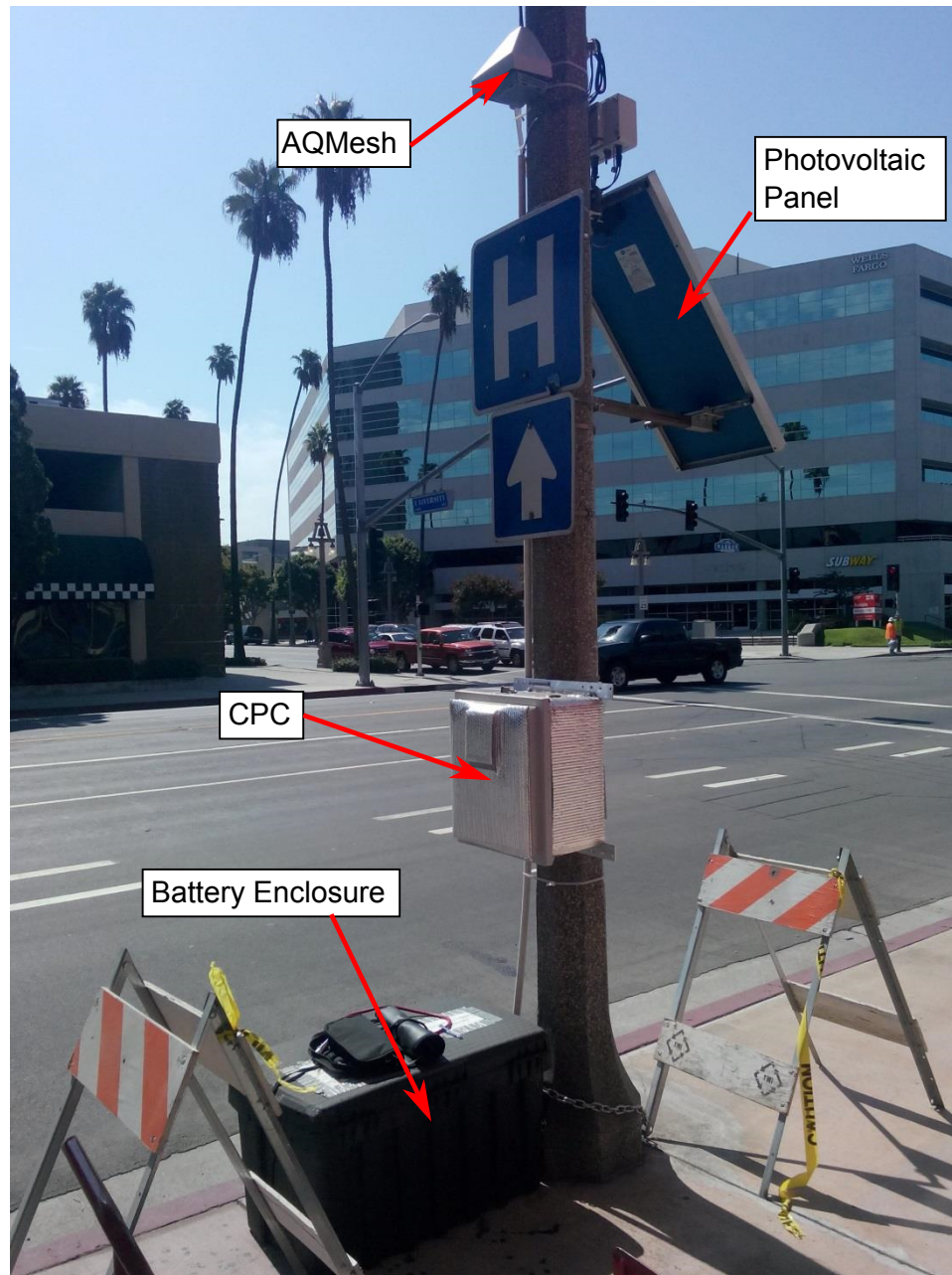


Figure B.8: CPC measurement system at the Riverside Market St field site.

## B.4 Data Logger

The data logger is based on the Raspberry Pi single board computer. The Raspberry Pi runs a variant of the Debian Linux operating system. An SD card provides storage of

the operating system files and the data recorded from the instruments. Several general purpose input/output connections are available for use on a pin header on the Raspberry Pi board. A custom circuit board was designed to interface with the pin header on the Raspberry pi. The custom circuit provides a real time battery backed clock, a serial port compliant with RS232 voltage levels, and an analog to digital converter. Figure B.9 shows a schematic of the data logger circuit. The DS3231 provides real time clock functions. The MAX3232 provides level shifting to convert the Raspberry Pi serial port voltages to RS232 voltage levels. Several additional connections are made with the serial port connector J1. These connections provide signals to the CPC that control the thermoelectric cooler and fans used to cool the CPC saturator. The MAX1416 and MAX6071 provide analog to digital functions. A switch and two LEDs allow user interaction with the data logger.

Software to collect data from the instruments and provide other data logger functions was written in python. The software consists of several components. One program is responsible for sending commands to the CPC and receiving data, and then subsequently appending the data to a text file. A new text file is created every 30 minutes. The Linux cron utility is used to start data collection with a new file every at each half hour. A separate program is run when the data logger is first started. This program scans the data files to ensure that valid data is being recorded. If valid data is not received, the program sends a notification message to a chosen email address. The program also sends a notification every hour to allow users to verify that the systems are functioning. The cellular modem is connected to a USB port of the Raspberry Pi to provide network access to the data logger.

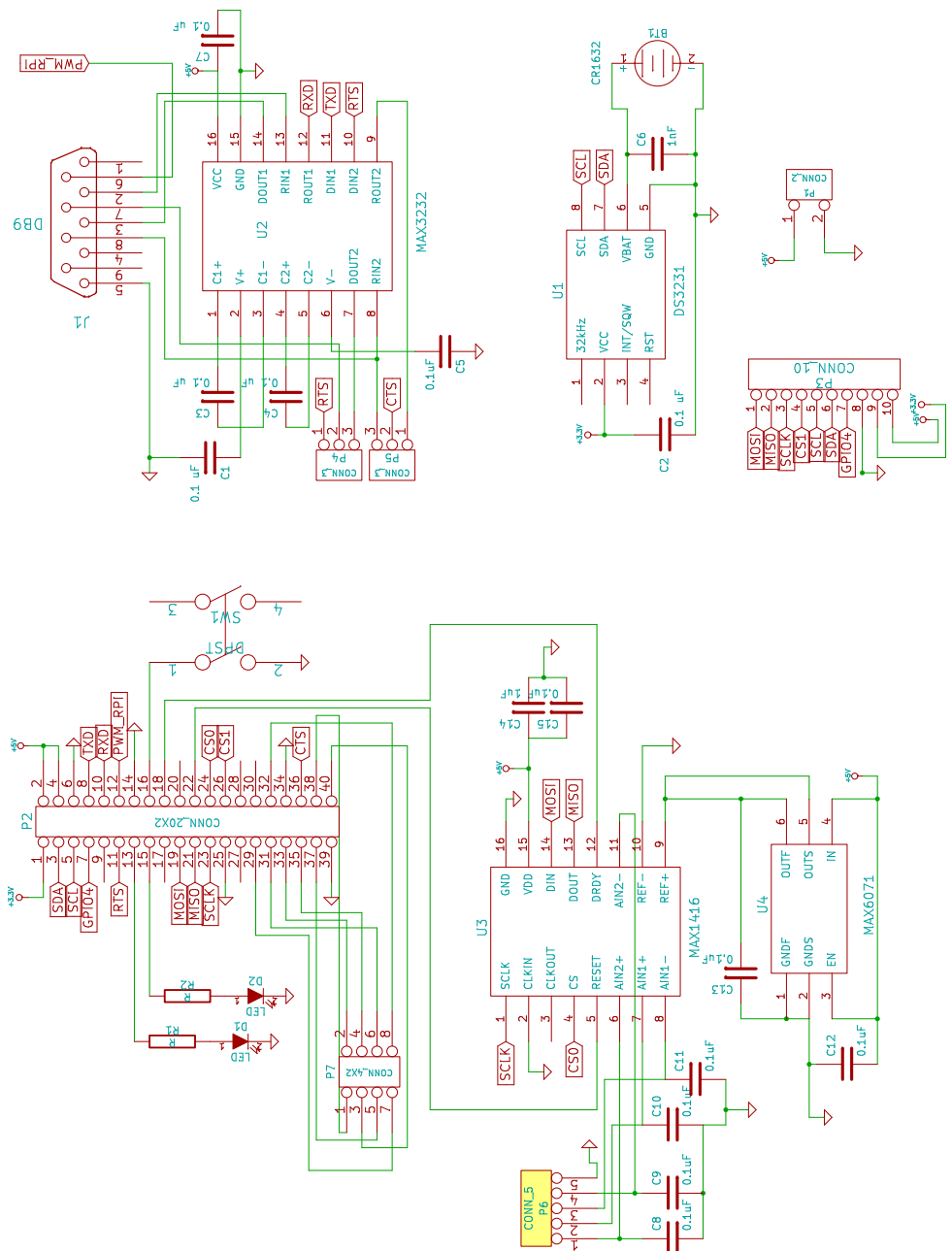


Figure B.9: Schematic of data logger.

# Bibliography

- Allwine, K. J., Shinn, J. H., Streit, G. E., Clawson, K. L., & Brown, M. (2002). Overview of urban 2000 A Multiscale Field Study of Dispersion through an Urban Environment. *Bulletin of the American Meteorological Society*, *83*, 521–536.
- Arnold, S. J., ApSimon, H., Barlow, J., Belcher, S., Bell, M., Boddy, J. W., Britter, R., Cheng, H., Clark, R., Colvile, R. N., Dimitroulopoulou, S., Dobre, a., Grealley, B., Kaur, S., Knights, a., Lawton, T., Makepeace, a., Martin, D., Neophytou, M., Neville, S., Nieuwenhuijsen, M., Nickless, G., Price, C., Robins, a., Shallcross, D., Simmonds, P., Smalley, R. J., Tate, J., Tomlin, a. S., Wang, H., & Walsh, P. (2004). Introduction to the DAPPLE Air Pollution Project. *The Science of the total environment*, *332*, 139–53. doi:10.1016/j.scitotenv.2004.04.020. arXiv:15336898.
- Baldauf, R., Thoma, E., Khlystov, A., Isakov, V., Bowker, G., Long, T., & Snow, R. (2008). Impacts of noise barriers on near-road air quality. *Atmospheric Environment*, *42*, 7502–7507. doi:10.1016/j.atmosenv.2008.05.051.
- Barlow, J. F., & Belcher, S. E. (2002). A Wind Tunnel Model for Quantifying Fluxes In The Urban Boundary Layer. *Boundary-Layer Meteorology*, *104*, 131–150.
- Belcher, S. E., Jerram, N., & Hunt, J. C. R. (2003). Adjustment of a turbulent boundary layer to a canopy of roughness elements. *Journal of Fluid Mechanics*, *488*, 369–398. doi:10.1017/S0022112003005019.
- Bentham, T., & Britter, R. (2003). Spatially averaged flow within obstacle arrays. *Atmospheric Environment*, *37*, 2037–2043. doi:10.1016/S1352-2310(03)00123-7.
- Berkowicz, R. (2000). OSPM - A Parameterised Street Pollution Model. *Environmental Monitoring and Assessment*, *65*, 323–331.
- Berkowicz, R., Hertel, O., Larsen, S. E., Sorensen, N. N., & Nielsen, M. (1997). *Modelling traffic pollution in streets*. Technical Report National Environmental Research Institute.
- Boarnet, M., & Crane, R. (2007). L. A. Story, A Reality Check for Transit-Based Housing. *Journal of the American Planning Association*, *63*, 189–204.
- Bowker, G., Baldauf, R., Isakov, V., Khlystov, A., & Petersen, W. (2007). The effects of roadside structures on the transport and dispersion of ultrafine particles from highways. *Atmospheric Environment*, *41*, 8128–8139. doi:10.1016/j.atmosenv.2007.06.064.

- Brauer, M. (2002). Air Pollution from Traffic and the Development of Respiratory Infections and Asthmatic and Allergic Symptoms in Children. *American Journal of Respiratory and Critical Care Medicine*, *166*, 1092–1098. doi:10.1164/rccm.200108-0070C.
- Britter, R. E., & Hanna, S. R. (2003). Flow and Dispersion in Urban Areas. *Annual Review of Fluid Mechanics*, *35*, 469–496. doi:10.1146/annurev.fluid.35.101101.161147.
- Bukowiecki, N., Dommen, J., Prévôt, A. S. H., Richter, R., Weingartner, E., & Baltensperger, U. (2002). A mobile pollutant measurement laboratory—measuring gas phase and aerosol ambient concentrations with high spatial and temporal resolution. *Atmospheric Environment*, *36*, 5569–5579. doi:10.1016/S1352-2310(02)00694-5.
- Businger, J. A., Wyngaard, J. C., Izumi, Y., & Bradley, E. F. (1971). Flux-Profile Relationships in the Atmospheric Surface Layer. *Journal of Applied Meteorology*, *28*, 181–189.
- CARB (2015a). Air Quality and Meteorological Information System. URL: <http://www.arb.ca.gov/aqmis2/aqmis2.php>.
- CARB (2015b). Mobile Source Emission Inventory. URL: <http://www.arb.ca.gov/msei/msei.htm>.
- Caton, F., Britter, R., & Dalziel, S. (2003). Dispersion mechanisms in a street canyon. *Atmospheric Environment*, *37*, 693–702. doi:10.1016/S1352-2310(02)00830-0.
- Chein, R., & Huang, G. (2004). Thermoelectric cooler application in electronic cooling. *Applied Thermal Engineering*, *24*, 2207–2217. doi:10.1016/j.applthermaleng.2004.03.001.
- Coccal, O., & Belcher, S. (2004). A canopy model of mean winds through urban areas. *Quarterly Journal of the Royal Meteorological Society*, *130*, 1349–1372. doi:10.1256/qj.03.40.
- Dabberdt, W. F., Ludwig, F. L., & Warren B. Johnson, J. (1973). VALIDATION AND APPLICATIONS OF AN URBAN DIFFUSION MODEL FOR VEHICULAR POLLUTANTS. *Atmospheric Environment*, *7*, 603–618.
- DePaul, F. T., & Sheih (1985). A TRACER STUDY OF DISPERSION IN AN URBAN STREET CANYON. *Atmospheric Environment*, *19*, 555–559.
- DePaul, F. T., & Sheih, C. M. (1986). Measurements of wind velocities in a street canyon. *Atmospheric Environment*, *20*, 455–459. doi:10.1016/0004-6981(86)90085-5.
- Di Sabatino, S., Buccolieri, R., Pulvirenti, B., & Britter, R. (2007). Simulations of pollutant dispersion within idealised urban-type geometries with CFD and integral models. *Atmospheric Environment*, *41*, 8316–8329. doi:10.1016/j.atmosenv.2007.06.052.
- Finkelstein, M. M., Jerrett, M., & Sears, M. R. (2004). Traffic air pollution and mortality rate advancement periods. *American journal of epidemiology*, *160*, 173–177. doi:10.1093/aje/kwh181. arXiv:15234939.

- Finn, D., Clawson, K. L., Carter, R. G., Rich, J. D., Eckman, R. M., Perry, S. G., Isakov, V., & Heist, D. K. (2010). Tracer studies to characterize the effects of roadside noise barriers on near-road pollutant dispersion under varying atmospheric stability conditions. *Atmospheric Environment*, *44*, 204–214. doi:10.1016/j.atmosenv.2009.10.012.
- Fisher, B., Kukkonen, J., Piringer, M., Rotach, M. W., & Schatzmann, M. (2006). Meteorology applied to urban air pollution problems: concepts from COST 715. *Atmospheric Chemistry and Physics*, *6*, 555–564. doi:10.5194/acp-6-555-2006.
- Garratt, J. R. (1990). The Internal Boundary Layer - A Review. *Boundary-Layer Meteorology*, *50*, 171–203.
- Grimmond, C., & Oke, T. R. (1999). Aerodynamic Properties of Urban Areas Derived from Analysis of Surface Form. *Journal of Applied Meteorology*, *38*, 1262–1292.
- Hagler, G. S., Tang, W., Freeman, M. J., Heist, D. K., Perry, S. G., & Vette, A. F. (2011). Model evaluation of roadside barrier impact on near-road air pollution. *Atmospheric Environment*, *45*, 2522–2530. doi:10.1016/j.atmosenv.2011.02.030.
- Hanna, S., Chang, J. C., & Flaherty, J. (2014). Observed Ratios of Rooftop to Surface Concentrations in Built-Up City Centers. URL: [www.ametsoc.org](http://www.ametsoc.org).
- Hanna, S., White, J., & Zhou, Y. (2007). Observed winds, turbulence, and dispersion in built-up downtown areas of Oklahoma City and Manhattan. *Boundary-Layer Meteorology*, *125*, 441–468. doi:10.1007/s10546-007-9197-2.
- Hanna, S. R. (1989). Confidence limits for air quality model evaluations, as estimated by bootstrap and jackknife resampling methods. *Atmospheric Environment (1967)*, *23*, 1385–1398. doi:10.1016/0004-6981(89)90161-3.
- Hanna, S. R., & Zhou, Y. (2009). Space and Time Variations in Turbulence during the Manhattan Midtown 2005 Field Experiment. *Journal of Applied Meteorology and Climatology*, *48*, 2295–2304. doi:10.1175/2009JAMC2046.1.
- Harrison, R. M., Leung, P. L., Somerville, L., Smith, R., & Gilman, E. (1999). Analysis of incidence of childhood cancer in the West Midlands of the United Kingdom in relation to proximity to main roads and petrol stations. *Occupational and environmental medicine*, *56*, 774–780.
- Heist, D. K., Perry, S. G., & Brixey, L. A. (2009). A wind tunnel study of the effect of roadway configurations on the dispersion of traffic-related pollution. *Atmospheric Environment*, *43*, 5101–5111. doi:10.1016/j.atmosenv.2009.06.034.
- Hess, D. B., Ray, P. D., Stinson, A. E., & Park, J. (2010). Determinants of exposure to fine particulate matter (PM<sub>2.5</sub>) for waiting passengers at bus stops. *Atmospheric Environment*, *44*, 5174–5182. doi:10.1016/j.atmosenv.2010.08.046.
- Hitchins, J., Morawska, L., Wolff, R., & Gilbert, D. (2000). Concentrations of submicrometre particles from vehicle emissions near a major road. *Atmospheric Environment*, *34*, 51–59. doi:10.1016/S1352-2310(99)00304-0.

- Hoek, G., Brunekreef, B., Goldbohm, S., Fischer, P., & van den Brandt, P. (2002). Association between mortality and indicators of traffic-related air pollution in the Netherlands: a cohort study. *Lancet*, *360*, 1203–1209. doi:10.1016/S0140-6736(02)11280-3. arXiv:12401246.
- Holtzlag, A. A. M., & Van Ulden, A. P. (1983). A Simple Scheme for Daytime Estimates of the Surface Fluxes from Routine Weather Data. *Journal of Climate and Applied Meteorology*, *22*, 517–529.
- Hooghwerff, J., Tollenaar, C. C., & van der Heijden, W. J. (2010). In-situ air quality measurements on existing and innovative noise barriers. In C. Brebbia, & J. Longhurst (Eds.), *Air Pollution XVIII* (pp. 129–139). WIT Press.
- Hoydysh, W. G., & Dabberdt, W. F. (1988). Kinematics and Dispersion Characteristics of Flows in Asymmetric Street Canyons. *Atmospheric Environment*, *22*, 2677–2689.
- Huber, A. H. (1984). Evaluation of a method for estimating pollution concentrations downwind of influencing buildings. *Atmospheric Environment*, *18*, 2313–2338. doi:10.1016/0004-6981(84)90003-9.
- Huber, A. H. (1988). Performance of a Gaussian model for centerline concentrations in the wake of buildings. *Atmospheric Environment*, *22*, 1039–1050. doi:10.1016/0004-6981(88)90334-4.
- Huber, A. H., & Snyder, W. H. (1982). Wind tunnel investigation of the effects of a rectangular-shaped building on dispersion of effluents from short adjacent stacks. *Atmospheric Environment*, *16*, 2837–2848. doi:10.1016/0004-6981(82)90034-8.
- Incropera, F. P., & DeWitt, D. P. (1996). *Fundamentals of Heat and Mass Transfer*. (4th ed.). John Wiley & Sons.
- Iser, F., & Scharl, C. (2009). *EU-LIFE Projekt SPAS Task 3: Simulationen Abschlussbericht*. Technical Report Kompetenzzentrum - Das virtuelle Fahrzeug Forschungsgesellschaft mbH (ViF). URL: [http://www.life-spas.at/deutsch/includes/Iser\\_SPAS\\_Endbericht\\_-\\_Final\(1\).pdf](http://www.life-spas.at/deutsch/includes/Iser_SPAS_Endbericht_-_Final(1).pdf).
- Jackson, P. S., & Hunt, J. C. R. (1975). Turbulent wind flow over a low hill. *Quarterly Journal of the Royal Meteorological Society*, *101*, 929–955. doi:10.1002/qj.49710143015.
- James L McElroy (1969). A Comparative Study of Urban and Rural Dispersion. *Journal of Applied Meteorology*, *8*, 19–31.
- James L McElroy, & Francis Pooler, Jr. (1968). *St. Louis Dispersion Study Volume I - Instrumentation, Procedures, And Data Tabulations*. Technical Report APTD-68-12 National Air Pollution Control Administration.
- Johnson, W. B., Ludwig, F. L., Dabberdt, W. F., & Allen, R. J. (1973). An Urban Diffusion Simulation Model For Carbon Monoxide. *Journal of the Air Pollution Control Association*, *23*, 490–498.

- Kaimal, J. C., & Finnigan, J. J. (1994). *Atmospheric boundary layer flows: their structure and measurement*. Oxford University Press.
- Kastner-Klein, P., & Plate, E. (1999). Wind-tunnel study of concentration fields in street canyons. *Atmospheric Environment*, *33*, 3973–3979. doi:10.1016/S1352-2310(99)00139-9.
- Ketzel, M., Wählin, P., Berkowicz, R., & Palmgren, F. (2003). Particle and trace gas emission factors under urban driving conditions in Copenhagen based on street and roof-level observations. *Atmospheric Environment*, *37*, 2735–2749. doi:10.1016/S1352-2310(03)00245-0.
- Kim, J., Smorodinsky, S., Ostro, B., Lipsett, M., Singer, B., & Hogdson, A. (2002). Traffic-related Air Pollution and Respiratory Health: the East Bay Children's Respiratory Health Study. *Epidemiology*, *13*, S100–S100.
- Kittelson, D. B., Watts, W. F., & Johnson, J. P. (2004). Nanoparticle emissions on Minnesota highways. *Atmospheric Environment*, *38*, 9–19. doi:10.1016/j.atmosenv.2003.09.037.
- Knibbs, L. D., Cole-Hunter, T., & Morawska, L. (2011). A review of commuter exposure to ultrafine particles and its health effects. *Atmospheric Environment*, *45*, 2611–2622. doi:10.1016/j.atmosenv.2011.02.065.
- Kukkonen, J., Partanen, L., Karppinen, A., Walden, J., Kartastenpää, R., Aarnio, P., Koskentalo, T., & Berkowicz, R. (2003). Evaluation of the OSPM model combined with an urban background model against the data measured in 1997 in Runeberg Street, Helsinki. *Atmospheric Environment*, *37*, 1101–1112. doi:10.1016/S1352-2310(02)00957-3.
- Kumar, P., Ketzel, M., Vardoulakis, S., Pirjola, L., & Britter, R. (2011). Dynamics and dispersion modelling of nanoparticles from road traffic in the urban atmospheric environment—A review. *Journal of Aerosol Science*, *42*, 580–603. doi:10.1016/j.jaerosci.2011.06.001.
- Los Angeles County (2008). Countywide Building Outlines. URL: <http://egis3.lacounty.gov/dataportal/2011/04/28/countywide-building-outlines/>.
- Louka, P., Belcher, S. E., & Harrison, R. G. (2000). Coupling between air flow in streets and the well-developed boundary layer aloft. *Atmospheric Environment*, *34*, 2613–2621.
- MacDonald, R., Griffiths, R., & Hall, D. (1998). An improved method for the estimation of surface roughness of obstacle arrays. *Atmospheric Environment*, *32*, 1857–1864. doi:10.1016/S1352-2310(97)00403-2.
- MacDonald, R. W. (2000). Modelling the Mean Velocity Profile in the Urban Canopy Layer. *Boundary-Layer Meteorology*, *97*, 25–45.
- Magistrat Klagenfurt (2011). EU-LIFE project SPAS. URL: <http://www.life-spas.at>.

- McCrae, I. (2010). *Scientific Board Review: International review of the Air Quality Innovation Programme (IPL)*. Technical Report Rijkswaterstaat - Dienst Verkeer en Scheepvaart Afdeling Innovatie & Implementatie (MII) Innovatieprogramma Luchtkwaliteit (IPL). URL: <http://www.ipl-airquality.nl/data/Eindrapport%0020SB%0020definitief.pdf>.
- Meroney, R. N., Pavageau, M., Rafailidis, S., & Schatzmann, M. (1996). Study of line source characteristics for 2-D physical modelling of pollutant dispersion in street canyons. *Journal of Wind Engineering and Industrial Aerodynamics*, *62*, 37–56.
- Nakamura, Y., & Oke, T. (1988). Wind, temperature and stability conditions in an east-west oriented urban canyon. *Atmospheric Environment*, *22*, 2691–2700. doi:10.1016/0004-6981(88)90437-4.
- Nelson, M. A., Pardyjak, E. R., Klewicki, J. C., Pol, S. U., & Brown, M. J. (2007). Properties of the Wind Field within the Oklahoma City Park Avenue Street Canyon. Part I: Mean Flow and Turbulence Statistics. *Journal of Applied Meteorology and Climatology*, *46*, 2038–2054. doi:10.1175/2006JAMC1427.1.
- Nicholson, S. E. (1975). A Pollution Model For Street-Level Air. *Atmospheric Environment*, *9*, 19–31.
- Ning, Z., Hudda, N., Daher, N., Kam, W., Herner, J., Kozawa, K., Mara, S., & Sioutas, C. (2010). Impact of roadside noise barriers on particle size distributions and pollutants concentrations near freeways. *Atmospheric Environment*, *44*, 3118–3127. doi:10.1016/j.atmosenv.2010.05.033.
- Oke, T. (1988). Street design and urban canopy layer climate. *Energy and Buildings*, *11*, 103–113. doi:10.1016/0378-7788(88)90026-6.
- Paulson, C. A. (1970). The Mathematical Representation of Wind Speed and Temperature Profiles in the Unstable Atmospheric Surface Layer. *Journal of Applied Meteorology*, *9*, 857–861.
- Puttock, J. S., & Hunt, J. C. R. (1979). Turbulent Diffusion From Sources Near Obstacles with Separated Wakes - Part I. An Eddy Diffusivity Model. *Atmospheric Environment*, *13*, 1–13.
- Rodler, J., & Henn, M. (2009). *Filter Effect of SPAS and Impact on Air Quality*. Technical Report Graz University of Technology. URL: [www.life-spas.at/deutsch/includes/19\\_SPAS\\_Rodler\\_eng.pdf](http://www.life-spas.at/deutsch/includes/19_SPAS_Rodler_eng.pdf).
- Rotach, M. W., Vogt, R., Bernhofer, C., Batchvarova, E., Christen, A., Clappier, A., Feddersen, B., Gryning, S.-E., Martucci, G., Mayer, H., Mitev, V., Oke, T. R., Parlow, E., Richner, H., Roth, M., Roulet, Y.-a., Ruffieux, D., a. Salmond, J., Schatzmann, M., & a. Voogt, J. (2005). BUBBLE – an Urban Boundary Layer Meteorology Project. *Theoretical and Applied Climatology*, *81*, 231–261. doi:10.1007/s00704-004-0117-9.
- Schulman, L. L., Strimaitis, D. G., & Scire, J. S. (2000). Development and Evaluation of the PRIME Plume Rise and Building Downwash Model. *Journal of the Air & Waste Management Association*, *50*, 378–390.

- Schulte, N., Snyder, M., Isakov, V., Heist, D., & Venkatram, A. (2014). Effects of solid barriers on dispersion of roadway emissions. *Atmospheric Environment*, *97*, 286–295. doi:10.1016/j.atmosenv.2014.08.026.
- Schulte, N., Tan, S., & Venkatram, A. (2015). The Ratio of Effective Building Height to Street Width Governs Dispersion of Local Vehicle Emissions. *Atmospheric Environment*, *112*, 54–63.
- Smit, R., Brown, A. L., & Chan, Y. C. (2008). Do air pollution emissions and fuel consumption models for roadways include the effects of congestion in the roadway traffic flow? *Environmental Modelling & Software*, *23*, 1262–1270. doi:10.1016/j.envsoft.2008.03.001.
- Smit, R., Ntziachristos, L., & Boulter, P. (2010). Validation of road vehicle and traffic emission models – A review and meta-analysis. *Atmospheric Environment*, *44*, 2943–2953. doi:10.1016/j.atmosenv.2010.05.022.
- Soulhac, L., Salizzoni, P., Cierco, F.-X., & Perkins, R. (2011). The model SIRANE for atmospheric urban pollutant dispersion; part I, presentation of the model. *Atmospheric Environment*, *45*, 7379–7395. doi:10.1016/j.atmosenv.2011.07.008.
- Steffens, J. T., Heist, D. K., Perry, S. G., & Zhang, K. M. (2013). Modeling the effects of a solid barrier on pollutant dispersion under various atmospheric stability conditions. *Atmospheric Environment*, *69*, 76–85. doi:10.1016/j.atmosenv.2012.11.051.
- Stockie, J. M. (2011). The Mathematics of Atmospheric Dispersion Modeling. *Society for Industrial and Applied Mathematics*, *53*, 349–372.
- Tennekes, H., & Lumley, J. (1972). *A First Course in Turbulence*. MIT Press.
- TSI (2002). Model 3022A Condensation Particle Counter Instruction Manual.
- Vardoulakis, S., Fisher, B. E., Pericleous, K., & Gonzalez-Flesca, N. (2003). Modelling air quality in street canyons: a review. *Atmospheric Environment*, *37*, 155–182. doi:10.1016/S1352-2310(02)00857-9.
- Venkatram, A., & Horst, T. (2006). Approximating dispersion from a finite line source. *Atmospheric Environment*, *40*, 2401–2408. doi:10.1016/j.atmosenv.2005.12.014.
- Venkatram, A., Isakov, V., Thoma, E., & Baldauf, R. (2007). Analysis of air quality data near roadways using a dispersion model. *Atmospheric Environment*, *41*, 9481–9497. doi:10.1016/j.atmosenv.2007.08.045.
- Venkatram, A., Snyder, M. G., Heist, D. K., Perry, S. G., Petersen, W. B., & Isakov, V. (2013). Re-formulation of Plume Spread for Near-Surface Dispersion. *Atmospheric Environment*, *77*, 846–855. doi:10.1016/j.atmosenv.2013.05.073.
- Walker, M. (1964). *The Schwarz-Christoffel transformation and its applications; a simple exposition*. Dover Publications.
- Weil, J. C. (1996). (pp. 333–337). American Meteorological Society.

- Wilson, D. J., & Britter, R. E. (1982). Estimates of building surface concentrations from nearby point sources. *Atmospheric Environment*, *16*, 2631–2646. URL: <http://www.sciencedirect.com/science/article/pii/0004698182903456>.
- Yamartino, R. J., & Wiegand, G. (1986). Development and evaluation of simple models for the flow, turbulence and pollutant concentration fields within an urban street canyon. *Atmospheric Environment*, *20*, 2137–2156. doi:10.1016/0004-6981(86)90307-0.
- Zhou, Y., & Levy, J. (2008). The impact of urban street canyons on population exposure to traffic-related primary pollutants. *Atmospheric Environment*, *42*, 3087–3098. doi:10.1016/j.atmosenv.2007.12.037.
- Zhu, Y., Hinds, W. C., Kim, S., Shen, S., & Sioutas, C. (2002a). Study of ultrafine particles near a major highway with heavy-duty diesel traffic. *Atmospheric Environment*, *36*, 4323–4335. doi:10.1016/S1352-2310(02)00354-0.
- Zhu, Y., Hinds, W. C., Kim, S., & Sioutas, C. (2002b). Concentration and Size Distribution of Ultrafine Particles Near a Major Highway. *Journal of the Air & Waste Management Association*, *52*, 1032–1042.